UNIVERSITY OF SOUTHAMPTON

FACULTY OF ENGINEERING AND THE ENVIRONMENT

Fluid Structure Interactions Group

Experimental and numerical investigation of slamming loads on high-speed craft including hydroelastic effects

by

Josef Camilleri

Thesis for the degree of Doctor of Philosophy

2017

UNIVERSITY OF SOUTHAMPTON

ABSTRACT

FACULTY OF ENGINEERING AND THE ENVIRONMENT

Thesis for the degree of Doctor of Philosophy

EXPERIMENTAL AND NUMERICAL INVESTIGATION OF SLAMMING LOADS ON HIGH-SPEED CRAFT INCLUDING HYDROELASTIC EFFECTS

Josef Camilleri

This thesis investigates the problem of slamming loads on high-speed planing craft and related global rigid body and local structural responses using numerical simulations and full-scale tests. The aim of this work is to improve the safety and efficiency of high-speed craft structural designs for realistic operational loads.

A numerical model for simulating the water impact of two- and three-dimensional rigid and flexible structures is developed. The model uses the commercial CFD software Star CCM+ to solve for the fluid flow and the FE code ABAQUS to solve for the structural response. Two different water entry problems are studied - the water impact of a free-falling rigid wedge and the constant velocity water entry of a flexible composite panel - and the results are compared with the experimental data of Lewis et al. (2010) and Allen & Battley (2015), respectively, for validation. The influence of several numerical and experimental parameters on the solution, including grid and time step size, fluid compressibility, three-dimensional effects, structural boundary conditions and hydroelastic effects, is investigated. The model is then applied to simulate the full-scale drop tests of a realistic hull, also conducted within the framework of this thesis, and the results are compared with the measured data for validation. The effect of three-dimensional flow and spray rails is investigated.

Full-scale rough water trials and drop tests on a 9.6m high-speed planing craft have also been performed. Measurements of rigid body motions, accelerations, pressures, strains and global hull deflections were made for various sea conditions, speeds and headings (rough water trials) and drop heights (drop tests). Methods for processing the experimental data, including low pass filtering the acceleration signals, removing baseline drifts from the strain signals and identifying the peaks in the pressure and strain signals are developed and successfully applied. Characteristic results from the rough water trials including, segments of the time signals, histograms of the identified peaks, calculated averages of the largest $1/3^{rd}$ and $1/10^{th}$ peak values, and the loads and responses recorded in a typical impact event, and characteristic drop test measurements are presented and discussed. The repeatability and symmetry of the drop test is also investigated. Statistical analysis of the rough water trials measurements is also performed. The Weibull and generalized Pareto models are fitted to the samples of identified pressure and strain peaks for estimating extreme loads and responses. Automated algorithms for fitting the statistical models to the peak value distributions are developed and the goodness-of-fit of the models to the data is examined.

The suitability of the design loads used in current practice is assessed by comparing the acceleration and pressure measurements from the rough water trials with the predictions based on the ISO (2008) standard and DNV GL (2015) and Lloyd's Register (2016) rules. Preliminary comparisons between pressure and strain measurements from the rough water trials and the drop tests measurements are also made to examine the relationship between the two tests.

Table of Contents

List of Tables

List of Figures

Declaration of authorship

I, **Josef Camilleri** declare that this thesis entitled

Experimental and numerical investigation of slamming loads on high-speed craft including hydroelastic effects

and the work presented in it are my own and has been generated by me as the result of my own original research. I confirm that:

- this work was done wholly or mainly while in candidature for a research degree at this University;
- where any part of this thesis has previously been submitted for a degree or any other qualification at this University or any other institution, this has been clearly stated;
- where I have consulted the published work of others, this is always clearly attributed;
- where I have quoted from the work of others, the source is always given. With the exception of such quotations, this thesis is entirely my own work;
- I have acknowledged all main sources of help;
- where the thesis is based on work done by myself jointly with others, I have made clear exactly what was done by others and what I have contributed myself;
- parts of this work have been published as listed in Appendix A.

Signed: .....

Date: .....

Acknowledgements

Many people have contributed to this thesis in many ways. Firstly, my sincere thanks to my supervisors - Prof Pandeli Temarel and Dr Dominic Taunton - for giving me the opportunity and for their continuous support, help and guidance throughout these years.

I am grateful for the financial support of the defence, science and technology laboratory (dstl). Thank you also to Dr Alan Groves, Chris Broadbent, Chris Saunders and Chris Hawkins from dstl for the helpful discussions during our quarterly meetings.

I would also like to thank Dr Tom Allen at the University of Auckland for providing the flexible composite panel experimental data and for explaining some of the details of the tests. I am also grateful for the help and assistance from the staff at ASV Global with setting up and conducting the full-scale tests.

Finally, I would like to thank my family and friends for their support and encouragement. I am especially appreciative of my partner, Doreen, whose love, patience, and support have made all of this possible.

Thank you all very much, Josef.

Nomenclature

Symbols are defined at the point of first use in the text and the most widely used are listed here. Some characters such as a are used differently in separate chapters.

Latin symbols

a	Weibull scale parameter	[kPa], [strain]
A	Area	[m^2]
b	Weibull shape parameter	[-]
B	Craft beam	[m]
c	Speed of sound, Generalized Pareto distribution shape parameter	[m/s], [-]
D	Flexural rigidity	[kNm]
E	Young Modulus	[GPa]
f	Frequency	[Hz]
F	Force	[N]
F(x)	Cumulative distribution function	[-]
G	Shear Modulus	[GPa]
h	Drop height	[m]
H	Craft height	[m]
H_s	Significant wave height	[m]
H_{max}	Maximum wave height	[m]
I	Impulse	[Ns]
k	Number of peaks above threshold	[-]
K_D	Pressure reduction coefficient	[-]
L	Craft length	[m]
m	Number of threshold values	[-]
n	Sample size	[-]
p, P	Pressure	[kPa]
R^2	Coefficient of determination	[-]
s^2	Sample variance	[kPa], [strain]
S	Shear stiffness	[kN/m]
t	Time	[s]
T	Craft draft	[m]
T_z	Zero crossing period	[s]
u	Threshold value	[-]
v	Poisson ratio	[-]

V	Velocity	[m/s]
x	Observed value	[kPa], [strain]
x_e	Extreme value	[kPa], [strain]
$\hat{x}$	Estimated value	[kPa], [strain]
$\bar{x}^2$	Sample mean	[kPa], [strain]
Δn, Δt, Δh	Grid cell size normal and tangential to body surface and in the vertical direction around free surface.	[mm]

Greek symbols

α	Probability of exceedance	[%]
β	Deadrise angle	[°]
Δ	Craft displacement	[kg]
λ	Generalized Pareto distribution scale parameter	[kPa], [strain]
μ	Mean	[kPa], [strain]
ρ	Density	[kg/m^3]
σ	Standard deviation	[kPa], [strain]
τ	Trim angle	[°]

Abbreviations and acronyms

2D	Two-dimensional
3D	Three-dimensional
BEM	Boundary Element Method
CFRP	Carbon Fibre Reinforced Plastic
CFD	Computational Fluid Dynamics
CPU	Central Processing Unit
CSE	Co-Simulation Engine
CV	Control Volume(s)
DFBI	Dynamic Fluid Body Interaction
DNV	Det Norske Veritas
FD	Finite Difference
FE	Finite Element
FFT	Fast Fourier Transform
FSI	Fluid Structure Interaction
FV	Finite Volume
GCI	Grid Convergence Index
GEV	Generalized Extreme Value
GL	Germanischer Lloyd

GPD	Generalized Pareto Distribution
GPS	Global Positioning System
GRP	Glass Reinforced Plastic
HRIC	High Resolution Interface Capturing
IMU	Inertial Measurement Unit
ISO	International Organization for Standardization
LCG	Longitudinal Centre of Gravity
LR	Lloyd's Register
Ma	Mach Number
MOM	Method of Moments
MPS	Moving Particle Semi-Implicit
NA	Not Applicable
NI	National Instruments
NR	Not Reported
NS	Navier Stoke
PIV	Particle Image Velocimetry
POT	Peak Over Threshold
RE	Richardson Extrapolation
RIB	Rigid-Inflatable Boat
RMS(E)	Root Mean Square (Error)
RNLI	Royal National Lifeboat Institution
RQS	Rigid/ Quasi-Static
SAN	Styrene Acrylonitrile
SCL	Space Conservation Law
SIMPLE	Semi-Implicit Method for Pressure Linked Equations
SPH	Smoothed Particle Hydrodynamics
SSTS	Servo-Hydraulic Slam Testing System
VOF	Volume of Fluid
WBL	Weibull

Chapter 1. Introduction

1.1. Motivation

High-speed planing craft, such as, patrol, military and search and rescue craft often have to operate at high speeds in rough seas to intercept threats or respond to emergencies. Figure 1 shows two examples of high-speed planing craft, the RNLI B class Atlantic 85 lifeboat launching off a wave and the Damen Interceptor 1102 airborne, moments before impacting the water surface. In such conditions, as can be seen from Figure 1, the craft frequently emerges from the water, partially or completely, and then slams back onto the free surface with a high relative velocity. Large transient hydrodynamic loads act on the craft during re-entry and can have an adverse effect on the hull structure such as local hull damage in extreme events or fatigue failure of the material/ structure due to cyclic loading. The slamming impact may also result in large and violent accelerations that can affect the comfort and performance of the crew and passengers or in the extreme case result in injury (see Townsend et al. (2012) for a detailed review), or damage the equipment systems.

Figure 1 - Examples of high-speed craft operating in rough sea: RNLI B class Atlantic 85 lifeboat (left, courtesy of Poole lifeboat station) and Damen Interceptor 1102 (right, courtesy of Damen).

The enhancements in technology over the last few decades, principally power and propulsion systems and structural materials, have seen faster and lighter craft being designed and constructed. For instance, composite materials such as fibre reinforced polymers and foam cored sandwich panels are being widely used in the construction of high-speed marine vehicles today because of their high strength to weight ratio and excellent fatigue and environmental resistance (Mouritz et al., 2001; Battley et al., 2009).The enhanced speed potential of high-speed craft and the use of lighter and more flexible materials implies larger and more frequent slamming impacts and hydroelastic effects may have greater significant. Accurate prediction of the loads and responses is, therefore, crucial for designing safe and reliable and also efficient structures.

The importance of slamming loads for small high-speed craft has led to a significant body of research on understanding the complex physics involved and modelling the impact problem using a wide range of methods. A common approach has been to simplify the complex three-dimensional problem of a craft travelling at speed in waves to that of a two-dimensional transverse section of the hull or even a hull bottom panel free falling or impacting at a constant vertical velocity into the water. The two-dimensional problem has been widely studied using analytical, numerical and also experimental methods (see Temarel et al. (2016) for example). It is not clear, however, whether the

loads acting on a two-dimensional body entering the water accurately reflect the loads experienced by high-speed planing in waves. And if so, there are no practical guidelines on how the results of such studies can be used in the design of high-speed craft.

The structural design of high-speed planing craft, particularly craft having length smaller than 20m, is largely governed by the slamming impact loads. The designer must ensure that the structure is strong enough to withstand these loads and at the same time minimize structural weight since this is a critical parameter in terms of operational cost and performance and environmental impact (Stenius et al., 2011). Despite the advances in methods for predicting slamming loads, the structural design of high-speed craft today is still largely based on semi-empirical design methods, such as the Savitsky & Brown (1976) and Allen & Jones (1978) methods. In these methods, which are also implemented in the design rules of several classification societies, e.g. DNV GL (2015), Lloyd's Register (2016) and the ISO (2008) standard for small craft hull construction and scantlings, the highly dynamic and non-uniform slamming loads are treated as uniformly distributed static pressures and hydroelastic effects are not considered. The advantage of these methods is that they are simple and easy to use and require minimal input, however, they are not aimed at a specific craft and limit the ability to design more efficient high-speed craft structures or may result in weak structure. The latter has been found to be particularly true for modern high-speed craft structures where large sandwich panels with shear critical cores are commonly used (Razola et al., 2014).

With the increasing power of modern computers computational fluid dynamics (CFD) is becoming a more practical design tool for hydrodynamic analysis of high-speed planing craft. CFD is the numerical solution of fluid flows and related phenomena described by the Navier Stokes equations. The advantage of CFD is that complex phenomena such as flow separation and hydroelastic effects (through coupling with structural models), and complex geometries including stepped hulls, hard chines and spray rails can be easily handled, which is important if the accuracy of the predictions is to be improved. At present, despite the advances in computational power and increased efficiency of numerical solution methods, CFD simulations still require large computational resources, particularly transient three-dimensional hydroelastic simulations, and are not viable for a large number of simulations. This is primarily the reason why design offices still largely rely on the simple and efficient semi-empirical methods. However, with intelligent design of the numerical model and together with the continuing increase of computational power, future design methods for high-speed craft are more likely to be based on CFD.

1.2. Aim and objectives

The aim of this work is to improve the safety and efficiency of high-speed craft structural designs for realistic operational loads.

There are four main objectives to achieve this aim. The first is the development of a numerical model which is capable of simulating the water impact of two- and three-dimensional rigid and flexible structures using commercial CFD software and FE codes. It is validated using the drop test experiments on a rigid wedge by Lewis et al. (2010) and the constant velocity entry tests on a flexible composite sandwich panel by Allen & Battley (2015).

The second objective is to conduct an in-depth experimental investigation, in full-scale, into the impact loads on a high-speed planing craft and related responses whilst travelling at high speed in

waves (rough water trials) and as it free-falls into the water (drop tests). This includes, designing and performing the experiments and developing methods to post-process and analyse the data.

The third objective is to apply the numerical model to simulate the full-scale drop tests, both drop test of the three-dimensional rigid hull and drop tests of two-dimensional rigid transverse sections of the hull, to investigate the accuracy of two-dimensional models for simulating slamming impacts.

The final objective is to compare the accelerations and pressures measured in the rough water trials with predictions from two classification society rules and the ISO standard to assess the suitability of the design loads used in current practice. Preliminary comparisons between the loads and responses measured in the rough water trials and drop tests are made to examine any correlation between the two tests.

1.3. Layout of thesis and novel contributions

The importance of slamming loads for high-speed planing craft and issues with the methods currently used in structural design have been outlined in the Introduction. The remaining chapters of this thesis are organized as follows.

Chapter 2 gives a description of the physics of slamming impacts and related hydroelastic effects and reviews the analytical, numerical and experimental approaches taken to solve the problem of slamming impacts. Methods commonly used in the structural design of high-speed craft are also discussed.

The development and validation of the numerical model for simulating the water impact of 2D and 3D rigid and flexible structures is described in Chapter 3. The model uses the commercial CFD software Star CCM+ to solve for the fluid flow and the FE code ABAQUS to solve for the structural response (implicit direct integration method). The SIMULIA Co-Simulation Engine is used for coupling Star CCM+ and ABAQUS in a two-way manner. Two different water entry problems are studied and the first is the impact of a free-falling rigid wedge. The second problem studied is the constant velocity entry of a flexible composite hull panel. This is the first time that this particular modelling approach (coupled CFD-FEA with the structural response solved using the direct integration method) has been extensively applied to model the highly nonlinear problem of water impact of flexible structures. The influence of various numerical and experimental parameters on the rigid body kinematics, hydrodynamic loading and structural response are investigated. The investigations into the effect of three-dimensional flow and the gap between the test section and tank wall on the loads and responses and the effect of fluid compressibility on the stability and accuracy of coupled simulations are particularly novel.

Chapter 4 presents the full-scale trials on a high-speed planing craft in waves. An extensive set of rigid body motion, acceleration, pressure, strain and global hull deflection data for various sea conditions, forward speeds and headings was acquired. The tests and data processing procedure are described in detail and characteristic results, including results of statistical analysis of the measured data, are presented and discussed. Novel contributions made in the course of this work include the methods developed for removing time varying offsets from the strain signals and identifying the peaks in the pressure and strain signals, and the automated algorithm for fitting the Generalized Pareto model to the measured data.

The full-scale drop tests are described in Chapter 5. The first part of this chapter details the experiment and data processing procedure and presents characteristic results. To the best of the author's knowledge, this is the first work that measures the loads and responses during water entry of a realistic hull. Numerical simulations of the full-scale drop tests are described in the second part of Chapter 5. These include both drop tests of the three-dimensional rigid hull and two-dimensional rigid transverse sections of the hull. The three-dimensional results are compared with the experimental data for validation and the effect of three-dimensional flow and spray rails is investigated.

In Chapter 6 the pressures from the rough water trials and compared with the predictions based on the ISO standard and DNV GL and LR rules to assess the suitability of the design loads used in current practice. Preliminary comparisons between the loads and responses measured in rough water trials and drop tests are also made in an attempt to establish a correlation between the two tests. The issues encountered are discussed.

The final chapters conclude the thesis, emphasise the most significant novel contributions and outline possible directions of further work.

In summary, the major contributions of this work are,

- Comprehensive investigation into impact loads and responses using a fully coupled numerical method that uses Finite Volume CFD with a VOF interface capturing method to solve for the fluid flow and an implicit direct-integration FE method to solve for the structure.
- Full-scale rough water trials and drop tests – acquisition, processing and analysis of large sets of systematic data.
- Investigation into the correlation between full-scale measurements (rough water trials and drop tests), numerical predictions and design criteria.

Chapter 2. Background and related work

In this chapter, the physics of slamming impacts and related physical phenomena is described. Methodologies for analysing slamming impacts, including analytical, numerical and experimental techniques are reviewed. The literature review covers papers that most closely relate to the present problem of two-dimensional water impact of rigid and flexible structures. Full-scale trials and model scale seakeeping tests are also reviewed. Finally, the methods commonly used for structural design of high-speed craft are reviewed.

2.1. Physics of slamming

Slamming is the impact between the hull bottom and the water surface. It is generally the result of large relative craft motions that force the boat to emerge out of the water and subsequently re-enter the water with a large relative velocity. The nonlinear nature of high-speed craft motions and the randomness of the wave environment imply that no slamming impact is like any other with regards to the shape, magnitude and evolution of the loads on the hull surface and the related responses. The most important parameters in terms of severity of impact are the trim angle, deadrise angle, forward speed and wave geometry at the instant of impact (Allen & Jones, 1978; Savitsky, 2016).

Figure 2 shows a typical transverse section of a high-speed craft during a slamming impact. The section geometry is characterised by the deadrise angle β, i.e., the angle between the hull bottom and water surface. At the boat enters the water, water piles up at the intersection between the hull bottom and water surface and a thin jet forms. The spray root and jet move along the hull bottom surface with a speed that is much higher than the vertical entry velocity of the boat V. The resulting pressure distribution is characterised by a large peak at the spray root and a much lower and fairly constant pressure over the remaining part of the wetted surface. The pressure in the jet is close to atmospheric. The magnitude of pressure and propagation speed increase with increasing entry velocity and decreasing deadrise angle. When the spray root leaves the chine and the hull bottom is fully wetted the magnitude of the load decreases and the pressure becomes more uniformly distributed. The slamming impact loads act to decelerate the craft as it enters the water. As a result the pressure magnitude and propagation speed decrease with immersion.

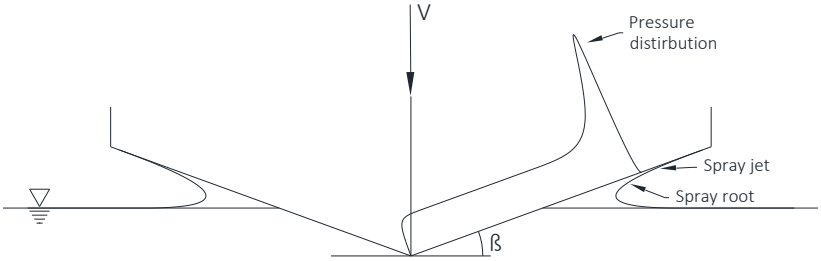

Figure 2 - Schematic illustration of a transverse hull section entering the water; V is the entry velocity and β the deadrise angle.

Slamming is a complex process and several physical phenomena may have an influence, such as, fluid compressibility, air entrapment, cushioning and subsequent formation of air bubbles, and hydroelastic effects (Faltinsen, 2005). Fluid compressibility may have an influence on the flow in the very early stages of impact when the fluid is suddenly accelerated by the entering body and spray root moves at a speed exceeding the speed of sound (Korobkin, 1996). Air entrapment occurs when the local angle between the body and water surface is small – less than about 5° - and the body velocity is large such that air does not have enough time to escape the impact region. The compressible air pocket acts as a cushion reducing the pressure on the body and eventually collapses into bubbles. Hydroelastic effects are typically present in cases where the local angle between the body and water surface is small and the entry velocity is large resulting in large slamming pressures and the structure has a high natural period, i.e. flexible structure. Hydroelastic effects are discussed in more detail in the following section. Faltinsen (2005) states that the practical relevance of these effects must be considered in the framework of the structural response, i.e., to only consider the physical features of fluid flow that have a non-negligible effect on the structural elastic and rigid body vibrations.

The effect of slamming impacts on the ship structural response can be both global and local. The global effect is known as whipping and refers to the transient vibration of the hull girder due to impulsive loads in slamming impacts. Springing is another global effect similar to whipping. Springing is steady-state vibration caused by oscillating wave forces along the hull. Whipping and springing are more important for fatigue rather than extreme design loads. The local effect is the local structural vibration in the area of impact which in the extreme case may lead to catastrophic hull failure.

2.1.1. Local hydroelastic effects

Hydroelasticity is the mutual coupling between fluid flow and the response of a flexible structure, that is, the structural vibrations affect the fluid flow with a pressure field and the hydrodynamic loading affects the structural vibrations. Faltinsen (2005) identifies two main phases in the hydroelastic response of a structure to slamming impact, called the structural inertia phase and the free vibration phase. In the first phase, the structure experiences a large hydrodynamic force in a short time relative to its natural period and accelerates rapidly. The structure is fully wetted at the end of this phase. In the second phase, the structure vibrates freely in water with the initial conditions obtained from the first phase. Maximum strains occur during the second phase.

Stenius et al. (2011a) distinguish between two forms of local hydroelastic effects that act during the first phase of impact, kinematic and inertia effects. Kinematic effects are related to the structural deformations which change the local kinematics i.e., geometry, velocity and acceleration conditions and, hence, the pressure distribution at the fluid structure boundary. Inertia effects are related to the excitation of the structure's natural frequencies when the loading occurs at the time scale of these structural natural periods. In practice, kinematic and inertia effects act together with the significance of each depending on the loading conditions and structural properties.

Criteria for establishing the relative importance of hydroelastic effects have been presented by Faltinsen (1999), Bereznitski (2001) and Stenius et al. (2007). These criteria are based on the ratio between the duration of loading and the natural period of the structure, thereby considering only inertia related effects. The common principle is that hydroelastic effects need to be considered if the

loading period is comparable to the structure natural period. Otherwise the hydrodynamic loading can be calculated by assuming a rigid structure and the loading applied in a quasi-static manner.

2.2. Methodologies for slamming analysis

The importance of slamming impact loads for the design of high-speed planing craft has led to a significant body of work on understanding the complex physics involved and modelling these impacts using a wide range of methods. In general, slamming impacts have been studied by simplifying the complex three-dimensional problem to the water impact of a two-dimensional transverse hull section, or even further a hull bottom panel. The literature review that follows will cover the papers that most closely relate to the present problem of two-dimensional water impact of rigid and flexible structures. Full-scale trials and model scale seakeeping tests are also reviewed.

2.2.1. Analytical models

Analytical models for the prediction of hydrodynamic loads during water entry are well established. One of the earliest works reported in the literature is that of von Karman (1929) who applied momentum theory to estimate the forces acting on seaplane floats during landing. Wagner (1932) further extended the von Karman (1929) model by taking into account the water pile-up at the intersection between the impacting body and water surface. The Wagner model is based on a flat-disc approximation and potential flow theory for ideal and incompressible flow. The original Wagner model cannot describe some important details of the impact. In particular, the Wagner model predicts both unbounded velocities and pressure at the intersection between the free surface and body (Korobkin, 2004). In the following years, several researchers have attempted to develop more accurate analytical models of slamming impacts, most of which are based on the concepts and ideas introduced by Wagner (1932). Extensive reviews of the developments in analytical models for predicting slamming impacts and comparative studies have been presented, for instance, in Faltinsen et al. (2004), Korobkin (2004), Tassin et al. (2010) and Abrate (2013). More recently, progress has also been made on analytical models of water impact of flexible structures, see for example Faltinsen (2000), Korobkin et al. (2006), Qin & Batra (2009) and Khabakhpasheva & Korobkin (2013). The Wagner model is typically used to solve for the fluid flow and the flexible structure is represented using either beam or plate theory or the finite element model combined with the modal method.

Analytical models are very robust and time-efficient compared to CFD methods (Faltinsen et al., 2004) however they cannot handle the complex phenomena involved in water impacts and require reasonable simplifications to obtain a solution, particularly for hydroelastic impacts (Korobkin, 2004; Khabakhpasheva & Korobkin, 2013). Nevertheless, analytical models are usually viewed as complementary to CFD and experiments and are commonly employed to assess the accuracy of CFD techniques (Faltinsen et al., 2004).

2.2.2. Boundary element method (2D)

Boundary element methods (BEM) are numerical methods solving potential flow problems using boundary integral formulations. In potential flow, the fluid is assumed to be inviscid and incompressible, and the flow irrotational such that the flow field can be described by a scalar potential function – the velocity potential – that satisfies Laplace's equation. With appropriate conditions defined on the domain boundaries the velocity potential can be found. The pressure then

follows from Bernoulli's equation. Boundary element methods (and panel methods in three-dimensions) need only to discretize the boundaries of the fluid domain, which simplifies grid generation and reduces computational costs significantly compared to field methods. In general, a BEM method is expected to be faster than a CFD method and more accurate than an analytical model (Sun & Faltinsen, 2006).

BEMs are known to encounter several numerical difficulties when applied to solve slamming impacts. These include, handling of the thin jet spray jet that develops at the intersection between the body and water surface (very small contact angles), the rapid changes in the free surface profile when the body initially touches the water surface and non-viscous flow separation. Local analytical solutions or empirical factors are typically used to overcome these difficulties.

Zhao & Faltinsen (1993) presented a nonlinear BEM for studying the water entry of two-dimensional bodies of arbitrary shape. The jet that forms at the intersection between the body and water surface is cut to avoid numerical difficulties and instead a control surface is introduced at the spray root normal to the body. The pressure in this part of the jet is close to atmospheric and does not contribute much to the total force on the body. The pressure distribution on the body and free surface elevation were found to agree well with the results from a similarity solution for a wide range of deadrise angles. Zhao et al. (1996) further extended the model of Zhao & Faltinsen (1993) to general asymmetric bodies and included flow separation from knuckles or fixed separation points (determined empirically) on bodies with curved surfaces. The effect of flow separation is incorporated by a Kutta condition. The numerical model is validated by comparisons with new experimental results from drop tests of a wedge and typical ship bow section (Aarsnes, 1996). The experimental time history of entry velocity is imposed in the numerical model. The predicted vertical force and pressure at different locations on the bottom surface agree well with the experiments during the initial stages but are overestimated at a later stage – around the time of peak force. This was attributed to three-dimensional flow effects. The authors were able to analytically estimate these effects and successfully correct their 2D results. Wu et al. (2004) developed a BEM for simulating the water entry of a free falling wedge. The thin jet is maintained to avoid common problems of pressure oscillations in the small area where the jet is cut, which in this case would lead to errors in the calculation of the body acceleration. The similarity solution of Dobrovol'skaya (1969) is used to compute the initial flow at the instant the wedge tip touches the water surface after which the BEM takes over the calculations. The predicted vertical accelerations for wedges with different deadrise angle and mass and different drop heights agree well with the experimental results. Some differences are observed when flow separation occurs, which is not accounted for in the model.

Sun & Faltinsen (2006) studied the water impact of a horizontal circular rigid cylinder and flexible cylindrical shell using a 2D BEM. Non-viscous flow separation is modelled by merging an analytical solution with the numerical method. Flat plate theory, either the von Karman (1929) or Wagner (1932) theory, is used in an initial short period to avoid numerical problems. The numerically predicted free surface profiles for the impact of a rigid cylinder are in good agreement with the experimental pictures of Greenhow & Lin (1983). The structural response is represented using thin shell theory and solved using modal analysis. The influence of structural deformations on the fluid is accounted for by an elastic vibration term in the body boundary condition. The predicted strains compare well with experimental results in terms of shape of the time history, however, the phase and extreme values show some differences. Several experimental and numerical factors were found

to have an influence on predicting strains including, the mass of cables and connectors located inside the shell model, friction force in the sliding system, the method used for calculating the flow during the short initial phase and the formula used to calculate the natural frequencies in the modal model. Lu et al. (2000) studied the hydroelastic interaction during the constant velocity impact of a flexible structure with water using a coupled 2D BEM-FEM method. The jet is treated following the approach of Zhao & Faltinsen (1993). In addition, a condition is imposed on the jet thickness to remove the oscillations in the pressure near the intersection, which would otherwise introduce error in the computed deformations. Time histories of deflection at the middle of a plate with different thickness are presented. No comparisons with other solutions or experiments are made.

2.2.3. Computational fluid dynamics

Computational fluid dynamics (CFD) is a branch of fluid mechanics primarily associated with but not limited to the numerical solution of fluid flows and related phenomena described by the Navier-Stokes equations, i.e., the mass and momentum conservation equations. The Navier-Stokes model provides a more accurate representation of the fluid behaviour than the potential flow model – it includes the effects of viscosity and removes the assumptions of irrotational and incompressible flow. Nonlinear flow phenomena such as flow separation and wave breaking can, when required, be modelled and complex geometries and hydroelastic effects can be handled. However, the whole fluid domain needs to be discretized rather than just the boundaries, which increases the computational costs quite significantly. With the increasing power of modern computers CFD has turned into a practical design tool and is being used to solve a wide range of marine hydrodynamics problems including slamming impacts, see for example Kim et al. (2014) and Temarel et al. (2016). This is also evident from the increasing number of commercial, academic and open source software packages available to solve fluid flow problems such as ANSYS FLUENT and CFX, Flow 3D, Star CCM+, LS DYNA, OpenFOAM and CFDShip-Iowa.

CFD based methods can be largely grouped into two main categories: grid methods and particle methods. In grid methods, such as the Finite Element (FE), Finite Difference (FD) and Finite Volume (FV) methods, the solution domain is subdivided into a finite number of control volumes and the governing equations are solved at these discrete locations. In fluid dynamics, grid methods are most commonly treated in the Eulerian reference frame where the grid is fixed in space and the fluid moves through the grid as opposed to a Lagrangian reference frame where the grid moves and deforms with the fluid. In particle methods, such as the Smoothed Particle Hydrodynamics (SPH) and Moving Particle Semi-Implicit (MPS) methods, the fluid domain is discretized by a finite number of particles each representing a finite volume of the fluid and the governing equations are solved using their interactions. Particle methods are Lagrangian methods.

In slamming impacts the position of the free surface – the interface between air and water - is not known in advance and must be determined as part of the solution. Methods used to compute dynamic shape of the free surface in grid methods include interface tracking method which treat the free surface as a sharp boundary and use boundary-fitted grids that follow its motion very accurately and interface capturing methods where the grid is fixed in space and the position of the free surface is determined by solving an additional transport equation (Ferziger & Perić, 2002). Interface tracking methods can only be applied to problems with smooth free surface otherwise problems related to grid distortion can arise. On the other hand interface capturing methods can easily handle large free surface deformations including wave breaking and splashing (Muzaferija et al., 1998). The most

commonly used interface capturing method is the Volume-of-Fluid (VOF) method proposed by Hirt & Nichols (1981). Muzaferija et al. (1998) used a finite volume method with a VOF approach to capture the free surface to simulate the water entry of a flared ship section and compared the results with the experimental data of Zhao et al. (1996). The free surface deformations are well captured by the model, including breaking and overturning of waves. However, it was shown that a fine mesh is needed to accurately resolve the free surface and small details of the flow. The domain size was found to have an influence on the solution with larger vertical force being predicted when the boundary was located too close to the body (ratio of domain width to breadth of ship section equal to 4). Three-dimensional effects were also found to have an influence on the solution. The vertical force and pressures on the wedge computed with the 3D model were lower than the 2D results and agree better with the experiments.

In contrast to grid methods, the numerical treatment of the free surface in particle methods is more straightforward. In most particle methods, the shape of the free surface is determined by introducing particles on the free surface and following their motion throughout the simulation (Liu & Liu, 2010). Moving bodies and deformable boundaries are also easier to handle with particle methods in that problems related to grid deformation are avoided (Liu & Liu, 2010). Numerical studies of slamming impacts using particle methods have been presented in Oger et al. (2006), Brizzolara et al. (2008), Shao (2009), Akimoto (2013) and Sun et al. (2015, 2016) amongst others. Despite their ability to handle complex free surface shapes, moving bodies and structural deformations with relative ease, particle methods suffer from issues of numerical instabilities and unphysical pressure oscillations amongst others and most of the research is focused on enhancing the stability and accuracy of the numerical methods rather than the physical aspects of the problem which is more of interest here. Comprehensive reviews of particle methods including overviews of the current challenges and proposed modifications to improve the method are presented in Liu & Liu (2010) and Gotoh & Khayyer (2016).

In water entry problems, rigid body motion can be modelled either by prescribing a constant or time varying (e.g. experimental) velocity profile or by solving the equations of motion together with the flow solution. Sames et al. (1999) used a linear panel code to calculate the relative velocities of a 2400 TEU containership in North Atlantic wave conditions. They applied a 2D two-fluid FV method to investigate the bow flare slamming loads. Simulations with a constant entry velocity were also performed. The impact velocity was found to have a significant influence on the fluid loading with larger pressures obtained for the constant velocity entries. It was concluded that constant velocity entries are not physically justified but can be regarded as upper limits and coupling with a rigid body motion solver is required to achieve realistic design pressures. Brizzolara et al. (2008) performed a comparative study of various boundary element and CFD methods for predicting the pressures and forces on a bow section impacting the water and different speeds and heel angles. The numerical methods used comprised two BEMs, explicit FE code LS-DYNA, FV software FLUENT, FV-FD software FLOW-3D and an SPH method. The numerical results were compared with the experimental measurements of Aarsnes (1996). Overall the numerical predictions show good qualitative and quantitative agreement with each other and the experiments with few exceptions for cases at high impact speed and heeled impacts. The time history of entry velocity was found to have a significant influence on the predicted pressures and forces, particularly at low impact speeds. To obtain good comparison with the experiments it is therefore important that the velocity profile is accurately predicted or prescribed.

Seng et al. (2012) performed a detailed investigation into the effects of three-dimensional flow and the accuracy and performance of the commonly used 2D simulations. The simulations were performed using the open source CFD software OpenFOAM, a Finite Volume based solver with the free surface modelled using the VOF approach. The simulations performed include 3D simulations of a fine-form Panamax container ship bow impacting the water at a constant trim angle as well as 2D simulations of 2D strips of the hull impacting the water vertically. The vertical force on the 3D hull compares relatively well with the vertical force obtained by integration of the vertical forces on the 2D section. However, differences are observed when comparing the forces per unit hull length particularly in the most forward sections of the hull. In particular the 2D results show a sharp peak, which is caused by the secondary impact of water separating from the bulbous bow with the bow flare at a very small angle. In the 3D simulations such relatively small contact angles between water and bow structure causing large local pressure peaks were not found to occur.

In more recent years, progress has been made on simulating the impact of flexible structures with water using CFD methods. Fluid-Structure Interaction (FSI) problems can be solved in a monolithic or partitioned way. In the monolithic approach, the flow and structural equations are solved simultaneously as a single linear system such that their mutual influence can be taken into account directly which is favourable for the stability of the calculation. In the partitioned approach, the flow and structural equations are solved separately and a coupling algorithm is used to allow for their interaction and to determine the solution of the coupled problem. The advantage of the latter approach is that software modularity is preserved, although the solution accuracy relies heavily on the stability of the coupling algorithm, particularly for strongly coupled problems (Degroote et al., 2009). The coupling between the fluid and structural solvers in the partitioned approach can be either one-way or two-way. In one-way coupling the structure is initially assumed rigid and a flow field is computed independently. The computed history of fluid loading is then passed to a separate structural solver to obtain the response of the structure in time. In two-way coupling data is passed between the fluid and structural solvers at regular intervals thereby taking into account the effect of structural deformation on the flow.

Maki et al. (2011) studied the constant velocity water impact of an elastic wedge using a one-way coupled method. The open source CFD library OpenFOAM is used to calculate the fluid loading on the rigid wedge, which is then transferred to a modal idealisation of the structure to obtain the response in time. In slamming impacts, the loading occurs during the transition from dry to completely wet. The change in added fluid mass during this period changes the natural period of vibration of the structure. In one-way coupled methods, this effect cannot be taken into account and the structure has to be assumed dry, partially or fully wet. Maki et al. (2011) studied the effect of assumed wetness of the wedge by generating two modal models, dry and fully wet. For the wet model, acoustic elements were used to represent the added mass due to flexure. The deflection time histories show clear differences in terms of maximum value and frequency of oscillations, particularly for the case where hydroelastic effects are important (thin plates). As expected, the dry structure vibrates at a higher frequency due to the neglect of the added mass, whereas the wet structure vibrates at a frequency that is too low. The predicted maximum deflection from the wet model agrees well with analytical predictions, although the time accuracy is poor.

Stenius et al. (2011a) used the explicit Finite Element code LS-DYNA to study the fundamental mechanisms involved in hydroelastic panel-water impacts. Simulations comprising different impact

velocities, deadrise angles, boundary conditions and panel properties were performed. The in-plane boundary fixation and panel stiffness were found to have a significant effect on the structural responses (deflections and strains) and hydroelastic effects. For instance, clear hydroelastic effects in the transverse shear stresses were observed for sandwich panels with low in-plane stiffness. Furthermore, the significance of hydroelasticity increases with increasing impact velocity or decreasing deadrise angle. The influence of hydroelasticity on the structural response is quantified by comparing the deflections and strains from hydroelastic simulations with corresponding rigid/ quasi-static (RQS) solutions. The RQS solution was found to yield larger structural responses during the initial stages of the impact event and smaller responses towards the end. The authors attribute these differences to structural and added inertia in the hydroelastic solution and also to structural deformation, which changes the pressure distribution at the interface. Das & Batra (2011) also used LS-DYNA to simulate the slamming impact of sandwich composite hull bottom panels. It was shown that the core absorbs a considerable amount of the impact energy due to its transverse shear deformations.

Piro & Maki (2013) developed a *tightly* coupled numerical method to study the water entry and exit of a 2D hydroelastic wedge. The fluid domain is modelled using Finite-Volume CFD in OpenFOAM and the flexible structure is represented using a modal model. An approximate boundary condition is used on the mutual interface where the fluid velocity is defined to be the structural velocity on the undeformed position of the structure to avoid mesh distortion problems. The results from the tightly coupled simulations are used to assess the accuracy of the commonly used approximate methods for industrial applications namely, rigid/ quasi-static and rigid-dynamic methods. A wide range of plate thickness is considered to study the influence of hydroelastic effects. In general, compared to the tightly coupled solution, the maximum structural response (deflection and stress) is always underpredicted by the RQS approximation, whereas the rigid-dynamic approximation may over or underpredict the response but is more accurate than the RQS solution. The differences are largest for the thin plates where the natural periods of the structures are comparable to the loading periods and hydroelastic effects have large influence.

2.2.4. Experiments

2.2.4.1 Model scale testing

Model scale testing refers to experiments performed in a controlled environment such as towing tanks and includes both free-fall or constant velocity water impact tests in calm water with two-dimensional (2D) sections and towed or free running tests with scaled models in waves. Table 1 presents a list of experimental investigations of water impact of two-dimensional rigid and flexible bodies. It includes details of the test section, test parameters, measurements made, the number of times the test was repeated and the type of uncertainty analysis performed.

Table 1 - Experimental investigations of water impact of two-dimensional rigid and flexible bodies. β is the deadrise angle, NR stands for not reported and NA not applicable.

Reference	Test section			Drop height, m or velocity, m/s	Measurements	Repeatability test	Uncertainty analysis
	Geometry	Flexibility	Mass, kg				
Aarsnes (1996)	Wedge (β = 30°) and bow flare section	Rigid	288 & 261	0.13, 0.2 & 0.5 m	Force, pressure, rigid body acceleration, wetted surface & free surface profile	2 drops/ test condition	NR
Judge et al. (2004)	Wedge (β = 37°)	Rigid	NR	NR	Free surface profile	3 drops/ test condition	NR
Yettou et al. (2006)	Wedge (β = 15, 20, 25, 30 & 35°)	Rigid	89 - 158	1.0 & 1.3 m	Pressure & rigid body position	10 drops/ test condition	Statistical & cumulative
Tveitnes et al. (2008)	Wedge (β = 5, 10, 15, 30 & 45°)	Rigid	9.9 – 12.3	0.24 - 1.19 m/s	Force, rigid body velocity & free surface profile	4 runs/ test condition	Statistical & cumulative
Lewis et al. (2010)	Wedge (β = 25°)	Rigid	23.4 & 33.4	0.5 & 0.75 m	Pressure, rigid body position & acceleration, & free surface profile	3 drops/ test condition	Statistical & cumulative
Huera-Huarte et al. (2011)	Panel (β = 0.3, 1, 1.7, 2.3, 2.7, 4.3, 5.7, 10.7, 17 & 25°)	Rigid	NA	NR – 6 m/s	Force, rigid body velocity & free surface profile	2 runs/ test condition	NR
Wang et al. (2015)	Wedge (β = 30°)	Rigid	12.8	0.013 - 0.32 m	Pressure, rigid body position & acceleration, & free surface profile	10 drops/ test condition	NR
Hayman et al. (1992)	Wedge (β = 30°); sandwich composite	Flexible	1350	1.0 – 7.0 m	Pressure, rigid body acceleration, & panel acceleration and strain (core & laminate)	NR	NR
Battley et al. (2009)	Panel (β = 10°); sandwich composite	Flexible	NA	0.5 – 7.0 m/s	Force, pressure, rigid body acceleration & panel deflection & strain	NR	NR
Panciroli & Porfiri (2015)	Wedge (β = 22°); aluminium	Flexible	0.342	0.25, 0.5 & 0.75 m	Velocity field (PIV)	3 drops/ test condition	NR
Allen & Battley (2015)	Panel (β = 10°); Fibre & sandwich composite	Flexible	NA	1.0 – 6.0 m/s	Force, pressure & panel deflection & strain	3 runs/ test condition	NR

Aarsnes (1996) dropped a wedge and bow flare section from different heights and at different roll angles and measured the slamming loads. The pressure is found to increase with increasing roll angle, i.e., with reducing the relative angle between the body and water surface. The experiments of Aarsnes (1996) which are also reported in Zhao et al. (1996) have been widely used for validation of numerical and analytical models. Yettou et al. (2006) investigated the effect of drop height, deadrise angle and wedge mass on the impact pressure and dynamic behaviour of a free-falling wedge. The impact pressures were found to increase with increasing wedge mass and drop height and decreasing deadrise angle. Similar trends have been observed by Lewis et al. (2010) who dropped a 25° deadrise angle wedge from two different heights and for each height two different wedge masses were tested. A high-speed camera was used to capture the flow during impact and the pressure and acceleration measurements were synchronized with the camera images to better understand the wedge behaviour. A comprehensive set of high-quality experimental data was presented including a detailed uncertainty analysis. The reported uncertainties in the pressure, acceleration and position measurements are low, and show that the data is of high quality and well suited for validation of numerical and analytical models. More recently, Wang et al. (2015) investigated the dynamics of the cavity that forms above the impacting body at deep immersions. It was found that the compressibility of air inside the cavity matters and affects the cavity pressure, impact pressure and wedge dynamics.

Constant velocity water impact tests are not a completely true representation of high-speed craft slamming where the body experiences a rapid deceleration on impact with the water, but more of calm water planing. For larger ships however, the entry velocity may be only slightly reduced by slamming impact forces and constant velocity tests may be better suited. Nonetheless they provide useful insights into the problem. Tveitnes et al. (2008) measured the hydrodynamic force on wedges having deadrise angles varying from 5° to 45° during constant velocity entry, oscillation and exit tests with the aim to further understand the dynamic behaviour of planing hulls in waves. The measurements were found to contain significant amount of dynamic noise particularly after chine immersion, which limits their accuracy. Huera-Huarte et al. (2011) studied the effect of air entrapment and air cushioning on the impact loads. The panels were tested at high constant impact velocities and relatively low deadrise angles. Significant air entrapment was found to occur for deadrise angles less than 5°. The trapped air acts as a cushion and contributes to decreasing the impact loads. The high-speed camera images show air being pushed by the panel into the water and subsequent formation of air bubbles.

Drop tests with flexible bodies have also been performed. Hayman et al. (1992) dropped a GRP sandwich hull section from a range of heights and at different heel angles to establish the maximum load the core material can withstand, and investigate the resulting pressure distributions and strains. The critical failure mode was found to be core shear failure near the chine followed by delamination. Battley et al. (2009) performed constant velocity impact tests with three composite panels having different stiffness to study the effect of hydroelasticity on the loads and responses. The maximum panel deflection and laminate strains were found to increase with decreasing panel stiffness for the same impact velocity. Furthermore, significant reductions in both the local impact velocity at the panel centre and local deadrise angle at the outer edge were observed due to panel deformation, leading to lower and higher peak pressures than for the rigid panel respectively. For instance, at a nominal testing velocity of 3 m/s and 10° deadrise angle, the most flexible panel (solid glass fibre laminate) has a minimum local velocity at the centre of 1.12 m/s and minimum local

deadrise angle at the chine of 2.94°. The increase in load at the outer edge with increasing panel flexibility is particularly important for sandwich panels, as this is the most critical region for transverse shear failures. Allen & Battley (2015) performed a more comprehensive study to further characterise the variations in loads and responses due to structural flexibility. The trends observed are similar to those presented in Battley et al. (2009). The pressure and deflection measurements for a foam cored sandwich panel with carbon skins are used for validation of the fully-coupled numerical model.

Panciroli & Porfiri (2015) used Particle Image Velocimetry (PIV) to study the effect of structural flexibility on the hydrodynamic loads measured during free-fall drop tests of a 2D wedge. The advantage of this technique is that the entire velocity field can be measured rather than just point measurements. The pressure field is then obtained by integrating the PIV velocity using the Navier-Stokes equations. The deflection and velocities at different points on the wedge are also derived from the images. The wedge consists of a thin aluminium sheet, bent at its mid-span to the required deadrise angle and mounted to the drop test rig from the centre. The two sides of the wedge therefore act as two independent cantilever plates. The wedge has been purposely designed this way to induce hydroelastic effects even at low impact speeds. The tip of the panel is found to deflect downward during the early stages of impact due to structural inertia. In the later stages, when the loading acts over a larger area, the deformed shape of the wedge changes with the tip deflecting upwards. Furthermore, the tip velocity relative to the keel is characterised by the superposition of multiple harmonics, with the influence of higher harmonics increasing with impact velocity. Finally, comparisons of the reconstructed pressure distribution with analytical predictions obtained using Wagner (1932) theory show that the structural vibrations have an influence on the hydrodynamic loading, particularly in the later stages of the impact event.

Slamming impacts are characterised by complex free surface deformations, highly localized pressure distribution and high velocities. Accurate measurements of slamming impacts are, therefore, difficult to make. The uncertainty of the measurement system should be clearly documented and ideally, the test is repeated multiple times to increase the confidence in the measurements. Van Nuffel et al. (2013) performed a detailed study on the parameters influencing the accuracy and reproducibility of pressure measurements during water impact. The sampling frequency, position of the sensor diaphragm relative to the body surface, water temperature, and the smoothness of the body and water surface were found to have a significant influence. Drop tests with two rigid cylinders were performed to quantify this influence and suggestions are given. Another common issue regarding experiments with 2D sections is three-dimensional flow effects. Judge et al. (2004) kept the clearance between the test section and tank wall small to preserve the two-dimensionality of the flow, however, even a small gap was found to produce significant end flow effects. A vertical laser sheet and coated hollow glass spheres were therefore used to accurately visualize the flow field during vertical and oblique (horizontal velocity) entries of symmetric and asymmetric (heeled) wedges and track the free surface. Aarsnes (1996) used dummy sections on each side of the measuring section to ensure that the flow is two-dimensional, while Tveitnes et al. (2008) and Allen & Battley (2015) placed vertical plates at the ends of the test section.

Model scale seakeeping experiments of high speed planing craft include those of Fridsma (1971), Rosén & Garme (2004), Taunton et al. (2011) and Judge et al. (2015) amongst others. Towing tank tests are a better representation of the full-scale problem compared to water impact tests. Rosén &

Garme (2004) performed a detailed investigation into the pressure distribution on planing craft in waves. The 1:10 scaled model is a simplified version of the full-scale craft tested by Garme & Rosén (2003), and measurements of rigid body motions and acceleration and pressures were made. A dense matrix of pressure sensors and high sampling frequency (2.5 kHz) was used to accurately capture the transient and highly localized pressure distribution. The sampling frequency was found to be sufficient in most cases except for extreme impacts where the rise times are in the order of 1ms. A method for reconstructing the complete pressure distribution on the hull surface from the discrete point measurements is presented. The impact loads obtained from integrating the reconstructed pressure distribution are found to correlate relatively well with the inertia force derived from the acceleration signal. It is concluded that observed differences are due to the fact that the derived pressure force only considers the load acting on the forward part of the hull (the instrumented area), whereas the acceleration-derived force is related to the total load on the hull. Taunton et al. (2011) developed a new series of high-speed hard chine planing hulls and performed an extensive investigation into their motions and accelerations in waves. The Cartwright & Longuet-Higgins and Gamma distributions were fitted to heave and pitch motions and accelerations respectively. A method for predicting human performance on-board full-scale craft using the statistical data is presented. The ITTC (2011) recommends the ISO-GUM (International Organization for Standardization, Guide to the Expression of Uncertainty in Measurements) approach to conducting uncertainty analysis in model seakeeping experiment measurements, which applies equally well to drop test experiments. In this approach the uncertainty is grouped into two categories, type A and type B. The type A uncertainty represents the randomness of the experiment and is evaluated by repeated measurement of the same experimental condition. The type B uncertainty represents the uncertainties that are an inherent part of each sensor, its calibration, the data acquisition system, processing and analysis and are generally obtained from the manufacturer's specification sheets.

2.2.4.2 Full-scale measurements

Full-scale measurements are expensive to conduct and usually confidential to the ship builder or owner. Full-scale data for loads and responses on high-speed planing craft in waves is, therefore, not widely available. One of the early and most significant works is that of Allen & Jones (1978) who measured pressure, acceleration and strain on two planing hulls in waves. The measured data together with the results from a semi-empirical method were used to develop a simplified method for predicting the hull bottom impact pressure loads for structural design purposes that is still widely used today. Garme & Rosén (2003) conducted full-scale rough water trials on a 10 m high-speed planing craft made of composite material to study the characteristics of slamming impacts and gather data for validating their numerical model. Measurements of rigid body motions and accelerations, pressures and laminate and shear strain were made in different sea states at different speed and headings. The impact pressures recorded in bow seas were found to be significantly higher than in head seas, which are generally considered as the most severe condition regarding impact loads because here the largest relative motions and velocities are experienced. This was concluded to be due to smaller effective deadrise angle, i.e. the relative angle between the hull and water surface at the moment of impact, in bow seas. The vertical accelerations recorded in bow seas were, however, lower than head seas, which is attributed to the fact that in bow seas the high pressure loading acts on a smaller area of the hull, thus resulting in lower forces and accelerations.

The semi-empirical methods used in the design of high-speed craft assume direct relationship between rigid body accelerations and pressure and, thus, may underestimate the loading in such conditions. The statistical averages of the peak pressures and structural responses were found to correlate well. Mørch & Hermundstad (2005) measured accelerations, pressures, strains, and local panel deflections on a 6 m high-speed recreational craft made of composite material to understand better the impact loads experienced in waves for design purposes. The craft was tested in different sea states at various speeds and headings in both fully and partially loaded conditions. The loads and responses measured in the fully loaded condition were found to be lower. From comparisons of the pressure and strain measurements with the DNV design rules it is found that design pressures are too low and that there is a large safety margin for the required laminate thickness based on design pressures. Riley et al. (2014) performed a detailed investigation into the characteristics of accelerations measured on high-speed craft in waves and presented a method quantifying wave impacts loads using full-scale acceleration data, in particular the amplitude and duration of rigid body heave acceleration.

The lack of full-scale experimental studies in the literature is also partly due to the complexities involved in making full-scale measurements and processing the data. Two common issues related to measurements on high speed planing craft in waves are noise in the acceleration signals and identification of peaks. Data measured on high-speed planing craft in waves, in particular acceleration data, often contain unwanted high-frequency noise caused by structural vibrations and engine and propeller vibrations in full-scale or towing tank carriage vibration in model scale. Low pass filtering is commonly used to extract the rigid body response from the noisy signal, see for example Rosén & Garme (2004), Riley et al. (2014) and Savitsky (2016). Riley et al. (2014) concluded from the analysis of a large number of signals that a cut-off frequency of 10Hz effectively removes the high-frequency vibration content without significantly affecting the rigid body response. Savitsky (2016) showed that the frequency content of individual hull-wave impact accelerations is a function of the impact velocity, deadrise angle and craft weight. The cut-off frequency, thus, needs to be chosen carefully.

Peak values are often used for characterization of slamming impacts, for example the average of largest $1/10^{th}$ pressure or strain peaks, and for estimating extreme loads or responses. Accurate identification of the peaks is, therefore, important however challenging. Allen et al. (2008) presented an algorithm for identifying peaks in acceleration signals recorded on an Atlantic 75 RIB. The algorithm uses the signal characteristics, in particular the high rate of change of acceleration associated with impact, to identify the timing of events from which the peak magnitude and changes in boat motion, i.e., pitch, roll and yaw, following impact are determined. Jacobi et al. (2014) used a rate of change of stress criterion together with the pitch motion signal to accurately identify the peaks in stress signals recorded on a 98 m wave piercer catamaran. In their algorithm a slam event is defined as one where (1) the rate of change of stress exceeds the product of a specified constant and the yield stress of the material and (2) the pitch is positive indicating bow down motion. The second criterion is used because the whipping after a slam event was also found to have a high rate of change of stress which resulted in many whipping events being incorrectly identified as slam events. The peak is then the maximum stress in the identified slam event. Riley et al. (2014) used two criteria to identify valid acceleration peaks – a vertical threshold equal to the Root Mean Square (RMS) of the signal and a horizontal threshold (sliding time window) calculated from the wave encounter frequency.

The behaviour of a high-speed planing craft in waves is strongly nonlinear and statistical methods are commonly used for characterization of the loads and responses and for extreme value prediction. Methods for calculating extreme loads and responses are well established (e.g. Ochi, 1981) and involve fitting of analytical distribution functions to samples of observed or computed data and extrapolating for extreme values. Garme & Rosén (2003) fitted a two-parameter Weibull distribution to the measured pressure peaks. The peaks were found to belong to two different statistical distributions, namely the low magnitude peaks resulting from linear hull-wave interaction were found to follow a Rayleigh distribution whilst the large slamming induced peaks are approximately exponentially distributed. McCue (2012) studied the suitability of several statistical distributions to describe high-speed craft peak acceleration data. The distributions considered are the exponential, Rayleigh, lognormal, Gumbel, Weibull, Fréchet and Generalized Extreme Value (GEV). The exponential distribution suggested by Fridsma (1971), which is often used to estimate design loads, was consistently the worst fit to the data whilst GEV typically provided the best fit. The exponential distribution was found to be too conservative, adding that 'extra' factor of safety into the structural design process.

The accuracy of extreme value estimates strongly depends on how well the statistical model fits the data, particularly in the tail of the distribution. The Peak-Over-Threshold (POT) method fits a distribution to the peaks above a threshold, thus improving the modelling of the largest peaks and hence, the extreme value estimates. The POT method is based on Pickands (1975) theorem, which states that, for a large class of underlying distribution functions and large threshold, the distribution of the excesses is well approximated by the Generalized Pareto distribution (GPD). The POT method has been widely used for estimation of extreme wave loads on large ships (e.g. Wang & Moan, 2004 and Wu & Moan, 2006), sloshing loads (e.g. Graczyk & Moan, 2008) and, more recently, high-speed craft accelerations (Razola et al., 2016). Razola et al. (2016) studied in detail the statistical character of high-speed craft accelerations. The Weibull and Generalized Pareto distributions are used to describe the acceleration peaks and estimate extreme values. The Weibull model is only fitted to a fraction of the largest peak values to improve the accuracy of the extreme value estimates and an automated threshold selection algorithm is developed to reduce the subjectivity in selecting the threshold. An automated algorithm for selecting the GPD threshold based on the shape parameter stability plots is also presented. Both models fit the data well and predict similar most probable largest values. The extreme values with 1% probability of exceedance show, however, less agreement even for such large samples used, highlighting the challenges involved in predicting extreme events with low probability of occurrence.

2.3. Structural design of high-speed craft

The structural design of high-speed craft is largely governed by the slamming impact loads that act on the hull bottom as the craft travels at high speed in waves. Many designers of high-speed craft today still rely on either experience and trial and error or semi-empirical methods for the prediction of design loads. In the semi-empirical methods, which are also implemented in the design rules of several classification societies (e.g. DNV GL, 2015 and Lloyd's Register, 2016) and standards (e.g. ISO, 2008) with some modifications, a design pressure load is calculated for each hull structural component (e.g. plating, stiffeners etc.) for stress analysis and scantling determination. Two classical examples are the methods of Heller & Jasper (1961) and Allen & Jones (1978). The design pressure load is typically expressed in terms of the craft displacement, vertical acceleration at the longitudinal

centre of gravity and the size and location of the structural component considered. The vertical accelerations are also commonly determined using semi-empirical methods, e.g. Savitsky & Brown (1976) and Hoggard & Jones (1980).

Savitsky & Brown (1976) presented a formula for predicting the impact accelerations at the craft's centre of gravity based on the model test data of Fridsma (1971). The main parameters are the craft particulars (length, beam, deadrise angle and displacement), speed, significant wave height, and running trim angle. The authors stress that the equations are empirical and based on limited data, and the range of applicability must be respected.

Allen & Jones (1978) developed a simplified method for calculating an equivalent uniform static pressure load for each structural component of the hull for scantling determination based on analytical and full-scale experimental data. The equivalent pressure load is defined as that pressure "which if applied to the component, will result in approximately the same deformation and the same maximum stress as produced by the actual loading in the actual structure". In the course of developing the method, the authors made two important observations. The first is that peak pressures act over relatively small areas of the hull, thus constituting a small portion of the total impact load and lower pressures were measured over a greater portion of the hull representing a higher portion of the total load. Heller & Jasper (1961) had also made similar observations. The second observation was that for each slamming impact the pressure distribution was non-uniform with the forward part of the hull most likely to experience the largest impact pressures. Allen and Jones took account of both observations in their method through pressure adjusting factors.

Accurate prediction of the slamming loads and structural strength is crucial for designing a lightweight and efficient structure without compromising safety. Semi-empirical methods have the advantage of being simple and straightforward to use and require minimal input, which is important during the early stages of the design. However, these methods are generally not optimized for a specific craft and the classification societies often introduce large safety factors in their rules to ensure that the safety is not compromised. Koelbel (1995) discusses the hydrodynamic and structural uncertainties inherent in these semi-empirical methods. These include uncertainties in selection of sea state (the range of wave heights covered by a particular sea state is quite wide), calculation of maximum speed in a seaway, vertical accelerations for a given speed and sea state, and local design pressures, as well as uncertainties in the boundary conditions used for calculating the required scantlings. It is recommended that the design acceleration be selected on the basis of crew endurance (plus a small margin to ensure structural strength) rather than by calculation to remove some of the uncertainty from the design procedure. Koelbel (1995) also states that the single most pressing problem in the structural design of planing boats is the selection of appropriate vertical acceleration for design.

Razola et al. (2014b) compared the structural loads (bending moments and shear forces) obtained using the equivalent uniform pressure model used in the semi-empirical method of Allen & Jones (1978) with the loads calculated using a reconstructed pressure distribution from point measurements made in model scale tests. The latter method, thus, takes into account spatial (non-uniform distribution) and temporal variation. The equivalent uniform pressure model was found to underestimate the structural loads, particularly the shear forces, and the underestimation was found to increase with increasing structural component size. This is particularly important for modern sandwich structures where larger panels and shear critical cores are commonly used. Razola

et al. (2014a) further evaluated the Allen and Jones design method in more detail. The factors that link the local design pressure to the global slamming load are derived following the same methodology of Allen and Jones but using modern analysis techniques and compared to the original factors individually. Comparisons between the design pressures predicted using the Allen and Jones method and the simulated pressures (modern techniques) are also made. The Allen and Jones method is found to accurately predict the pressures for smaller high-aspect ratio panels located close to the keel. However, for larger panels with smaller aspect ratios located further away, the Allen and Jones method is found to predict significantly larger pressures. Potential improvements to the Allen and Jones method including accounting for the aspect ratio and transverse position of the panel are discussed. The relationship between the vertical accelerations at LCG and design slamming pressures, and the statistical level used to represent the vertical accelerations are also investigated.

Another limitation of the semi-empirical methods is that the transient and non-uniform slamming loads are treated as uniformly distributed static pressures and hydroelastic effects are neglected. An alternative approach is to use direct calculation methods where the non-uniform and time-dependent pressure distribution is calculated using, for instance, time domain strip methods or CFD methods, and applied on the FE model of the structure in a quasi-static manner. Direct calculation methods are more accurate in representing the structural loads (Razola et al., 2014b) although hydroelastic effects are also not considered in these methods. As lighter and more flexible materials are being used to construct high speed planing-craft and the speed increases, hydroelastic effects are becoming more and more important and need to be accurately considered for safe, reliable and efficient structural design.

2.4. Summary

Slamming, the impact between a structure and a body of fluid is a complex physical process involving large and nonlinear free surface deformations and flow separation, rapid changes in fluid velocities and corresponding changes in hydrodynamic loads, and dynamic interaction between the fluid flow and flexible structure. The importance of slamming impacts, particularly for small high-speed craft, has led to a significant body of work trying to understand the physics of the problem and model these impacts using a wide range of analytical, numerical and experimental methods. Each approach has its advantages and limitations.

Experimental methods are still considered as the most reliable source of information; however, experiments can be costly and time-consuming. In addition, accurate measurements of, for instance, the highly dynamic and peaked pressure distribution, large free surface deformations and rigid body accelerations are difficult to make. Experimental uncertainty analysis, including repeating the test multiple times and quantifying the uncertainty of each component of the system, should be performed to increase the confidence in the results.

Analytical models are simple, robust and time-efficient; however, they involve several limitations and simplifications. For instance, the Wagner (1932) models are only valid for small deadrise angles and during the chines dry phase, and linearized free surface conditions are used. Furthermore, these models are often limited to the analysis of simplified geometries having little practical usefulness – chines and spray rails for instance cannot be modelled.

BEMs are more accurate than analytical models – for example the exact free surface conditions are generally satisfied – and faster than CFD methods as only the domain boundaries need to be

discretized. However, they are known to encounter some numerical difficulties when used to solve the slamming problem and local analytical solutions or empirical factors are typically used to overcome these difficulties.

CFD methods solving the Navier-Stokes equations provide the most accurate representation of fluid flow and can easily handle nonlinear flow phenomena such as flow separation and complex free surface deformations. Furthermore, complex geometries and hydroelastic effects are easily handled. However, the main drawback of CFD methods is the large computational power required. This is particularly true for three-dimensional models. However, for two-dimensional models and with careful setup of the model (grid design, selection of physics models and solvers settings, etc.), the computational efficiency can be significantly improved. Verification and Validation studies must also be performed to assess the accuracy and reliability of the simulation results and instil confidence in the reader. This involves performing time step and grid convergence studies and comparing the results with experimental data.

Despite the progress in predicting the pressure impact loads and structural responses, the designers of high-speed craft and classification societies still largely rely on semi-empirical methods developed in the 1970s. These methods are not aimed at a specific craft and have limited ranges of applicability. In addition, the transient and non-uniform slamming loads are treated as uniformly distributed static pressures and hydroelastic effects are neglected. Consequences of these simplifications might be structural damage or overly conservative and heavy structures.

Chapter 3. Numerical modelling of water impact

In this chapter a numerical model for simulating the impact of rigid and flexible bodies with water is developed using the commercial CFD software Star CCM+ and the FE code ABAQUS. The numerical solution method including the numerical solution of the fluid and the structural domains and the coupling are described. The model is applied to two different water entry problems and the numerical predictions are compared with published experimental data for validation.

The first problem studied is the impact of a free-falling rigid wedge with water. The requirements on the mesh and time step resolution to accurately capture the transient and localized impact loads are investigated. The effect of three-dimensional flow and the gap between the test section and the tank wall is investigated by simulating the case in both 2D (slice of the wedge) and 3D and comparing the results. Parametric studies on the effect of drop height, wedge mass and deadrise angle on the impact accelerations and pressures are also performed. Finally, simulations replicating the experimental test conditions of Lewis et al. (2010) are performed and the computed time histories of acceleration and pressure are compared with the experimental data to examine the accuracy of the numerical model.

The second problem studied is the constant velocity water impact of a flexible sandwich composite panel representative of a marine hull bottom panel using Star CCM+ and ABAQUS coupled in a two-way manner. Convergence of the fluid model with respect to time step and grid size is studied by simulating the constant velocity impact of a 2D rigid panel using different time step and grid sizes. The fluids, air and water, are modelled as compressible to improve the numerical stability of coupled simulations and the effect of fluid compressibility on the 2D rigid panel solution is also studied. The composite panel is modelled as a 2D beam and a 3D panel and in the 2D case, two beam FE models with different boundary conditions are considered to investigate their effect on the response. The numerical model is validated by comparing the predicted pressure and deflection histories obtained from two- and three-dimensional simulations with the experimental data of Allen & Battley (2015). Finally, the effect of structural flexibility on the hydrodynamic loads and structural responses is investigated by comparing the flexible panel solutions with corresponding rigid/ quasi-static (RQS) solutions for a range of impact velocities.

3.1. Numerical solution method

The simulations reported in this thesis were performed using the commercial CFD software Star CCM+ and the FE code ABAQUS. In coupled simulations, the SIMULIA co-simulation engine (CSE) is used to coupled Star CCM+ and ABAQUS. In this section, a brief overview of the numerical simulation method is given. For more details the reader is referred to the User Manuals (Dassault Systèmes, 2013 and CD-adapco, 2014) and Ferziger & Perić (2002).

3.1.1. Fluid domain

The flow is assumed to be governed by the Navier-Stokes equations, i.e., the mass and momentum conservation equations. In addition, the space conservation law (SCL) must also be satisfied because the cells will have to move and change their location with moving walls and in the case of coupled simulations, also change their shape. The SCL ensures that the sum of the volume fluxes through all the faces of a cell due to their movement is equal to the rate of change of the volume. The flow is further assumed laminar and incompressible. The time scales over which viscosity and compressibility act on the flow are much shorter in duration than the time scales of the impact problems studied in the present work. However, for coupled simulations, the flow is modelled as compressible to enhance the stability of the solution (CD-adapco, 2014). Compressible flows assume that the fluid density varies in space and time and require two additional equations to close the system – the energy conservation equation and an equation of state relating density and pressure. In compressible simulations, the flow is further assumed isothermal – the duration of impacts is too short for significant changes in temperature to occur. Gravity effects are included.

The Volume of Fluid (VOF) interface capturing method is used to solve for the complex and nonlinear free surface. In the VOF method, air and water are considered as a single effective fluid with variable physical properties and the spatial distribution of each fluid at a given time is obtained by solving an additional transport equation for the phase volume fraction.

To close the above mathematical model, the state of the flow at the start of the simulation and on the boundaries of the solution domain has to be specified. The initial and boundary conditions can be of two types, Dirichlet or Neumann. A Dirichlet condition specifies the actual value of the flow variable (e.g. velocity inlet and wall boundaries) whereas a Neumann condition specifies its gradient (e.g. pressure outlet boundary). It is also possible that for the same boundary a Dirichlet condition is applied for some variables and a Neumann condition for others (e.g. symmetry boundaries assume zero normal velocity and zero normal gradients of all variables at the symmetry plane).

Star CCM+ uses the Finite Volume (FV) method to transform the governing equations into a system of algebraic equations that can be solved numerically. The solution domain is first divided into a finite number of control volumes (CV) that define the discrete locations at which the variables are to be calculated. The CVs can be of any shape, however, for accuracy reasons hexahedral cells are used whenever possible, and are typically made smaller in the regions of rapid variation of the flow variables. The time interval of interest is also subdivided into a finite number of time steps. The governing equations in integral form contain surface and volume integrals, as well as time and space derivatives. These are approximated for each CV and time step using suitable approximations. The surface, volume and time integrals are evaluated using the midpoint-rule approximation, i.e., the product of the integrand at the centre of the integration domain and the integration range (cell volume or time step). These approximations are second order accurate. The variable values are computed at the CV centres and linear interpolation is predominantly used to obtain the values at the CV-face centres. The gradients at CV faces for computing diffusive fluxes are also computed from linear shape functions. The High Resolution Interface Capturing (HRIC) scheme of Muzaferija et al. (1998) is used to discretize the convective fluxes in the volume fraction equation in order to achieve a sharp resolution of the interface and avoid unphysical solutions. The time derivative is discretized using the solution at the current time level as well as the solutions from the previous two time levels – second order scheme – to improve the solution accuracy.

The resulting system of algebraic equations is coupled and nonlinear and is solved in a segregated and iterative manner using the Algebraic Multigrid method. It involves guessing a solution, linearizing the equations about that solution, and improving that solution – this process is repeated until a converged solution is obtained after which the solution advances to the next time step. The complete formulation can be described as using a colocated variable arrangement and a Rhie-and-Chow-type pressure-velocity coupling combined with a SIMPLE-type algorithm. For compressible flows a density correction is introduced in the discretized continuity equation in addition to the velocity correction for incompressible flows. The density correction is also expressed in terms of the pressure correction using the equation of state (Demirdžić et al., 1993). The solution method is fully implicit, allowing for relatively large time steps and better stability compared to explicit schemes.

The accuracy, stability and efficiency of the iterative solution mainly depend on the time step size, number of iterations per time step and the under relaxation factors for pressure and velocity. The Courant number represents the distance moved by a fluid particle in one time step and is a helpful indication for selecting the time step size. For time-accurate simulations, the convective Courant number should be 1.0 on average in the zone of interest (CD-adapco, 2014). The under-relaxation factors are used to under-relax the changes of the solution during the iterative process in order to promote convergence. Low values of relaxation factors help maintain numerical stability, however, at the expense of slow convergence thus requiring more iterations per time step and conversely. In transient simulations, the contribution of the transient term to the discretized equations has the same effect as under-relaxation and, hence, the under-relaxation factors for velocity and pressure can be increased to accelerate convergence (CD-adapco, 2014). The number of iterations per time step should be chosen together with the under-relaxation factors. For tough coupled problems such as problems involving free surface flows and rigid body motion, provided that the time step is adequate, 10 iterations per time step are generally sufficient (CD-adapco, 2014). The effect of the under-relaxation factors and number of iterations per time step on the solution was systematically investigated in Camilleri et al. (2015), where it was found that, provided the time step size is adequate (Courant number < 1.0), their effect on the solution is small. In the simulations presented in this thesis, the default values of under relaxation for pressure and velocity of 0.2 and 0.8, respectively, are used. The number of iterations per time step is set to 10 in the rigid body simulations and 20 in the coupled simulations. Iterative convergence at every time step was assessed by monitoring the variation of residuals with iterations as well as the vertical force in the case of the flexible panel.

3.1.2. Structural domain

ABAQUS uses the displacement Finite Element (FE) method to find an approximate (finite element) solution for the response of a structure (displacements, deformations, strains, stresses and so on) that is subjected to some history of loading. In the displacement-based finite element formulation the “weak form” of the equilibrium equations is used as the basic equilibrium statement. The term “weak form” means that force and moment equilibrium must be maintained in an average sense over a finite number of divisions of the volume of the body rather than at all times over any arbitrary volume of the body – exact solution. This equivalent “weak form” is the virtual work principle and has a simple physical interpretation: the rate of work done by the external forces subjected to any

virtual velocity field is equal to the rate of work done by the equilibrating stresses on the rate of deformation of the same virtual velocity field (Dassault Systèmes, 2013).

The structural geometry is divided into a number of finite elements connected at discrete points called nodes. ABAQUS offers a wide variety of elements including solid, shell, beam, and membrane elements. In the present work, 8-node continuum shell elements with reduced integration (SC8R) are used. The element behaviour is based on the Lagrangian formulation where the element deforms with the material as opposed to the Eulerian formulation used in the Finite Volume method, where the cells are fixed in space and fluid flows through them. Continuum shell elements have only displacement degrees of freedom which are calculated at the nodes of the element while at any other point in the element interpolation is used. For elements that have nodes only at their corners, such as element SC8R, linear interpolation is used. These elements are called linear elements or first-order elements. The element stiffnesses matrix is formed using reduced (lower-order) integration while the mass matrix is integrated exactly.

The nonlinear transient dynamic response is calculated using implicit direct integration. It employs a Hilber-Hughes-Taylor solver for time integration, which is an extension of the Newmark-β with controllable numerical damping. The time step is chosen automatically on the basis of the "half-increment residual", i.e., the time step is adjusted appropriately by monitoring the values of equilibrium residuals at half increments once the solution at the end of the step has been obtained. A limit on the maximum time step size, equal to the time step size used in the CFD model, is also set. In an implicit dynamic analysis the integration operator matrix must be inverted and a set of nonlinear equilibrium equations must be solved at each time increment. The nonlinear equilibrium equations are solved at each time step in an iterative manner using Newton's method.

3.1.3. Coupling of fluid and structural domains

Fluid-structure interaction simulations are solved following the partitioned approach as opposed to the monolithic approach. In the partitioned approach, the fluid and structural domains are solved within independent solvers and information is exchanged across the fluid-structure interface at each time step in an alternating fashion. The coupling is two-way. The SIMULIA Co-Simulation Engine is the software component responsible for communication between Star CCM+ and ABAQUS. The advantage of this approach is that the specialization and capabilities of each solver are preserved; however, the accuracy of the solution relies heavily on the stability of the coupling algorithm (CD-adapco, 2014).

The implicit coupling scheme is used to as it allows Star CCM+ and ABAQUS to exchange data more than once per time-step and ensures strong coupling, as opposed to the explicit scheme where data exchange takes place only once per time step and a sufficiently small time step must be used to maintain stability. Implicit coupling is necessary when a relatively light or compliant structure interacts with a relatively heavy, almost incompressible fluid, such as the water impact of flexible composite hull panels. In the present work, the number of exchanges per time step is set to 10, which means that for each exchange the fluid solver performs two iterations for the purposes of numerical stability. This value is chosen based on the results of a systematic study where coupled simulations of the problem studied in section 3.3 with 20, 10, 5 and 4 exchanges per time step and 20 iterations per time step were performed. The simulations with 5 and 4 exchanges per time step

were found to encounter issues with numerical stability – see the time history of pressure at P5 (i.e. near the chine edge of the panel) in Figure 3 where high frequency oscillations are observed between t ≈ 0.021s and t ≈ 0.024s – and thus the number of exchanges per time step is set to 10. The number of exchanges also has a significant influence on the computational time – the computational times for 0.05s of simulation time using a single core of an Intel Core i7 processor running at 3.40 GHz are 22.4, 13.9, 11.4 and 10.4 hours for 20, 10, 5 and 4 exchanges respectively.

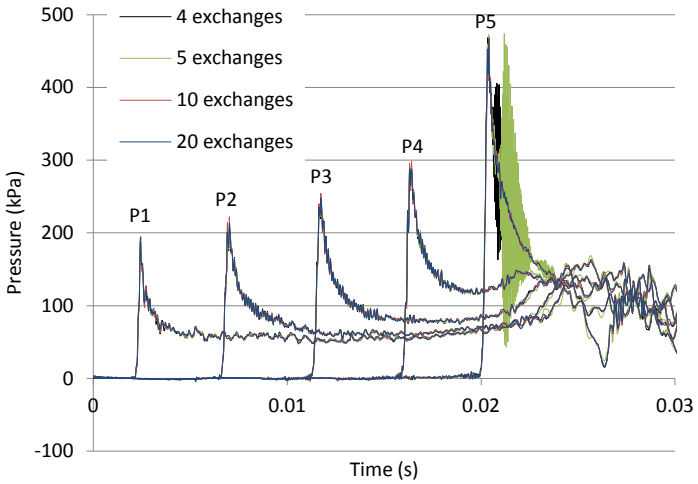

Figure 3 - Effect of the number of exchanges per time step on solution accuracy and stability.

Star CCM+ exports traction data (pressure and wall shear stress) to ABAQUS and imports nodal displacements. Data is exchanged across the fluid-structure interface between Star CCM+ boundaries and ABAQUS surfaces (surface-to-surface coupling). In the fluid solver, the response of the fluid to motion of the structure is accounted for by the grid flux, an additional term in the momentum equations. The grid flux is the volume swept out by the movement of a face in one time step divided by the time step and is effectively the normal velocity of the face multiplied by its area. The morphing motion model is used to displace the fluid grid in response to the structural deformations. The morpher uses the imported nodal displacements together with displacements of other boundaries within the morphing region to generate an interpolation field that is then used to displace the actual vertices of the grid to their new position. The displacements of the boundaries other than the coupled boundaries are controlled by specifying morpher boundary conditions. The grid vertices on symmetry boundaries are only allowed to move in the plane of symmetry, while the vertices on other boundaries are fixed in space.

3.2. Impact of a free-falling rigid wedge with water

3.2.1. Test case

In this section the impact of a free-falling rigid wedge with water is studied and the computed results are compared to the experimental data of Lewis et al. (2010) for validation. The experimental setup is shown in Figure 4. The water tank is 5.8 m long, 0.75 m wide and filled to a level of 0.59 m with fresh water at room temperature. The wedge slides on two vertical cylindrical aluminium posts on either side of the tank using two pairs of linear bearings 0.13 m apart. The wedge dimensions are

0.944 m by 0.735 m by 0.22 m and the deadrise angle is 25°. It is constructed of plywood material and covered with a layer of GFRP to seal and further strengthen the wedge. The gap at each end between the wedge and tank is deliberately made small – 7.5 mm – to promote two-dimensional flow.

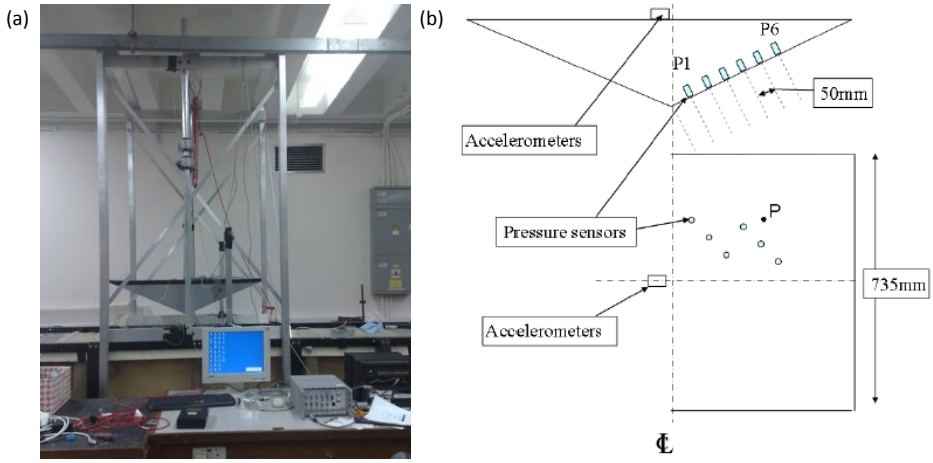

Figure 4 - Experimental setup: drop test rig and wedge (a) and position of the sensors on the wedge (b) (Lewis et al. 2010).

The wedge vertical position and acceleration, pressure at different locations on the wedge bottom surface, and free surface shape were measured during the tests. The position of the accelerometers and pressure sensors is shown in Figure 4. Pressure is measured at six positions with flush diaphragm pressure transducers with a diaphragm diameter of 9 mm. The sensors are recessed into the wedge by 0.6 mm to allow space for a thin layer of petroleum jelly to delay temperature shock[1]. The wedge vertical position and acceleration are measured with a potentiometer and two accelerometers (10g and 100g), respectively. The data is recorded at a rate of 10 kHz. A high-speed camera was also used to capture the impact and subsequent formation of jet and spray at 5000 frames/s. More details on the drop test rig and instrumentation can be found in Lewis et al. (2010).

The wedge was dropped from two heights (0.5 m and 0.75 m) and for each drop height two different masses were used (23.3 kg and 33.3 kg). Each test was repeated at least three times to confirm repeatability. The wedge impact velocity, calculated from the high-speed camera images, is 2.78 m/s and 3.58 m/s for 0.5m and 0.75 m drops respectively.

3.2.2. 2D model

Figure 5 shows the numerical model of the experimental setup of Lewis et al. (2010) in Star CCM+. Only half of the wedge is modelled and a symmetry boundary is applied on the symmetry plane of the wedge, i.e. the left wall of the domain. The wedge is modelled at full-scale and the width and height of the numerical tank are extended to limit the influence of the boundary conditions on the solution (CD-adapco, 2014). The 2D model has an in-plane thickness (x-axis) of 10 mm and a symmetry condition is applied on the front and back faces to ensure two-dimensional flow. The wedge surfaces and the right boundary of the domain are specified as a no-slip wall. The bottom

[1] The pressure diaphragm consists of thin stainless steel, which is sensitive to a high rate of temperature change. The pressure sensors were found to exhibit a zero shift in pressure output by up to 5% of the overall range of the sensor when slowly immersed into the water. This was found to be caused by the rapid change in temperature as the sensor passed from air to water.

boundary is specified as velocity inlet with zero inflow velocity and the top boundary as pressure outlet with atmospheric pressure conditions.

The grid is trimmed hexahedral with local refinements near the wedge and on the free surface and prism layers (orthogonal prismatic cells) on the wedge bottom surface to accurately capture the flow features of interest such as the rapidly moving large pressure gradient in the spray root and free surface deformations. Details of the computational grid around the wedge are shown in Figure 6.

The moving grid approach is used here where the grid is moved with the wedge and the location of the free surface is fixed in space. The Dynamic Fluid Body Interaction (DFBI) motion model is used to simulate the motion of the wedge and grid in response to gravity force and pressure and shear forces exerted by the fluid. The initial position of the free surface is set 0.5 m below the wedge apex and the wedge mass is 0.1585 kg (23.3kg wedge; linear scaling).

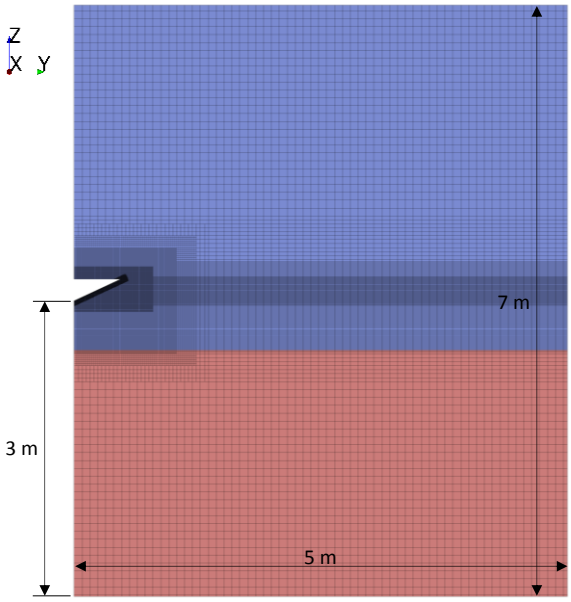

Figure 5 - Numerical model of the experimental setup of Lewis et al. (2010): geometry of the wedge and tank, trimmed hexahedral grid and the initial position of the free surface.

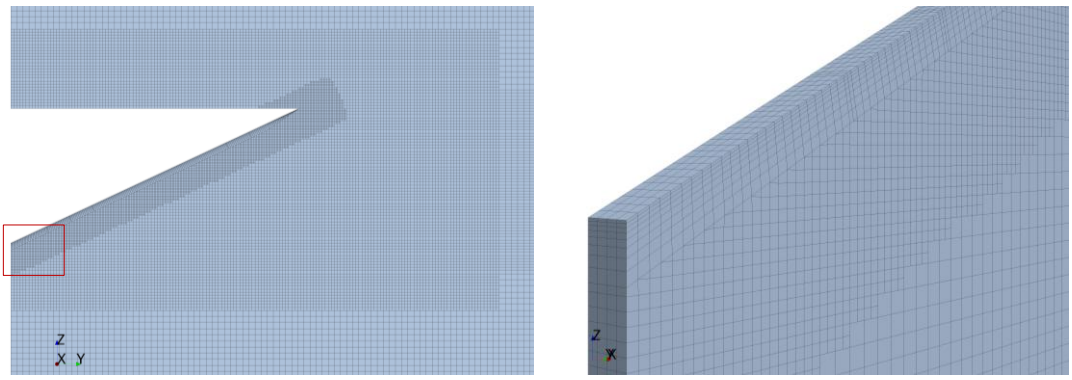

Figure 6 - Details of the computational grid around the wedge including local refinements and prism layers. The figure on the right is a close-up view of the wedge tip which is marked in red in the figure on the left.

3.2.2.1 Convergence studies

The sensitivity of the solution to time step and grid spacing is assessed by running simulations with varying time step and grid sizes – see Table 2 - and comparing the results. The grid shown in Figure 5

is here referred to as the medium grid. The coarse and fine grids are constructed by doubling and halving the medium grid spacing in the vertical and horizontal directions, respectively. The size of the first cell on the wedge bottom surface in the tangential (Δt) and normal (Δn) directions is given in Table 2. The time step sizes were chosen such that the Courant number is less than 1.0 on average in the region of the spray root and jet where the flow velocity is highest. The simulations were run on the Iridis 4 supercomputer of the University of Southampton on 2 nodes with 16 dual 2.6 GHz processors each.

Table 2 - Time step and grid sizes used for the convergence study.

Grid	Grid size, cells	Δt, mm	Δn, mm	Time step, ms	CPU time, hrs
Medium	57 554	2.5	0.5	0.025	2.98
Medium	57 554	2.5	0.5	0.05	0.97
Medium	57 554	2.5	0.5	0.1	0.76
Coarse	13 067	5	1.0	0.05	0.63
Fine	336 587	1.25	0.25	0.05	3.82

Figures 7 and 8 show the time histories of vertical wedge acceleration and pressure at P1 – P6 computed using the grid and time step sizes given in Table 2. For both studies, the three solutions agree well both in terms of shape of the time histories and magnitude and timing of the peaks. This indicates that the impact is well resolved both temporally and spatially and the numerical solution is independent of the time step and grid size. The fine time step and coarse grid solutions are relatively noisy which is likely to be that the time step is too fine for the grid. Based on these results, the medium grid and 0.05 ms time step size are chosen for further studies.

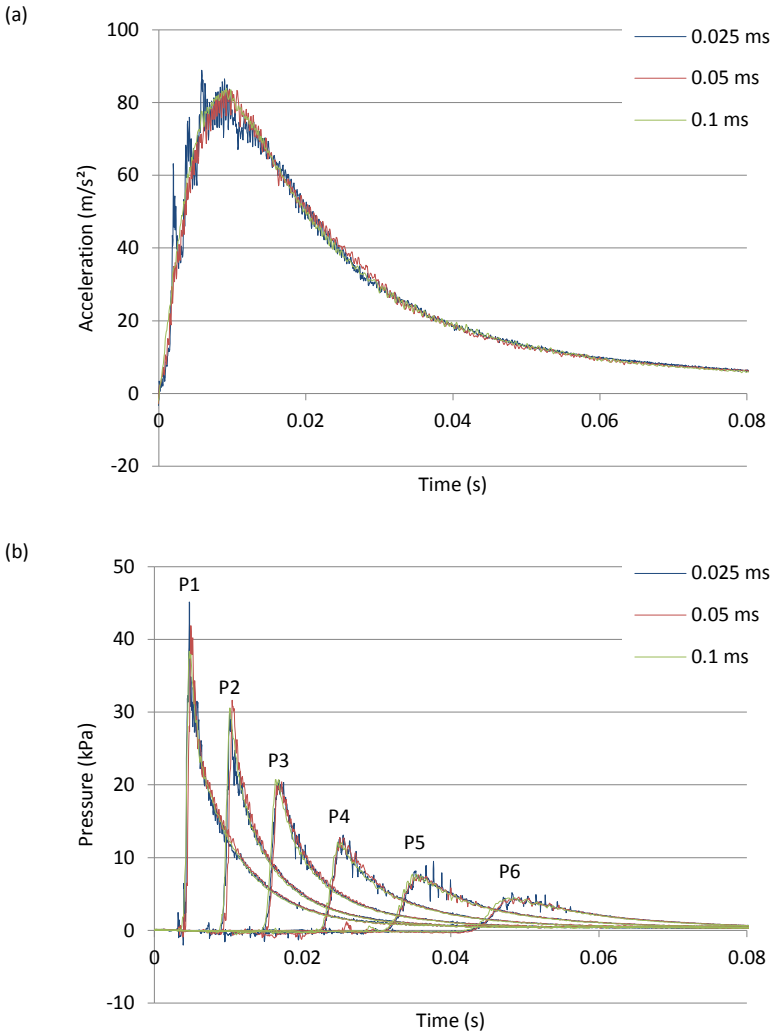

Figure 7 - Time histories of acceleration (a) and pressure at P1 – P6 (b) computed on the medium grid with time step sizes of 0.025, 0.05 and 0.1 ms.

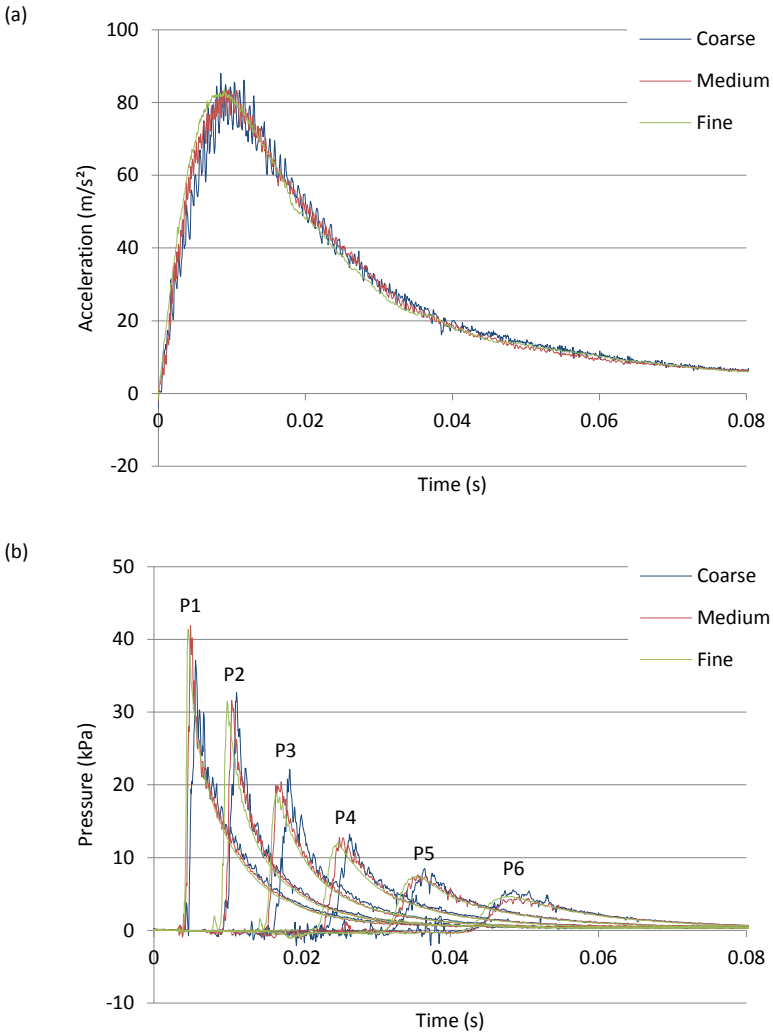

Figure 8 - Time histories of acceleration (a) and pressure at P1 - P6 (b) computed on the coarse, medium and fine grids with a time step size of 0.05 ms.

3.2.3. 3D model

Three-dimensional simulations were also performed to investigate the effect of three-dimensional flow and the effect of the gap between the wedge and tank wall on the fluid pressure and wedge kinematics. Due to symmetry only one quarter of the wedge is modelled. Two 3D models with gap widths of 7.5 mm (equal to the experimental gap width) and 4.6325 m (equal domain width and depth) as shown in Figure 9 are considered. The width (y-axis) and height (z-axis) of the 3D models are the same as for the 2D model. The 3D grid is constructed by extending the 2D medium grid in the x-direction. For the model with narrow gap, cells in the region between the wedge and tank wall are also refined and have the same size as those on the wedge bottom surface. The grid size for the narrow and wide gap models is 1.70M and 3.12M, respectively. The same boundary conditions as in the 2D simulations are used except for the back face, which is specified as wall boundary. Furthermore, the same physics models, solver settings, and test conditions (0.5 m drop height and 23.3 kg wedge mass) are used. It is also noted that the pressure sensors are located along the centreline of the wedge and not offset from the centreline as in the experiments (see Figure 4b).

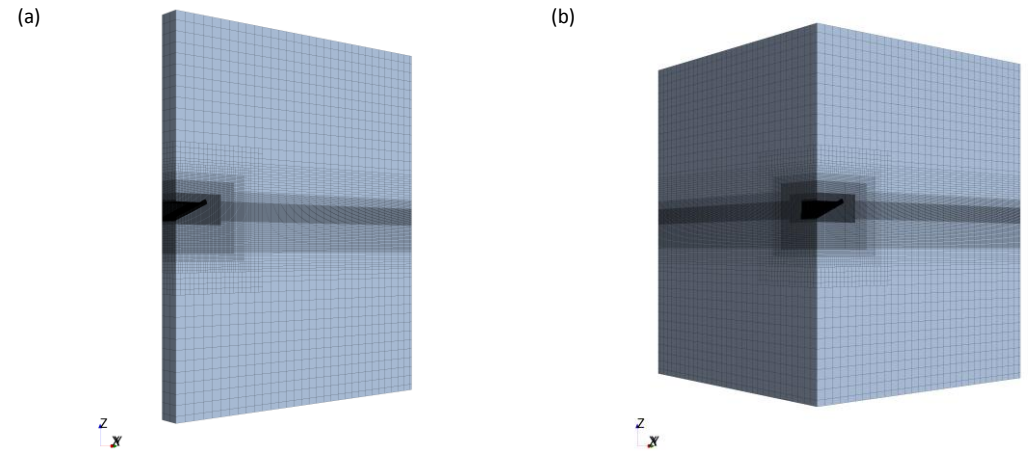

Figure 9 - 3D models: narrow gap (a) and wide gap (b).

Figure 10 compares the time histories of wedge vertical acceleration and pressure at P1 – P6 computed using the 2D model with those computed using the 3D models with narrow and wide gaps. The wedge impact velocity is 2.96 (2D model), 2.97 (3D model with narrow gap) and 3.05 m/s (3D model with wide gap). Comparing the results computed on the 2D grid and 3D grid with wide spacing (to remove the effect of boundary influence) it can be seen 3D flow effects are relatively small. There are some differences in the magnitude of peak acceleration and pressure, however these are small. The solution computed on the 3D grid with narrow gap agrees better with the 2D solution, which shows that the tank wall is working as intended, i.e., promoting 2D flow.

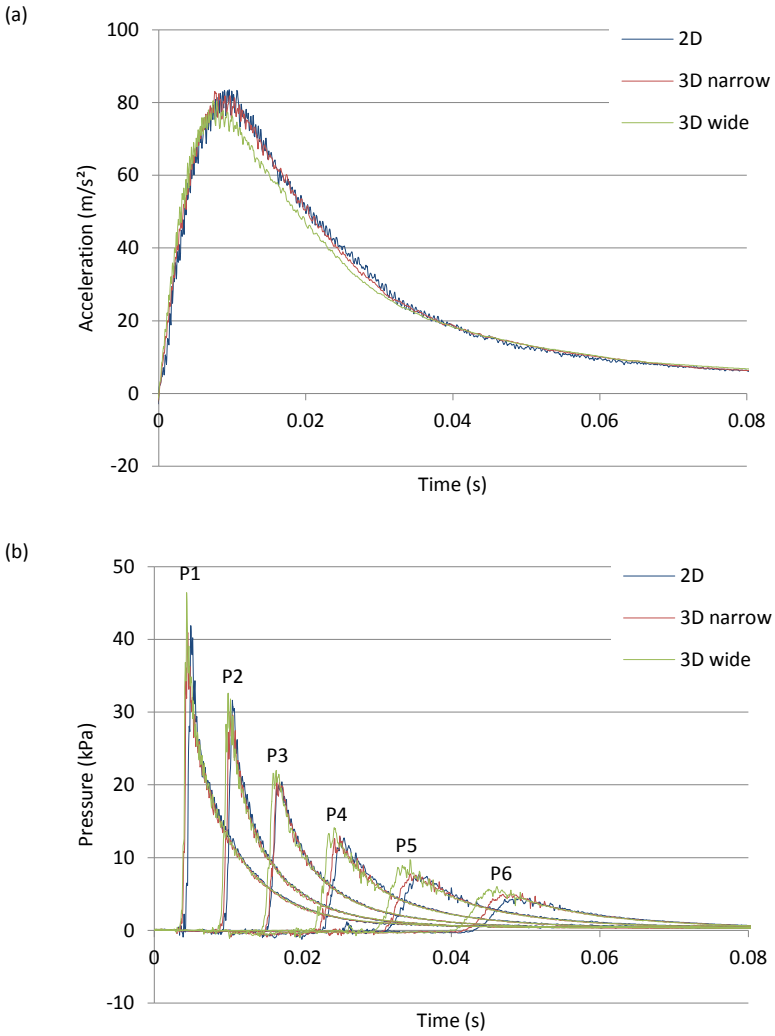

Figure 10 - Time histories of acceleration (a) and pressure at P1 - P6 (b) obtained from the 2D and 3D simulations.

3.2.4. Parametric studies

The effect of drop height, wedge mass and deadrise angle on the impact velocity, acceleration maximum and rise time and magnitude and time of the pressure peaks is studied using the 2D model. The test conditions and results are presented in Table 3 and Figure 11. The rise time is defined as the time period from impact (wedge touches the water surface) to maximum acceleration. The investigated parameters have negligible influence on the shape of the acceleration and pressure histories and hence only the magnitude and time of the peaks are presented. The following observations are made:

- Impact velocity increases with increasing drop height. The wedge mass and deadrise angle have relatively small influence on the impact velocity.
- Maximum acceleration increases and rise time decreases – more severe impact – with increasing drop height while the opposite is true with increasing wedge mass and deadrise angle.

- Pressure increases and the peaks are recorded earlier in time with increasing drop height and wedge mass, with drop height having a larger influence. The opposite is true with increasing the deadrise angle.

Table 3 - Effect of drop height, wedge mass and deadrise angle on the impact velocity and acceleration maximum and rise time.

Study	Drop height, m	Wedge mass, kg	Deadrise angle, °	Impact velocity, m/s	Max. acceleration, m/s^2	Rise time, ms
Base case	0.5	23.3	25	2.96	83.6	9.6
Drop height	0.25	23.3	25	2.13	43.3	12.6
	1	23.3	25	4.12	165.7	6.2
Wedge mass	0.5	18.6	25	2.92	90.8	7.9
	0.5	28.0	25	2.99	78.6	10.6
Deadrise angle	0.5	23.3	20	2.93	111.5	6.2
	0.5	23.3	30	2.98	66.4	11.8

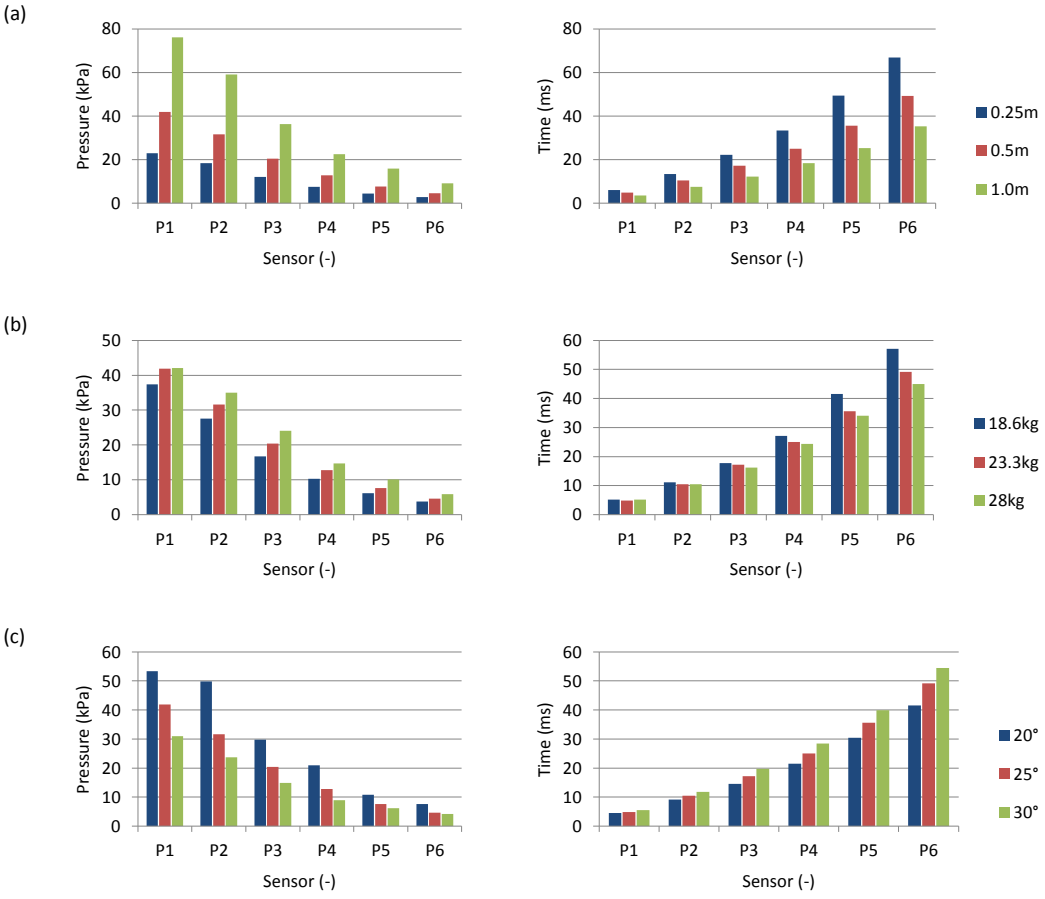

Figure 11 - Effect of drop height (a), wedge mass (b) and deadrise angle (c) on the magnitude and time of P1 - P6 pressure peaks.

3.2.5. Comparison with experiments

Figure 12 compares the time histories of vertical acceleration and pressure at P1 – P6 computed on the medium grid with a time step size of 0.05 ms with the experimental results of Lewis et al. (2010). The drop height in the numerical model was reduced from 0.5 m to 0.44 m to match the experimental impact velocity of 2.78 m/s. The reason for overestimating the impact velocity is most likely to be related to friction between the linear bearings and vertical posts in the experimental setup, which is not taken into account in the numerical model. The wedge mass is 23.3 kg and the deadrise angle is 25°. The experimental results are reproduced from the graphs in Lewis et al. (2010). The experimental acceleration and pressure signals are low pass filtered with a Butterworth filter and cut-off frequencies of 250 Hz and 1000 Hz, respectively. No filtering has been applied to the numerical signals. Zero time is defined at the moment the wedge apex reaches the undisturbed water level, determined by using the high-speed camera images in conjunction with markings on the wedge and the tank window in the experiments, and from the acceleration time history in the numerical simulations.

The first and largest peak is recorded by sensor P1, located 50 mm away from the wedge apex. Thereafter sensors P2 to P6 record increasingly lower peaks due deceleration of the wedge. Furthermore, the shape of the pressure time histories changes from a sharp peak at P1 to a more rounded one at P6. Qualitatively, the predicted time histories of acceleration and pressure at P1 – P6 agree well with the experiments. There is also reasonably good quantitative correlation between the numerical results and experiments. There are some slight differences in the magnitude of peak acceleration and the rise and decay times that are most likely due to friction in the experiments. It should be noted that even though the drop height was reduced to match the impact velocity, the effect of friction is still present as the wedge enters the water. The magnitude of the P3 – P6 peak pressures compare well with the experiments, however the P1 and P2 peaks are overpredicted. The timing of the pressure peaks show less favorable agreement, with the numerical pressures occurring earlier than seen experimentally. The difference in the timing of the peaks is about 3.5 ms for all sensors and is mainly attributed to uncertainty in determining the point of impact. Lewis et al. (2010) reported that the accelerometer begins to be affected by the impact 2.2 ms after the high-speed camera images show the wedge touching the water. In this time, the wedge travels approximately 10 mm.

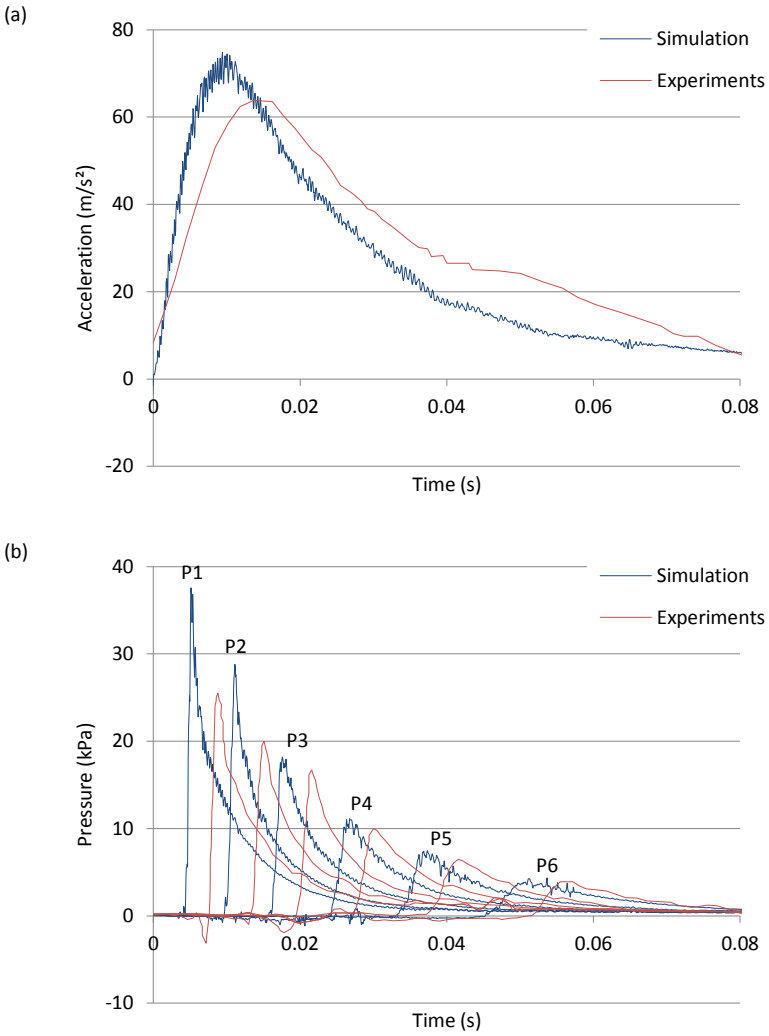

Figure 12 - Comparison of computed time histories of acceleration (a) and pressure at P1 - P6 (b) with experimental results of Lewis et al. (2010). Drop height is 0.44 m (0.5 m in the experiments) and wedge mass is 23.3 kg.

The results for the other test conditions are presented in Table 4 and Figure 13. The drop height has been adjusted in each case to match the experimental impact velocity. The best agreement with the experiments is seen for the case with a 0.5 m drop height and 33.3 kg wedge mass (sim2). This further suggests that friction has a significant influence on the wedge kinematics and fluid pressure.

Table 4 - Comparison of predicted and experimental impact velocity and acceleration maximum and rise time for all test conditions.

Case	Mass, kg	Drop height, m	Impact velocity, m/s	Max. acceleration, m/s²	Rise time, ms
Exp1 (Sim1)	23.3	0.5 (0.44)	2.78 (2.79)	63.9 (74.9)	13.7 (9.4)
Exp2 (Sim2)	33.3	0.5 (0.42)	2.78 (2.77)	58.2 (61.2)	15.5 (10.3)
Exp3 (Sim3)	23.3	0.75 (0.745)	3.58 (3.59)	90.4 (124.8)	12.8 (6.2)
Exp4 (Sim4)	33.3	0.75 (0.71)	3.58 (3.57)	77.6 (104.4)	13.8 (8.3)

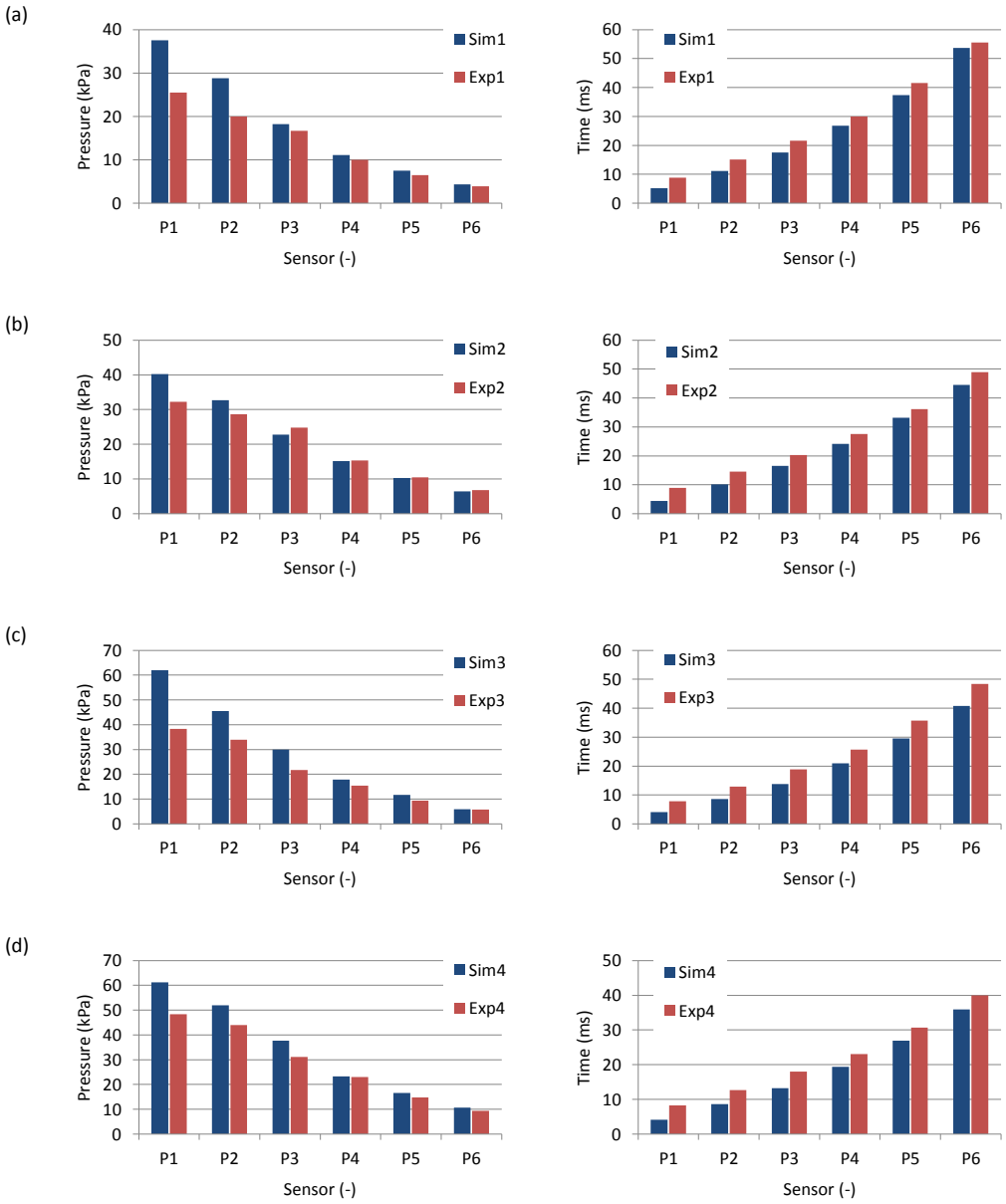

Figure 13 - Comparison of predicted magnitude and time of pressure peaks with experiments for all test conditions (a – d).

3.3. Constant velocity water impact of a flexible panel

3.3.1. Test case

The constant velocity water impact tests with a flexible composite hull panel of Allen & Battley (2015) are studied in this section. The tests were performed using a purpose built servo-hydraulic slam testing system (SSTS) at the University of Auckland, NZ, shown in Figure 14. It uses a 3.5 m diameter cylindrical tank approximately half filled with 13 000L of water. A high-speed servo-hydraulic system, located inside the tank, is used to drive the specimen fixture and test panel along linear tracks vertically into the water at a constant velocity. Three fixed vertical plates, two on the sides and one at the back of the test panel, are used to constrain the flow along the panel creating symmetrical, 2D impact conditions. More details on the SSTS can be found in Battley & Allen (2012).

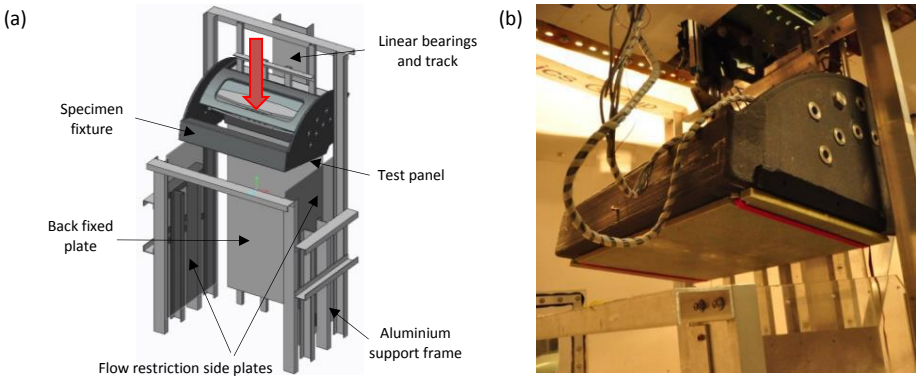

Figure 14 - SSTS: schematic of the specimen fixture and flow restriction panels (a) and test panel mounted on the specimen fixture (Battley & Allen 2012) (b).

The test panel considered in the present work is a sandwich panel with CFRP skins ($0/90_3$) and SAN foam core (Gurit M100). It was manufactured using a resin infusion process. The rectangular panel measures 1030 x 600 mm and the thickness of each skin and core is 2.02 mm and 14 mm respectively. The flexural rigidity, D, determined through a flexural beam test (ASTMC373) is 13.5 kNm and the calculated shear stiffness, S, is 744 kN/m. The test panel is simply supported by the specimen fixture with an unsupported area of approximately 1000 x 500 mm. Furthermore, the panel is strapped to the specimen fixture at the ends and steel rings are used to prevent in-plane motion.

The hydrodynamic loads and structural responses were measured using pressure sensors (PCB Piezoelectronics W113A26/003C20), displacement transducers (Schaevitz LCIT-1000) and strain gauges (Omega SGD-6/120-RYB81). The position of the specimen fixture is measured using a linear position sensor (Vishay 139L). Data was acquired at a sampling rate of 51.2 kHz. The layout of the instrumentation is given in Figure 15.

This particular test panel was tested at impact velocities up to 4.5 m/s and deadrise angle of 10°. The impact velocity considered for the verification and validation studies is 3.0 m/s.

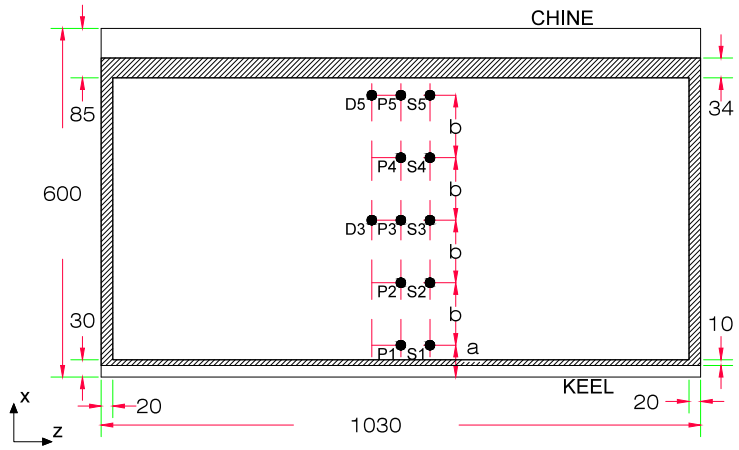

Figure 15 - Layout of the instrumentation: pressure sensors (P1 - P5), strain gauges (S1 – S5) and displacement transducers (D3 & D5). The shaded region represents the panel area in contact with the specimen fixture frame. The lower and upper edges are designated the keel and chine edges respectively. All dimensions are in mm. a = 55 mm and b = 107.5 mm.

3.3.2. 2D fluid model

Figure 16 shows the geometry of the panel and tank and the trimmed hexahedral grid used for the 2D simulations, following the same process as for the rigid wedge. The width and height of the tank were extended to limit the influence of the boundary conditions on the solution (CD-adapco, 2014). The model has an in-plane thickness (z-axis) of 5 mm. The gap between the keel end of the test panel and the fixed vertical plate at the back (right hand wall) is also modelled and is 10 mm wide. For the simulations with a flexible panel, the fluid domain is divided into two regions called morphing and stationary, as shown in Figure 16. In the morphing region the grid vertices move in response to the structural deformations whereas in the stationary region the grid is fixed. This was done to reduce the computational resources required by the mesh morpher, which are directly related to the number of control points present in the morphing region.

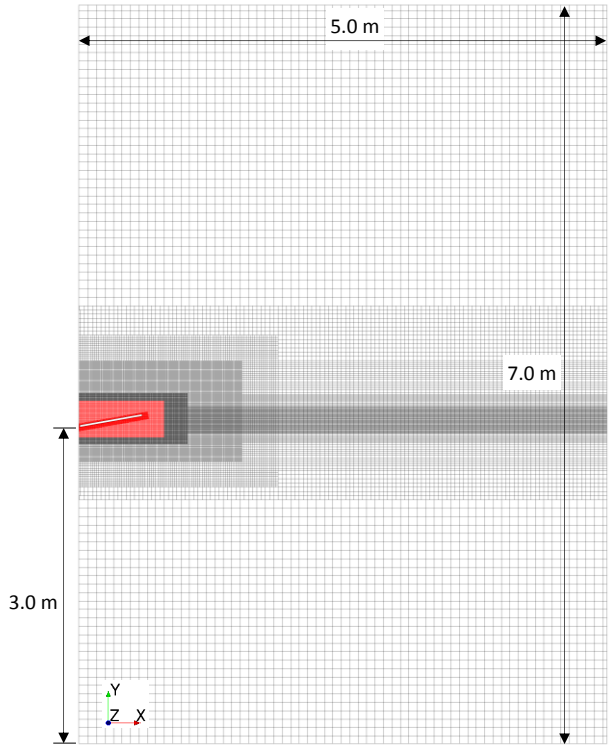

Figure 16 - Geometry of the panel and tank and the trimmed hexahedral grid used for 2D simulations. The area in red around the test panel represents the morphing region and the stationary region includes the rest of the domain.

In the present work, the panel and grid are fixed in space and the motion of the panel is simulated by moving the free surface vertically upwards. The bottom boundary is thus defined as velocity inlet with the inflow velocity set equal to the panel velocity (3 m/s), and the top as pressure outlet with atmospheric pressure conditions. This approach avoids unnecessary grid deformation associated with rigid body motions and facilitates data mapping between the fluid and structural solvers. A simulation with the panel and grid moving at a constant velocity downwards and the free surface location fixed in space was also tried and the results showed negligible differences. A no-slip wall condition is applied on the panel boundary and the right hand wall, and the left hand wall and the front and back faces are specified as symmetry boundaries. The initial position of the free surface is set 50 mm below the lower edge of the panel to allow for the flow to develop before the impact event (judged from the pressure and velocity fields and the pressure and force time histories).

A trimmed hexahedral grid, shown in Figures 16 and 17, is used in this study. The grid is locally refined in the vicinity of the panel and in the vertical direction around the free surface, and prism layers (orthogonal prismatic cells) are added on the panel to accurately resolve the flow features of interest, including the high-pressure region in the spray root and free surface deformations. The grid in Figures 16 and 17 is henceforth referred to as medium grid (see Table 5). The grid convergence study employs two additional grids, coarse and fine. The coarse grid is obtained by halving the medium grid spacing in vertical and horizontal directions, i.e., a grid refinement ratio of 2. The refinement ratio between the medium and fine grids was set to 1.5 to help ensure that the same level of physics is resolved on all grids. The particulars of the three grids are summarised in Table 5, where Δn is the grid spacing in the normal direction to the panel of the first cell, Δt in the tangential direction and Δh is the spacing in the vertical direction around the free surface.

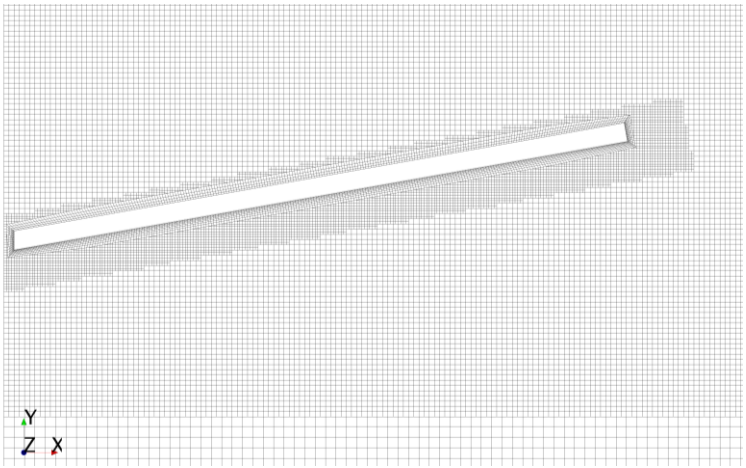

Figure 17 - Partial view of the computational grid showing the local refinement around and prism layers on the panel and the 10mm gap between the test panel (keel/ left edge) and the fixed vertical plate.

Table 5 - Particulars of the grids used in the convergence study.

Grid	Grid size	Δn (mm)	Δt (mm)	Δh (mm)	Impulse (Ns)
Coarse	17 860	1.0	5.0	10.0	3.461
Medium	57 642	0.5	2.5	5.0	3.450
Fine	193 327	0.33	1.67	3.33	3.448

3.3.2.1 Convergence studies

Time step and grid convergence studies were carried out to assess the sensitivity of the solution to the time step size and grid spacing. The structure is modelled as rigid and the fluids incompressible. The Grid Convergence Index (GCI) method of the ASME standards (Celik et al., 2008), based on the Richardson Extrapolation (RE) method, was used to estimate the numerical errors and uncertainties in the simulations. The solution variable used in the GCI calculations is the vertical force impulse, I, written as,

$$I = \int_{t_0}^{t_d} F_v(t)\, dt \tag{1}$$

where t_0 corresponds to the time of initial contact with the free surface at the keel edge and t_d is the time at the instant when the spray root reaches the chine edge and the panel is fully immersed. The force impulse represents the transfer of momentum from the fluid to the structure. The integral is approximated using the trapezoidal rule.

For the time step study, the medium grid was used to obtain solutions with constant time steps of 0.01, 0.02 and 0.04 ms. The time steps were chosen such that the Courant number is less than an average of 1.0 in the region of the spray root and jet – the most critical region where the flow velocity is highest, for the purposes of both time-accuracy and numerical stability. Iterative convergence at every time step was assessed by monitoring the change in vertical force on the panel with iterations, as well as the residuals and 20 iterations per time step were deemed sufficient. The calculated force impulse for the coarse, medium and fine time steps is 3.401, 3.442 and 3.450 Ns respectively. The time order of accuracy is 2.39, which matches reasonably well the formal second order of the solver considering the complex physics models used. It should be noted that a higher order does not imply higher accuracy, only that the simulated values converge more rapidly than expected. The numerical uncertainties in the medium and fine time step solutions, calculated with a factor of safety of 1.25, are 0.36% and 0.07% respectively.

For the grid size study, solutions were obtained on the coarse, medium and fine grids with a (fine) time step of 0.01ms. The time histories of pressure at P1 – P5 and vertical force for the three grids are shown in Figure 18 and the vertical force impulse is given in Table 5. The broken line in Figure 18 represents the time t_d of chine wetting used in the force impulse calculations. The coarse grid is not able to capture the large pressure gradients at the spray root accurately – the pressure histories are poorly resolved around the peaks and large oscillations are observed in both the pressures and vertical force. The solutions computed on the medium and fine grids agree well, suggesting that the flow field is well resolved and the solution is independent of spatial resolution. The grid order of accuracy is 1.95 and the numerical uncertainty in the medium and fine grid solutions is quite low, 0.03% and 0.06% respectively. Based on the results of the time step and grid convergence studies, the medium grid and medium time step size of 0.02 ms are deemed sufficient to model the flow characteristics of this problem.

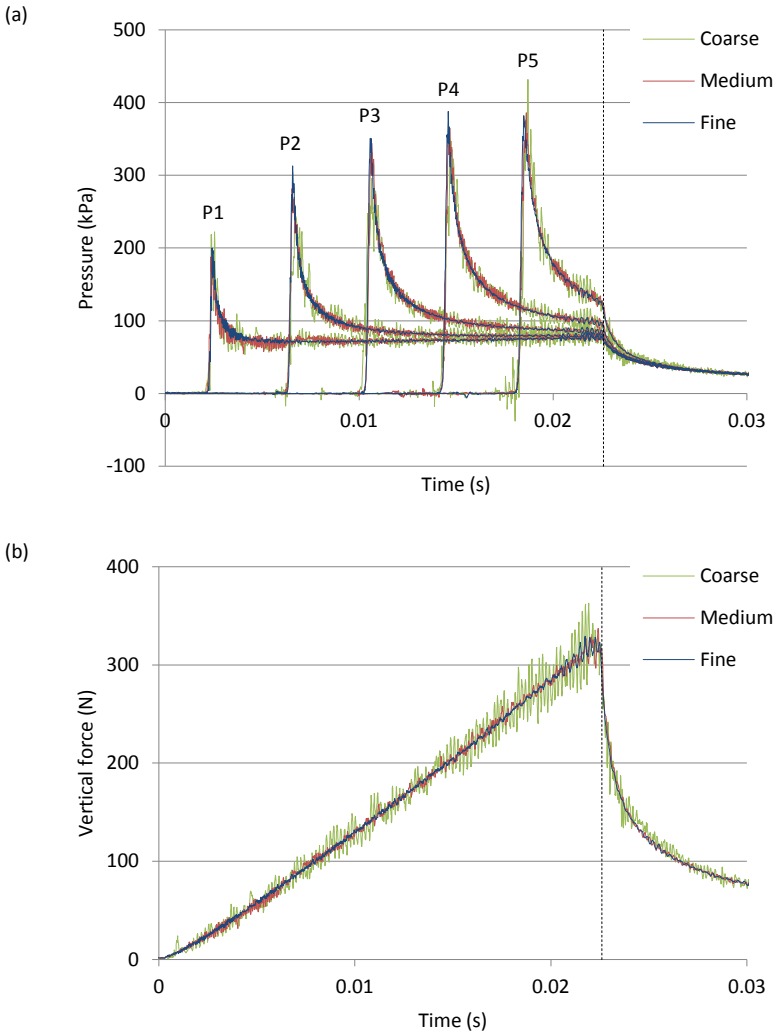

Figure 18 - Time histories of pressure at P1-P5 (a) and vertical force on the panel (b) computed on the coarse, medium and fine grids with a time step size of 0.01ms.

3.3.2.2 Fluid compressibility

Compressibility is inherent in every real fluid however most practical engineering flows can be safely assumed incompressible. The ratio of the flow speed to speed of sound in the fluid, called the Mach number, is used to determine whether compressibility can be safely neglected or not. For small Mach numbers, Ma < 0.3, changes in the fluid density are small everywhere in the flow field and the flow may be considered incompressible. Otherwise it is compressible (White, 2009). For hull slamming problems, the entry velocity is rather small compared to the speed of sound in water and compressibility can generally be neglected. However, in cases where the relative angle between the body and water surface is nearly zero i.e., flat or nearly flat bottom impacts, the spray root and jet move at a speed much higher than the entry velocity and compressibility effects can be important (Faltinsen, 1999).

For the test case considered, impact velocity of 3m/s and deadrise angle of 10°, the flow can be safely assumed incompressible. However, coupled fluid-structure interaction simulations are often more numerically stable if the fluids are allowed to be slightly compressible. This is particularly true for problems where the added fluid mass is comparable to the structural mass and/or there is a

dramatic change in the hydrodynamic loads and structural velocities, such as in slamming impacts (CD-adapco, 2014). To investigate this statement some preliminary coupled simulations with both incompressible and compressible models for air and water were run. The coupled simulation with incompressible fluids started to diverge shortly after initial contact with the free surface – large pressure oscillations were observed at the interface and the panel deformations did not appear to be consistent with the physics of the problem – and eventually failed due to cells with negative volume caused by excessive deformation. The coupled simulation with compressible fluids did not encounter any of these problems. Various combinations of compressibility models for air and water were therefore tested to investigate the effect of fluid compressibility on the solution and identify the most suitable model for each fluid, see Table 6. When modelled as compressible fluid, air is treated as an ideal gas with isothermal properties – temperature changes are not expected to be significant in such a short time period. The compressibility of water is defined by the following expressions for the density ρ, and density pressure derivative $d\rho/dp$,

$$\rho = \rho_o + \frac{p}{c^2} \tag{2}$$

$$\frac{d\rho}{dp} = \frac{1}{c^2} \tag{3}$$

where ρ_o is a constant and c is the speed of sound in the fluid. When the physical time scales of interest are much larger than the time scale of the speed of sound in water, lower values of sound speed can be used to further enhance the numerical stability and accelerate convergence, otherwise the exact nature of fluid compressibility has to be modelled (CD-adapco, 2014). The solutions were computed on the medium grid and a time step size of 0.02ms. The panel is modelled as rigid to be able to compare with the fully incompressible solution. The computational times are for 0.05 s of simulation time using a single core of an Intel Core i7 processor running at 3.40 GHz. The differences in the force impulse relative to the fully incompressible case are also given.

Table 6 - Summary of the results for different combinations of compressibility models.

Air	Water	c_{water} (m/s)	CPU time (h)	Impulse (Ns)	Impulse relative difference (%)
Constant density	Constant density	-	5.4	3.442	-
Ideal Gas	Constant density	-	8.2	3.435	0.2
Ideal Gas	Equation of State	1500	9.0	3.431	0.3
Ideal Gas	Equation of State	600	9.9	3.409	1.0
Ideal Gas	Equation of State	100	10.0	2.809	18.4

The compressible flow models are more computationally expensive as two additional equations need to be solved – the energy conservation equation and the equation of state relating the density and pressure. The fully compressible solutions with the speed of sound in water set as 1500 and 600 m/s and the partially compressible solution agree well with fully incompressible solution, the relative differences are less than 1.0% as can be seen in Table 6. However, the force impulse for the case with a speed of sound in water of 100 m/s is about 18% lower than the fully incompressible case. The main reason for this large difference is that in this case the magnitude of the speed of sound in water is of the same order of magnitude as the flow velocity, and therefore the fluid is

being compressed. The fully compressible model with the speed of sound in water set at 1500 m/s is chosen for the coupled simulations to enhance the numerical stability.

3.3.3. 2D structural model

The Finite Element (FE) model of the structure consists of a quasi-two-dimensional beam (one element thick) representing a transverse slice of the panel from the centre as shown in Figure 19. It has a length of 600 mm, height of 18.04 mm (total skins and core thickness), and an in-plane thickness (along the z-axis) of 5 mm to match the thickness of the fluid domain.

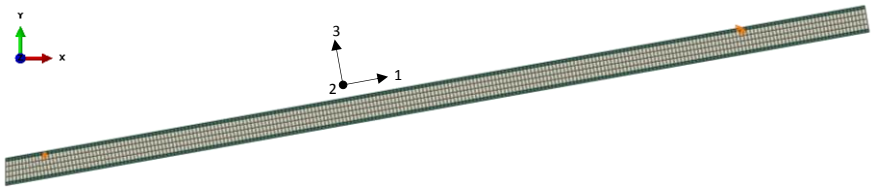

Figure 19 - Two-dimensional beam FE model with simply supported boundary conditions.

The beam is partitioned into three layers, representing the top and bottom skins and core, and for each layer the section and material properties were defined. This approach implicitly assumes the face sheets and core to be perfectly bonded and no delamination is possible between layers. The skins and core materials are assumed to behave linearly elastically. The experimental test conditions were chosen such that the resulting maximum stress in the panels is well below the yield stress of the materials (T Allen 2016, personal communication, 26th April). The skin material is plane stress orthotropic (Lamina model), with the stresses in the direction normal to the panel considered to be negligible, Young's modulus along the panel width E_1 = 46.16 GPa, Young's modulus along the panel length E_2 = 30.77 GPa, Poisson's ratio v = 0.3, and Shear Modulus $G_{12} = G_{13} = G_{23}$ = 4.2 GPa. The core material is orthotropic (Engineering constants model), with Young's modulus $E_1 = E_2 = E_3$ = 0.109 GPa, Poisson's ratio $v_{12} = v_{13} = v_{23}$ = 0.3, and Shear Modulus $G_{12} = G_{13} = G_{23}$ = 41 MPa. The density of skins and core is 1350 and 100 kg/m^3 respectively.

The beam model is discretized using 8-node continuum shell elements (SC8R) with enhanced hour glass control. Continuum shell elements include the effect of transverse shear deformation which is particularly important for foam cored sandwich structures. Enhanced hourglass control is used to prevent mesh instability, also known as "hourglassing", associated with first-order reduced integration elements. The element size along the beam length (1-direction) was set as 2.5 mm to closely match the size of the fluid cells at the interface. Four elements are stacked through the thickness of the core to provide more refined through-thickness response and better transverse shear stress and force prediction. The skins are discretized using only one element through the thickness. The FE mesh has a total of 1440 elements.

Two FE models with different boundary conditions are considered to investigate their effect on structural response. In the first model, the beam is simply supported from two points, 485 mm apart, representing the inner edges of the test fixture frame. The steel rings are modelled by restricting in-plane motion at the chine edge (see Figure 20a). In the second model, the portions of the beam extending beyond the inner edges of the test fixture frame are fixed (see Figure 20b). In both models a z-symmetry condition is specified on the front and back faces. The first natural

frequency of the simply supported and fixed beams, obtained from the modal analysis in ABAQUS, is 212 and 293Hz respectively.

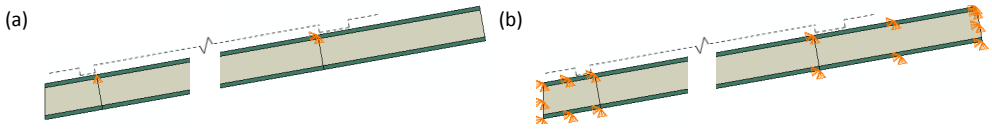

Figure 20 - Simply supported (a) and fixed (b) beam models. The broken line represents the test fixture frame.

Rayleigh damping is also introduced in the model to damp out the high frequency components and further enhance the stability of the solution, by 'smoothing' the imported nodal displacements. In the present work only the stiffness proportional damping factor is defined, calculated assuming 2% critical damping. Rayleigh damping acts in addition to the numerical damping associated with the time integrator using a Moderate Dissipation setting. Geometrical nonlinear effects are also considered for complete generality. However, for foam cored sandwich panels and these particular tests conditions, Stenius et al. (2013) have shown that the nonlinear effects are small.

3.3.4. 2D results and discussion

Figure 21 compares the time histories of pressure and deflection from the simulations with simply supported and fixed beams with the experimental data presented in Allen & Battley (2015). The test conditions are 3.0 m/s constant impact velocity and 10° deadrise angle. The numerical solutions were computed on the 'medium' grid with time step size of 0.02 ms, and with air and water were treated as compressible fluids for the purposes of numerical stability (c = 1500 m/s). Time t = 0s corresponds to the instant at which the keel edge of the panel touches the free surface.

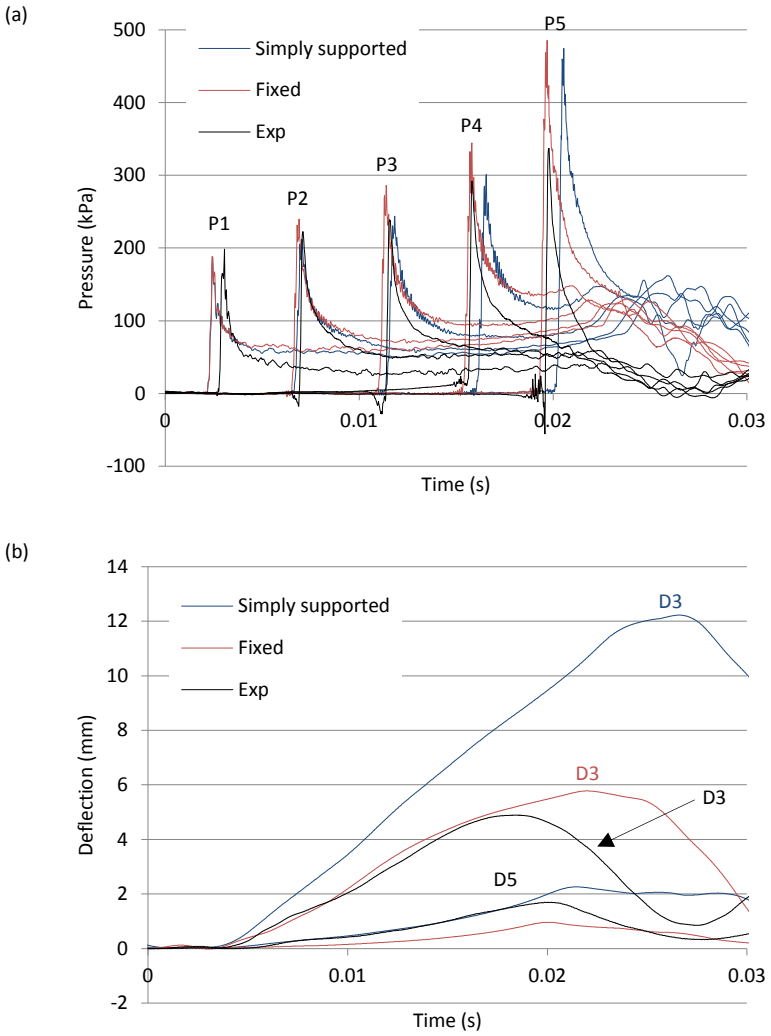

Figure 21 - Comparison of predicted time histories of pressure at P1-P5 (a) and deflection at D3 and D5 (b) with experimental results of Allen & Battley (2015).

The pressure histories are characterized by a large peak rapidly decaying to a much lower and fairly constant residual pressure level. The first and lowest peak is recorded by sensor P1, which is located close to the keel edge of the beam. Thereafter, sensors P2 – P5 record increasingly higher peaks. Similar trends are observed in both the numerical and experimental results. Figure 22 shows the contours of free surface, velocity and pressure at the time of P3 pressure peak. The vertical and horizontal dashed lines in Figure 22 mark the intersection between the beam and water surface, and the calm water surface respectively. The impact is characterized by water pile up at the intersection between the body and water surface, called the spray root, and spray jet formation. The spray root and jet travel along the beam with a velocity that is much higher than the entry velocity, as can be seen in Figure 22. The pressure contour shows a region of very high pressure confined in a very small area at the spray root. The pressure over the remaining part of the wetted surface is fairly constant and the pressure in the jet is nearly atmospheric. The deflection histories show that the beams/ panel do not begin to deform until after the peak pressure at sensor P1 is recorded, i.e., when the spray root moves within the edges of the specimen fixture frame. Thereafter the deflection gradually increases to a maximum which occurs just after chine wetting for the simply supported beam and within the wetting time for the fixed beam and the experimental test panel.

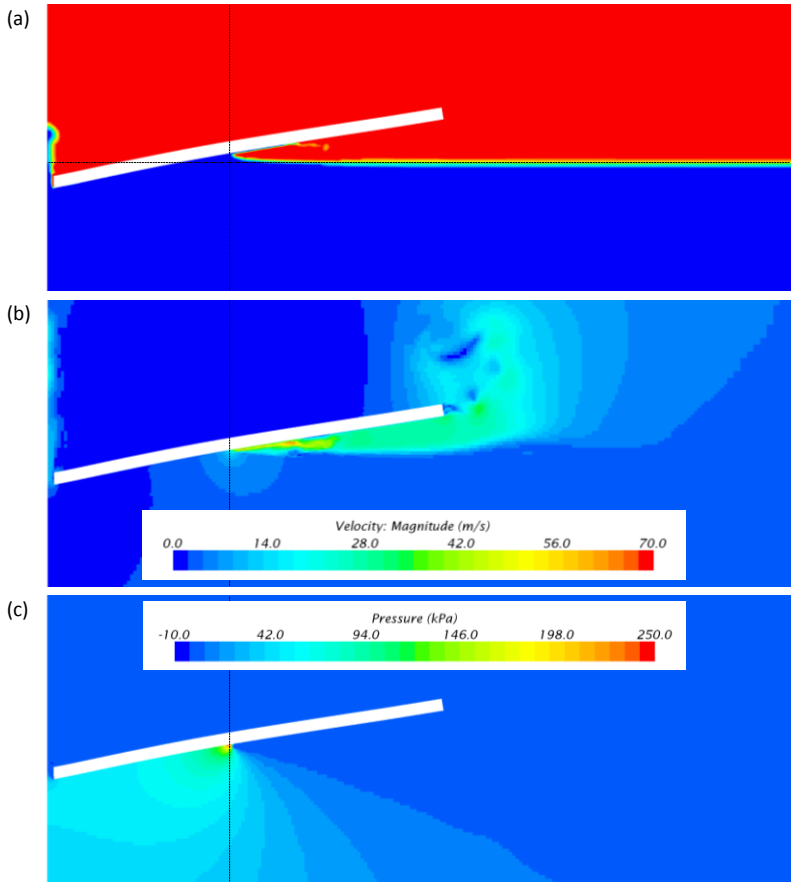

Figure 22 - Contours of free surface (a), velocity (b) and pressure (c) at the time of P3 pressure peak. Simply supported beam model.

Effect of structural boundary conditions

The pressure histories for the simply supported and fixed beams are similar and only show some small differences in the magnitude and timing of the P2 – P5 peaks, and the residual pressures towards the end of the impact event. The residual pressure for the simply supported beam show significant oscillations after the P5 pressure peak. These oscillations are caused by the flexural vibrations of the portion of the beam extending beyond the chine support as it enters the water, which affect the pressure distribution at the fluid-structure interface. In the case of the fixed beam, this part of the beam is constrained and the residual pressures display a smoother behaviour.

The deflection histories for the simply supported and fixed beams show significant differences, despite the two beams being subject to similar loading conditions as shown by the relatively good agreement between the pressure histories. As expected, the structural responses for the simply supported beam are significantly larger. The maximum deflection is 12.2 mm and occurs at t = 26.6 ms, whereas in the case of the fixed beam, the maximum deflection is 5.8 mm and occurs at t = 22.0ms. These differences are mainly attributed to the different structural boundary conditions which contribute to the panel's rigidity, in particular the in-plane boundary fixation in the case of the fixed beam where both bending and membrane forces act to resist deformation.

Comparison with experimental data

There is generally good correlation between the computed pressure histories and the experimental measurements with regards to overall shape of the plots and magnitude and timing of the P1 – P4

peaks. At P5 both numerical models predict a peak pressure that is about 35% larger than the experimental results. Furthermore, the numerical residual pressures settle to a value higher than in the experiments, and towards the end of the impact event the experimental residual pressures drop to a lower level whereas the numerical pressures show signs of a secondary peak. These discrepancies are most likely due to the variations in the experimental impact velocity profile. Figure 23 shows the experimental time histories of test fixture velocity and the local impact velocity at the centre of the test panel. The latter is obtained by subtracting the panel deformation velocity from the test fixture velocity. As can be seen, the test fixture velocity varies significantly during the impact event, particularly when the test panel is returning back from maximum deflection (approx. 0.02 – 0.03 s), where it decreases by approximately 0.4 m/s. In the numerical models, the test fixture velocity is maintained constant and as a result the local impact velocity at the panel centre after maximum deflection is greater than the test fixture velocity (during this time the panel is deflecting in the same direction as the direction of motion of the test fixture), hence the secondary peaks.

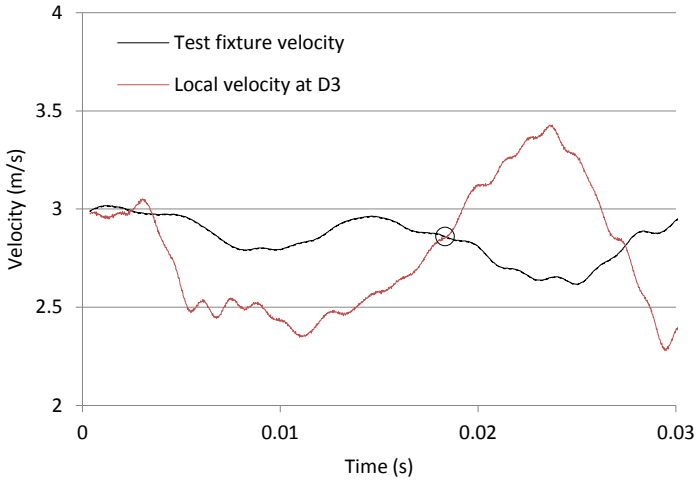

Figure 23 - Experimental time histories of test fixture and local velocity. The time of D3 peak deflection is marked with an o.

The two beam models generally give good qualitative description of the structural response. The fixed beam model also shows good quantitative correlation with the experimental measurements, particularly at the centre (D3) whereas the simply supported beam model overpredicts the deflection – maximum deflection is about 85% larger. In both cases, the largest differences between the numerical and experimental results are observed after the experimental maximum deflection, where the experimental plot reduces to nearly zero deflection in a short period of time. These are mainly attributed to the drop in the experimental impact velocity profile when the panel is returning back from maximum deflection which reduces the load on the panel during this time. At the chine (D5), the response of the simply supported beam agrees well with the experiments initially and after the experimental peak deflection the numerical model starts to overpredict the deflection whereas the fixed beam model generally underpredicts the deflection. The SSTS is designed such that the edges of the test specimen are simply supported by the fixture with fabric straps and steel rings to hold the panel against the specimen fixture and prevent in-plane motion respectively. The experimental support conditions are most closely represented in 2D as simply supported without in-plane fixation at the chine edge. The large difference in deflection suggests that the restraining effect at the panel ends has a larger than anticipated effect.

3.3.5. 3D model

Three-dimensional simulations were performed to investigate the effect of three-dimensional flow and the accuracy of 2D simulations for predicting the hydrodynamic loads and to further investigate the effect of the structural boundary conditions on the panel response. The 3D fluid model was constructed by extending the 2D model in the z-direction up to the side plate. Due to the symmetric nature of the problem, only half of the panel was modelled and the gap between the test panel and fixed vertical side plate is 25 mm wide. The fixed vertical back plate used in the experiments is 800 mm wide, centred on the test panel. In the numerical model, the back plate is assumed to span across the whole length of the panel. The geometry of the 3D tank and panel is shown in Figure 24. A wall condition was specified on the side and back boundaries, representing the fixed vertical side and back plates. The same conditions used in the 2D model were specified on the other boundaries. The 3D grid was also constructed by extending the 2D 'medium' grid in the z-direction. It has 4.38M cells. Details of the 3D grid around the panel are shown in Figure 24. The same physics models and fluid compressibility and solver settings applied in the 2D simulations are used here.

The FE model representing one half of the panel is shown in Figure 24. The element size was set as 5 mm to limit computational costs. The convergence of the structural response with respect to the number of elements is studied in Piro & Maki (2013) and Stenius et al. (2013) for panels of similar size where in both studies it was concluded that the structural response can be accurately modelled with an element size of 5 mm. The thickness of the skins and core was again discretized using one and four elements respectively. The FE mesh has a total of 73,542 SC8R elements. The experimental support conditions can be represented more accurately in the 3D model. On the inner edges of the specimen fixture frame, the panel is simply supported without in-plane fixation. The steel rings are modelled by applying a fixed boundary condition at the corners of the frame and the fabric straps are modelled by constraining panel movement in the vertical direction. Finally, a z-symmetry condition was specified on the symmetry boundary. The first dry natural frequency of the panel is 246.8 Hz, which matches reasonably well the analytical value of 270.4 Hz calculated using the formula given in Zenkert (1997) for a simply supported sandwich panel with isotropic faces.

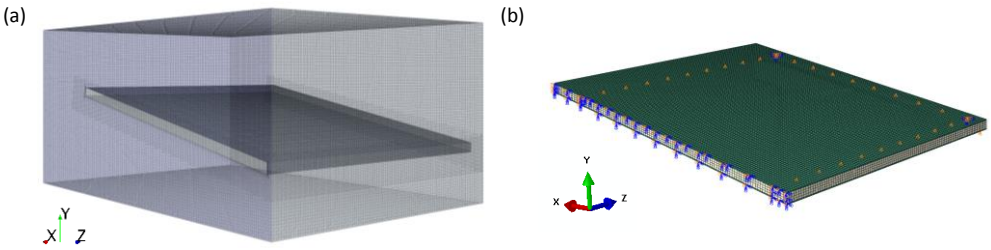

Figure 24 - 3D model: morphing region and details of the mesh around the panel (a) and FE model of one-half of the panel, mesh and boundary conditions (b).

The pressure and deflection histories computed using the 3D model are compared with the results from the 2D model with simply supported boundary conditions and the experimental measurements in Figure 25. The computational costs of the 3D simulation are significantly larger. The computational time for 0.05s of simulation time using 48 cores of the IRIDIS supercomputing facility at the University of Southampton is nearly 96 hours.

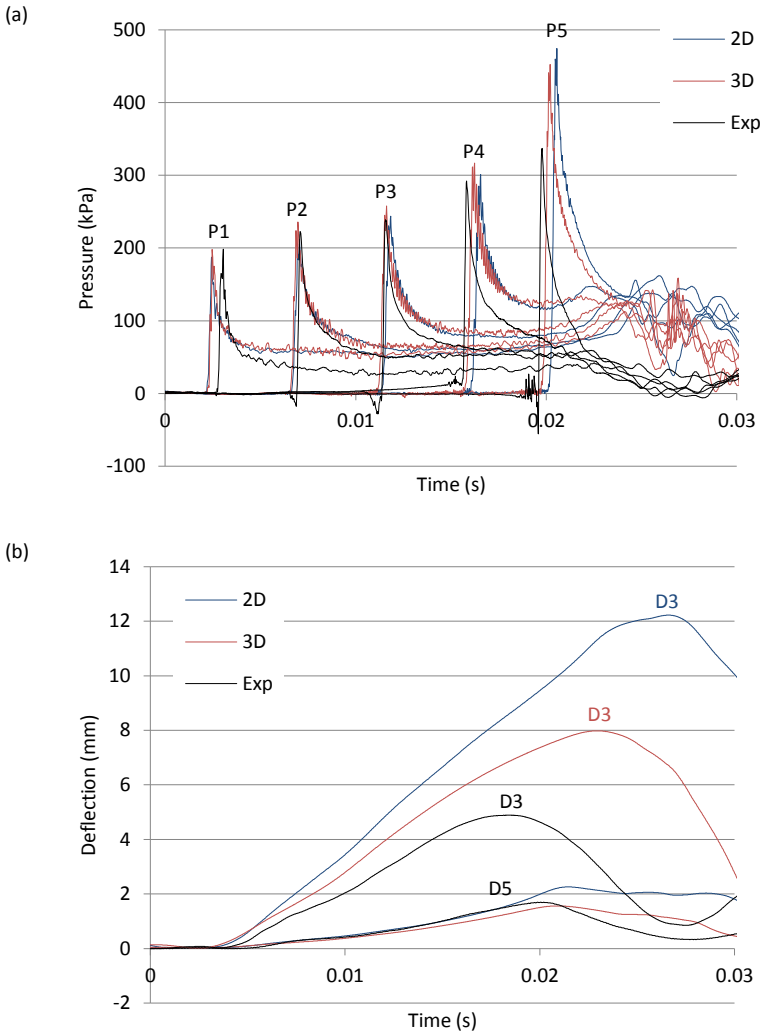

Figure 25 - Comparison of pressure (a) and deflection (b) histories from the 2D and 3D models with experiments.

The numerical pressure histories show negligible differences, suggesting that 3D flow effects are small and the more economical 2D model can be used to accurately predict the hydrodynamic loads. This is most likely due to the close proximity of the flow constraining panels to the test panel. The deflections obtained from the 3D simulation are lower than the 2D results and show better agreement with the experiments. The peak deflection at D3 is 8.0 mm, 48% larger than the experimental peak, and occurs at t = 23ms. The differences between the 2D and 3D numerical solutions are mainly due to the inclusion of the restraining effect at the panel end, i.e. the fabric straps in the 3D model. Some discrepancies between the 3D and experimental results are again observed after the experimental peak, which are mainly attributed to the variations in the experimental velocity profile as explained previously.

3.3.6. Effect of structural flexibility on loads and responses

The effect of the flexibility of the structure, i.e., hydroelastic effect, on the hydrodynamic loads is studied by comparing the pressure and force histories for the 2D rigid and flexible beams, as shown in Figures 26 and 28. The interest here lies in a qualitative comparison rather than a quantitative one; hence, the more flexible simply supported beam model is used. As can be seen from Figure 26

the pressure peaks for the flexible beam are lower at P2 – P4 and higher at P5. Furthermore, there is a slight delay in the timing of the peaks which increases with more immersion. These differences are mainly attributed to the deformation of the structure, which changes the local kinematics, i.e. geometry, velocity, and acceleration, conditions at the fluid-structure boundary and has a significant influence on the pressure distribution (Stenius et al., 2011; Allen & Battley, 2015).

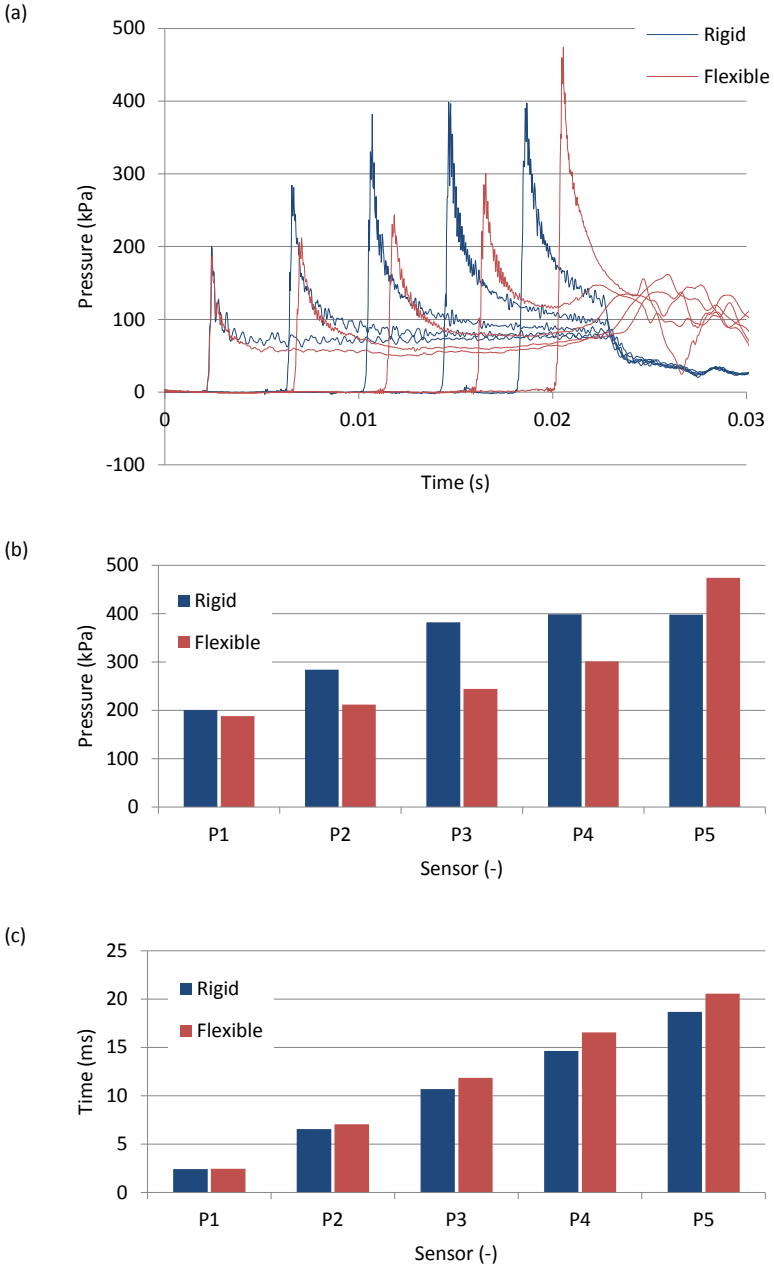

Figure 26 - Rigid and flexible pressures: time histories (a), and magnitude (b) and timing (c) of the P1 - P5 pressure peaks.

Figure 27 compares the time histories of local impact velocity at D3 and local deadrise angle at D5 for the rigid and flexible beams. The local impact velocity is obtained by subtracting the beam deformation velocity from the test fixture velocity, i.e., 3.0 m/s, and the local deadrise angle is approximated from the deflection history at D5 (Battley et al., 2009). As can be seen, the structural deformations lead to significant reduction in both the local impact velocity at the centre of the panel and deadrise angle at the chine. For instance, the local velocity at D3 at the time sensor P3 records

its peak is 2.32 m/s whereas the local deadrise angle at D5 at the time of P5 pressure peak is 5.91°. As a result the P3 and P5 pressure peaks for the flexible beam are lower and higher respectively compared to the rigid solution. The delay in the timing of the peaks is also related to the deformation of the structure. As the beam deflects away from the supports, the vertical distance from the keel edge to the location of the sensor increases and thus, the time it takes for the sensor to reach the free surface also increases.

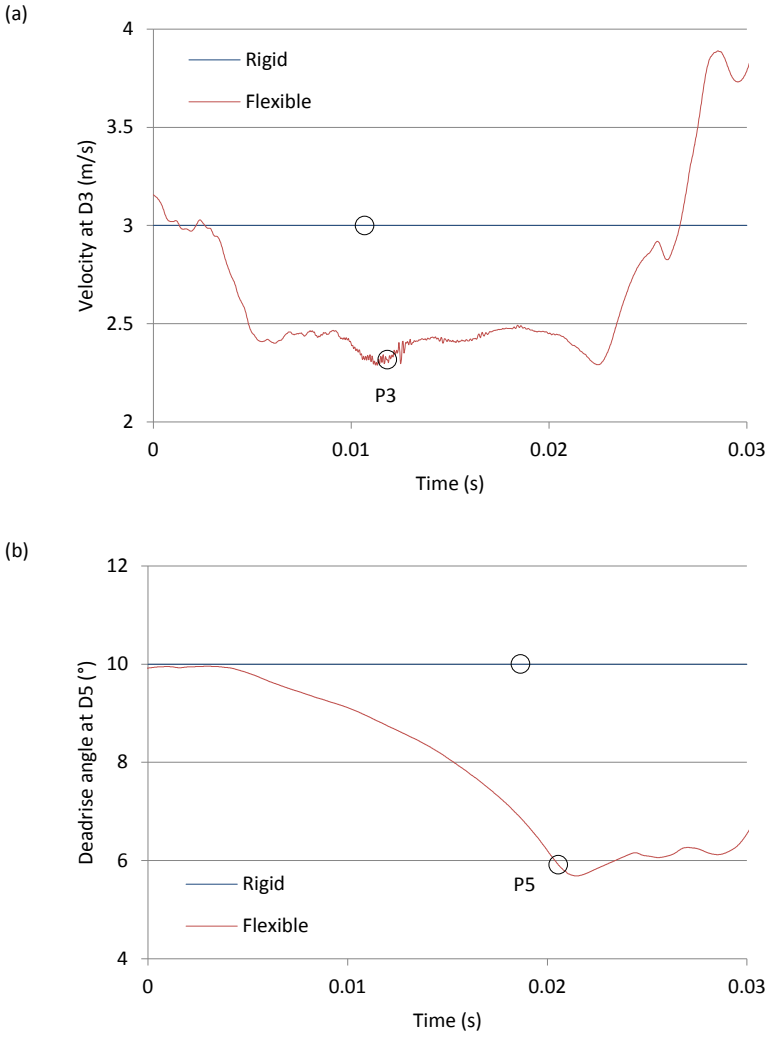

Figure 27 - Time histories of local impact velocity at D3 (a) and deadrise angle at D5 (b). The timing of the P3 and P5 pressure peaks are marked with an o.

The force histories in Figure 28 show similar trends, namely the force acting on the flexible panel is lower during the initial stages of the impact event, but increases to a higher level in the later stages. The force impulse for the flexible beam is 3.195 Ns, 7.1% lower than the value given in Table 6 for a rigid beam. These trends agree well with the experimental results in Battley et al. (2009) and Allen & Battley (2015) and the numerical results in Stenius et al. (2011a), i.e., decrease in load at the centre and increase at the outer edge of the panel.

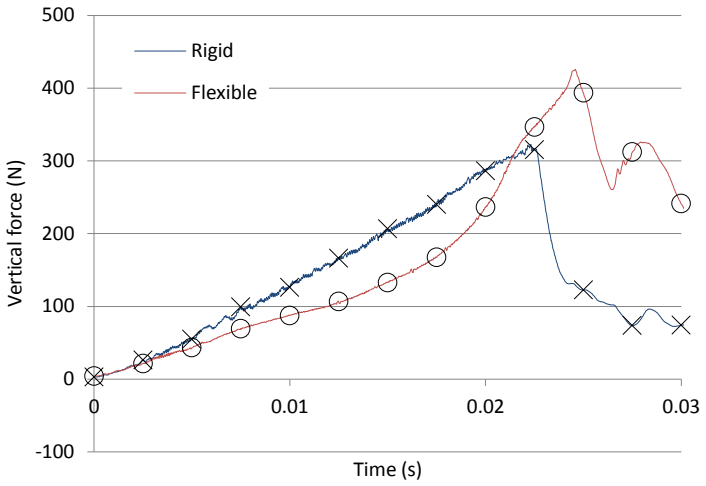

Figure 28 - Rigid and flexible force time histories. The time instants at which the quasi-static analysis using the pressure distribution from the rigid panel is performed are marked with an x and the corresponding flexible solution is marked with an (o).

The effect of the flexibility of the structure on the response is studied by comparing the deflection histories from the simulation with the simply supported beam model with corresponding rigid/ quasi-static (RQS) solutions following the work in Stenius et al. (2011a). The RQS solutions are obtained by first running the CFD simulation with a rigid structure to obtain the pressure distribution at different time instants during the impact event, that is, the hydrodynamic load is not affected by the structural flexibility. The pressure distributions are then applied on the structure in a quasi-static manner, assuming that the structural response is unaffected by the structural inertia. The results are presented in Figure 29. The RQS solutions were obtained at every 2.5 ms starting from t = 0s.

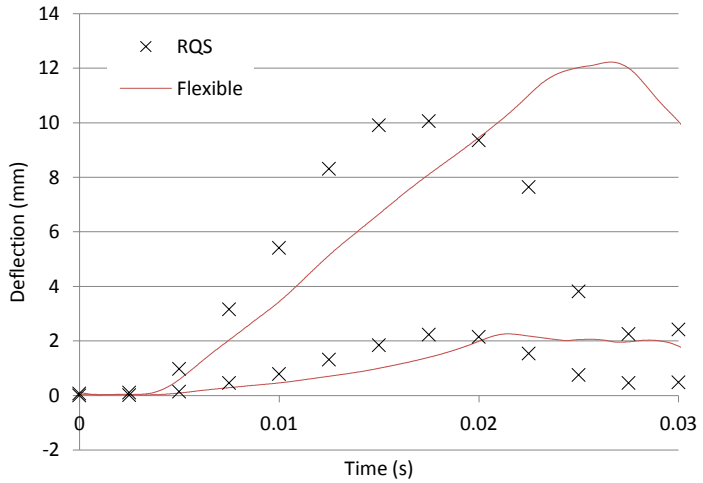

Figure 29 - Comparison of RQS and flexible deflections at D3 and D5.

The hydroelastic solution yields smaller deflections at both D3 and D5 than the RQS solution during the initial stages of the impact event (t < 20 ms), and larger deflections in the later stage (t > 20 ms) where it reaches a maximum of 12.2 mm at t = 26.6ms. This was also observed by Stenius et al. (2011a). Maximum deflection for the RQS solution is 10.1mm at t = 17.5ms. These differences are mainly attributed to the variation in loading. As can be seen by comparing Figure 28 and Figure 29 the RQS solution yields larger deflections when the force acting on the rigid panel is larger, and the

peak force on the flexible panel occurs at about the same time of peak deflection, both of which are larger than the corresponding RQS values. The differences in the results can also be partly attributed to the added mass and to a lesser extent (in this case of a thin sandwich beam) structural inertia in the hydroelastic solution. Stenius et al. (2011a) developed a simplified method based on engineering beam theory and generalized Wagner (1932) theory to study the different force components that act during slamming impacts. They found that structural inertia effects are only significant during the early stages of the impact and mainly contribute to reducing the structural response, whereas the added mass dominates in the later stages and mainly contributes to increasing the structural response.

Impact velocity

To further investigate the effect of hydroelasticity on the hydrodynamic loads and structural responses different impact velocities were studied. The results are summarised in Figures 30 and 31 where the magnitude and timing of the pressure and deflection peaks from the simulation with a flexible beam (simply supported beam) are made dimensionless using the corresponding RQS solution. Linear trend lines have also been added to the plots together with the R^2 fitting statistic. A high R^2 value indicates strong dependence between the two variables, whilst for a low R^2 value the opposite is true. As seen, unsurprisingly, the effect of hydroelasticity on the hydrodynamic loads becomes more significant with increasing impact velocity, particularly at the centre (P3) and chine (P5), where there are clear trends of decreasing and increasing peak pressures, respectively. The delay in the timing of the peaks also increases with impact velocity. Faltinsen (1999) also observed increase in the influence of hydroelastic effects with increasing impact velocity. At P1, the hydroelastic effects are small. The peak deflections, however, do not show any significant trends in the magnitudes as the velocity increases. Furthermore, the maximum deflection (D3) from the RQS solution is for all impact speeds lower than that from the hydroelastic solution and the difference is nearly constant. Hydroelastic effects are seen to have a larger influence on the time of peak deflection, as shown in Figure 31(b), where the delay in the timing of peak deflection at both D3 and D5 is seen to increase with impact velocity. This is most likely due to the added mass.

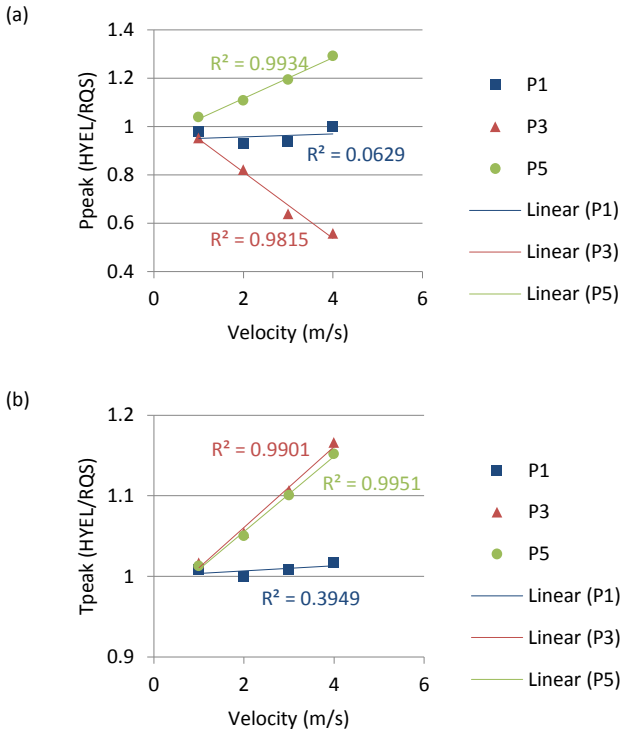

Figure 30 - Ratio of the magnitude (a) and timing (b) of the P1, P3 and P5 pressure peaks for different impact velocities, together with fitted linear trend lines.

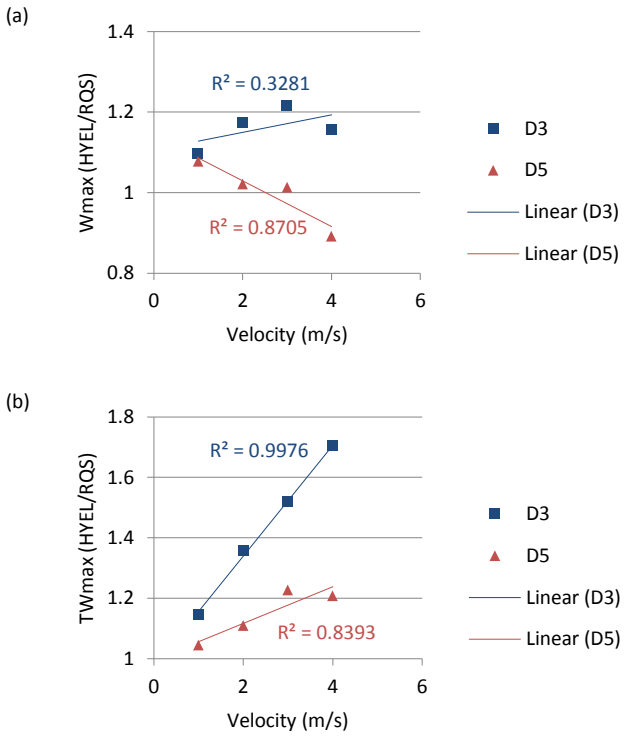

Figure 31 - Ratio of (a) magnitude and (b) timing of D3 and D5 peak deflection for different impact velocities, together with fitted linear trend lines.

3.4. Summary

In this chapter a numerical model for simulating the impact of two- and three-dimensional rigid and flexible structures with water is presented. The commercial CFD software Star CCM+ and FE code ABAQUS are used to solve for the fluid flow and structural response respectively. Two different water impact problems have been studied; the impact of a free-falling rigid wedge with water and the constant velocity water impact of a flexible composite hull panel. The geometrical characteristics of the studied test sections are relevant to high-speed marine craft. The computed results were compared with published experimental data for validation of the numerical model. The main conclusions drawn from this study are:

- Slamming impacts are characterized by very small time and length scales for which very short time steps and fine grids, hence, large computational resources are required to resolve accurately. Numerical verification studies in time and space have been performed for both problems and show convergence for the time histories of acceleration and pressure and vertical force impulse, respectively. Solution convergence is important to assure accurate resolution of the slamming impact and allows selection of appropriate time step and grid resolution.
- The effect of three-dimensional flow on the hydrodynamic loading is found to be negligible for the cases investigated. Some differences between the 2D and 3D solutions were observed for the rigid wedge case with wide gaps, however, small. This further shows that, the tank walls in the case of the rigid wedge, and the fixed vertical panels at the sides and back in the case of the flexible composite panel are working as intended, that is, constraining the flow along the test section and providing 2D flow.
- The effect of drop height, wedge mass and deadrise angle on the wedge kinematics and hydrodynamic loading has been investigated. It is shown that the magnitude of acceleration increases and the rise time decreases – more severe impact - with increasing drop height and decreasing wedge mass and deadrise angle. The magnitude of pressure increases and the peaks are recorded earlier in time (spray root travels faster across the wedge bottom) with increasing drop height and wedge mass and decreasing deadrise angle. It is also noted that the drop height and deadrise angle have more significant influence compared to the wedge mass.
- The computed time histories of vertical wedge acceleration and pressure at six different locations across the bottom surface compare relatively well with the experimental measurements of Lewis et al. (2010). The differences observed are mainly attributed to friction between the vertical posts and linear bearings in the experiments, which are not taken into account in the numerical model.
- The numerical stability of coupled simulations can be improved by modelling the fluids as compressible. Furthermore, the speed of sound in water can be set lower than its 'true' value to further enhance the stability and accelerate convergence. It is found the 'artificial' compressibility only affects the solution accuracy in cases where the speed of sound in water is of the same order of magnitude as the flow velocity. The number of exchanges per time step also has an effect on the stability of the solution. For the cases investigated, it was shown that at least 10 exchanges per time step are required to maintain numerical stability.

- The structural boundary conditions are found to have a large influence on the response. In particular, the beam with fixed supports is found to deflect significantly less than the simply supported beam. This is concluded to be mainly due to the in-plane boundary fixation in the case of the fixed beam which results in both bending and membrane forces acting to resist deformation. Accurate modelling of the experimental support conditions is concluded to be important.
- The computed time histories of pressure at five different locations on the flexible panel and deflection at the panel centre and chine show overall reasonably good agreement with the experimental data of Allen & Battley (2015). The peak pressures are well captured in the early phases of impact, however the peak pressure in the later phases and the residual pressures are overpredicted. The agreement with the experiments in terms of deflections is seen to improve with modelling the experimental support conditions accurately in 3D (when compared to the results for a simply supported beam). The differences in the later stages of the impact event ($t > 20$ ms) are mainly attributed to the variations in the experimental impact velocity profile.
- The effect of structural flexibility on the hydrodynamic loads and structural response is studied by comparing the hydroelastic solutions with corresponding rigid/ quasi-static solutions for a range of impact velocities. Hydroelastic effects are found to have a large influence on the hydrodynamic loading and increase with impact velocity. The structural deformations reduce the local impact velocity at the panel centre and effective deadrise angle at the chine, which increases and decreases the relevant pressures, respectively. The force impulse on the flexible structure is lower, which implies that hydroelastic effects overall lead to decrease in load. The effect of hydroelasticity on the structural response is less clear. The RQS method was found to under predict, with reference to the fully-coupled case, the maximum deflection for all impact velocities. The difference is more or less constant suggesting that hydroelastic effects are limited. The delay in the timing of the peak in the hydroelastic solution however, is seen to increase with increasing impact velocity.

Chapter 4. Full-scale rough water trials on a high-speed planing craft

An extensive experimental investigation into the loads on a high-speed planing craft in waves and related responses has been conducted. Measurements of rigid body motions, accelerations, pressures and strains at various locations on the hull bottom surface and global hull deflections were made in different sea conditions and at different speeds and headings. This chapter describes the experiment and data processing procedure in detail and presents characteristic findings. Data processing includes low pass filtering of the acceleration signals to remove the high frequency noise, removing the time varying offsets from the strain signals and identifying the peaks in the pressure and strain signals. Characteristic time series of pressure, acceleration and strain, and histograms of the peaks are presented and illustrate the nonlinear and stochastic nature of the problem. The averages of the largest $1/3^{rd}$ and $1/10^{th}$ peak values are calculated and together with the number of peaks identified in each signal, the symmetry of impacts, variation of loads and responses across the hull bottom, and the effect of forward speed and sea conditions is investigated. The characteristics of a typical impact event are also studied. Furthermore, the pressure and strain measurements are analysed statistically. The Weibull and Generalized Pareto models are fitted to the samples of identified peaks for estimating extreme values. Automated algorithms for fitting the statistical models to the peak value distributions are developed and the goodness-of-fit of the models to the data is examined.

4.1. Test description

4.1.1. Test craft

The C-Target 9 is a high-speed marine target used for naval gunnery training, weapons testing, and ship command and control assessments. It is designed and built by Autonomous Surface Vehicles (ASV) Ltd. The craft is shown in Figure 32 and the principal particulars are given in Table 7. The hull form is characterised by v-shaped sections and hard chines. Spray rails are also fitted. The lightweight aluminium craft is powered by two Mercury Verado 300HP outboards and can reach a speed of up to 50 knots (ASV, 2017).

Figure 32 - C-Target 9 (ASV 2017).

Table 7 - Principal particulars of the C-Target 9 (ASV 2017).

Length overall, L_{OA}	9.6 m
Beam, B	2.4 m
Height, H	3.5 m
Draft, T	0.4 m
Deadrise angle, $\beta_{amidships}$	24 °
Displacement, Δ	≈2750 kg

4.1.2. Measurements and instrumentation

Measurements of rigid body motions, accelerations, impact pressure and local panel strains and global hull deflections were made during the trials. The locations of the sensors are shown in Figures 33 and 46.

The speed, position and heading of the craft were measured using the GPS plotter (GARMIN GPSmap 750s) installed on-board sampled at a rate of at 1Hz. The plotter was also used to mark the waypoints (route) to improve the repeatability of the tests. Rigid body rotations were measured in all three degrees of freedom using an Inertial Measurement Unit (IMU) (YEI Technology TSS-DL-S, Range 360° about all axes, Accuracy ±1°) sampled at a rate of 200Hz. The IMU was mounted to the floor inside the cabin using double-sided tape. The accelerations were measured using tri-axial accelerometers at the bow and in the cockpit behind the seats (close to the craft's LCG). The bow accelerometer (Crossbow CXL100HF3, Range ±100g, Frequency 0.3 – 10,000 Hz) was bolted to the underside of the deck in the anchor hatch and the cockpit accelerometer (CFX USCA-TX, Range ±10g, Frequency DC – 200 Hz) was glued and strapped to the cockpit floor.

The impact loads were measured with a matrix of ICP® (Integrated Circuit Piezoelectric) pressure sensors positioned in a three-row grid pattern symmetric about the keel line as shown in Figure 33. The longitudinal position of the sensors was chosen based on the results of numerical simulations. The time-domain simulation model of Blake & Wilson (2001) was used to predict the vertical response of the craft in waves for a range of forward speeds, significant wave heights and zero crossing periods. The mean dynamic sinkage and trim were then calculated to identify which transverse hull sections are more likely to experience the largest number of slamming impacts. In addition, two sensors were mounted further aft to help identify when the craft is airborne. The sensors were mounted midway between the transverse frames (longitudinal position) and away from the spray rails to avoid separated flow (transverse position). Care has also been taken to ensure that the sensors' diaphragm is mounted flush with the hull bottom surface. Pressure sensor model 113B28 from PCB Piezoelectronics, Inc. was chosen for its size, high sensitivity, fast response and ruggedness. It has a measurement range of 344.7 kPa, resonant frequency ≥500 kHz, sensitivity of 14.5 mV/kPa and a diaphragm diameter of 5.5 mm.

Local panel responses were measured using a matrix of linear strain gauges (Vishay C2A-06-125LW-350, Gauge Length 3.18 mm, Resistance 350 Ω) positioned as shown in Figure 33. The gauges were mounted at the centre of the panels i.e., the hull plating area between two consecutive longitudinal stiffeners and transverse frames, and aligned parallel to the transverse frames. In the case where pressure sensors are installed at the centre of the panel, the strain gauges were offset in the longitudinal direction by 50 mm. The underlying surface has been properly prepared before bonding the gauges following the procedure in the Vishay (2009) application note. The gauges were then

installed using the tape-assisted method. Global hull deflections were measured using linear position sensors (Variohm VLP200, Stroke Length 200 mm) in the cabin and cockpit. The sensors were mounted on a telescopic rod to increase the distance between the measuring ends and the rod ends, marked with a cross in Figure 33, were bolted to the transverse frames.

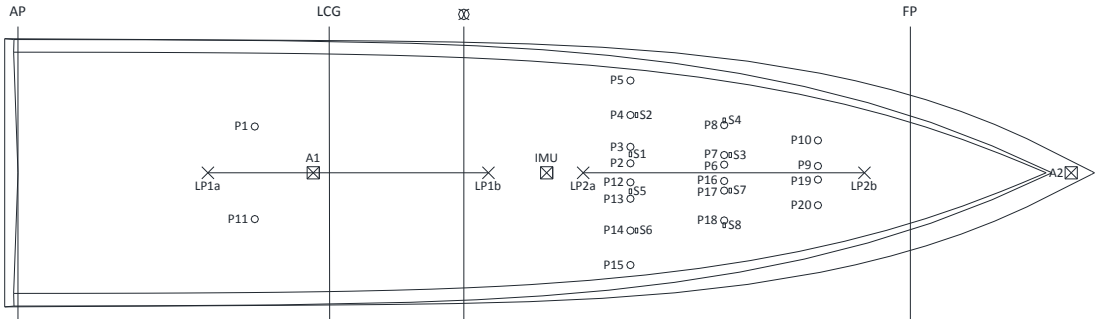

Figure 33 - Layout of the instrumentation: pressure sensors (P1 - P20), strain gauges (S1 - S8), accelerometers (A1 and A2), linear position sensors (LP1 and LP2) and IMU.

The data was logged with a National Instruments (NI) data acquisition system and stored on a 32 GB Industrial grade SD card. The NI system consists of a cDAQ-9135 Controller with integrated 1.33 GHz dual-core Intel Atom processor, five NI 9234 Integrated Electronic Piezoelectric (IEPE) modules with built-in anti-aliasing filters for the pressure measurements, an NI 9236 Strain Gauge module with built-in quarter bridge completion circuits for 350 Ω strain gauges, and an NI 9205 Analog Voltage Input module to read the output voltage from the accelerometers and linear position sensors. The GPS and IMU data was logged into the controller via the Ethernet and USB ports respectively. The data logger and sensors were powered using two 14VDC rechargeable batteries and a voltage regulator was used to provide a stable reference voltage for accelerometers and linear position sensors. The data logger, voltage regulator and batteries were held in a waterproof and impact resistant case inside the cabin strapped to the underlying hull structure. The stated manufacturer's uncertainty for the accelerometers, pressure sensors, strain gauges, and NI modules are given in Table 8.

Table 8 – Uncertainty in the acceleration, pressure and strain measurements.

Acceleration	
Bow sensor non-linearity	1% of FS
Cockpit sensor output noise	< 1% of FS
NI 9205 module accuracy	0.06% (Percent of full scale)
Pressure	
Sensor non-linearity	≤ 1% of FS
NI 9234 module accuracy	± 0.04% (Percent of range - offset error) 0.48% (Percent of reading - gain error)
Strain	
Gauge factor uncertainty	±0.5%
NI 9236 module accuracy	0.79% (Percent of range – offset error) 0.15% (Percent of reading – gain error)

4.1.3. Rough water trials

The trials were performed in the Solent, UK, near the Hayling Island Wave Buoy between July and November 2015. The wave buoy (Datawell Directional WaveRider Mk III) is operated by the Channel

Coast Observatory and records several wave parameters of interest such as height, period and direction. The data is freely available to the public on the Channel Coast Observatory website (www.channelcoast.org). Three trials were performed in different sea conditions with significant wave heights ranging between 0.29 m and 0.64 m and zero crossing periods between 2.6 s and 3.8 s. In each trial the boat was driven at the highest speed possible, determined by the comfort limits of the crew on-board and keeping within reasonable safety limits. The boat speeds tested range between 25 knots in the rough conditions ($H_s = 0.64\ m$) and 45 knots in moderate conditions ($H_s = 0.33m$). Multiple runs were performed in each trial. Most of the runs were done in head seas however some runs in following, beam, and quartering seas were also performed. The heading was visually estimated by the coxswain. The total number of test runs is 24 and in each run the boat was driven at constant speed and heading for at least five minutes. The sampling rate was 5.12 kHz in the first trial and 10.24 kHz in the other two, except for the GPS and IMU, which were sampled at 1Hz and 200 Hz respectively in all three trials. To limit the size of the data files, the data logger was set to start writing in a new file every 5 minutes, which may result in data being saved in two different files for a single run.

In the present work, four head sea runs covering a good range of sea and operational conditions are considered. The aim is to illustrate the data processing and analysis methods and present characteristic results. The details of the runs are given in Table 9 where the mean speed values over the five minute period (± the standard deviation), significant H_s and maximum H_{max} wave heights and zero crossing periods T_z are shown. The duration of each run is 5 minutes. From a preliminary check of the measured data it was found, by comparing with corresponding measurements for other planing hulls in waves (e.g. Taunton et al., 2011), that the IMU data is not reliable and cannot be used for further analysis. Furthermore, the signals from the two position sensors are found to have very similar shape and magnitude suggesting that the signals interfered with each other. The present analysis is therefore focused on the acceleration, pressure and local strain data. Furthermore, unfortunately, the voltage module did not work during the tests made on the 5th August 2015 and therefore acceleration data is not available for run 3.

Table 9 - Head sea runs studied in the present work.

Run	Date	Speed, knots	H_s, m	H_{max}, m	T_z, s
1	09/07/15	40 ± 0.3	0.29	0.43	3.1
2		45 ± 0.5	0.33	0.49	2.7
3	05/08/15	35 ± 0.6	0.39	0.43	2.9
4	20/11/15	26 ± 1.9	0.6	0.99	3.4

4.2. Data processing

The experimental data is post-processed using the commercial software DIAdem from National Instruments. DIAdem offers several built-in functions for signal processing and also allows the user to write their own code using the built-in Visual Basic script host (National Instruments, 2017). The following post-processing was carried out:

1. The data files that make up a single test run are merged together and the GPS data is used to identify a five-minute segment where the speed and heading are more or less constant.

2. The voltage signals (acceleration and position) were set to have a zero offset of approximately 2.5 V. This is removed by subtracting the mean of the signal from the signal using the Offset Correction function available in DIAdem. The signals are then converted from voltage to acceleration and displacement respectively using the manufacturer-specified sensitivity of the sensors and low-pass filtered as discussed in 4.2.1.
3. The baseline drift in strain signals is removed using the algorithm described in 4.2.2.
4. The pressure and strain peaks are identified using the algorithm described in 4.2.3.
5. Histograms of the pressure and strain peaks and other quantities of interest such as the average of the largest 1/3rd and 1/10th peaks are calculated.
6. Analytical distributions are fitted to the samples of pressure and strain peak values and extreme values are estimated.

4.2.1. Low pass filtering

Figure 34 shows a short segment of typical unfiltered vertical bow acceleration response recorded in run 2 where five separate wave impact events can be observed. The impacts are characterised by a rapid increase in acceleration followed by high frequency and large amplitude oscillations. The oscillations damp out prior to the next impact, which means that each impact can be considered independent of the others and analysed separately (Riley et al., 2014; Savitsky, 2016).

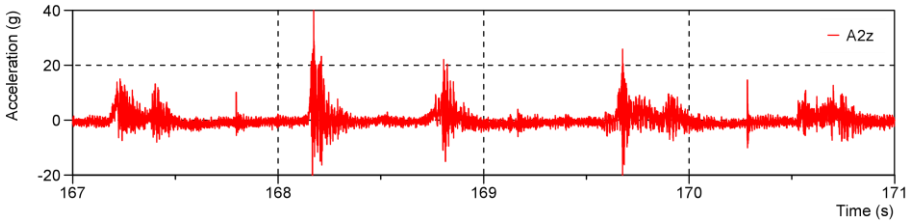

Figure 34 - Characteristic unfiltered vertical acceleration response measured at the bow, run 2.

The Fourier spectrum of the raw vertical bow acceleration signal recorded in run 2 is presented in Figure 35. The spectrum shows a large peak near 1 Hz which represents the rigid-body interaction with waves and several lower amplitude peaks across a range of frequencies from roughly 50 Hz to 500 Hz that are most likely due to structural vibrations caused by wave impacts and engine noise (Riley et al., 2014). The high-frequency vibration content can be removed by low pass filtering the raw signal. Figure 36 compares the raw signal with low-pass filtered signals at different cut-off frequencies for the impact event at time ≈168 s. A 10th-order Butterworth filter is used. The results show that with decreasing the cut-off frequency more high frequency vibration content is removed and the magnitude of peak acceleration decreases. The 10 Hz cut-off frequency recommended by Riley et al. (2014) is too low and does not capture the sharp acceleration rise accurately. The 30Hz low-pass filter is found to effectively remove the high frequency content without significantly affecting the rigid body response and is chosen in the present work. Similar observations were made for the cockpit acceleration signal and other runs.

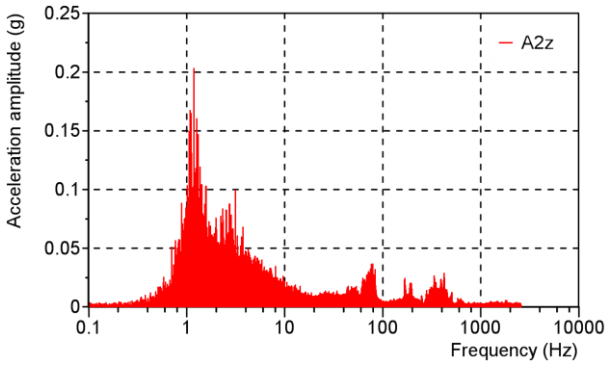

Figure 35 - Fourier spectrum of the raw bow vertical acceleration signal, run 2.

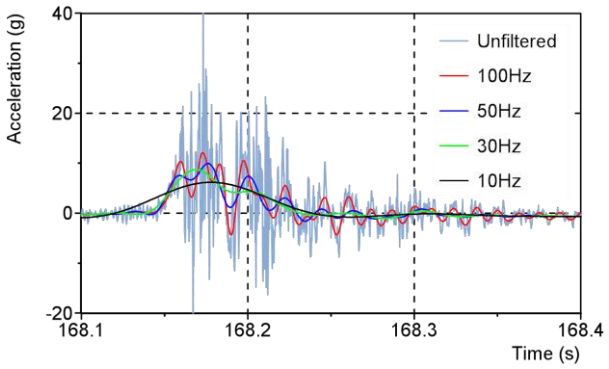

Figure 36 - Effect of cut-off frequency on the acceleration data.

4.2.2. Baseline correction

The strain signals contain undesirable baseline drift that is removed by subtracting a baseline estimate from the signal as follows:

1. Low pass filter the raw signal at 50 Hz with a 10^{th}-order Butterworth filter to remove high frequency noise.
2. Differentiate the filtered signal to accentuate the high rates of change associated with impacts and attenuate the intervals in between.
3. Search for the 'flat' intervals between impacts in the signal derivative – the intervals in which the values of the signal derivative are in a specified window – and remove intervals of short duration which generally result from inflection points or local maxima/ minima in the strain signals. For each interval identified calculate the mean of the signal and the time midpoint.
4. Fit a line to the data points (calculated means and midpoints) to obtain the baseline estimate and subtract it from the raw strain signal.

Figure 37 shows an example of application of this algorithm to signal S1. It must be emphasized that the baseline estimate is subtracted from the raw signal, which is then used for further analysis, and not the filtered signal. Low pass filtering is only applied for the purpose of limiting the noise in the differentiated signal to help identify the 'flat' intervals better. The cut-off frequency used (50Hz) is higher than that chosen for the acceleration signals (30Hz) mainly because the strain rise times are typically shorter than the acceleration rise times and, hence, higher frequency is required to accurately capture the strain rise which is important here.

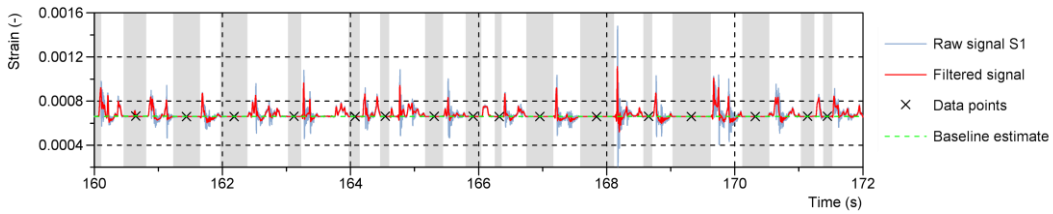

Figure 37 - Baseline correction algorithm applied to signal S1, run 2.

4.2.3. Peak identification

The peaks in the pressure and strain signals are identified by first identifying the impact events in the signals and then searching for the peak within each event. The characteristics of the signals, in particular the rapid increase in pressure and strain associated with water impact, are used to identify the impact events. With this approach identified impact events can also be extracted from the signal for comparisons with, for instance, numerical predictions or drop test measurements. The algorithm for identifying the peaks in the pressure and strain signals is as follows:

1. Low pass filter the raw signal with a 10^{th}-order Butterworth filter and 100 Hz cut-off frequency to remove the high frequency noise. This step is only applied to the strain signals; the pressure signals contain less noise, particularly between impacts.
2. Differentiate the (filtered) signal to accentuate the high rates of change associated with impacts and attenuate the intervals in between (see Figure 38a).
3. Search for the 'flat' intervals between impacts in the signal derivative and remove intervals of short duration (peaks/ valleys; pressure signals: duration ≤ 10 ms; strain signals: duration ≤ 5ms) which generally result from inflection points or local maxima/ minima in the noisy signals. The search results are stored as a binary signal (shaded areas in Figure 38a).
4. Invert the binary signal to obtain the impact events (see Figure 38b).
5. Remove gaps between impact events and impact events of short duration from the search results,
    a. Remove gaps of duration ≤ 100 ms (see Figure 38c).
    b. Calculate the duration of each impact with a maximum value greater than the root mean square (RMS) of the signal and the mean duration.
    c. Filter out short impact areas. In the case of the pressure signals, remove impacts of duration ≤ 50 ms from signals with mean duration ≥ 100 ms (see Figure 38d). In the case of the strain signals remove impacts of duration ≤ 120 ms if the mean duration > 200 ms and ≤ 60 ms otherwise.
6. Search for the maximum in each area, i.e. here referred to as the peak, and output the magnitude and time. It should be noted that the maximum peak is not necessarily the first one. The circles in Figure 38d represent the identified peaks.
7. Sort the peaks in ascending order and remove peaks of magnitude less than the signal RMS.

The threshold values were selected from testing the algorithm on the four data sets and were found to accurately identify the impact events and peaks which would have been identified manually. Figure 38 shows an example of application of the peak identification algorithm to signal pressure P2 from run 2.

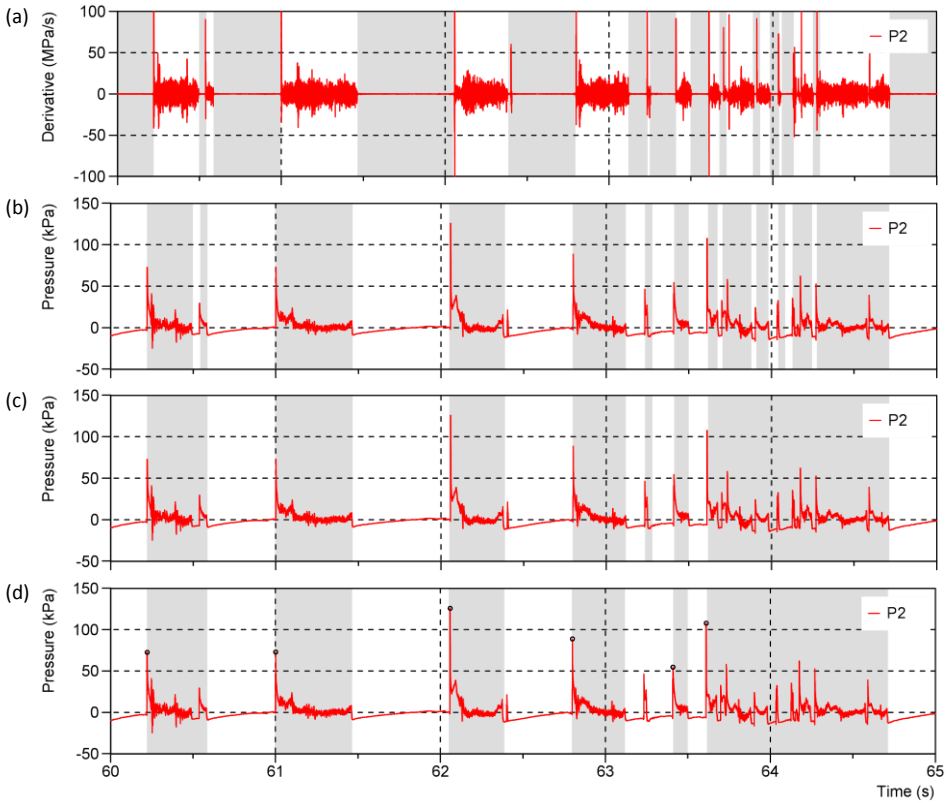

Figure 38 - Peak identification algorithm applied to signal P2, run 2: (a) signal derivative and 'flat' intervals identified, (b) pressure signal and impact areas identified, (c) impact areas with short gaps filtered out, and (d) impact areas with short peaks filtered out and identified peaks.

4.3. Statistical methods and distributions

Let $x_{(1)}, x_{(2)} \dots, x_{(n)}$ be an ordered sample of independent and identically distributed data of size n with cumulative distribution function $F(x)$. From order statistics, the cumulative distribution function $F_e(x)$ of the extreme value $x_{(n)} = \max\{x_{(1)}, x_{(2)}, \dots, x_{(n)}\}$ is related to $F(x)$ by (Ochi, 1981),

$$F_e(x) = F^n(x) \tag{4}$$

and the probability α of exceeding a characteristic extreme value x_α is (Ochi, 1981),

$$P[response > x_\alpha] = \alpha = 1 - F^n(x_\alpha). \tag{5}$$

Considering that α is small and n is large,

$$F(x_e) = (1-\alpha)^{\frac{1}{n}} \approx 1 - \frac{\alpha}{n}. \tag{6}$$

Characteristic extreme values with low probability of exceedance can therefore be estimated if the cumulative distribution function of the sample $F(x)$ is known. In the present work, two analytical models are fitted to the sample of peak values to approximate $F(x)$, namely the two-parameter Weibull and the Generalized Pareto distributions. The goodness of fit of Weibull and Generalized

Pareto models to the peak value distributions is examined using Quantile-Quantile plots and the root mean square error (RMSE) statistic written as,

$$RMSE = \sqrt{\frac{1}{n}\sum_{i=1}^{n}(x_i - \hat{x}_i)^2} \tag{7}$$

where x_i and $\hat{x}_i$ are the measured and estimated peaks at the same quantile level, respectively. The RMSE is normalized using the mean of the measured data to enable comparisons between data sets with different scales.

4.3.1. Weibull distribution

The cumulative distribution function of the two-parameter Weibull distribution is given by,

$$F(x; a, b) = 1 - e^{-\left(\frac{x}{a}\right)^b} \tag{8}$$

where a and b are the scale and shape parameters respectively. The Rayleigh and Exponential distributions are both special cases of Weibull distribution corresponding to $b = 2$ and $b = 1$ respectively.

4.3.1.1 Weibull parameters estimation and threshold selection

The parameters of the Weibull distribution are estimated using the least squares method. Taking the natural logarithm of equation (8) twice the equation,

$$\ln\left[-\ln\left(1 - F(x)\right)\right] = bln(x) - bln(a), \tag{9}$$

is obtained which represents a linear relationship between $\ln\left[-\ln\left(1 - F(x)\right)\right]$ and $\ln(x)$ with slope b and y-intercept $-\,b\ln(a)$. Thus, the shape and scale parameters can be estimated by least-square fitting equation (9) to the data where the cumulative probability associated with each observation is $F(x) = i/(n+1)$ for $x_{(i)} \leq x < x_{(i+1)}$ (Coles, 2001).

To better capture the tail of the distribution a threshold value is introduced and the Weibull distribution is only fitted to the peak values above the threshold. The procedure for choosing the optimal threshold value and estimating the Weibull parameters is similar to that presented in Razola et al. (2016) and is as follows,

1. Sort the sample of peak values in increasing order and for each peak value calculate the cumulative probability, $\ln\left[-\ln\left(1 - F(x)\right)\right]$ and $\ln(x)$.
2. Let $u_1 < u_2 < \cdots < u_m$ be a range of suitable threshold values.
    a. For each threshold value, use the least squares method to fit a straight line on the transformed axes to the peaks above the threshold and calculate the coefficient of determination (R^2 statistic).
    b. Choose the threshold value that yields the maximum R^2 value.
3. Calculate the shape and scale parameters from the slope and intercept of the fitted line.

4.3.1.2 Extreme value

The extreme value with probability of exceedance α is obtained by substituting equation (8) into (6) resulting in,

$$x_e = a\left[\ln\left(\frac{n}{\alpha}\right)\right]^{\frac{1}{b}}. \tag{10}$$

The most probable extreme value, defined as the extreme value most likely to occur in n observations, is obtained by setting $\alpha = 1$.

4.3.2. Peak-Over-Threshold method

The cumulative distribution function of the peaks over a high threshold u is,

$$F_u(x) = P(X \le x | X > u) = \frac{F(x) - F(u)}{1 - F(u)} \tag{11}$$

and is related to the distribution function of the excesses, $F_{x-u}(x-u)$, by,

$$F_{x-u}(x-u) = F_u(x). \tag{12}$$

Pickands (1975) showed that for large enough threshold the distribution of excesses is well approximated by the Generalized Pareto distribution. The cumulative distribution function of the Generalized Pareto distribution (GPD) is given by,

$$G(x;c,\lambda) = \begin{cases} 1 - \left(1 + \frac{cx}{\lambda}\right)^{-\frac{1}{c}} & c \neq 0 \\ 1 - e^{-\frac{x}{\lambda}} & c = 0 \end{cases}. \tag{13}$$

The parameters c and λ are the shape and scale parameters, respectively, and the support is $0 \le x < \infty$ for $c \ge 0$ while for $c < 0$ the support is $0 \le x \le -\lambda/c$. The case $c = 0$ represents the exponential distribution with mean λ, $c > 0$ indicates a heavier tail than the exponential one (sub exponential), while $c < 0$ implies a lighter tail (super exponential).

4.3.2.1 Threshold selection and GPD parameters estimation

The choice of the threshold requires balancing bias and variance – the threshold needs to be sufficiently high for the asymptotic approximation to be valid, thus reducing the bias. However, a high threshold implies smaller samples of excesses, which increases the variance in the parameter estimates. The GPD satisfies a threshold stability property: if for a particular threshold u_o the excesses follow a GPD then, for higher thresholds ($u > u_o$) the shape and normalised scale ($\lambda^* = \lambda - cu$) parameter estimates should tend to constant values (Coles, 2001). These properties are used to choose the threshold value. The approach is to estimate the shape and scale parameters for a range of thresholds and examine their variation with threshold.

The GPD parameters are estimated using the Method of Moments (MOM), that is, the sample mean and variance are equated to the analytical moments of the GPD resulting in,

$$c = \frac{1}{2}\left(1 - \frac{\bar{x}^2}{s^2}\right) \tag{14}$$

$$\lambda = \frac{1}{2}\bar{x}\left(\frac{\bar{x}^2}{s^2} + 1\right) \tag{15}$$

where $\bar{x}$ and s^2 are the sample mean and variance, respectively. The MOM may produce non-feasible estimates, in the sense that there are samples for which c is negative and the peak magnitudes are larger than the upper limit for the GPD, i.e., $x > -\lambda/c$. The hybrid-MOM of Dupuis & Tsao (1998) is always feasible and is used in the present study. This hybrid estimator takes the values of the MOM estimator if the results are feasible and sets $c = -\lambda/x_{(n)}$ otherwise.

The automated procedure developed for choosing the threshold is as follows,

1. Let $u_1 < u_2 < \cdots < u_m$be a range of suitable threshold values. For each threshold u calculate the shape and scale parameters using the Hybrid-MOM.
2. Fit a non-parametrical approximating spline to the shape parameter curve. The x-range (threshold range) is divided into twenty equidistant sections and in each section a straight line is fitted to the data using the least square error method.
3. Calculate the forward difference derivative of the spline curve and normalize the derivative signal using the range of the threshold values.
4. Search the sections in which the derivative is within specified low limits and filter out areas (clusters of adjacent sections) with two sections or less.
    a. If the search returns zero areas select the 0.8-quantile as the threshold.
    b. If several areas are identified (the shape parameter plot reaches multiple plateaus) select the area with the largest number of sections. If two areas have equal number of sections, select the area that corresponds to the larger threshold.
    c. The threshold is the minimum value of the chosen area.

4.3.2.2 Extreme value

From equations (6) and (13) the extreme value x_e with a probability of exceedance α is,

$$x_e = \begin{cases} u + \dfrac{\lambda}{c}\left[\left(\dfrac{k}{\alpha}\right)^c - 1\right], & c \neq 0 \\ u + \lambda \ln\left(\dfrac{k}{\alpha}\right), & c = 0 \end{cases} \tag{16}$$

where k is the number of peaks above the threshold u and $F(u) = (n-k)/n$.

4.4. Results and discussion

4.4.1. Characteristic results

In Figures 39 – 41 segments of typical acceleration, pressure and strain time series are presented. The craft was travelling into head seas at 45 knots with significant wave height $H_s = 0.33\,m$ and

zero crossing period $T_z = 2.7\ s$ – run 2. The acceleration signals are low pass filtered with a 10^{th}-order Butterworth filter and a cut-off frequency of 30 Hz as discussed in section 4.2.1. The pressure and strain peaks identified using the algorithm described in section 4.2.3 are also included. The signals consist of repeated hull-water impacts with each impact having different characteristics, such as, shape of the signal, peak magnitude, rise and decay time and impact duration. For a high-speed planing craft travelling in waves the trim angle, vertical velocity, deadrise angle and wave geometry are different for each individual hull-water impact and as a result each event is unique (Allen & Jones, 1978; Savitsky, 2016). The rise and decay times are typically of the order of a few milliseconds and duration of impact events is generally less than 0.5 seconds. Example histograms of the pressure and strain peaks are presented in Figure 42. The distributions are generally skewed to the right with low magnitude peaks occurring frequently and few large magnitude peaks, some of which differ greatly from the other observations – see for instance the distribution for S2 in Figure 42. The largest pressure peak was measured at P6 during run 2 and has a magnitude of 342 kPa and the largest strain peak is 1182 μs measured at S3 during run 4.

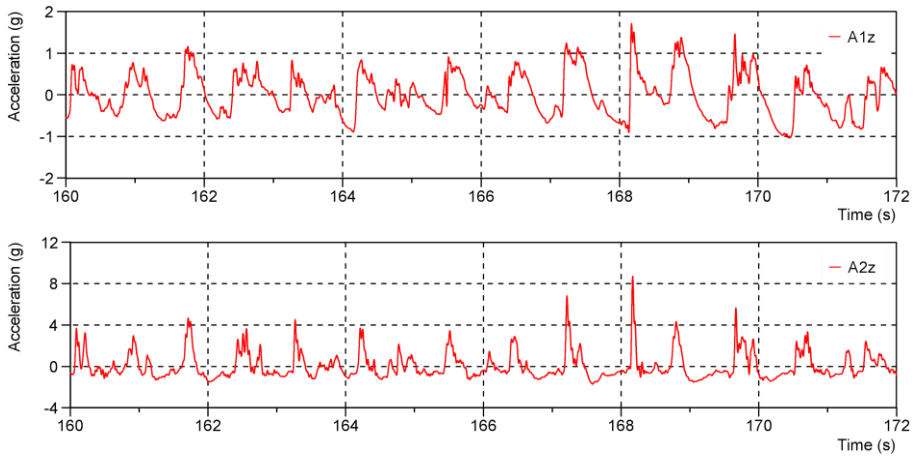

Figure 39 - Characteristic time series of cockpit (A1z) and bow (A2z) acceleration, run 2.

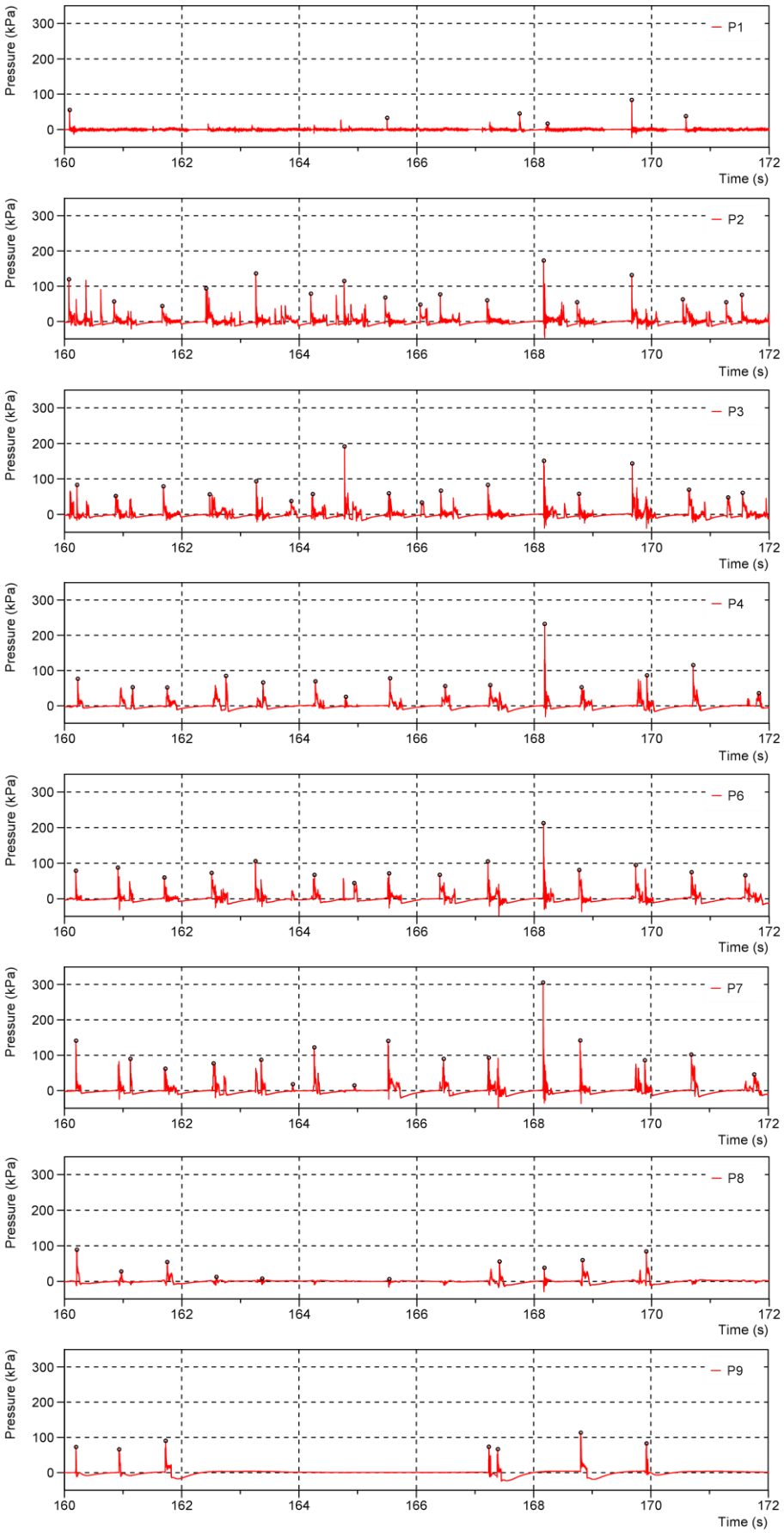

Figure 40 - Characteristic time series of pressure and identified peaks, run 2.

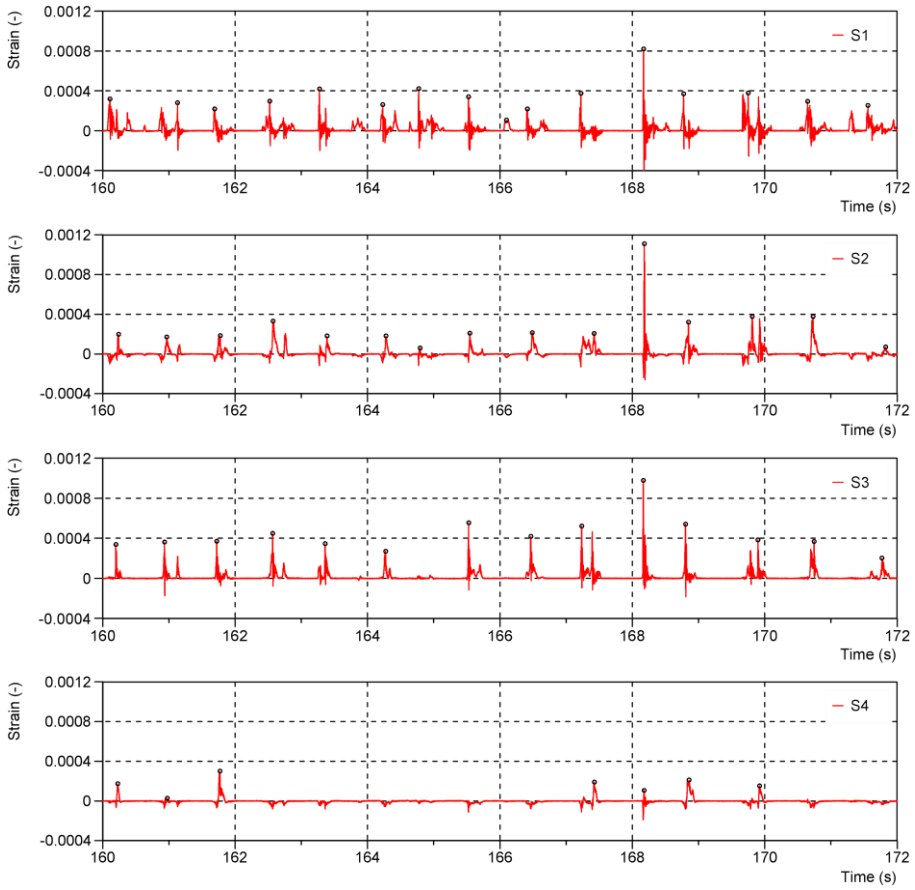

Figure 41 - Characteristic time series of strain and identified peaks, run 2.

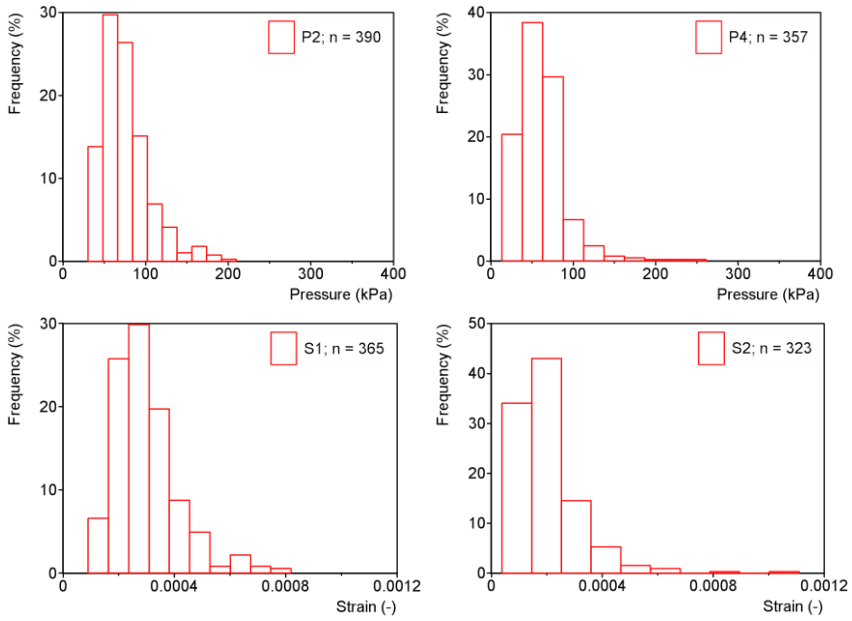

Figure 42 - Characteristic histograms of pressure (P2, P4) and strain (S1, S2) peaks, run 2.

The number of peaks identified in each pressure and strain signal for all runs are given in Tables 13 and 14 in Appendix B. The impacts are fairly symmetric in terms of the number of peaks recorded on port and starboard sides, particularly for the sensors located near the keel. Furthermore, the number of peaks recorded by the sensors located near the chine and most forward, i.e., sensors P5, P8, P9, P10 and S4 and corresponding sensors on the starboard side, is significantly lower. As can be

seen, the peak identification algorithm developed in the present work accurately identifies the peaks in all pressure and strain signals considering that the duration of the interval between impacts and the duration of impacts varies within each signal and also between signals. By accurately I mean that the algorithm identifies the peaks that would have been chosen manually. This is because our algorithm uses the characteristics of the actual signal to define the search area (impact events), i.e., the rapid changes in pressure and strain associated with impact and the intervals of nearly zero pressure/ strain in-between events. The peak is then taken as the maximum pressure or strain during that time interval. There are, however, impact events that are characterised by multiple peaks (the time duration between these peaks is very short otherwise the algorithm would assume two events) and the algorithm only considers the maximum value as the peak. The physical mechanism behind these multiple peaks is difficult to explain without knowing the relative velocity of the craft, free surface profile and so on. It is also noted that the horizontal threshold method commonly used to identify the acceleration peaks (see for example McCue, 2012, Riley et al., 2013 and Razola et al., 2016), which uses a constant sliding time window calculated from the wave encounter frequency to search for the peak, would identify false peaks in this case.

The averages of the largest $1/3^{rd}$ and $1/10^{th}$ pressure and strain peaks are presented in Figure 43 and Tables 15 – 18 in Appendix B. The ratio of the average of the largest $1/3^{rd}$ pressure and strain peaks to the average of the largest $1/10^{th}$ is typically between 0.6 and 0.8 for all samples and runs. While the number of impacts recorded on port and starboard sides agree relatively well, the peak magnitudes show some differences. In particular, the pressure and strain peaks recorded on the port side, i.e. sensors P1-P10 and S1-S4, are larger than the starboard side peaks except for run 3 where no clear trends are observed. The averages of the largest $1/3^{rd}$ and $1/10^{th}$ also provide insight into how the magnitude of the loads and responses varies across the hull bottom surface. As can be seen, the largest peaks are recorded by the sensors located near the keel i.e. sensors P2, P3, P6, P7, P9 and the corresponding starboard side sensors, and the magnitude of pressure generally decreases with increasing distance from the keel towards the chines. The pressures measured by the second row of sensors, i.e. sensors P6 – P8 and P16 – P18, however, don't follow this trend. In particular the pressure peaks measured at P17 are for all runs greater than the P16 peaks while the P7 peaks are greater than the P6 peaks for runs 1 and 2. Furthermore, the strains measured on the panels next to the keel, i.e., S1, S3, S5 and S7, are larger than strains measured on the adjacent panels for all runs. Comparing the averages of the largest $1/3^{rd}$ and $1/10^{th}$ for runs 1 and 2 (high forward speed and moderate seas) with those for run 4 (moderate speed and rough seas) it can be observed that larger pressures and strains were measured when the boat was travelling at high speed.

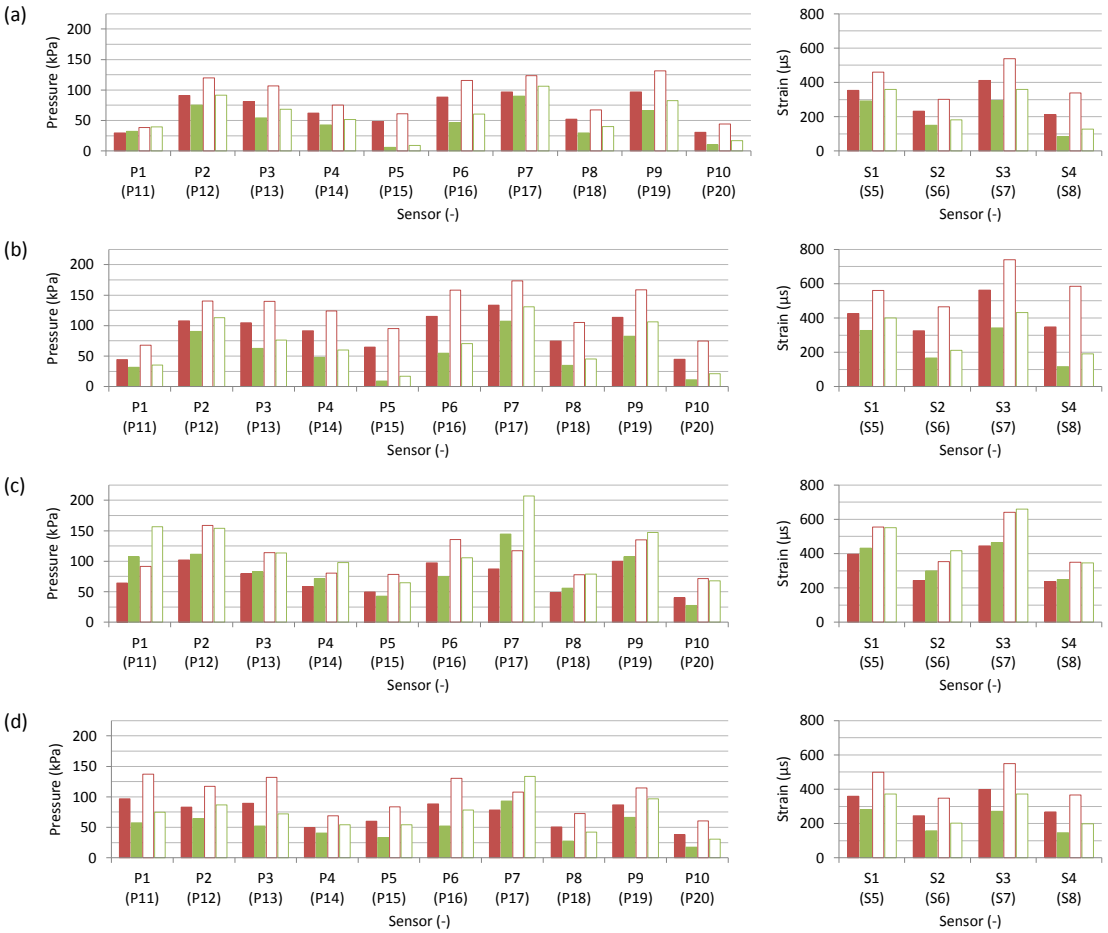

Figure 43 - Average of largest 1/3rd (filled bars) and 1/10th (empty bars) pressure and strain peaks for P1–P10 and S1–S4 (red) and P11-P20 and S5-S8 (green), runs 1-4 (a – d).

Figure 44 shows the cockpit and bow vertical accelerations responses recorded during the impact event at time ≈ 168s, which is the most severe impact recorded in run 2. Prior to impact (t = 168.135s - marked with a red vertical line in Figure 44) the cockpit accelerometer records a fairly constant acceleration of about - 0.7g, which suggests that the craft is moving downwards but is not in free-fall condition – it is most likely that the craft is pitching downwards with the stern in the water. Riley et al. (2014) categorise such event as 'Type Charlie Slam' where the energy of impact is mainly due to the relative forward velocity between the craft and incident wave, and has little to do with significant vertical drop at the LCG. This is further supported by the fairly low pressure measured at P1 - see Figure 40 – which suggests that the stern was in the water. At time = 168.135s the craft impacts the incident wave and the acceleration in the cockpit and at the bow rises sharply and reaches a maximum of 1.7 g and 8.7 g, respectively. The cockpit and bow acceleration rise times are 38 ms and 34 ms, respectively.

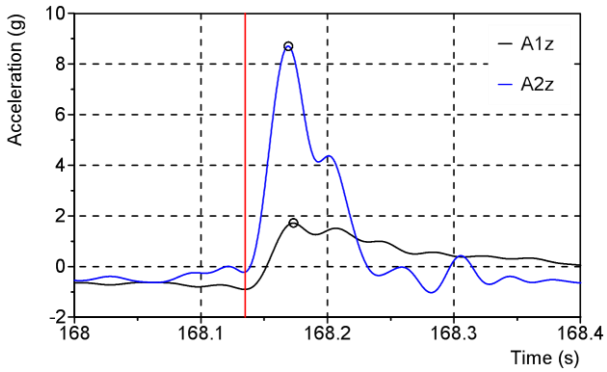

Figure 44 - Cockpit (A1z) and bow (A2z) acceleration responses recorded during the impact event at t ≈ 168s, run 2. The time of impact and maximum cockpit and bow accelerations are marked by the vertical red line and markers, respectively.

The pressures and strains recorded by sensors P2 – P4, P6 – P8 and S1 – S4 during this particular impact event are presented in Figure 45. The signals are plotted based on the longitudinal and transverse (relative to the longitudinal stringers) location of the sensors - see Figure 46. As the boat enters the water a high pressure pulse located at the intersection between the hull bottom and water surface, also known as the spray root, rapidly propagates across the hull bottom surface from the keel towards the chine over the instrumented area – see Figure 45 where the first peak is recorded by the sensors located next to the keel, i.e., P2 and P6 and the sensors located further out record the peak later in time.

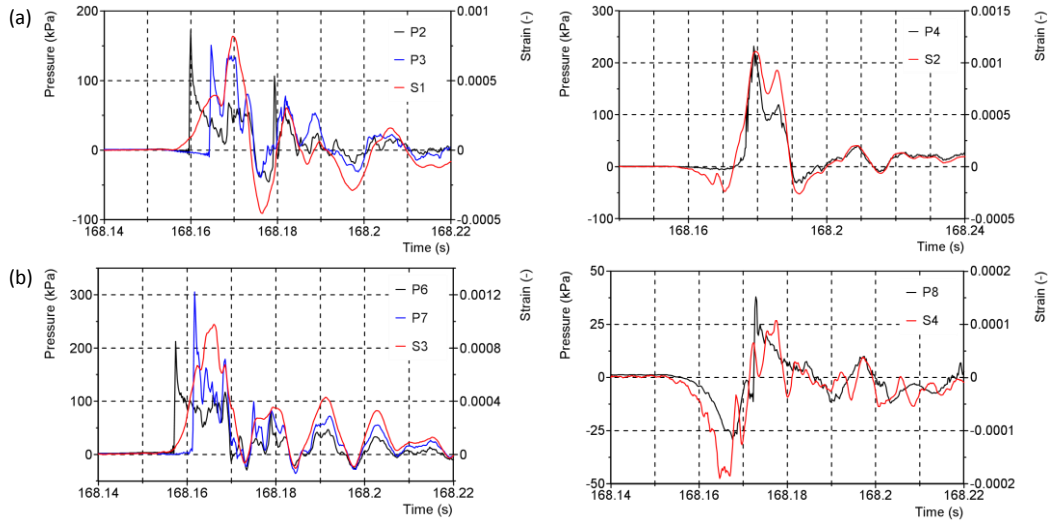

Figure 45 - Pressure and strain signals recorded by the first (a) and second (b) row of port side sensors during the impact at t ≈ 168s, run 2.

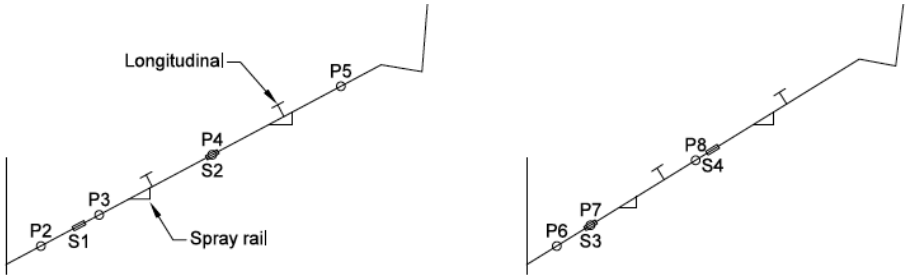

Figure 46 - Schematic illustration of the hull sections showing the relative position of the pressure sensors (P2 – P8), strain gages (S1 – S4), longitudinal stiffeners and spray rails.

The pressure signals are characterised by a sharp rise and large initial peak rapidly decaying to a lower residual pressure level. The rise time is in the order of 0.5 ms, which implies that the sampling frequency of 5.12 kHz is too low for this extreme event. The strains measured on the hull bottom area between the keel and the first longitudinal stringer i.e., S1 and S3, are characterised by a moderate rise (compared to the pressure rise time) and large initial peak followed by large amplitude oscillations about a much lower residual strain level. The panels begin to deflect inwards (positive strain) at about the same time sensors P2 and P6 record their peaks. The strains measured on the hull bottom area between the two longitudinal stringers i.e., S2 and S4, show a negative initial peak followed by a rapid increase to a positive peak. The negative peak occurs at the time of maximum S1 and S3 strain respectively which suggests that the as the panel area between the keel and first longitudinal stringer is deflecting inwards, the longitudinal stringer acts as a pivot and the panel area between the two stringers deflects outwards. A second peak is observed in signals P2, P3 and S1 at time ≈ 168.17s and in signals P4 and S2 at time ≈ 168.185s. The second peaks are also observed in the drop tests measurements and are found to be caused by the spray rails – see more detailed discussions in sections 5.1.3.3 and 5.2.2.2. It can also be observed that the pressures and strains correlate quite well, particularly the shape of the signals following the peak.

4.4.2. Statistical results (extreme values)

In the present work the Weibull and Generalized Pareto models are only fitted to samples containing more than 200 pressure or strain peaks to limit the variance of the parameter estimates. The number of candidate thresholds in the Weibull and Generalized Pareto threshold selection algorithms is $m = 50$ and u_1 and u_m are set as the 0.4 and 0.9 quantiles of the sampled peak values, respectively. This implies that in the extreme case of the 0.9 quantile at least 20 peaks are used to estimate the model parameters.

Figure 47 shows examples of the Weibull threshold selection algorithm applied to samples of pressure and strain peaks. The first column presents the transformed sample distribution (step 1 of the procedure in 4.3.1.1) and the transformed Weibull model fitted to the peaks above the chosen threshold using the least squares method. The second column presents the variation of the Weibull shape parameter b and R^2 statistic with threshold value. The vertical line represents the chosen threshold value corresponding to the maximum R^2 value. As can be seen the slope of the transformed sample distributions, which corresponds to the Weibull shape parameter, changes with increasing threshold suggesting that the peaks on different levels belong to different statistical distributions. More specifically, the slope becomes less steep and the shape parameter decreases with increasing threshold suggesting that the largest peaks, which are most likely related to extreme slamming impacts, are more nonlinear. This is generally the case for both pressure and strain peak samples with very few exceptions, and justifies the use of a threshold to accurately capture the largest peaks.

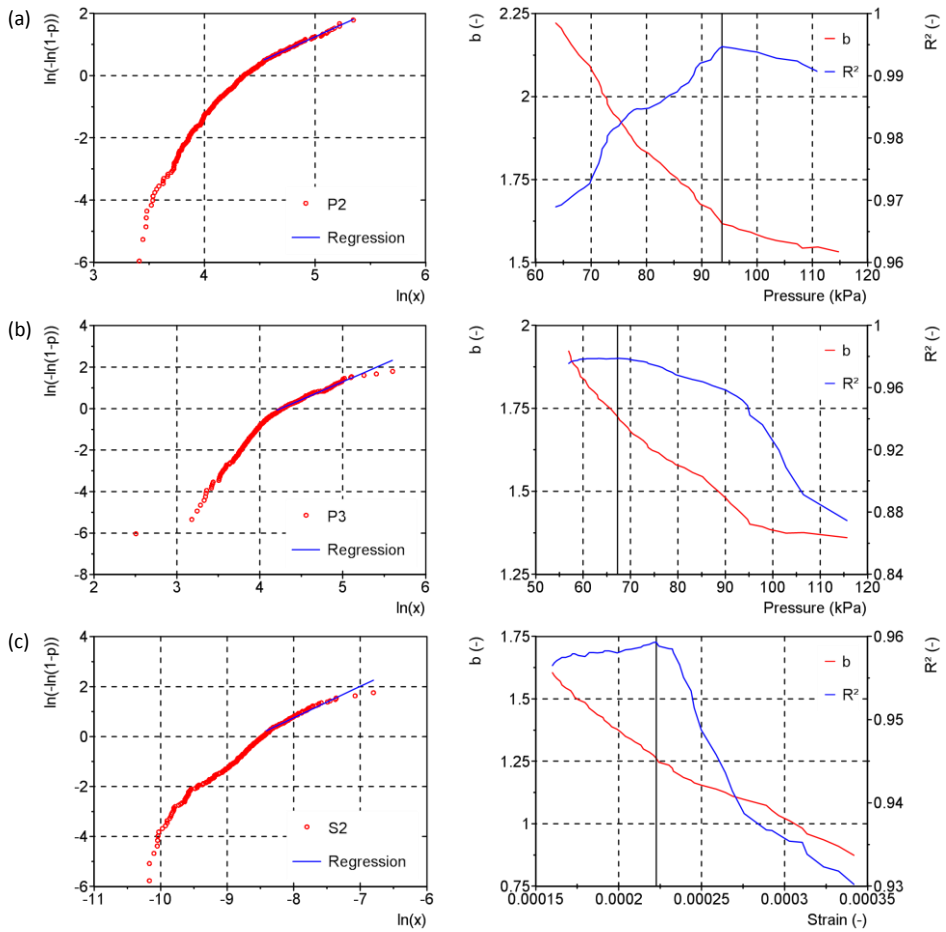

Figure 47 - Weibull threshold selection algorithm applied to peak samples P2 (a), P3 (b) and S2 (c), run 2.

Examples of application of the GPD threshold selection algorithm to pressure and strain peak samples are presented in Figure 48 where the variation of the estimated GPD shape parameter with threshold and the non-parametric approximating spline curve are shown. The vertical line represents the threshold chosen by the algorithm. The shape parameter estimates should be constant above the threshold at which the GPD model becomes valid. In practice, however, due to the relatively small sample sizes, the plots will not look constant even when the GPD model becomes valid. The GPD shape parameter estimates were found to vary quite significantly over the range of thresholds considered for many of the peak samples, particularly the strain peak samples and including peak sample P2 in Figure 48. In such event the algorithm selects the 0.8 quantile as the threshold value. The 0.8 quantile level was determined by assessment of the shape parameter stability plots for all peak samples where it was found that above this level the parameter estimates typically become highly unstable. For peak sample P3 and S2 the shape parameter appears to reach a near-constant value in the low threshold range and the algorithm selects the starting point of the identified area as threshold (step 4 of the procedure in 4.3.2.1).

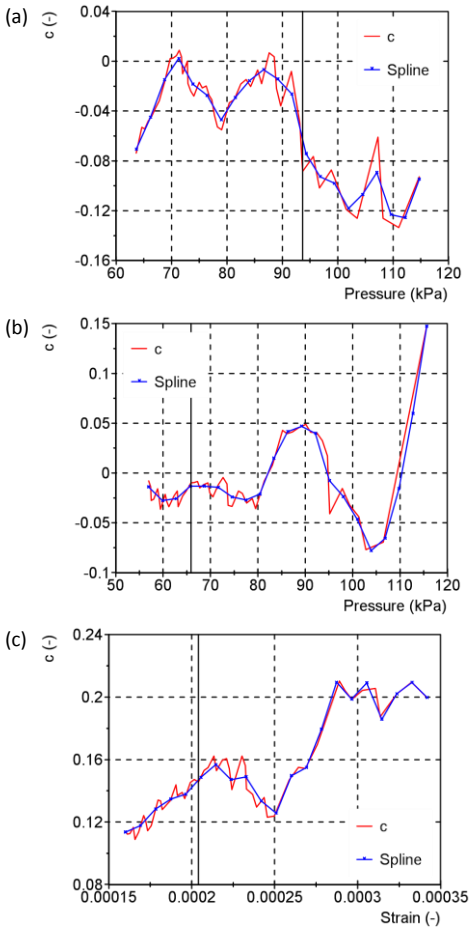

Figure 48 - GPD threshold selection algorithm applied to peak samples P2 (a), P3 (b) and S2 (c), run 2.

In Figures 49 and 50 characteristic cumulative distributions of pressure and strain peaks and fitted Weibull and Generalized Pareto models and corresponding Quantile-Quantile plots are presented. The Weibull and Generalized Pareto shape and scale parameters are presented in Figure 51 and Tables 19 - 22 in Appendix B. The number of peaks used in the Weibull and Generalized Pareto fittings range from approximately 30 to 270. The Weibull shape parameter values range between 0.74 and 2.94 for the pressure distributions and 0.93 and 2.48 for strain distributions. However, most of the pressure and strain peak distributions fall between the exponential (b = 1) and Rayleigh (b = 2) distributions, particularly the peak samples for runs 3 and 4. Furthermore, for runs 1 and 2, the shape parameter is typically greater than two for the starboard side peak samples which contain lower magnitude peaks - see Figure 43. Shape parameter value greater than 2 implies that the distribution tail is lighter than the tail of the Rayleigh distribution and indicates small nonlinearity. The GPD shape parameter values range between -0.41 and 0.25 for the pressure distributions and -0.44 and 0.16 for the strain distributions. In general, for runs 1 and 2 the GPD shape parameter is near or less than zero for both pressure and strain peaks, implying that the distributions are light-tailed, while for runs 3 and 4 the GPD shape parameter is typically positive implying that the distributions are heavy-tailed.

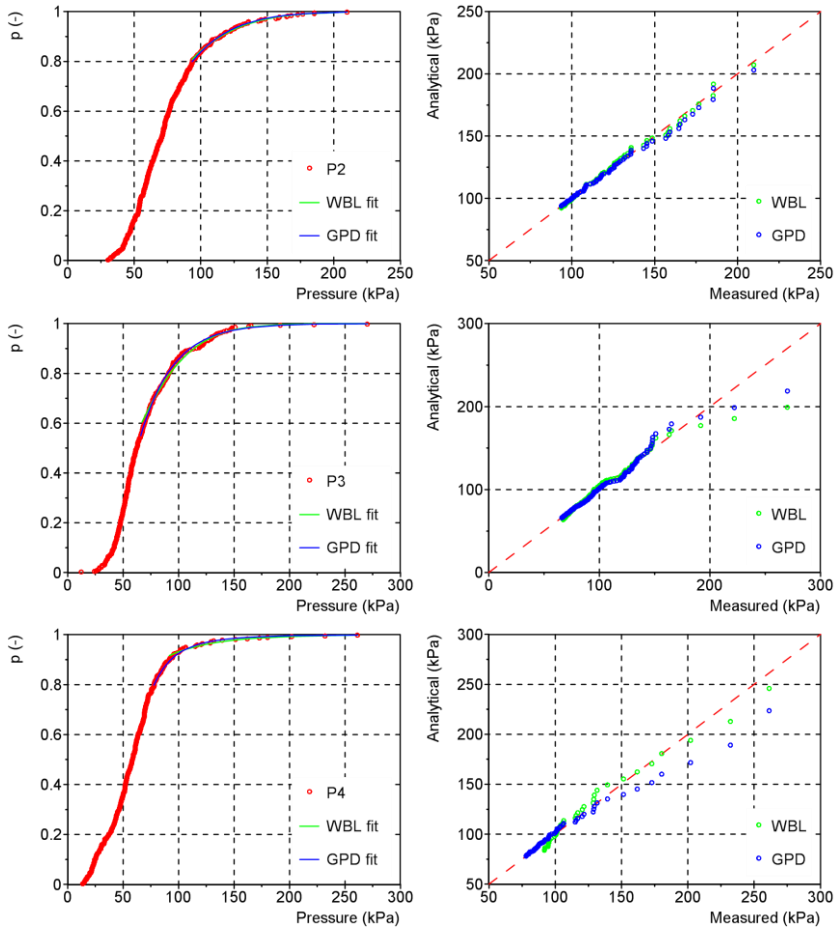

Figure 49 - Cumulative distributions of pressure peaks and fitted analytical models (first column) and corresponding Quantile-Quantile plots (second column) for peak samples P2, P3 and P4, run 2.

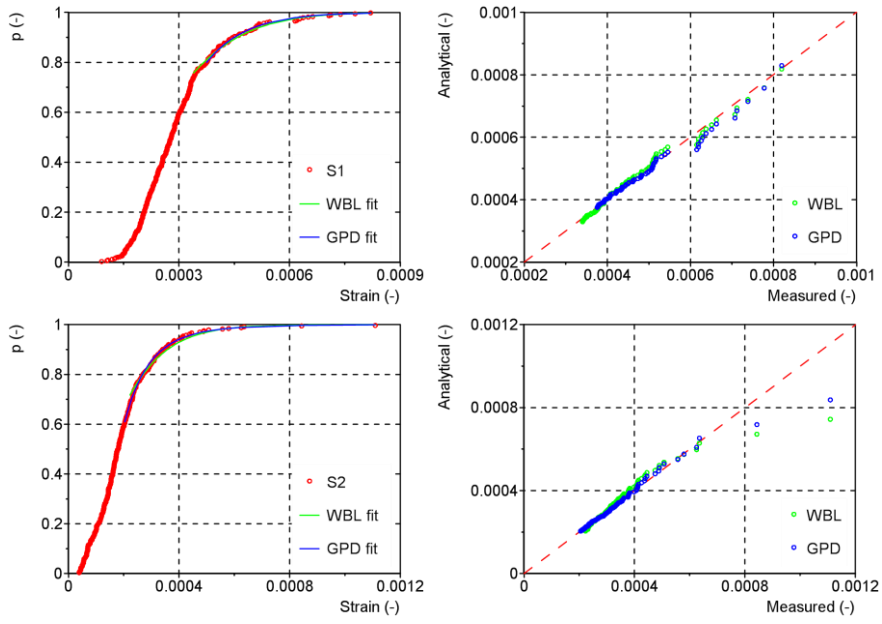

Figure 50 - Cumulative distributions of strain peaks and fitted analytical models (first column) and corresponding Quantile-Quantile plots (second column) for peak samples S1 and S2, run 2.

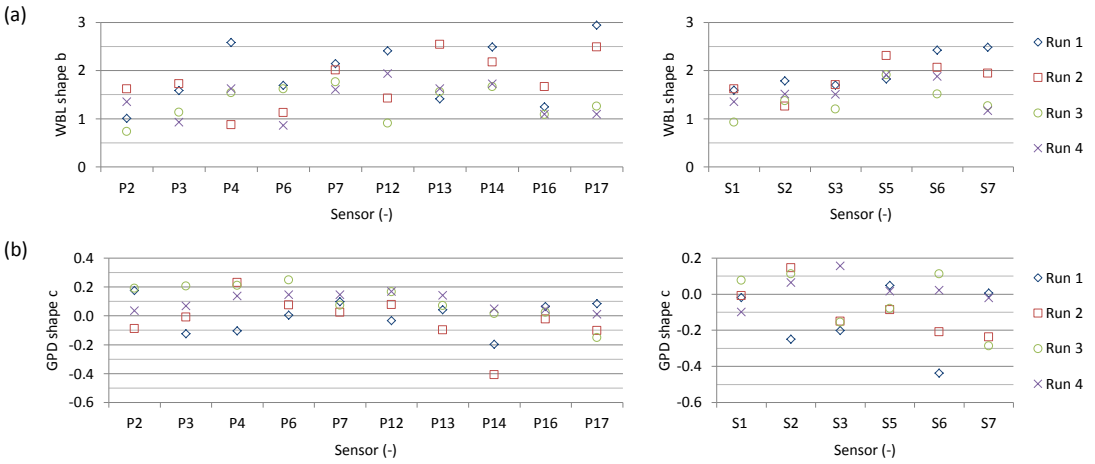

Figure 51 - Weibull (a) and Generalized Pareto (b) shape parameters for the pressure and strain peak samples, runs 1 - 4.

Extreme value estimates are sensitive to the accuracy of the model fit to the data - if a model does not accurately represent the measured data it will most likely not work well when extrapolating for extreme values (Coles, 2001). In the present work, the relative goodness of fit of the models is examined using Quantile-Quantile plots and the RMSE statistic. In Quantile-Quantile plots the measured data is plotted against the theoretical quantile values from the fitted model and if the model is a good fit to the data points, they should fall on a straight y = x line. As can be seen from Figures 49 and 50 both the Weibull and Generalized Pareto models fit the data relatively well. In general, the models fail to accurately predict the tail of the distribution; in particular the largest peaks that differ greatly from rest of the peaks in the sample, e.g. the largest three peaks recorded at S2 are 1110 µs, 843 µs and 635 µs, respectively. This is also reflected in the root mean square errors (RMSE), presented in Figure 52 and Tables 23 and 24 in Appendix B. The RMSE range from 1.4 to 16.8 % and are generally larger for both pressure and strain distributions from runs 3 and 4. The Weibull and Generalized Pareto errors are comparable for runs 1 – 3, while for run 4 the Generalized Pareto is generally a better fit to both the pressure and strain distributions. From assessment of the Quantile-Quantile plots and RMSE for all peak samples it can be concluded that a RMSE value of less than about 2 percent indicates that the model is an excellent fit to the data, while larger errors typically indicate that the largest peaks are not very well predicted by the statistical models.

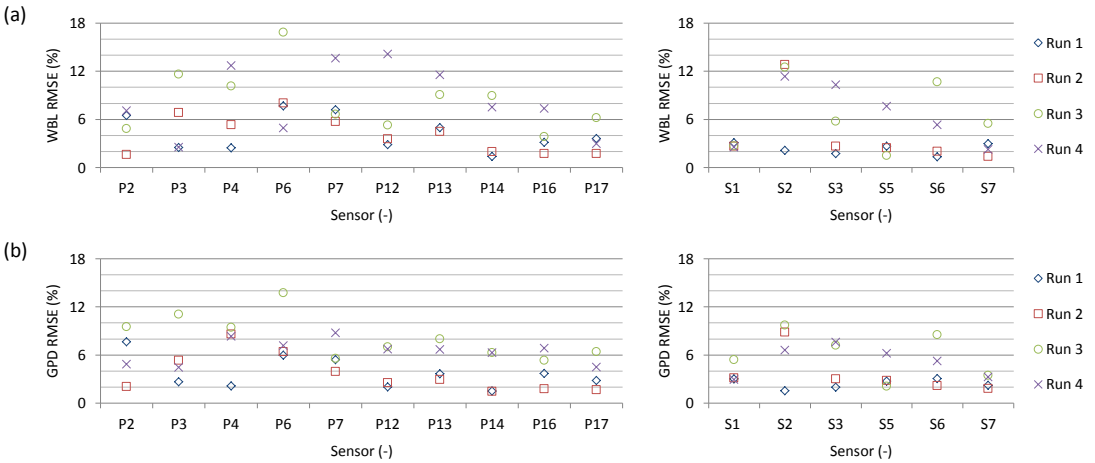

Figure 52 - Normalized root mean square errors (RMSE) (%) for the Weibull (a) and Generalized Pareto (b) models - pressure and strain peaks samples and runs 1 – 4.

In Figure 53 the most probable extreme values and extreme values with 1% probability of being exceeded in a 5 minute period (run time) estimated using the Weibull and Generalized Pareto models are presented. As can be seen, the estimated most probable extreme values using the Weibull and Generalized Pareto models (solid bars) agree relatively well. The difference between the two estimates is in most cases less than 15% and the largest difference is 32.6 % for peak sample P12 in run 4. The estimated extreme values with low probability of exceedance, however, show quite significant differences. This is mainly attributed to the inaccurate modelling of the distribution tail – largest differences are generally observed for the cases with high RMSE.

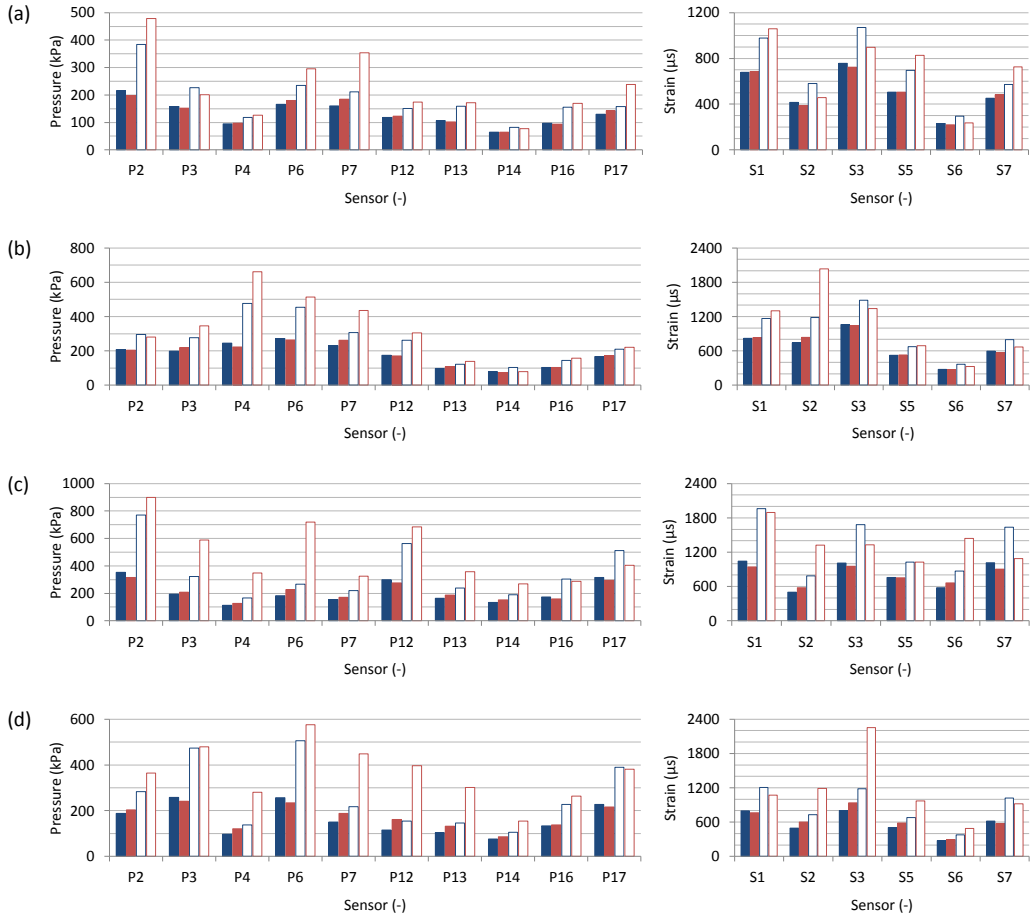

Figure 53 - Estimates of most probable extreme pressures and strains (solid bars) and extreme pressures and strains with 1% probability of exceedance (empty bars) using Weibull (blue) and Generalized Pareto (red) models for runs 1 – 4 (a – d).

4.5. Summary

Full-scale trials on a 9.6m high-speed planing craft in waves have been performed with the aim to gain further insight into the characteristics of slamming impacts and resulting related rigid body and structural response. An extensive set of data consisting of accelerations at the bow and near the LCG and pressure and panel strains at various locations on the hull bottom surface in different sea conditions and at different forward speeds and headings was recorded. In the present study, four head sea runs covering a good range of sea and operational conditions are considered with the aim to illustrate the data processing procedure and present and discuss characteristic findings. A

statistical analysis of the pressure and strain measurements is also performed. The main conclusions drawn from this study are:

- The raw acceleration signals are found to contain unwanted high frequency noise that is concluded to be due to structural vibrations caused by wave impacts and operating engines. Fast Fourier Transform (FFT) analysis and low pass filtering are used to calculate the energy content of the signal and identify the dominant frequency, and remove the high-frequency noise, respectively. It is found that a cut-off frequency of 30Hz effectively removes the high-frequency noise without significantly affecting the signal characteristics, particularly the rapid increase in acceleration at impact. The cut-off frequency used in the baseline correction and peak identification algorithms to filter the strain signals is higher than the chosen frequency for the acceleration signals mainly because the strain rise times are shorter and require higher frequencies to capture accurately.
- Methods for removing baseline drifts from strain signals and identifying the peaks in the pressure and strain signals are developed and successfully applied. The peak identification method is shown to accurately identify the impact events and peaks which would have been identified manually (from a visual examination), considering that the duration of the interval between impacts and the duration of impacts varies within each signal and also between signals.
- The stochastic and nonlinear behaviour of a planing craft travelling at high speed in waves is clearly illustrated in the measurements where each hull-water impact is different. In general the impacts are characterised by short rise time and large peaks of short duration, with the magnitude of pressure and strain decreasing with increasing distance from the keel and forward. Strong correlation between the pressure and strain signals is also observed. The impacts are fairly symmetric in terms of the number of peaks recorded on the port and starboard sides the averages of the largest $1/3^{rd}$ and $1/10^{th}$ peak values show some differences with the port side measurements being generally larger. The statistical averages also show that larger pressures and strains were measured at high speed in moderate seas rather than at moderate speed in rough seas.
- The statistical analysis showed that pressure and strain peaks on different levels belong to different statistical distributions, with large magnitude peaks which are most likely to be due to extreme slamming impacts being more nonlinear. This observation justifies the use of a threshold in fitting the Weibull model to better model the largest peaks. Overall, the statistical models were found to fit the data well except in the tail of the distribution, particularly for samples that contain outliers. The methods used in the present work to estimate the model parameters and select the threshold (least square method for the Weibull and method of moments and shape parameter stability plots for the GPD) have been shown to perform well in statistical analyses of wave loads on large ships and were chosen because of their simplicity and ease-of-use. However for full-scale measurements of slamming loads on high-speed craft, where samples can contain outliers and the sample sizes are generally small, more robust methods may be needed (see for instance de Zea Bermudez & Kotz (2010) for a review of robust methods).

Chapter 5. Full-scale drop tests: experiments and simulations

In this chapter, the loads experienced by a high-speed planing craft as it falls freely into the water and related global and local responses are investigated using full-scale tests and numerical simulations. The same boat (C-Target 9) and instrumentation system used for the rough water trials were used. The boat was dropped from two heights and for each height the test was repeated three times. The tests and the data processing procedure are described. The repeatability and symmetry of the measurements is studied and characteristic results are presented and discussed.

Numerical simulations of the full-scale drop tests are also performed. The numerical model is set up based on the lessons learned from the problems studied in Chapter 3. Parametric studies on the effect of drop height and initial trim angle on the boat kinematics and impact pressures are performed. The numerical time histories of vertical acceleration at LCG, pitch motion and pressure at various locations on the hull bottom surface are compared with the experimental results for validation and the comparisons are discussed. Two-dimensional simulations of transverse sections of the hull free falling vertically into the water are also performed and the results are compared to the 3D solutions to investigate the accuracy of 2D models for simulating slamming impacts. The 2D model is also used to investigate the effect of the spray rails.

5.1. Experiments

5.1.1. Test description

The drop tests were performed at the Trafalgar Wharf marina in Portsmouth, on the 22nd February 2016. The experimental set-up is shown in Figure 54. The boat was lifted out of the water with a crane equipped with a remote controlled release hook. The same instrumentation and data acquisition system used for the sea trials (described in section 4.1.2) were used for the drop tests. The measurements made in the rough water trials include rigid body motions, accelerations, pressure and strain at various locations on the hull bottom surface and global hull deflections. From analysis of the sea trials data it was found that the IMU data is not consistent with the other signals and the physics of the problem. A second IMU (Xsens MTi-G-700) was therefore installed near the first to measure the rigid body motions. The position of the sensors is shown in Figure 33. The mass of the boat was measured on the morning of the test using load cells and is 2550 kg. The difference between the measured value and that given in Table 7 is mainly the mass of fuel in the tanks. The drop height was measured using a marked length of rope (rope with knots tied at equal intervals) fitted to the transom. The boat was dropped from heights of 0.5 m and 1.0 m and for each drop height the test was repeated three times. The uncertainty in the drop height is estimated to be ± 0.1 m. The boat was released at the same trim angle in all but the first drop where it was oriented more bow up.

Figure 54 - Full-scale drop tests setup.

5.1.2. Data processing

The software DIAdem from National Instruments was also used to post-process the experimental drop test data. The data processing procedure is as follows:

1. The offset in the voltage and strain signals is removed by subtracting from the signal the mean value of the part of the signal prior to release.
2. The accelerometers and linear position sensors signals are converted from voltage to acceleration and displacement, respectively, using the sensitivity values given in the respective data sheets.
3. The acceleration and displacement signals are low pass filtered to remove the high-frequency noise – see section 5.1.2.1.
4. The time of release and impact and the duration of free-fall are determined from the cockpit vertical acceleration signal as follows:
    a. The signal is band-pass filtered with a 10^{th} order Butterworth filter and cut-off frequencies of 0.1 and 100 Hz to remove low frequency drift and high-frequency noise, respectively.
    b. The signal is multiplied by 9.81 to convert it from g's to m/s^2.
    c. The Event Search function in DIAdem is used to identify the intervals in the signal where the acceleration is nearly zero, i.e., prior to release, and between 9.2 and 12 m/s^2, i.e., the boat is free-falling. The end time of these two intervals are taken as the release time and impact time, respectively. The duration of free-fall is the difference between the time of impact and release.
5. The average free-fall acceleration, impact velocity and drop height are calculated from the cockpit vertical acceleration signal as follows:
    a. The band-pass filtered acceleration signal is integrated over time to obtain the velocity time history. The position time history is obtained in a similar manner, i.e., the velocity signal is first band-pass filtered (10^{th} order Butterworth; f_1 = 0.1Hz; f_2 = 100Hz) and then integrated.
    b. The average free-fall acceleration is taken as the mean value of the acceleration signal between the time of release and impact – free-fall period.

c. The impact velocity is the difference between the velocity at the times of impact and release and similarly for the drop height.

6. The trim angle of the boat while suspended in air is obtained from the pitch motion signal as the mean value of a 10 s segment of the signal prior to release.
7. The peak(s) in the pressure and strain signals are manually identified.

5.1.2.1 Low pass filtering

Figure 55 shows the raw cockpit (A1z) and bow (A2z) vertical acceleration signals recorded in drop 4 (see Table 10). The signals have similar characteristics to those recorded in the rough water trials, i.e., rapid increase and large initial peak followed by high frequency and large amplitude oscillations. The cockpit acceleration signal is seen to oscillate about a much higher residual acceleration level relative to the magnitude of the initial peak, compared to the bow acceleration signal. The Fourier spectrums of the two signals are presented in Figure 56 where both spectra show that the main energy content is below 10 Hz.

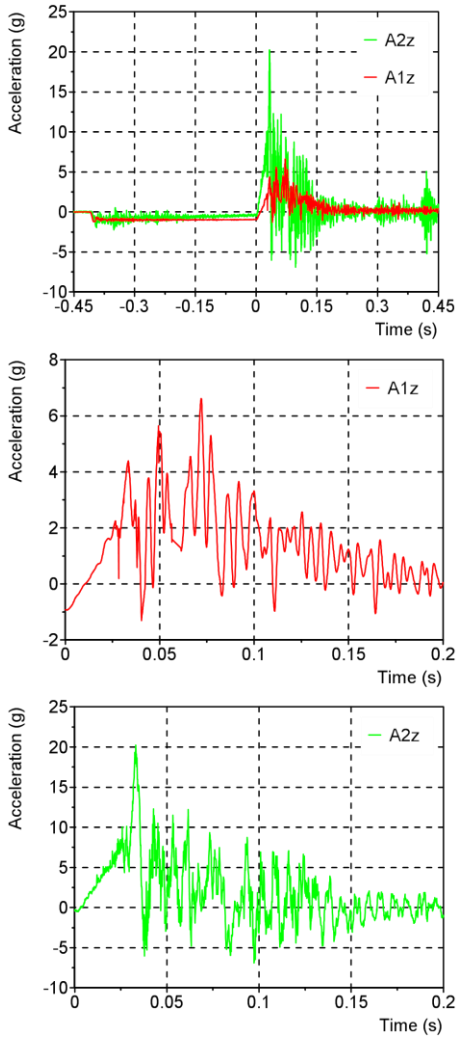

Figure 55 - Raw vertical acceleration signals recorded in the cockpit (A1z) and at the bow (A2z) in drop 4.

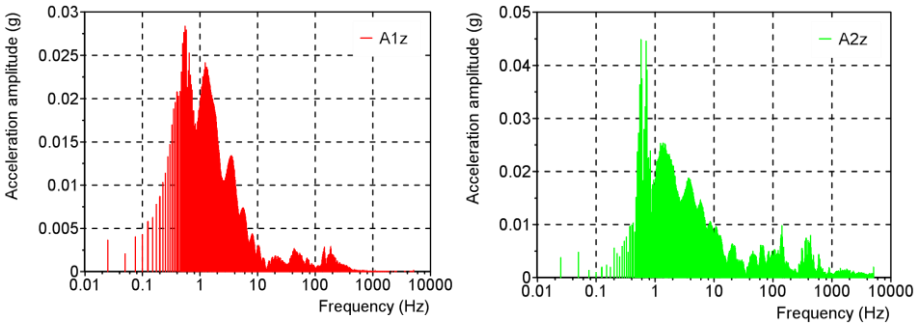

Figure 56 - Fourier spectrum of the cockpit (A1z) and bow (A2z) vertical acceleration signals recorded in drop 4.

Figure 57 compares the raw signals with low pass filtered signals at different cut-off frequencies using a 10th order Butterworth filter. As can be seen, low pass filtering effectively removes the high-frequency noise from the signal without significantly affecting the rigid body response. Furthermore, the level of noise in the signal decreases with decreasing the cut-off frequency. It is again shown that the 10 Hz cut-off frequency is too low and does not capture the rapid increase in acceleration accurately. The acceleration signals are therefore low pass filtered using a 10th order Butterworth filter and the same cut-off frequency used to filter the rough water trials signals, i.e., 30 Hz. The same procedure was repeated for the linear position sensors signals and a cut-off frequency of 100 Hz was chosen.

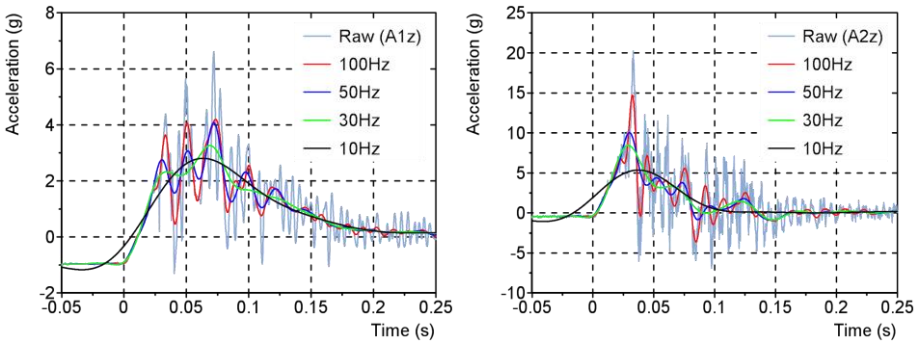

Figure 57 - Effect of cut-off frequency on the cockpit (A1z) and bow (A2z) vertical acceleration signals, drop 4.

5.1.3. Results and discussion

The tests performed are summarised in Table 10. The boat was dropped from heights of 0.5 m and 1.0 m (measured at transom – h_t in Figure 58), and for each drop height the test was repeated three times to assess the repeatability of the measurements. In the first test (drop 1) however, the boat was released with the keel more or less parallel to the water surface, whereas, in drops 2 – 6 the boat was released more bow down – larger positive trim angle. The trim angle is the angle between the keel line and the horizontal positive downwards (τ in Figure 58) and is obtained from the pitch motion signal. The trim angle of the boat at rest in calm water is measured to be -0.445°. The impact velocity and drop height are estimated using two different methods, (1) theoretically using the free-fall duration and acceleration values obtained from the cockpit acceleration signal and (2) from integration of the cockpit acceleration signal with respect to time. The impact velocities obtained from the two methods agree very well, however, the drop heights show significant differences which are concluded to be mainly due to errors related to double integration of the acceleration signal. It can also be observed that the estimated drop heights are lower than the measured values for all

drop tests except the first. This is because in tests 2 – 6 the boat was dropped bow down and thus the vertical distance between the hull bottom and water surface in the forward part of the hull is lower than at the transom – see Figure 58. The cockpit accelerometer senses the impact when the hull touches the water (in this case the initial point of contact is in the bow region), and since both methods use information derived from the cockpit acceleration signal, the estimated drop heights are lower. In the first test, it is likely that the measured drop height is incorrect and the boat was dropped from a height greater than 0.5 m.

Table 10 - Full-scale drop tests performed. The nominal drop height is measured height at the transom whereas the calculated drop heights are the minimum distance between hull bottom and water surface.

					Equations of motion (1)		Integration (2)	
Drop	Nominal drop height h_t, m	Trim angle, °	Free-fall duration, s	Free-fall acceleration, m/s²	Impact velocity, m/s	Drop height h_m, m	Impact velocity, m/s	Drop height h_m, m
1	0.5	0.90	0.370	9.45	3.49	0.65	3.49	0.53
2	0.5	4.58	0.233	9.27	2.16	0.25	2.16	0.18
3	0.5	4.45	0.216	9.50	2.06	0.22	2.05	0.20
4	1.0	4.37	0.409	9.46	3.87	0.79	3.87	0.65
5	1.0	4.27	0.409	9.52	3.90	0.80	3.89	0.68
6	1.0	4.68	0.399	9.41	3.76	0.75	3.76	0.60

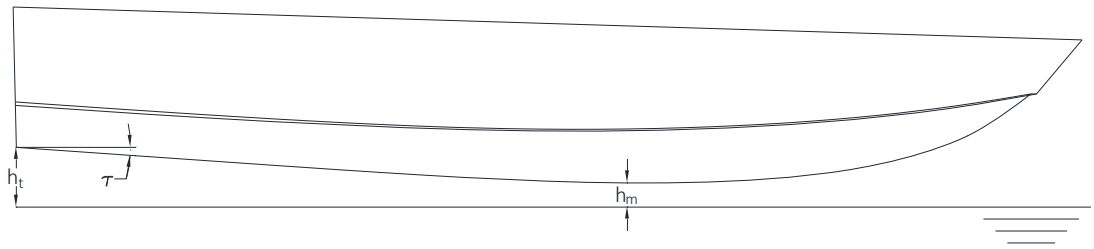

Figure 58 - Sketch of the experimental drop test setup describing the measured drop height at transom h_t, calculated (minimum) drop height h_m and trim angle τ.

5.1.3.1 Repeatability

The repeatability of the experiment is assessed by comparing the measurements from 'equivalent' tests, i.e., drops 2 and 3 and drops 4 – 6 respectively. Figure 59 shows the pitch and roll motion and cockpit and bow vertical acceleration signals recorded in drops 4 – 6. There is relatively good agreement both in terms of shape and magnitude and shows that the global behaviour of the boat is repeatable. The pitch, roll and acceleration signals recorded in drops 2 and 3 show similar low levels of variation.

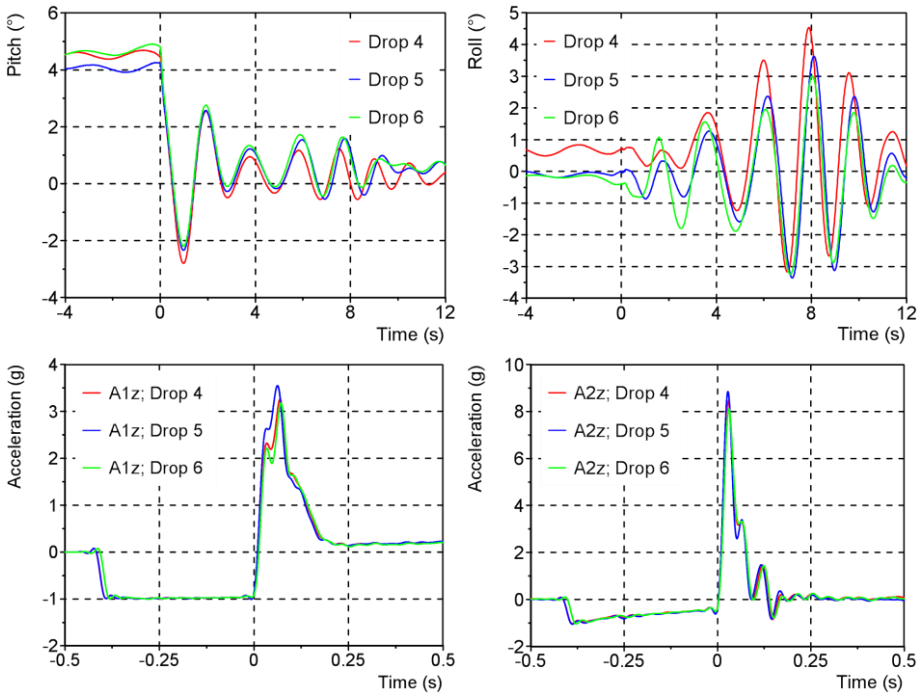

Figure 59 - Pitch and roll motion and cockpit (A1z) and bow (A2z) vertical acceleration signals recorded in drops 4 – 6.

The repeatability of the pressure and strain measurements is illustrated in Figures 60 - 62 where characteristic pressure and strain signals from drops 4 – 6 and the magnitude and time of the identified peaks for all pressure and strain signals from drops 2 – 6 are presented. In the case where a signal has two distinct peaks, such as pressure signals P1 and P7 and strain signal S1 in Figure 60, the magnitude and time of both peaks are included in Figures 61 and 62. Unfortunately, sensors P15, P18, P20 and S4 did not work during the drop tests and, hence, data is not available. The pressure and strain measurements also agree relatively well, both in terms of shape of the time histories and magnitude and timing of the peaks. The mean, standard deviation and coefficient of variation of the magnitude and time of the pressure and strain peaks from 'equivalent' drops are presented in Tables 25 - 28 in Appendix C. It must be emphasized that these statistical quantities are calculated using just 2 and 3 values, respectively.

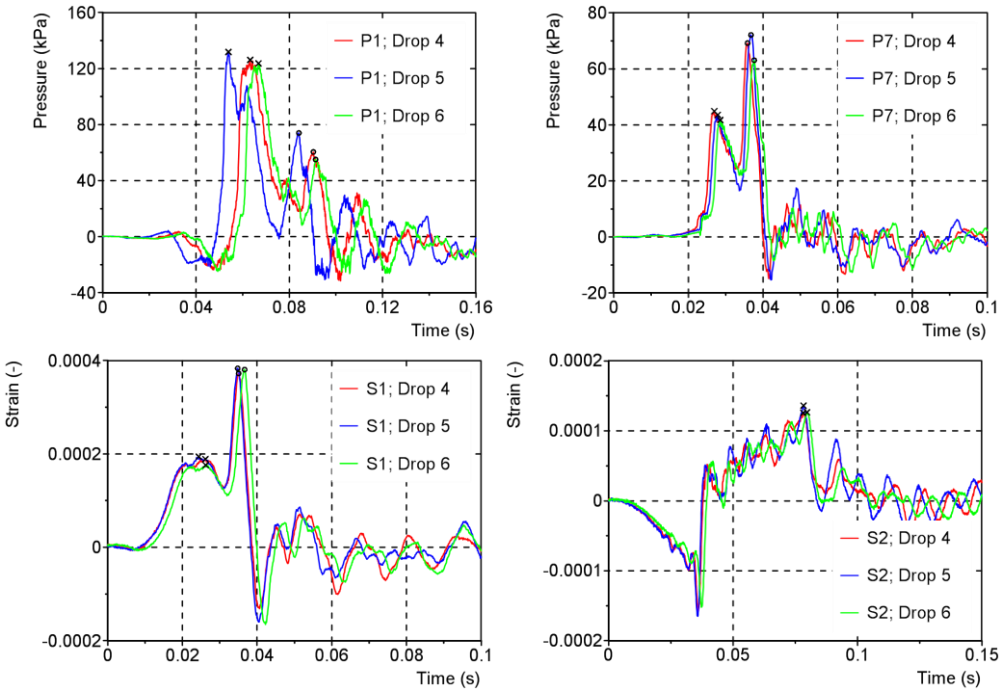

Figure 60 - Pressure (P1, P7) and strain (S1, S2) signals recorded in drops 4, 5 and 6. The peaks are marked with a cross (first peak) or circle (second peak).

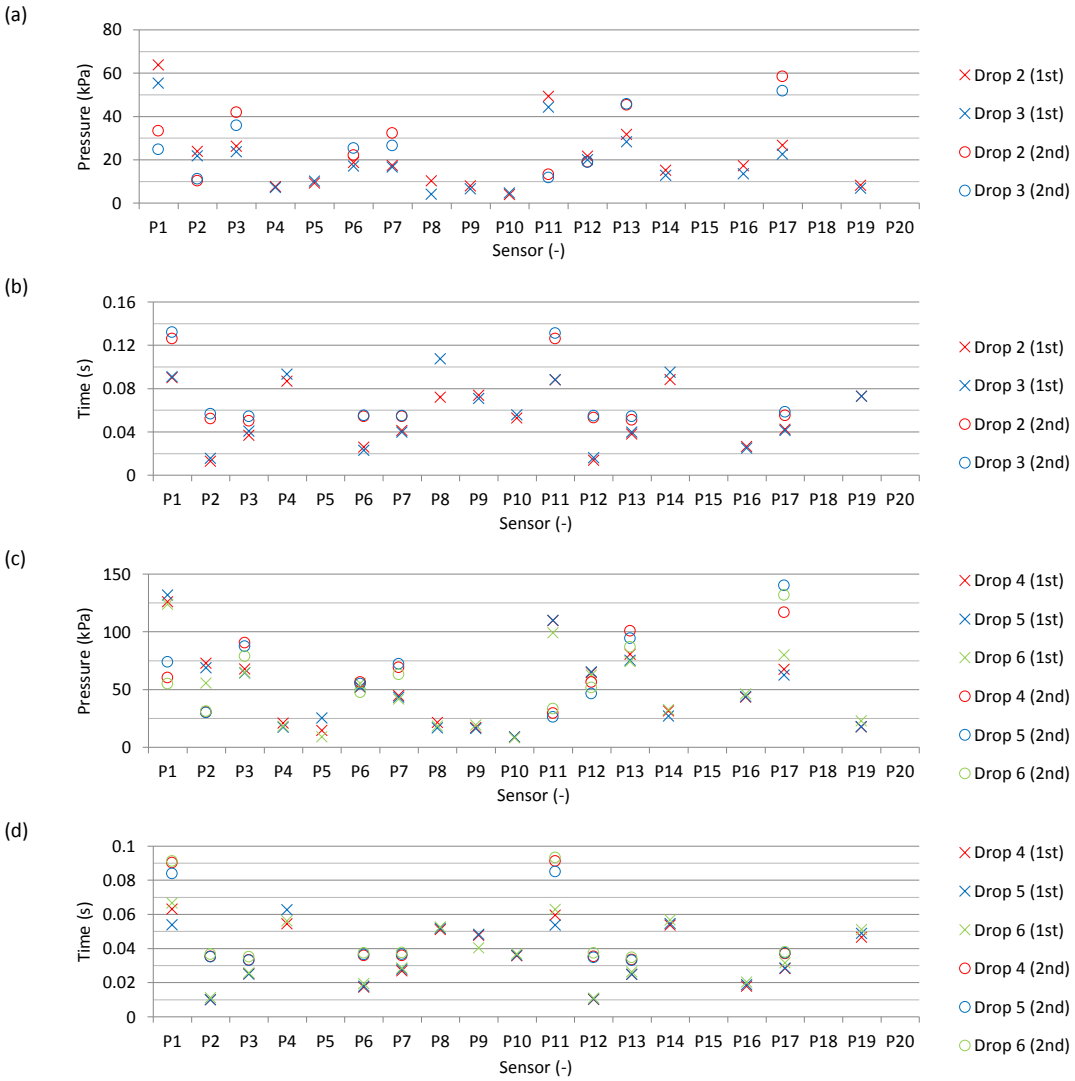

Figure 61 - Magnitude and time of the pressure peaks recorded in drops 2 & 3 (a, b) and drops 4 – 6 (c, d). The cross and circle represent the first and second (where it exists) peak, respectively.

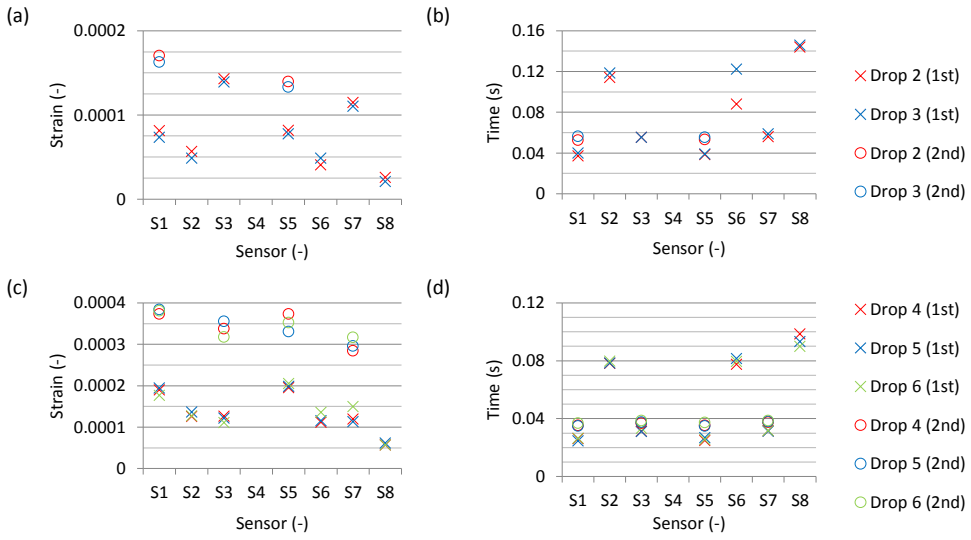

Figure 62 - Magnitude and time of the strain peaks recorded in drops 2 & 3 (a, b) and drops 4 – 6 (c, d). The cross and circle represent the first and second (where it exists) peak, respectively.

The linear position sensors measurements are less repeatable as shown in Figure 63. Furthermore, the signals recorded in the cockpit and cabin in any given drop, particularly drops 2 and 3, have very similar shape and magnitude, which does not follow expectations from physics. This has also been observed in the measurements from the sea trials, and is most likely to be due to interference between the two signals. Considering the high levels of uncertainty associated with the linear position sensor measurements, no further consideration is given.

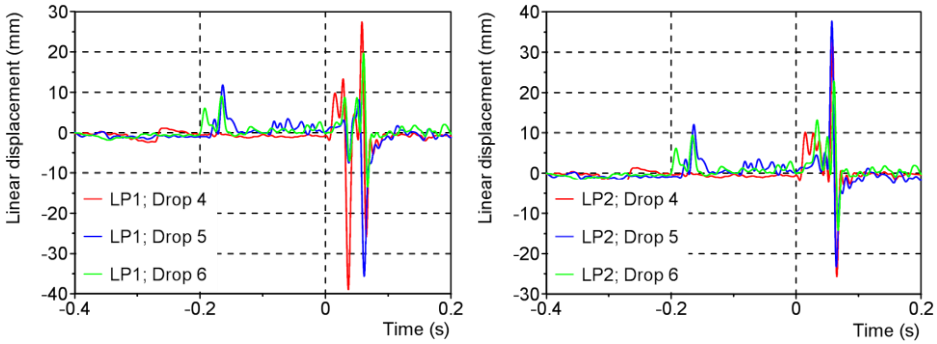

Figure 63 - Linear position sensor signals recorded in the cockpit (LP1) and cabin (LP2) in drops 4 - 6.

5.1.3.2 Symmetry

The symmetry of impacts is assessed by comparing the pressure and strain signals recorded at symmetric locations on port and starboard sides as shown in Figure 64. The signals compare reasonably well in terms of shape, particularly the strain signals, and some characteristics such as primary and secondary peaks are observed in both signals. The timing of the start of the impact, primary and secondary peaks etc. also match very well. However, the magnitude of the pressure peaks and the amplitude of oscillations during the 'vibration' phase (after peak pressure/ strain) show some differences. The strains show better agreement. The symmetry of pressure and strain measurements at locations other than those shown in Figure 64, in terms of magnitude and time of the peaks, can be assessed from Figures 61 and 62, by comparing for example the results for P3 and P13 and so on.

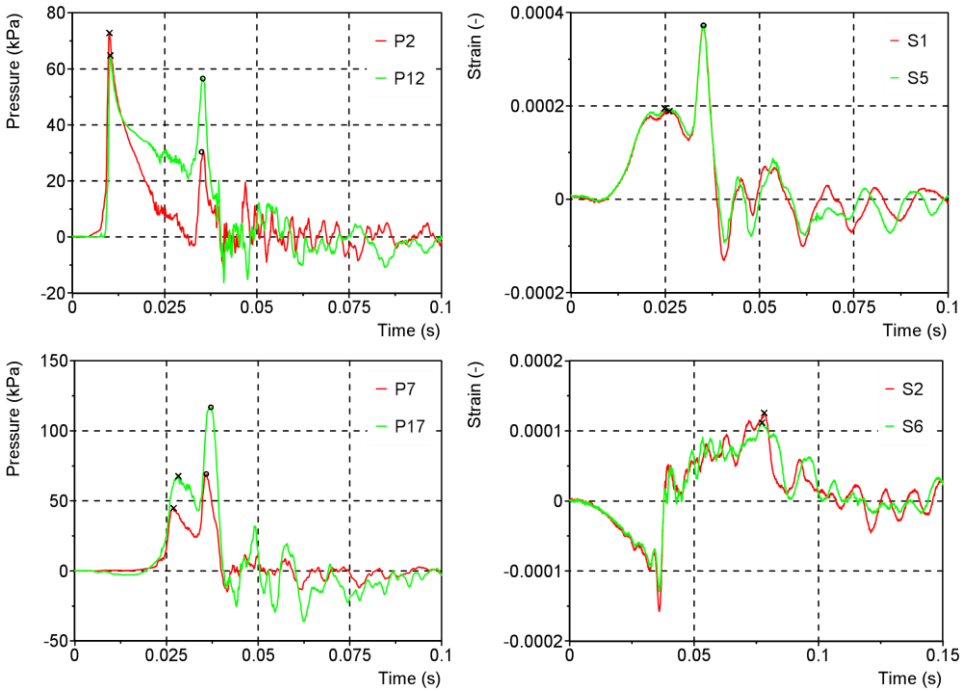

Figure 64 - Symmetry of pressure (P2&P12, P7&P17) and strain (S1&S5, S2&S6) signals, drop 4.

5.1.3.3 Characteristic results

Figure 65 shows the time series of pitch motion and cockpit and bow vertical acceleration signals recorded in drops 2 and 4. Zero time is the instant at which the boat touches the water surface, i.e., the cockpit accelerometer senses the impact. The cockpit accelerometer records an acceleration of about -1g during the free-fall phase. The bow accelerometer does not have a DC response, i.e., the sensor does not respond to gravity or other low frequency signals, which is why the bow acceleration is seen to increase during this period. When the boat hits the water the acceleration in the cockpit and at the bow rises sharply and the boat experiences a bow up rotation (the centre of mass of the boat is located aft of the initial point of water contact). The magnitude of acceleration at the bow is larger and the rise and decay times are shorter as a result of this bow up rotation.

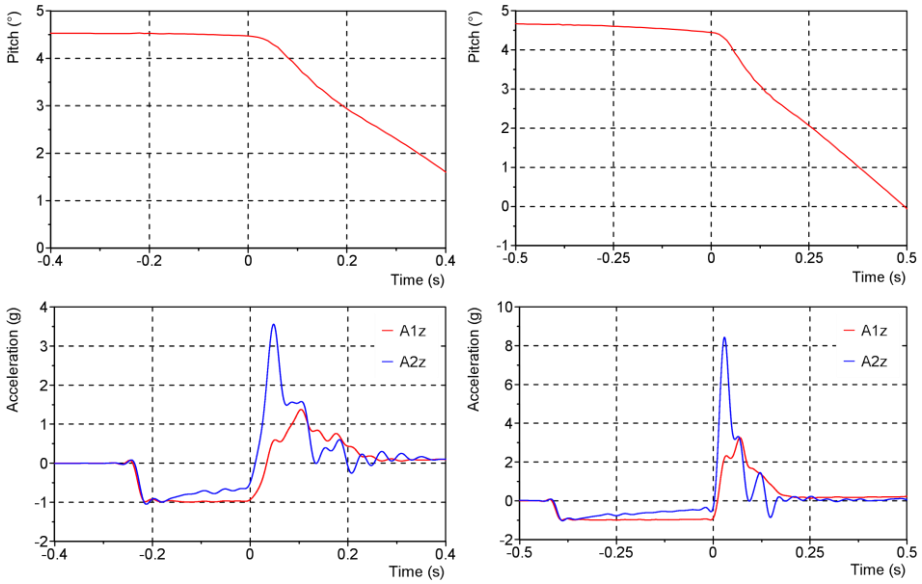

Figure 65 - Time series of pitch motion and cockpit (A1z) and bow (A2z) vertical acceleration recorded in drop 2 (first column) and drop 4 (second column).

Characteristic time series of pressure and strain recorded by the first and second rows of sensors are presented in Figure 66. The position of the pressure sensors and strain gauges relative to the keel, longitudinal stringers and spray rails is shown in Figure 46. In the initial stages of the impact (up to t ≈ 0.047s for drop 2 and t ≈ 0.032s for drop 4), the characteristics of the pressure and strain signals are similar to the measurements made on free-falling wedges, see for example Lewis et al. (2010) and Yettou et al. (2006). The pressures are characterised by a rapid increase and large initial peak followed by a moderate decay to a much lower residual pressure level. The first peak is recorded by the sensors located near the keel, i.e., sensors P2 and P6 respectively, while sensors located further out record their peak later in time. The hull structure deforms in response to this applied loading. The strains measured at the centre of the hull bottom area between the keel and the first longitudinal stiffener (here referred to as the first panel), i.e., signals S1 and S3, gradually increase to a positive maximum and then start to decrease, while the strains measured on the hull bottom area between the first and second longitudinal stiffeners (here referred to as the second panel), i.e., signal S2, is seen to gradually increase to a negative maximum. Positive strains mean that the panel is deflecting inwards and negative strains outwards. The measured strains suggest that as the loading is being applied on the first panel and it deflects inwards, the longitudinal stiffener acts as a pivot and the second panel deflects outwards as depicted in Figure 67.

A second peak is observed in the signals measured on the first panel, i.e., pressure signals P2, P3, P6 and P7 and strain signals S1 and S3, occurring at approximately the same time. The magnitude of the second peak is greater than the initial peak for all but signal P2. This secondary rise in pressure and strain is likely linked to the presence of the spray rail. The initial peak is recorded when the spray root passes over the sensor. When the spray root reaches the flat spray rail, i.e., zero effective deadrise, a high pressure is generated. This increased pressure at the spray root will potentially propagate back towards the keel increasing the pressure on the first panel and as a result the panel deflects further. The pressures and strains decrease rapidly after the second peak and oscillate about a much lower level with about the same frequency. The oscillations are most likely related to panel vibrations. The strains measured on the second panel reach a minimum (maximum outward deflection) at the same time of maximum strain on the first panel. Thereafter, the strain on the

second panel increases sharply to nearly zero strain. Maximum positive strain on the second panel is then recorded when the spray root traverses across the panel and sensor P4 records its peak.

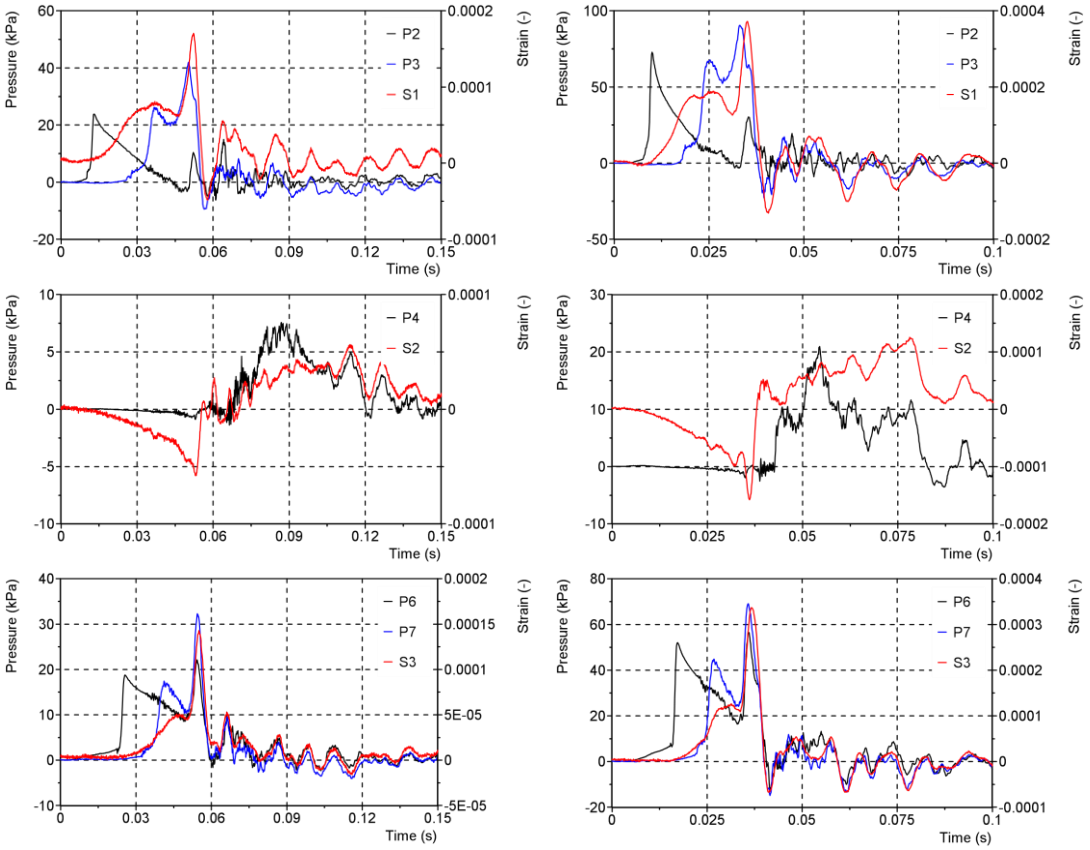

Figure 66 - Time series of pressure and strain recorded in drop 2 (first column) and drop 4 (second column).

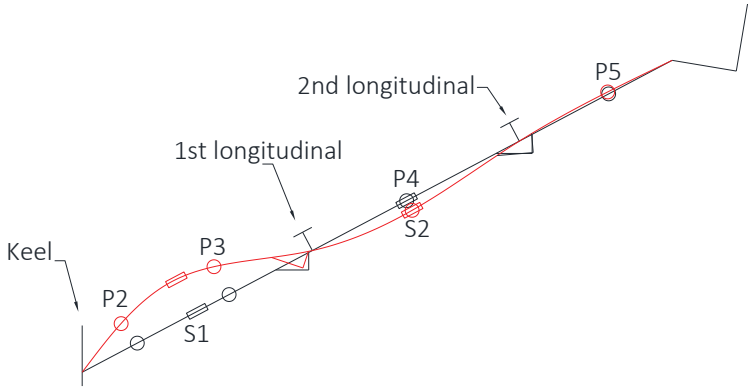

Figure 67 - Sketch of the deformed shape of hull bottom in response to the applied loading at the time of maximum S1 strain (shown in red). The undeformed shape of the hull bottom is also shown (in black).

The effect of drop height on the boat kinematics, impact loads and structural responses is studied by comparing the results for drops 2 and 4 – see Table 10 and Figures 61, 62, 65 and 66. As expected, the impact velocity and maximum acceleration in the cockpit and at the bow increase with increasing drop height, while the acceleration rise time decreases, i.e., the impact is more severe. The magnitude of pressures and strains also increases with drop height and the peaks are recorded earlier in time, however, the shape of the signals is fairly similar.

5.2. Numerical simulations

5.2.1. 3D model

The 3D numerical setup is shown in Figure 68. The impact is assumed symmetric and only half of the boat is modelled to reduce the computational cost of the simulation. The aluminium boat hull has a length of about 9 m, half width of 1.1 m and height of 1.5 m, and its form is characterised by v-shaped sections and hard chines. It also has two spray rails fitted on each side. In this study the structure is assumed rigid and the spray rails are not modelled. The overset grid approach is used to discretize the computational domain. In this approach the domain is divided into two regions, the background region encloses the entire solution domain and a smaller region containing the boat hull called the overset region. The background region is fixed in space while the overset region moves with the body. This approach is more useful in problems involving complicated body motions. The dimensions of the background and overset regions are given in Figure 68. The extents of the overset region were chosen such that the variables do not vary much in the overlapping zone. The outer boundary of the overset region that is coupled with the background grid is specified as Overset Mesh type boundary and a no-slip wall condition is imposed on the boat surface. The bottom, left and top boundaries of the background region are specified as velocity inlet, the right boundary as pressure outlet and the back boundary as no-slip wall. Symmetry conditions were imposed on the symmetry plane.

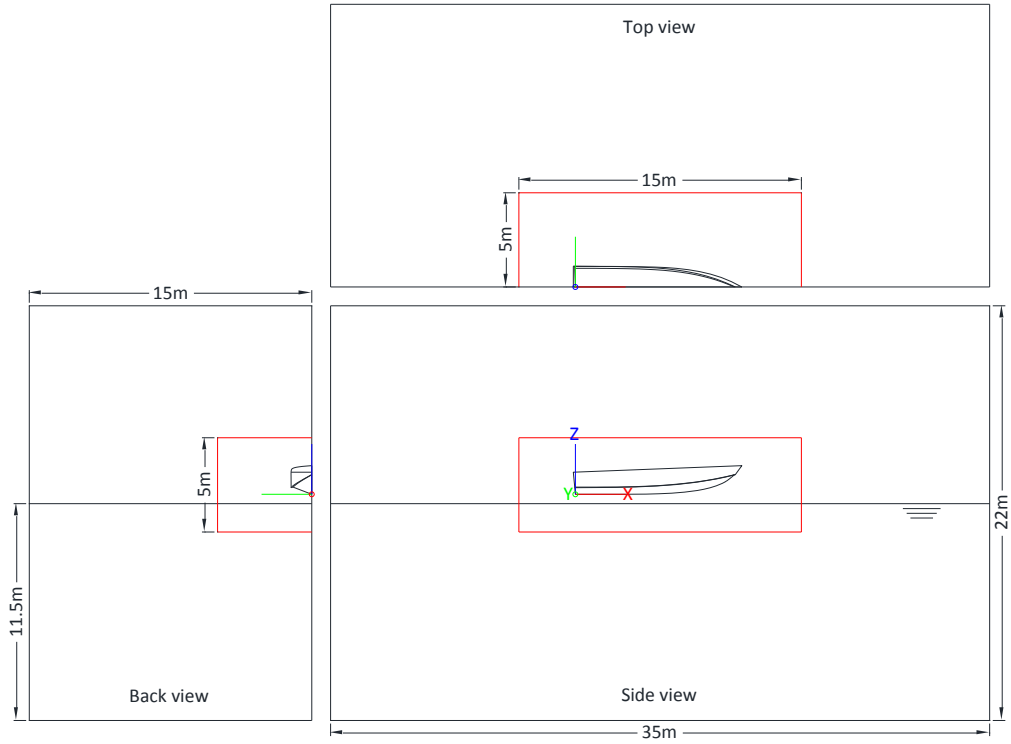

Figure 68 - Numerical setup of the 3D full-scale drop tests simulations. The overset region boundaries are marked in red.

The grid design is similar to that used for the wedge and flexible panel simulations and is shown in Figure 69. The background grid is Cartesian with refinements in the vertical direction around the free surface. The grid in the overset region is trimmed Cartesian with local refinement in the vicinity of the hull and prism layers along the bottom surface. Furthermore, the cells in the overlapping zone

are set to have the same size on both the background and overset grids to minimize errors in interpolating variables between the two grids (CD-adapco, 2014). The size of the first cell on the hull bottom surface is 10 x 10 x 1.73 mm and the height of the cells near the free surface is 20 mm. The grid has about 8.08 million cells with about 5.74 million cells in the overset region.

The same physics models and solver settings used in rigid wedge and panel simulations are used here. The motion of the boat falling into water is modelled with three degrees of freedom, vertical and horizontal (surge) translation and pitch rotation using the DFBI motion model. The boat mass is 2550 kg (measured), centre of mass is 2.524 m forward of the transom and the pitching moment of inertia about the centre of mass is 8061.7 kgm^2 (calculated). The time step size is set as 0.2 ms based on the results of the time step studies for the wedge and rigid panel simulations to keep the Courant number below 1.0 on average.

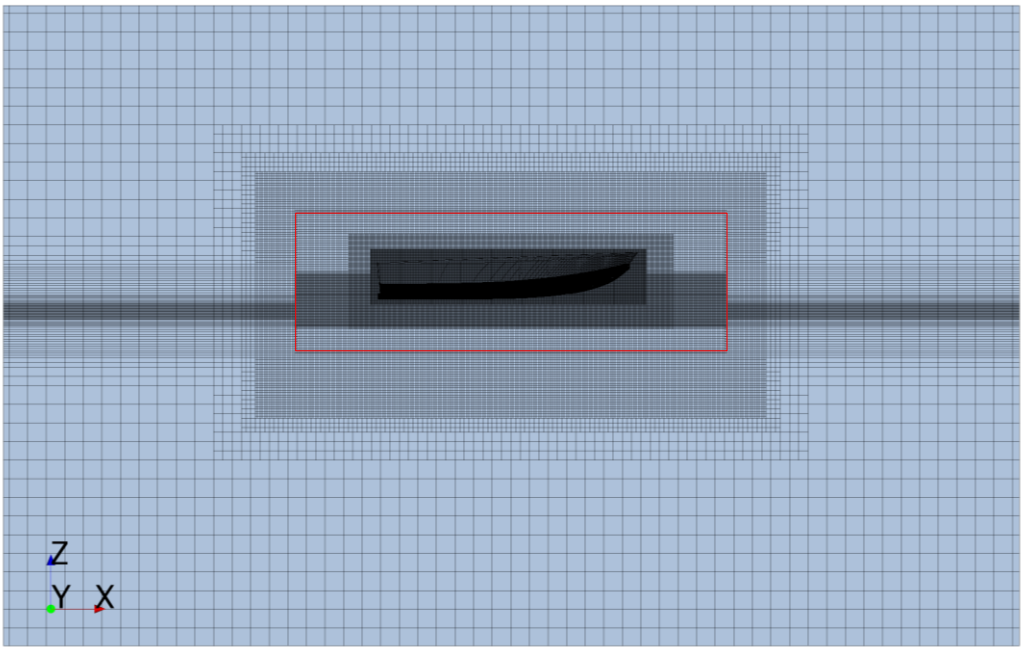

Figure 69 - Computational grid used for the full-scale drop tests simulations. The overset region boundaries are marked in red.

5.2.1.1 Parametric studies

The effect of drop height and initial trim angle on the boat kinematics and impact pressures is studied here. The test conditions studied are presented in Table 11 together with the resulting impact velocity and acceleration maximum and rise time. The drop height is also measured from the transom in the numerical model and the trim angle is defined as the angle between the keel and the horizontal (x-axis) positive downwards, see Figure 58. For the trim angle study, the drop height at the transom was varied to keep the minimum vertical distance between the hull bottom and water surface h_m = 0.5m (see Figure 58). The numerical results also show that with increasing drop height the impact velocity and maximum acceleration increase while the rise time decreases. As expected, the initial trim angle has relatively small influence on the impact velocity and maximum acceleration (constant drop height and mass); however, the acceleration rise time is seen to increase with trim angle. This is in part due to the variation in hull geometry along the length and in part due to the increased gradual wetting with increasing trim angle as explained in the following. The hull form is characterised by relatively constant deadrise and straight keel aft of amidships. Forward of

amidships, the deadrise angle increases gradually towards the bow and the keel starts to curve upwards. In the case of 0° initial trim angle the aft part of the hull (moderate deadrise angle and large impact area) impacts the water first and the craft experiences a sudden deceleration. With increasing the trim angle, i.e., more bow down, the initial point of contact shifts forward where the deadrise angle is higher and keel is curved, i.e., smaller impact area. Figure 70 shows the time histories of pitch motion for different initial trim angles. In all but the 0° initial trim angle case, the centre of mass is located aft of the initial point of water contact and as a result the boat experiences a bow up rotation with impact, i.e., more gradual wetting, while in the 0° the boat remains more or less horizontal. The rate of change of trim angle following impact increases with increasing the initial trim angle.

Table 11 - Numerical drop heights and trim angles studied and resulting impact velocity, acceleration maximum and rise time.

Study	Drop height, m	Initial trim angle, °	Impact velocity, m/s	Max. acceleration, m/s^2	Rise time, ms
Base case	0.5	0	3.05	23.0	37.4
Drop height	0.25	0	2.18	11.2	54.6
	1.0	0	4.3	45.9	29
Trim angle	0.555	1	3.10	24.8	36
	0.629	2	3.11	24.8	45.2
	0.708	3	3.12	23.9	64.8
	0.799	4	3.14	23.6	80.8

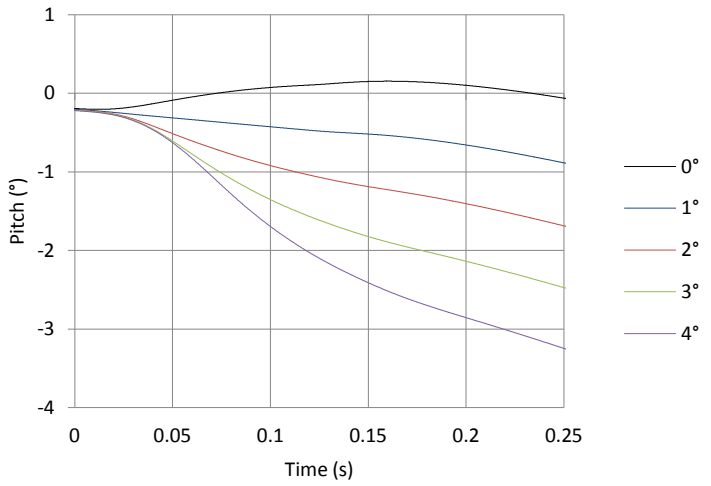

Figure 70 - Time histories of pitch motion for different initial trim angles.

The magnitude and time of the P1 – P10 pressure peaks for all test conditions are presented in Figure 71. As can be seen, with increasing drop height the magnitude of pressure increases and the peaks are recorded earlier in time. The differences in pressure magnitudes are largest for the sensors near the keel, while differences in peak timings are largest for sensors near the chine. Similar trends have been observed in the results for the rigid wedge, see section 3.2.4. The magnitude of the pressure peaks is also seen to increase with increasing the trim angle however the differences are less significant. Furthermore, the P1 peak is recorded later in time while the P2 – P10 peaks are recorded earlier with increasing the trim angle as a result of the bow up rotation.

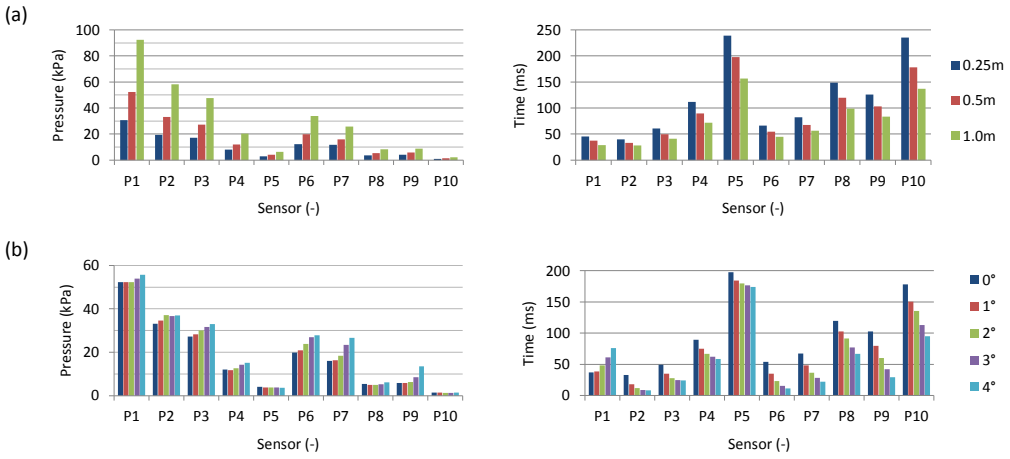

Figure 71 - Effect of drop height (a) and trim angle (b) on the magnitude and time of P1 - P10 pressure peaks.

5.2.1.2 Comparison with experimental measurements

Numerical simulations at similar conditions to experimental drops tests 2 and 4 are performed and the computed results are compared to the experimental measurements for validation. The numerical models are here referred to as case 2 and case 4, respectively. The drop height is set to match the experimental impact velocities of 2.16 m/s and 3.78 m/s, respectively. The drop height h_t is 0.44 m in case 2 and 0.99 m in case 4. The initial trim angle is set as 3° in both cases as it is found to match most closely the experimental time history of pitch motion and timing of the pressure peaks. Figures 72 - 76 compare the computed time histories of pitch motion, cockpit vertical acceleration and pressure at various locations on the hull bottom surface with the experimental measurements. The numerical results for case 2 and case 4 are labelled Num2 and Num4 respectively. Zero time is the instant at which the boat touches the water. Both port and starboard side pressure measurements are shown. The pitch motion and acceleration time histories agree well with the experiments, both in terms of shape of the time histories and magnitude. The pressures are, however, not very well predicted by the numerical model where the magnitude is generally underpredicted though the timing of the peaks matches quite well. The largest differences are observed for signals P1, P3 and P7 where the numerical models predict peak pressure that is about 50 % smaller than the experimental results (first peak; lowest of the port and starboard side peaks). These discrepancies may be caused by a number of factors including,

- The numerical simulation assumes upright impact and even distribution of weight about the keel and the boat is restricted in roll motion. As can be seen from Figures 73 - 76, the largest differences between port and starboard measurements are for the signals that are least well predicted by the numerical model, i.e., signals P1, P3 and P7. However, if this is the case one would expect the numerical predictions to lie somewhere in between the experimental measurements. The good agreement between the port and starboard measurements in terms of timing (start of impact and peak time) and the relatively small change in roll angle following impact (see Figure 59) further suggest that the effects of these assumptions are small.
- The boat is assumed rigid. The characteristic results in Figure 66 show that there is a strong correlation between the measured pressures and strains. For instance, sensor P3 recorded its first peak at nearly the same time of the first peak at S1. In section 3.3.6 it was shown

that, for a constant velocity impact, the structural deformations lead to a reduction in local impact velocity at the panel centre and effective deadrise angle at the chine, which increases and decrease the pressures at the fluid-structure interface, respectively. Hydroelastic effects were found to increase with increasing impact velocity, see Figure 30. In free-fall impacts these effects will be less pronounced because the body decelerates with immersion. Nonetheless they still provide useful insights and are used to examine the possible reasons for the discrepancies. As can be seen from Figure 46, sensors P3 and P7 are located near and at the panel centre, respectively, which from structural flexibility study in section 3.3.6, would mean that the measured pressures are lower than what would have been measured on a rigid body. However, it can also be seen from Figure 46, both sensors are located a short distance away from the spray rail which may have a similar effect as the reduction in effective deadrise at the chine leading to an increase in pressure.

- Experimental parameters that influence the pressure measurements, including pressure sensors not mount perfectly flush with the hull surface, temperature shock effect and water surface not perfectly flat, see studies in Lewis et al. (2010), Van Nuffel et al. (2013), Kim et al. (2015) and Judge et al. (2015).
- Other factors in the numerical model that can influence both the rigid body behaviour and pressure measurements, such as the exact location of the centre of gravity (the mass of the boat was measured but not the centre of gravity and had to be estimated) and the location of the sensors not accurately modelled.

Furthermore, the second peak observed in some signals and subsequent oscillations are not captured by the numerical model. Instead, the numerical pressures are seen to decrease smoothly after the peak. This is concluded to be mainly because the spray rails are not modelled and the boat is assumed rigid, respectively.

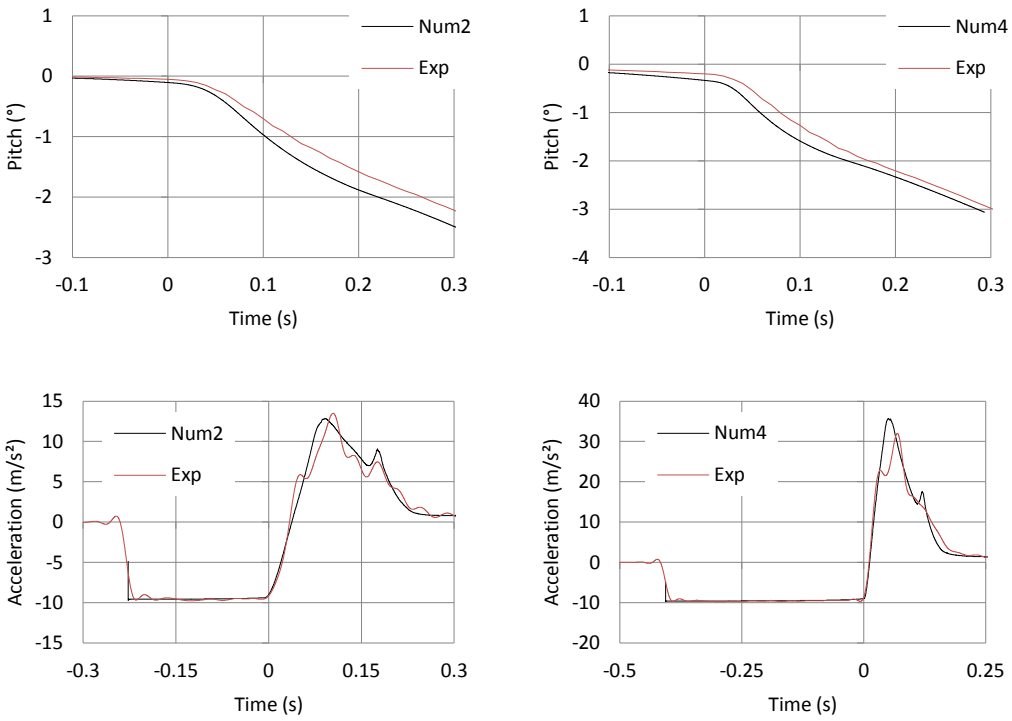

Figure 72 - Comparison of numerical time histories of pitch motion and cockpit vertical acceleration with experimental results for drop 2 (first column) and drop 4 (second column).

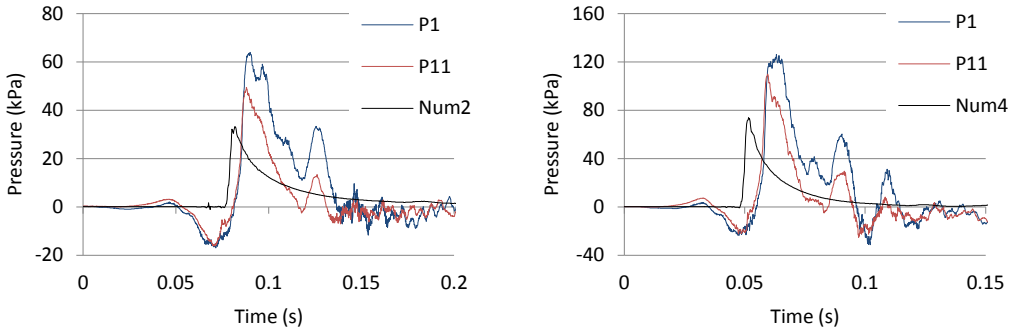

Figure 73 - Comparison of numerical time histories of pressure at P1 (1st row of sensors) with experimental results for drop 2 (first column) and drop 4 (second column).

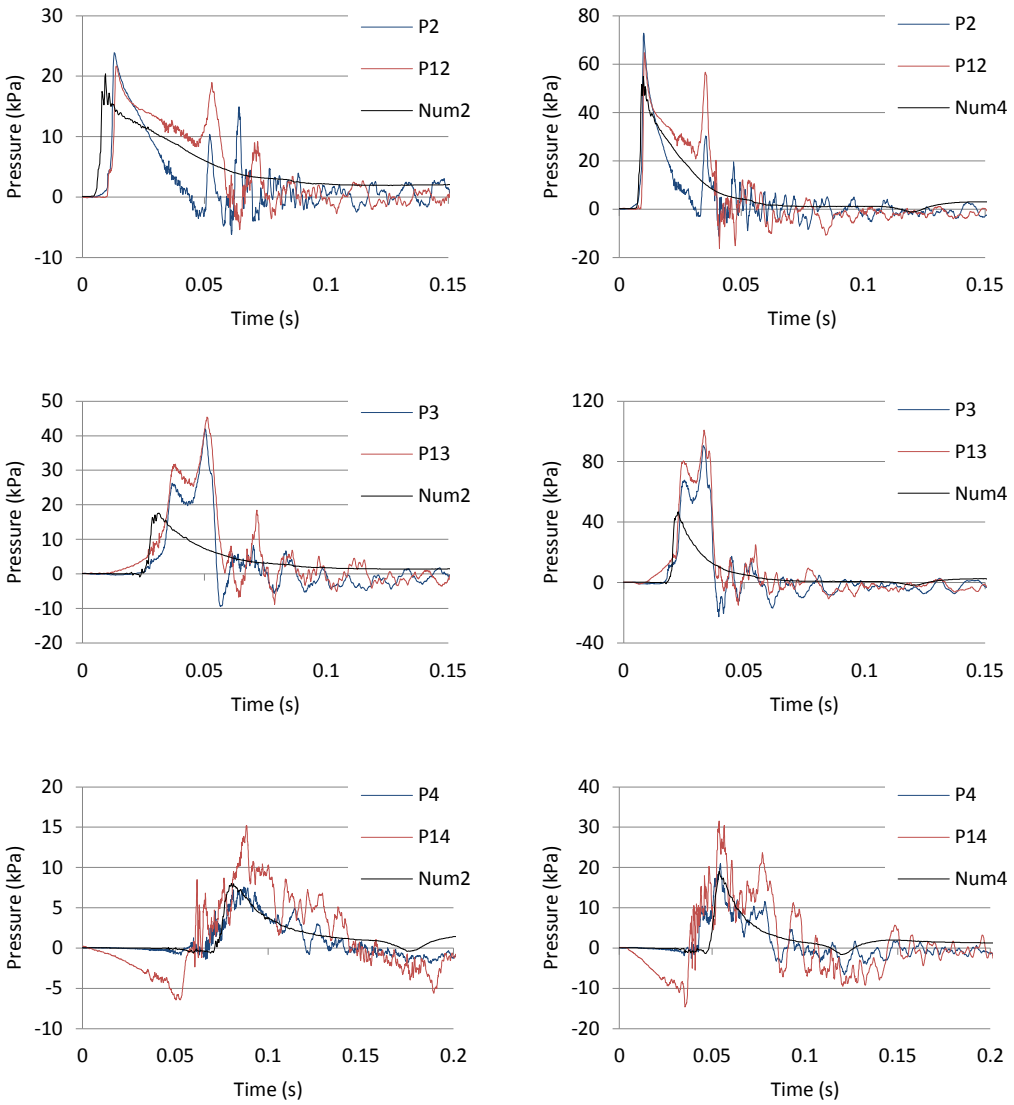

Figure 74 - Comparison of numerical time histories of pressure at P2, P3 and P4 (2nd row of sensors) with experimental results for drop 2 (first column) and drop 4 (second column).

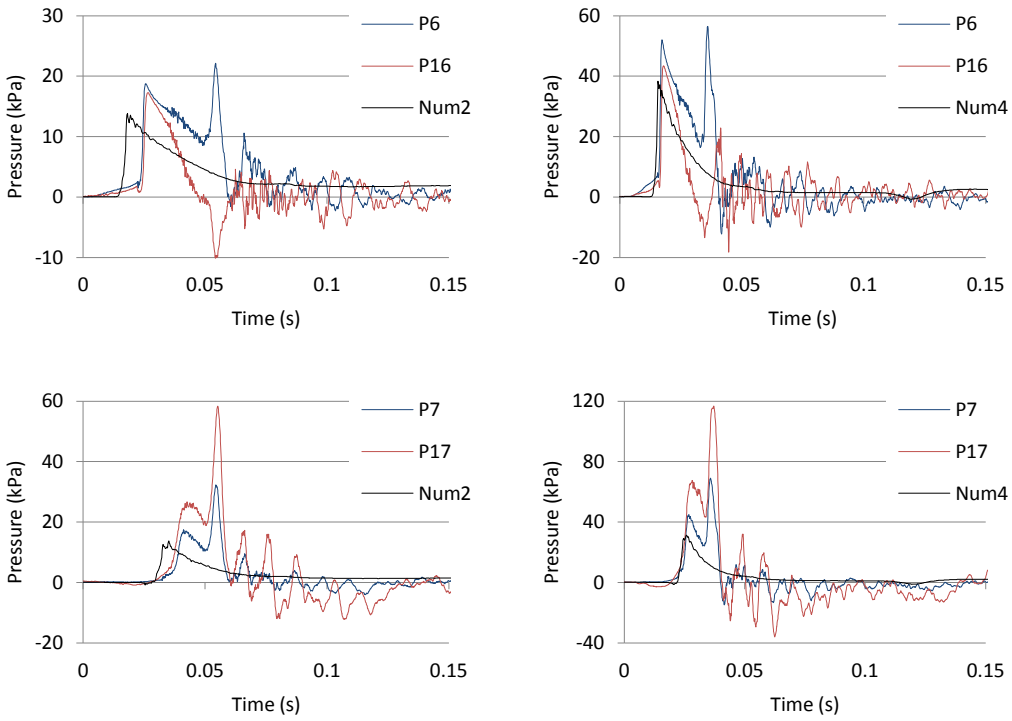

Figure 75 - Comparison of numerical time histories of pressure at P6 and P7 (3rd row of sensors) with experimental results for drop 2 (first column) and drop 4 (second column).

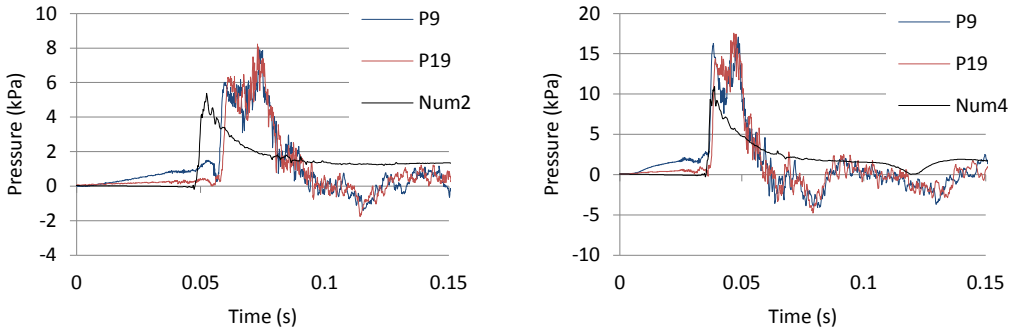

Figure 76 - Comparison of numerical time histories of pressure at P9 (4th row of sensors) with experimental results for drop 2 (first column) and drop 4 (second column).

5.2.2. 2D model

The 3D simulations are computationally expensive – the computational time for 0.7 s of simulation time run on the Iridis 4 supercomputer of the University of Southampton on 2 nodes with 16 dual 2.6 GHz processors each is 48 hours. From a practical perspective, it is therefore important to find ways to reduce the computational costs while still maintaining the same level of accuracy. This can be achieved by, for instance, considering only a transverse section of the hull that is more likely to experience slamming impacts rather than the entire craft. Most of the research works on slamming loads using analytical, numerical and also experimental methods are based this approach. In general, the 2D section is either allowed to fall freely into the water from a height or forced vertically downwards at a constant velocity. There is no consensus, however, as to whether the loads

measured on a 2D section accurately represent the loads on the 3D hull where the motion is more complex and three-dimensional flow effects are present.

Two-dimensional simulations of transverse sections of the hull (rigid) free falling vertically into the water were performed and the results compared to the 3D solution to examine the suitability of 2D models for predicting the loads. The transverse hull sections considered are the sections at longitudinal position of the sensors P2-P5 and P6-P8. The geometry of the two sections is shown in Figure 77. The same 3D model settings – domain width (y-direction) and height (z-direction), background and overset regions, boundary conditions, physics models and solvers settings are used for the 2D simulations. The thickness (x-direction) of the 2D model is 10 mm. The same 3D grid design is also used; however, the size of the cells is halved in all directions. The total number of cells is about 122 thousand for both models. The time step is also halved, i.e., it is set as 0.1 ms, to maintain a Courant number of less than 1.0 on average. A 2D simulation with the same cell and time step sizes used in the 3D simulations was also performed and results showed negligible differences. The mass of the 2D sections is obtained by scaling the mass of the boat using the overall hull length, assuming uniform distribution, and is 1.42 kg. The 2D sections are dropped from the same heights as the 3D hull (minimum vertical distance h_m) and only vertical translation is simulated. As expected, the impact velocity of the 2D sections and 3D hull dropped from the same height agree well (differences are less than 0.5%). The computational time for 0.7 s of simulation time also run on 2 nodes with 16 dual 2.6 GHz processors each and considering that finer grid and time step sizes are used is 1.5 hours.

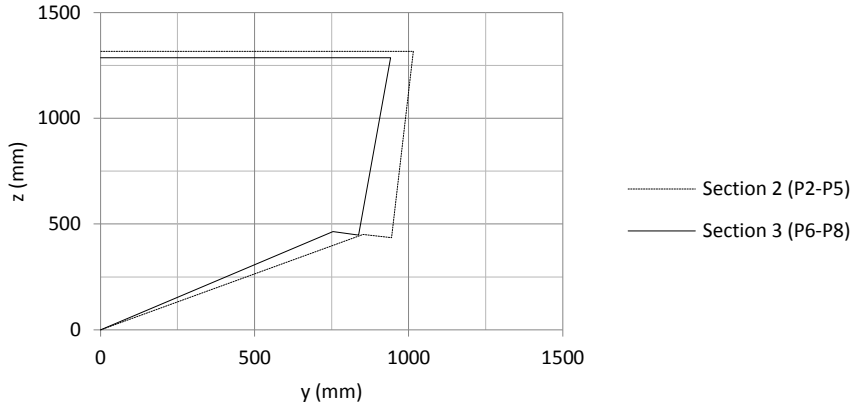

Figure 77 - Sketch of 2D transverse hull sections at the longitudinal position of sensors P2 - P5 and P6 – P8

5.2.2.1 Comparison between 2D and 3D solutions

Figure 78 compares the time histories of acceleration at LCG and the keel point of sections 2 and 3 obtained from the 3D simulation with the vertical acceleration history of the corresponding 2D sections. As can be seen, the accelerations in forward part of the hull, i.e. at sections 2 and 3, are larger and the rise times shorter when compared to the acceleration at the LCG. This can be explained by looking at the orientation of the boat when it impacts the water and subsequent pitch rotational motion. For this particular case of 3° initial trim angle and considering the bow-up rotation of the boat during its motion through air (0.1° for case 2 and 0.34° for case 4), the hull bottom area which first touches the water is near row 2. Following initial contact with water, the boat continues to rotate bow up and the aft portion of the hull gradually immerses into the water.

The forward part of the boat, therefore, experiences a more sudden deceleration. The time histories of acceleration of the 2D sections compare well with the acceleration histories at the keel point of sections 2 and 3 in terms of shape and time of maximum acceleration. However, the 2D models underestimate the magnitude of acceleration around the time of peak, with differences being larger for section 3. This is mainly attributed to bow-up rotation of the 3D boat. The increase in deadrise angle from sections 2 to 3 also has some effect – maximum acceleration for section 2 is larger than for section 3.

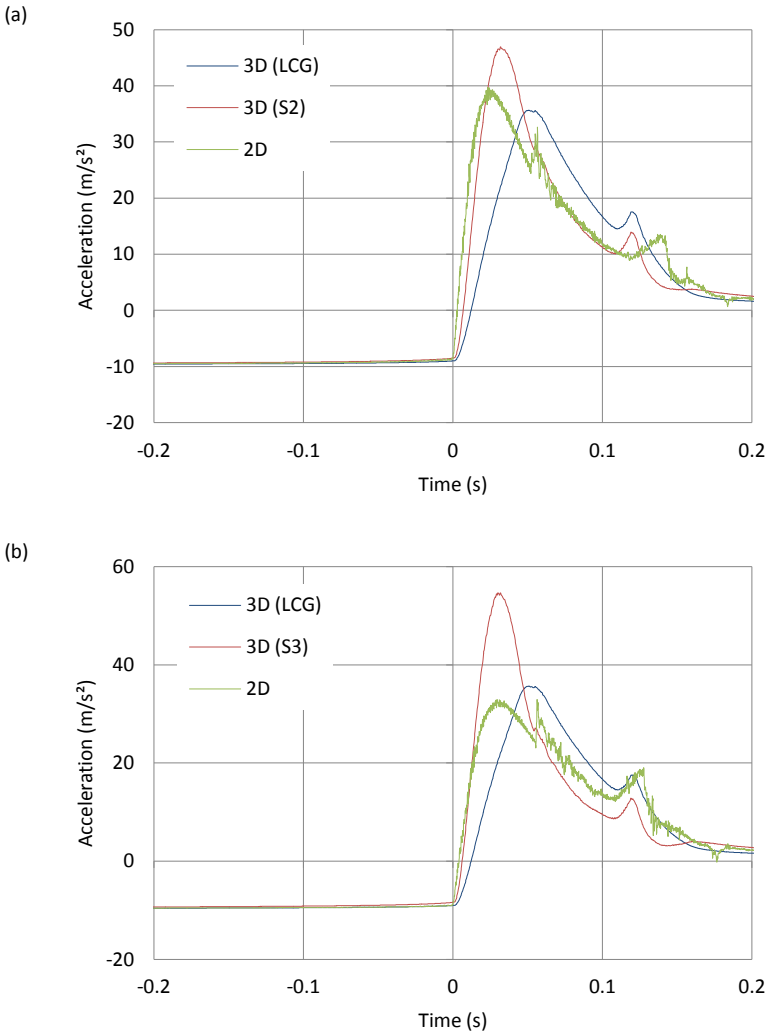

Figure 78 - Comparison of time histories of vertical acceleration at LCG and longitudinal position of sections 2 (a) and 3 (b) from 3D simulations with corresponding vertical acceleration histories of 2D sections, case 4.

The time histories of pressure at P2-P5 and P6-P8 obtained from the 2D and 3D simulations are compared in Figure 79. The pressures at P2 – P4 obtained from the 2D model show relatively good agreement with the 3D results both in terms of shape of time histories and magnitude and timing of peaks, while at P5 the 2D model predicts larger pressure at an earlier time. The P6 – P8 pressure histories show less favourable agreement. These differences are mainly attributed to the bow up rotation of the boat following impact with water, which results in (1) decrease in relative velocity and (2) increase in vertical distance between the sensor and water surface. Figure 80 shows the time histories of vertical entry velocity at the LCG and sections 2 and 3 obtained from the 3D simulation and the velocity histories of the 2D sections. The velocity at the keel point of sections 2 and 3

decreases more rapidly after impact as a result of the bow-up rotation. In the case of section 2, the 2D and 3D (S2) velocity histories agree well during the initial stages of water entry. At the time sensor P5 records the peak, the velocity of the 2D section is 1.09 m/s while that of the 3D hull is 0.92 m/s – difference of 16.3%. The differences in vertical entry velocity at the time sensors P2, P3 and P4 record the peak are 0.4%, 1.1% and 6.8%. The vertical entry velocity histories for section 3 show even larger differences, particularly in the later stages of impact.

The difference in the timing of P6 – P8 peaks is also partly due to the fact that, because the keel starts to curve upwards in the forward part of the hull, at the time of impact in the 3D simulation, section 3 is positioned slightly higher than section 2 (it takes longer for the sensors to reach the free surface in the 3D simulation). In the 2D simulations the drop height is set equal to the minimum vertical distance to match the impact velocity and as a result the peaks are recorded earlier in time. The fact that in 3D the transverse section is not perfectly vertical will also have some effect.

The comparisons between the 2D and 3D simulations for case 2 are similar.

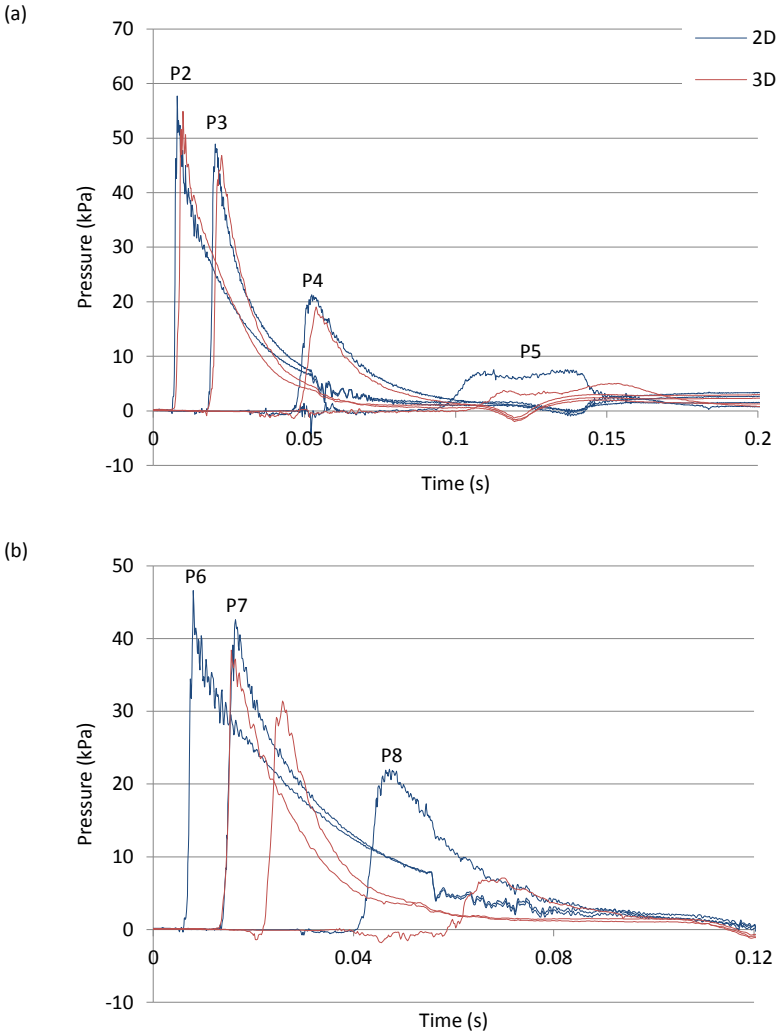

Figure 79 - Comparison of time histories of pressure at P2-P5 (a) and P6-P8 (b) computed using the 2D and 3D models, case 4.

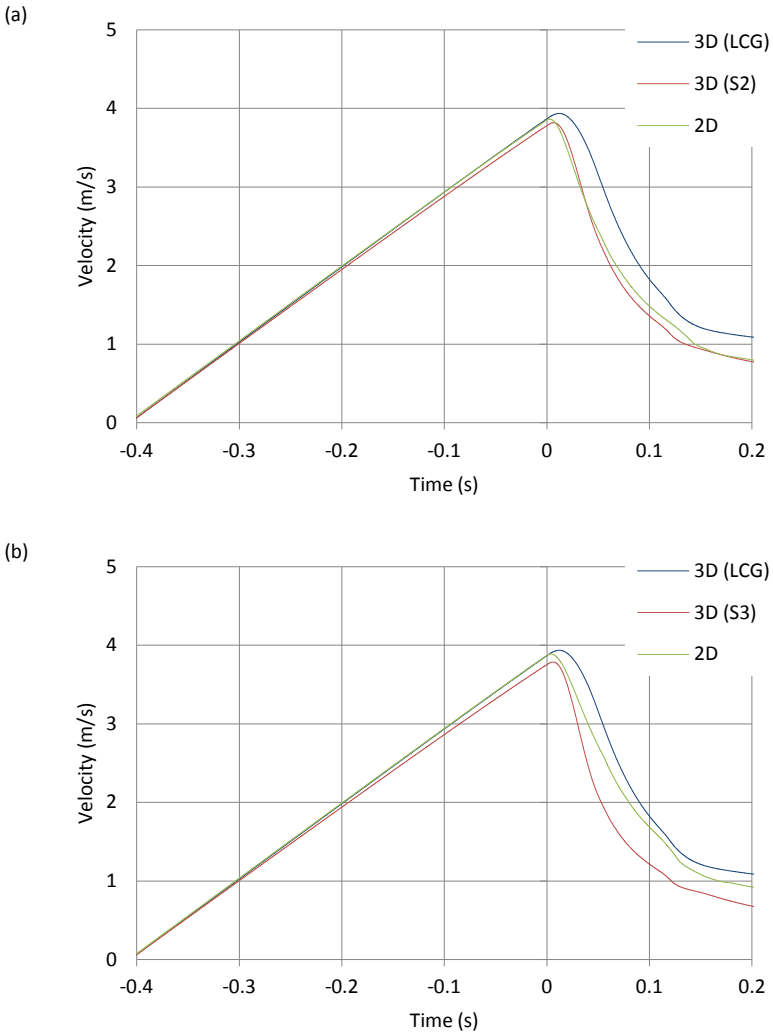

Figure 80 - Comparison of time histories of vertical entry velocity at LCG and longitudinal position of sections 2 (a) and 3 (b) from 3D simulation with vertical entry velocity histories of 2D sections, case 4

5.2.2.2 Effect of spray rails

Figures 81 and 82 compare the time histories of acceleration and pressure for sections 2 and 3 with and without spray rails. The spikes seen in the acceleration and pressure time histories for the sections with spray rails at time ≈ 0.12s for section 2 and time ≈ 0.038s and 0.12s for row 3 are purely numerically induced and occur when the water that separates from the spray rail impacts the hull bottom surface and forms a cavity. This instability is thought to be due to the fact that the computation is 2D with symmetry conditions applied on the front and back faces of the domain, which means that this region is infinitely long whereas in reality these cavities are of three-dimensional nature. Furthermore, in these simulations the fluids, air and water, are modelled as incompressible and accounting for compressibility effects, particularly those of air, should improve the solution and also provide better representation of reality. Nevertheless, this happens in the later stages of the impact event whereas the interest here is more in the early stages and the effect of spray rails on the pressures. As can be seen, the pressures at P3 and P7 and to a lesser extent P2 and P6 for the sections with spray rails show a second peak which is not observed in the pressures for the sections without spray rails and further shows that the second peak seen in the experimental

measurements is caused by the spray rails. The acceleration histories also show a spike at the time of the second peak, which is also observed in the raw acceleration signals in Figure 55.

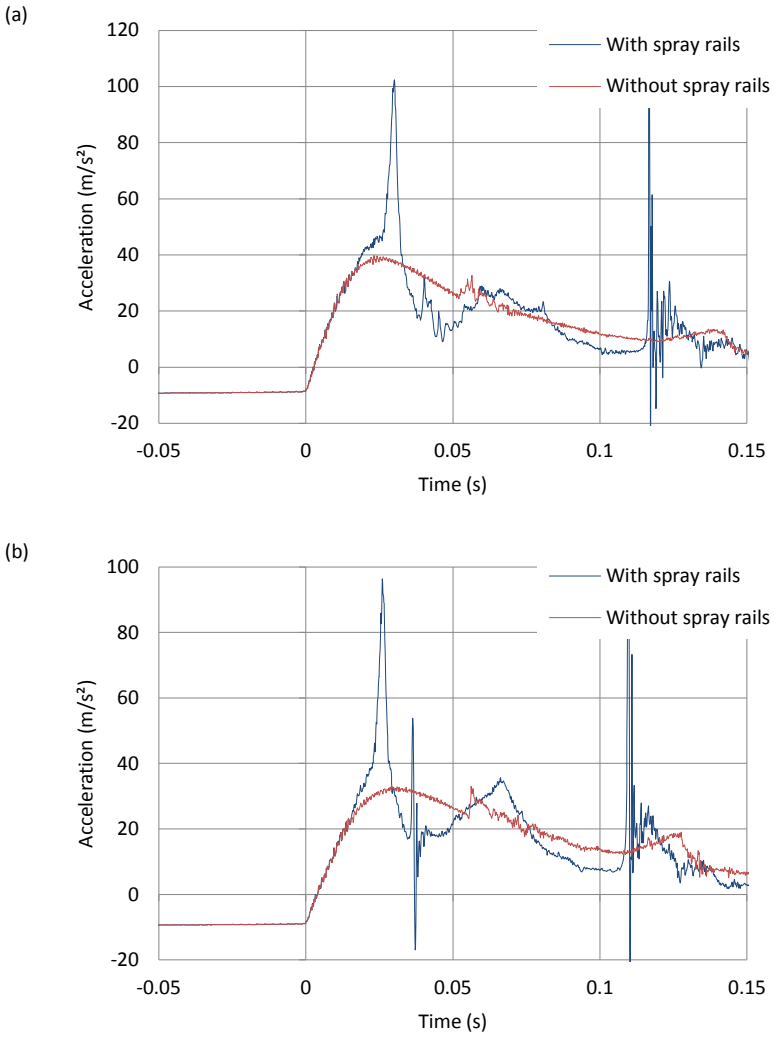

Figure 81 - Comparison of time histories of acceleration for sections 2 (a) and 3 (b) with and without spray rails.

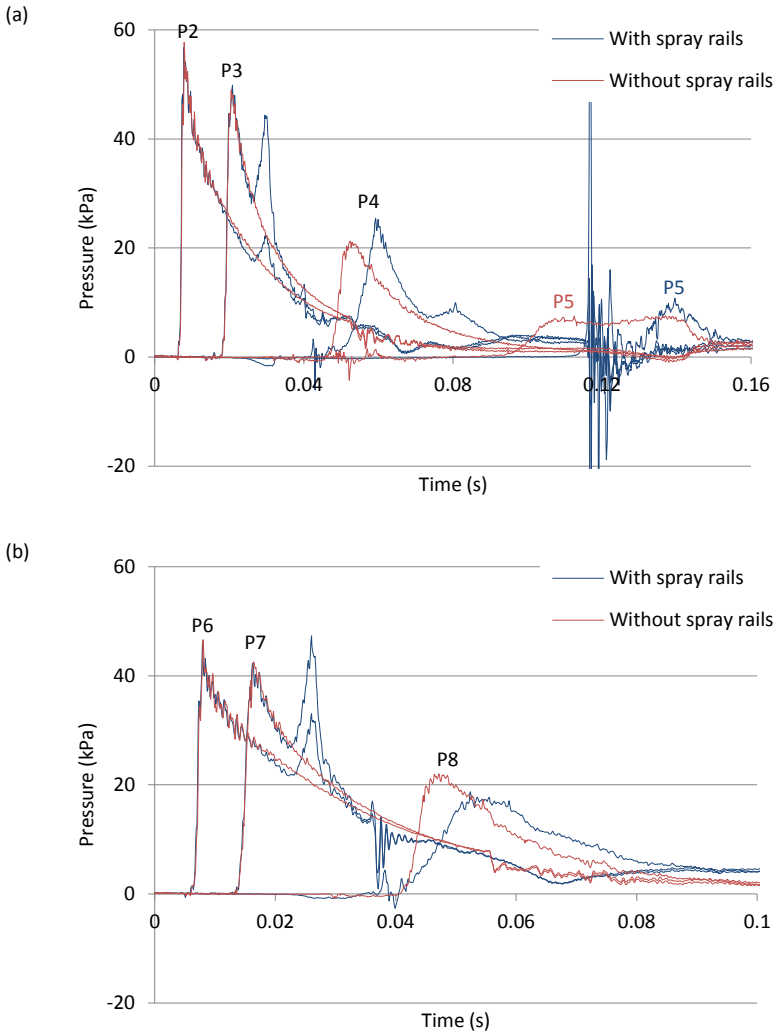

Figure 82 - Comparison of time histories of pressure for sections 2 (a; P2-P5) and 3 (b; P6-P8) with and without spray rails.

5.3. Summary

In this chapter, the loads experienced by a high-speed planing craft as it falls freely onto the water and the related responses are investigated using full-scale tests and numerical simulations. The full-scale tests and data processing procedure are described and characteristic results are presented and discussed. Numerical simulations of the full-scale drop tests (both 3D hull and 2D transverse hull sections) were performed using Star CCM+. The 3D numerical results are compared with the experimental measurements for validation. Comparisons between the 2D and 3D solutions are also performed and the effect of spray rails is investigated. The main conclusions drawn are:

- The signals from 'equivalent' drops, i.e., same drop height and initial trim angle, are found to compare relatively well both in terms of shape and magnitude and gives more confidence in the measurements. The signals recorded at symmetric locations on port and starboard sides also show reasonably good agreement.
- The spray rails are found to have a significant influence on the impact pressures and panel strains. More specifically, the pressures recorded by the sensors located near the spray rail are characterised by a double peak with the magnitude of the second peak being generally

greater than that of the first. The strain signals also show a large magnitude peak at this time. This secondary rise in pressure and strain occurs when the spray root reaches the flat spray rail (zero effective deadrise) and a high pressure is generated which propagates backwards towards the keel and as a result the panel deflects further. Numerical simulations of water impact of 2D transverse hull sections with and without spray rails further confirm this explanation.

- The impact velocity and maximum acceleration in the cockpit and at the bow increase with increasing drop height, while the acceleration rise time decreases. The magnitude of pressures and strains also increases with drop height and the peaks are recorded earlier in time. The numerical results show the same trends.
- The trim angle with which the craft impacts the water surface has a significant influence on the acceleration rise time. It is found that the rise time increases (i.e. less severe impact) with trim angle (i.e. more bow down). This has been attributed to be partly due to the higher deadrise angle and smaller impact area in the forward part of the hull and partly due to the increased gradual wetting with increasing trim angle (at zero degree trim the boat is more or less horizontal when it impacts the water whereas for larger trim angles the bow area impacts the water first and the boat experiences a bow up rotation, i.e. gradual immersion). The effect of trim angle on the magnitude of pressure is, however, not significant.
- The computed time histories of pitch motion and acceleration (3D boat) agree well with the experimental measurements indicating that the rigid body behaviour of the boat is well captured. However, the pressure histories show differences both in terms of shape and magnitude. This illustrates the difficulties in modelling a real hull as opposed to a relatively simple panel or wedge.
- For the 2D transverse hull sections studied, it is shown that 2D simulations can be used to represent the loads on a 3D hull free falling into the water provided that the entry velocity and orientation (deadrise angle and trim angle) are comparable.

Chapter 6. Rough water trials, drop tests and classification societies' rules and standards

In this chapter the acceleration and pressure measurements from the rough water trials are compared with the predictions based on the ISO standard and the DNV GL and LR rules to assess the suitability of the design loads used in current practice. Furthermore, the pressure and strain measurements from the rough water trials are compared with the drop tests measurements in an attempt to investigate whether the slamming loads experienced by a planing craft as it travels at high speed in waves and the resulting structural responses can be approximately estimated from the loads and responses for the craft as it falls freely into the water. The issues encountered and way forward are discussed.

6.1. Classification societies' rules and ISO standard

In this section, acceleration and pressure predictions from two classification society rules and the ISO standard for small hull construction ISO (2008) are compared against the full-scale measured data to assess the suitability of the design loads used in current practice. The classification society rules chosen are the DNV GL rules for classification of high speed and light craft (DNV GL, 2015) and Lloyd's Register rules and regulations for the classification of special service craft (Lloyd's Register, 2016). The methods and formulae used for calculating the design slamming pressures on craft bottom panels in each of these sets of rules are given in Appendix D. In general, the following comments can be made.

- The governing factor in the formulae for calculating the design slamming pressure is the design vertical acceleration at the craft's longitudinal centre of gravity (called the dynamic load factor in the ISO standard). The formula adopted by each method for calculating the design vertical acceleration is similar to the Savitsky & Brown (1976) formula. It is mainly expressed in terms of the craft particulars (length, beam, displacement and deadrise angle), speed and significant wave height (except for the ISO standard which takes into account the sea conditions when calculating the pressure through a 'design category factor'). The formula given in the LR rules also takes into account the running trim angle.
- The ISO standard gives an additional formula for calculating the design vertical acceleration at LCG which can be deliberately used if the value given by the Savitsky & Brown (1976) formula is greater than 3g (otherwise the Savitsky & Brown (1976) formula shall be used). It is simply expressed in terms of craft displacement and speed.
- For a particular craft i.e., constant geometrical characteristics, the accelerations increase with increasing forward speed and significant wave height - see Figure 83 - and decreasing craft displacement. The LR accelerations also vary with running trim angle as shown in Figure 84.
- The design bottom slamming pressure increases with vertical acceleration at LCG.
- The magnitude of the design slamming pressure varies along the length of the hull according to the longitudinal distribution factor shown in Figure 85. The ISO standard and

DNV GL rules also account for the size of the panel or stiffener being considered – larger design areas will have lower average uniform pressures. The DNV GL rules further account for the deadrise angle at the transverse section considered – pressure decreases with increasing deadrise angle.

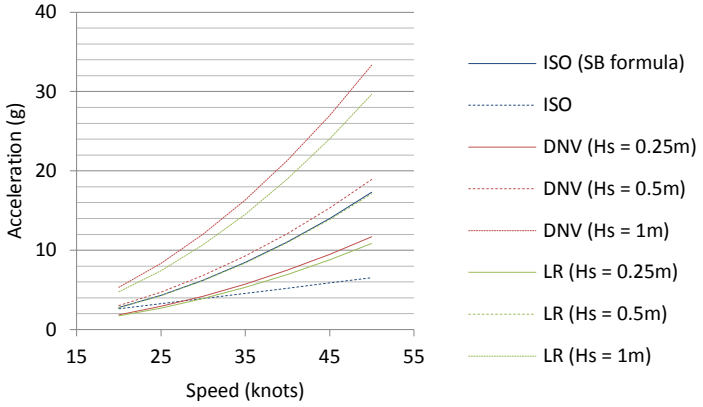

Figure 83 - Effect of forward speed and significant wave height on the vertical accelerations at LCG predicted with the ISO, DNV GL and LR formulas. The trim angle in the LR predictions is 3°.

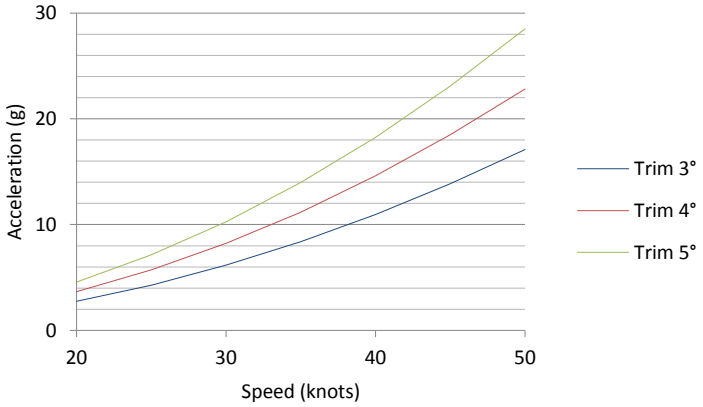

Figure 84 - Effect of trim angle on the LCG vertical acceleration based on the LR formula. The significant wave height is 0.5m.

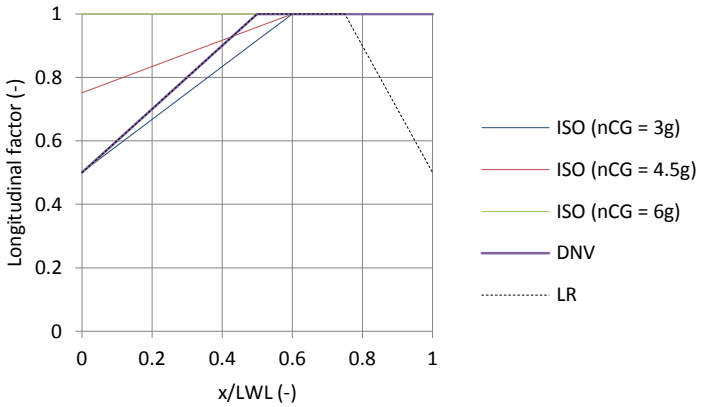

Figure 85 - Longitudinal pressure distribution factor. x/LWL = 0 and 1 are respectively the aft and for end of LWL.

Comparisons are made for the vertical accelerations measured in the cockpit and pressures measured on the panels where sensors P2 and P3 and sensors P6 and P7 are installed and the

corresponding starboard side pressure measurements – see Figure 46 – which are here referred to as panels A and B, respectively. The particulars of the craft required to calculate the slamming pressures were extracted from the CAD model. The ISO standard and class rules often define minimum and/or maximum values for certain particulars, which were followed. Figure 86 compares the maximum vertical cockpit accelerations measured in runs 1, 2 and 4 with the accelerations based on the formulas given in the ISO standard and the DNV GL and LR rules. The ISO accelerations include both the accelerations based on the Savitsky & Brown (1976) method and the accelerations based on the simple formula, labelled as ISO (SB) and ISO respectively. These two accelerations are plotted separately to assess which formula correlates better with the measurements. In reality, one or the other is used. The ISO accelerations are considered to be close to the single amplitude acceleration at the relevant frequency for a certain period of time, whereas the LR accelerations are the average of the $1/100^{th}$ highest accelerations. The DNV GL rules do not explicitly state the statistical level. Dr Anders Rosén states that the DNV GL accelerations represent the average of the largest 1/100 accelerations (A Rosén 2017, personal communication, 30 November). The ISO standard and DNV GL rules specify maximum limits on the design vertical acceleration of 7g and 6g, respectively. In Figure 86, predictions less than or equal to the maximum limit are represented by solid columns, while predictions that exceed the maximum limit are represented by stacked columns with the empty portion representing the difference between the predicted value and maximum limit. The LR rules do not specify maximum limits.

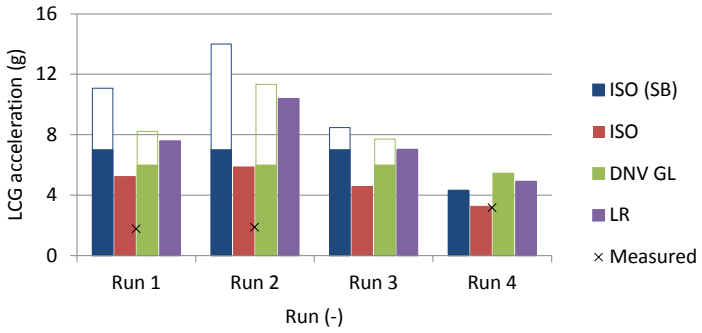

Figure 86 - Comparison of maximum vertical accelerations measured in the full-scale trials with ISO, DNV GL and LR acceleration predictions. ISO (SB) refers to the predictions made with the Savitsky & Brown (1976) (eq. 17) while ISO refers to the predictions made with the simple formula. The trim angle is 3° (LR).

It must be emphasised that direct comparisons between predictions and between predictions and measurements should be made with care because each method refers to a different definition of acceleration. For instance, the LR accelerations are the average of the $1/100^{th}$ highest accelerations whereas the measurements are maximum values. Furthermore, these methods are intended for the lifetime of the craft rather than particular runs. The accelerations predicted by each method are largest for run 2 – highest speed - and smallest for run 4 – slowest speed. The ISO accelerations based on the Savitsky & Brown (1976) method are larger than the DNV GL and LR accelerations for runs 1 – 3 but smaller for run 4. This is due to the fact that the ISO formula does not take into account the sea conditions; these are accounted for when calculating the design slamming pressure through a constant factor. The measured maximum accelerations are significantly lower than the predictions, particularly for runs 1 and 2 - high forward speed. For instance, the ISO accelerations based on the Savitsky & Brown (1976) method are about 6.3 and 7.5 times the measured values for runs 1 and 2, respectively, while the DNV GL accelerations are about 4.6 and 6.0 times the measured

values, respectively. The predictions for run 4 are more realistic with the ISO and DNV GL predictions being about 1.4 and 1.7 times the measured values, respectively. The accelerations predicted with the formula given in the ISO standard expressed in terms of speed and craft displacement show the best agreement with the experimental measurements. Two possible reasons why the predictions based on the Savitsky & Brown (1976) method differ greatly from the measurements are,

- The test conditions are outside the ranges of applicability of the Savitsky & Brown (1976) method. In particular, the significant wave heights are too low (range: $0.2 \leq H_s/B \leq 0.7$) while the speed (range: $2 \leq V/\sqrt{L} \leq 6$) is too high in runs 1 – 3.
- The Savitsky & Brown (1976) method assumes that the acceleration peaks are exponentially distributed and, hence, the acceleration at a particular statistical level, e.g. average of the largest $1/10^{th}$ or $1/100^{th}$ peak accelerations can be calculated from the average of the peak accelerations. However, several studies have shown that the exponential distribution does not accurately represent the data, see for example McCue (2012), Bowles & Soja (2014) and Razola et al. (2016). Bowles & Soja (2014) compared the average peak accelerations and average $1/10^{th}$ highest peak accelerations predicted by the Savitsky & Brown (1976) formula with model test data. The exponential distribution was used for extrapolation. The predicted average peak accelerations were found to correlate fairly well with the measured data; however, the Savitsky & Brown (1976) method was found to predict significantly higher accelerations when assuming an exponential distribution. It was concluded that the method is valid for its respective statistical measure, i.e., average peak accelerations; however, the exponential distribution is not appropriate for extrapolation. Razola et al. (2016) also compared the averages of the largest $1/10^{th}$ and $1/100^{th}$ acceleration peaks calculated directly from samples of simulated peaks with the statistical averages extrapolated from the average peak acceleration following the exponential distribution and the extrapolated values were found to be significantly larger than those derived from data.

Figure 87 shows the design slamming pressure predictions for panels A and B and runs 1 – 4 based on the ISO standard and DNV GL and LR rules. The results are presented in the same manner as the accelerations in Figure 87 regarding maximum limits. It must be noted that the statistical level used to describe the accelerations (e.g. average of $1/100^{th}$ etc.) is also the resulting statistical level of the design slamming pressures (Koelbel, 1995). The three methods predict similar design slamming pressure for panels A and B for all runs which is to be expected as the geometrical characteristics of these two panels are not that different.

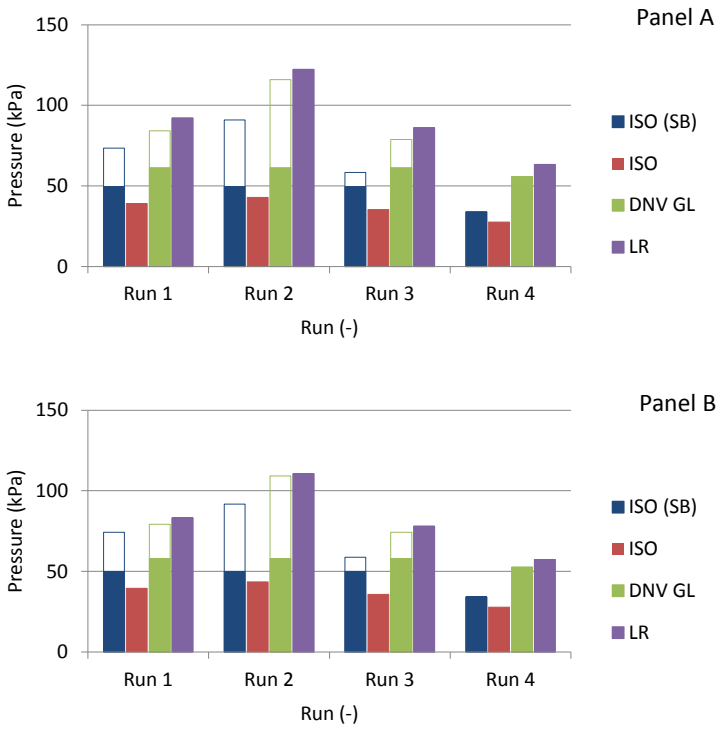

Figure 87 - ISO, DNV GL and LR pressure predictions for panels A and B, runs 1 - 4.

The design slamming pressures represent average uniform pressures over the area of the structural component being considered. The area of panels A and B is 0.262 m^2 and 0.253 m^2, respectively. On the other hand, the statistical quantities derived from the measured data, i.e., the averages of the largest $1/3^{rd}$ and $1/10^{th}$ peak values, most probable extreme values and so on, are based on maximum pressures measured by the sensors with a diaphragm area of 23.8 mm^2. To compare the measured and predicted pressures, the measured values are scaled using the pressure reduction coefficient of Allen & Jones (1978). This coefficient relates the maximum pressure P_M acting on the area of the structural component considered A_D to the average pressure P_D on the same area, and decreases with increasing area of the structural member (presented as a fraction of the reference area A_R) as shown in Figure 88 taken from figure 17 of Allen & Jones (1978). The reference area is defined as that approximate amount of the hull bottom involved in a major impact and was introduced to enable direct comparisons of data from different hulls. The reference area of the C-Target 9 is 4.45 m^2 and the ratio A_D/A_R is approximately 0.058 for both panels A and B. Thus, from Figure 88, the pressure reduction coefficient $K_D = P_D/P_M$ is 0.32. The experimental results presented in Chapter 4 are multiplied by this coefficient before comparing with the predictions.

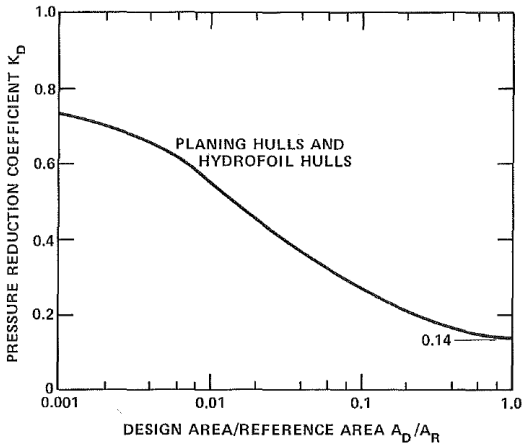

Figure 88 - Variation of pressure reduction coefficient with design area. Taken from Allen & Jones (1978).

Figure 89 compares the pressures measured on panels A (P2, P3, P12 and P13) and B (P6, P7, P16 and P17) in runs 1 – 4 with design slamming pressures based on the formulas given in the ISO standard and DNV GL and LR rules. The measurements include the averages of the largest $1/10^{th}$ peaks values, maximum values, and the Weibull and generalized Pareto most probable extreme values and are multiplied by the pressure reduction coefficient (= 0.32). The predicted values in Figure 89 take into account the maximum limit on the design vertical acceleration in order to represent the design slamming pressure that would be used by the designer. As can be seen, the ISO standard and DNV GL rules predict pressures that are significantly lower than the measured maximum pressures and estimated most probable extremes, for both panels and all runs but more particularly runs 2 – 4. The largest differences are seen for the ISO pressures with the accelerations calculated using the simple formula. The LR rules predict pressures that are higher than or comparable to the measured maximum pressures and estimated most probable extremes for runs 1 and 2 – high forward speed – while for runs 3 and 4 the predictions are lower than the measured data but greater than the ISO and DNV GL pressures. The large differences between the LR and the ISO and DNV GL pressure predictions are mainly due to the fact that the LR rules do not impose any maximum limits on the design vertical accelerations.

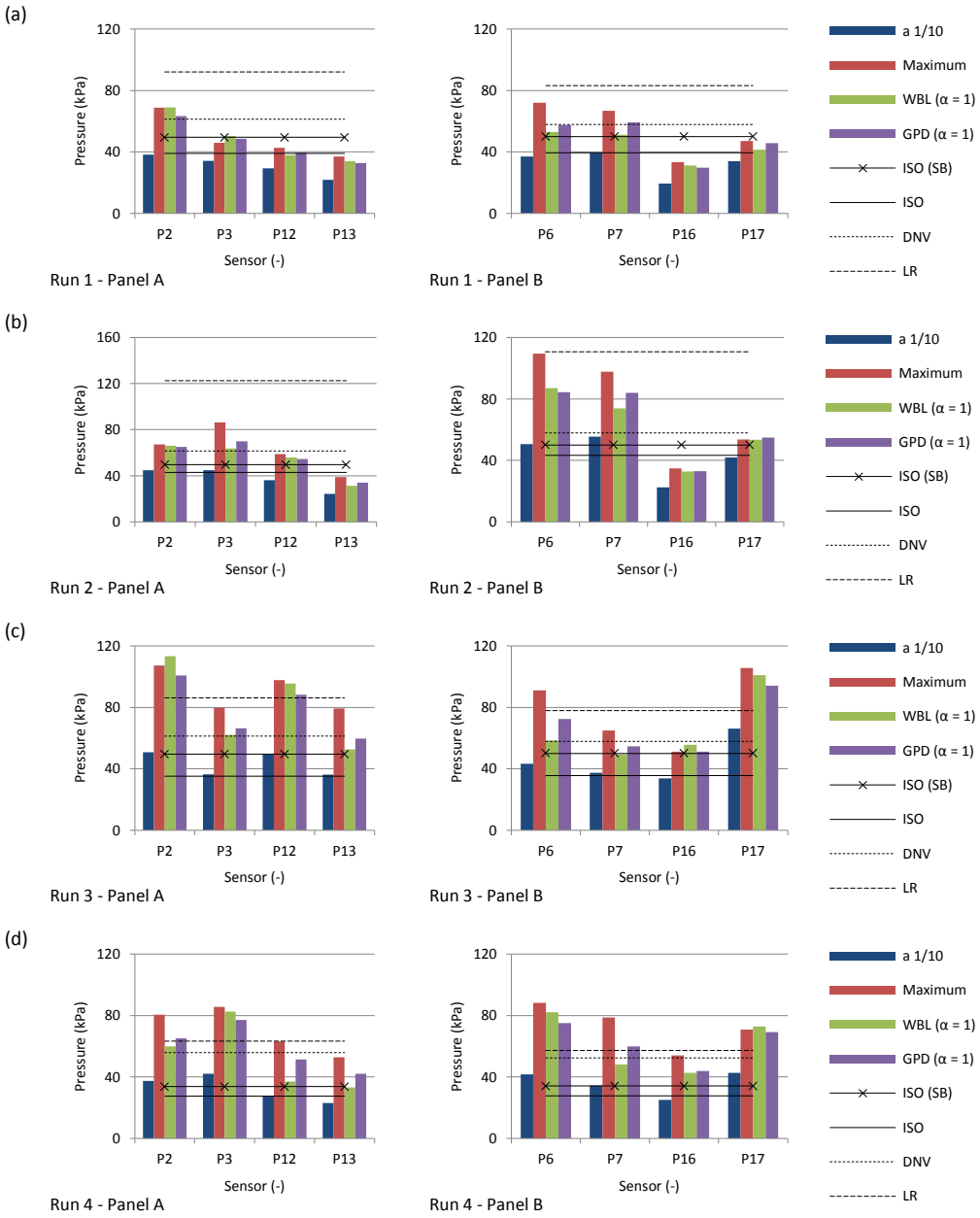

Figure 89 - Comparison of measured pressures with ISO, DNV GL and LR pressure predictions for panels A (1st column) and B (2nd column), runs 1 – 4 (a – d).

The minimum required thickness for panels A and B according to the ISO standard and DNV GL and LR rules for runs 1 – 4 are given in Table 12. The material is Aluminium 5083-O. The thickness of the hull bottom plating of the C-Target 9 is 8 mm, which satisfies the ISO, DNV GL and LR minimum thickness requirements for both panel and all runs, except for the LR requirement for panel A and run 2. However, it can be observed from Figure 89, that the LR pressures are significantly higher than the measured pressures for this particular panel and run.

Table 12 - Minimum required thickness for panels A and B, runs 1 - 4.

	Panel A, mm			Panel B, mm		
	ISO	DNV	LR	ISO	DNV	LR
Run 1	4.5	5.3	7.1	4.3	5.0	6.5
Run 2	4.7	5.3	8.2	4.6	5.0	7.5
Run 3	4.2	5.3	6.9	4.1	5.0	6.3
Run 4	3.8	5.1	5.9	3.7	4.8	5.4

6.2. Comparisons between rough water trials and drop tests

In this section, the pressure and strain measurements from the rough water trials are compared with the drop tests measurements to investigate whether the slamming loads experienced by a planing craft as it travels at high speed in waves and the resulting structural responses can be approximately estimated as the loads and responses for the craft as it falls freely into the water. The loads and responses experienced in the rough water trials are represented by a number of individual impact events manually chosen from runs 1, 2 and 4. The cockpit vertical acceleration signal was used for choosing the events and the criteria were sharp rise and peak greater than the root mean square value of the signal. The total number of impact events is 55; 18 from runs 1 and 2, respectively, and 19 from run 4. The measurements from drops 2 – 6 were chosen to represent the drop tests. Figures 90 - 93 show examples of the comparisons between the measurements from the rough water trials and drop tests where, for each signal, the maximum pressure or strain from each impact event and drop test are plotted against the corresponding maximum cockpit vertical acceleration. The asymmetry of the impacts can be again observed in these scatter plots where the peaks recorded on the port side are generally larger than those recorded at corresponding locations on the starboard side. Figures 96 - 101 in Appendix E show examples of the acceleration, pressure and strain signals recorded in these chosen events. These results further illustrate the random and nonlinear nature of hull-water impacts, namely that the shape, magnitude and development of the pressure distribution and hence the resulting responses are different for each impact event.

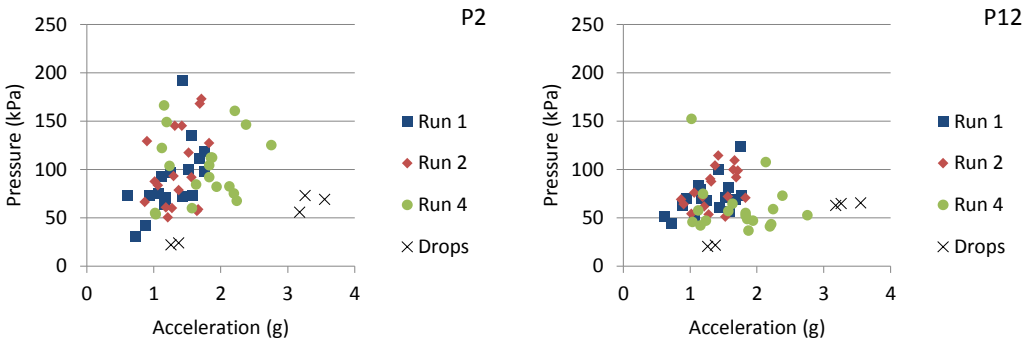

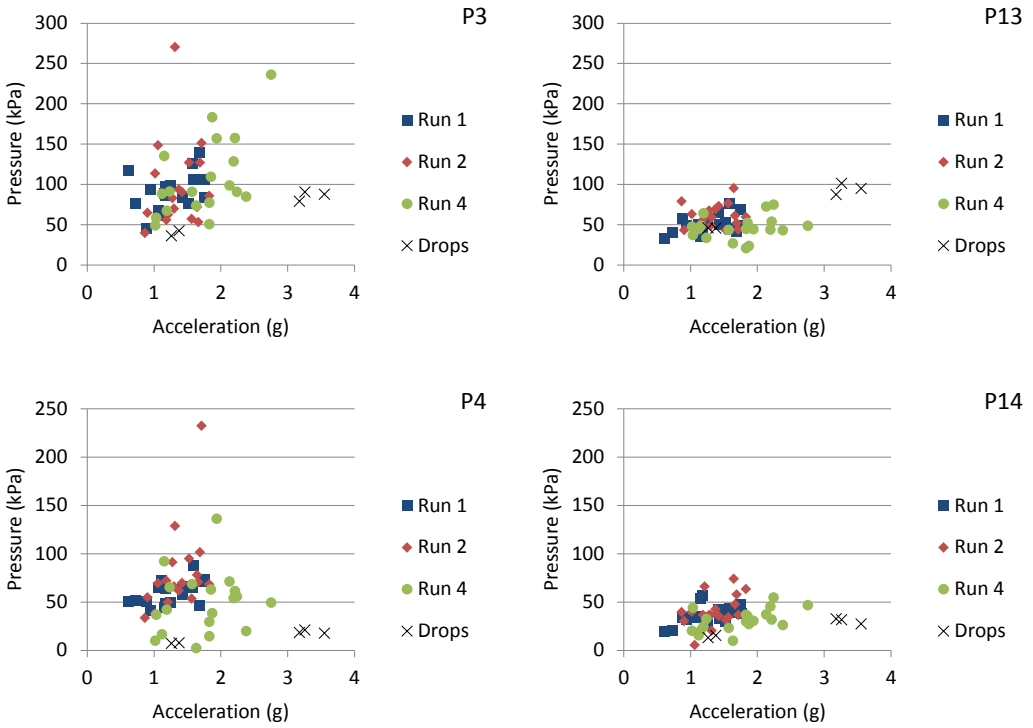

Figure 90 - Comparison of P2 – P4 and P12 – P14 (2nd row of sensors) maximum pressures from the impact events in run 1, 2 and 4 and drop 2 – 6.

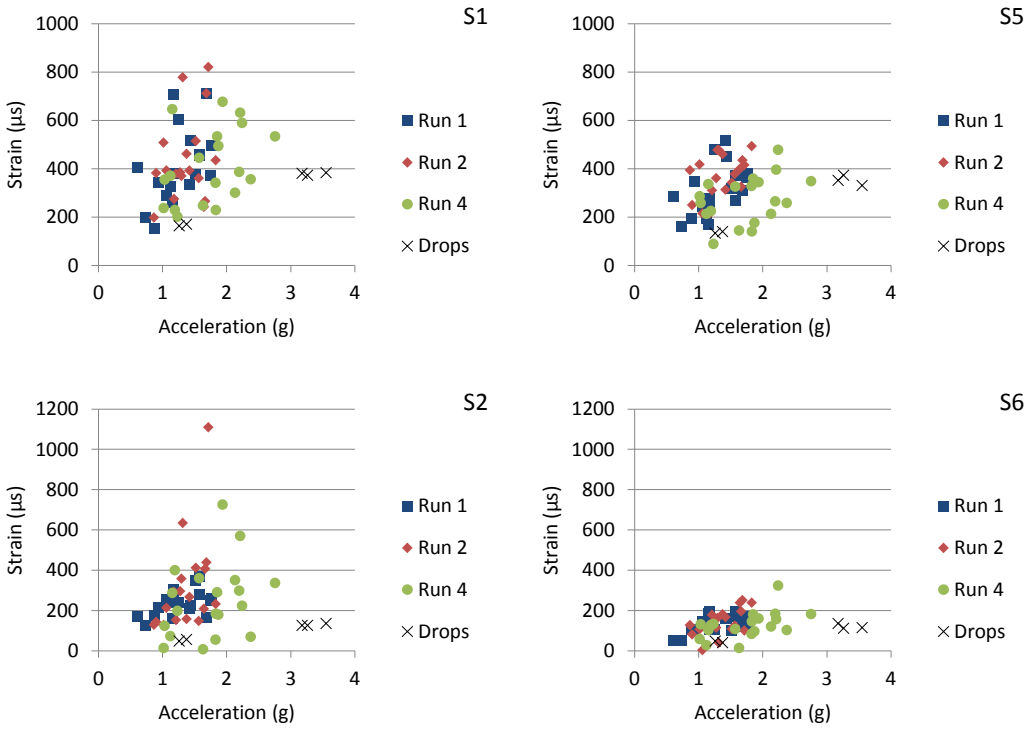

Figure 91 - Comparison of S1, S2, S5 and S6 (2nd row of sensors) maximum strains from the impact events in run 1, 2 and 4 and drop 2 – 6.

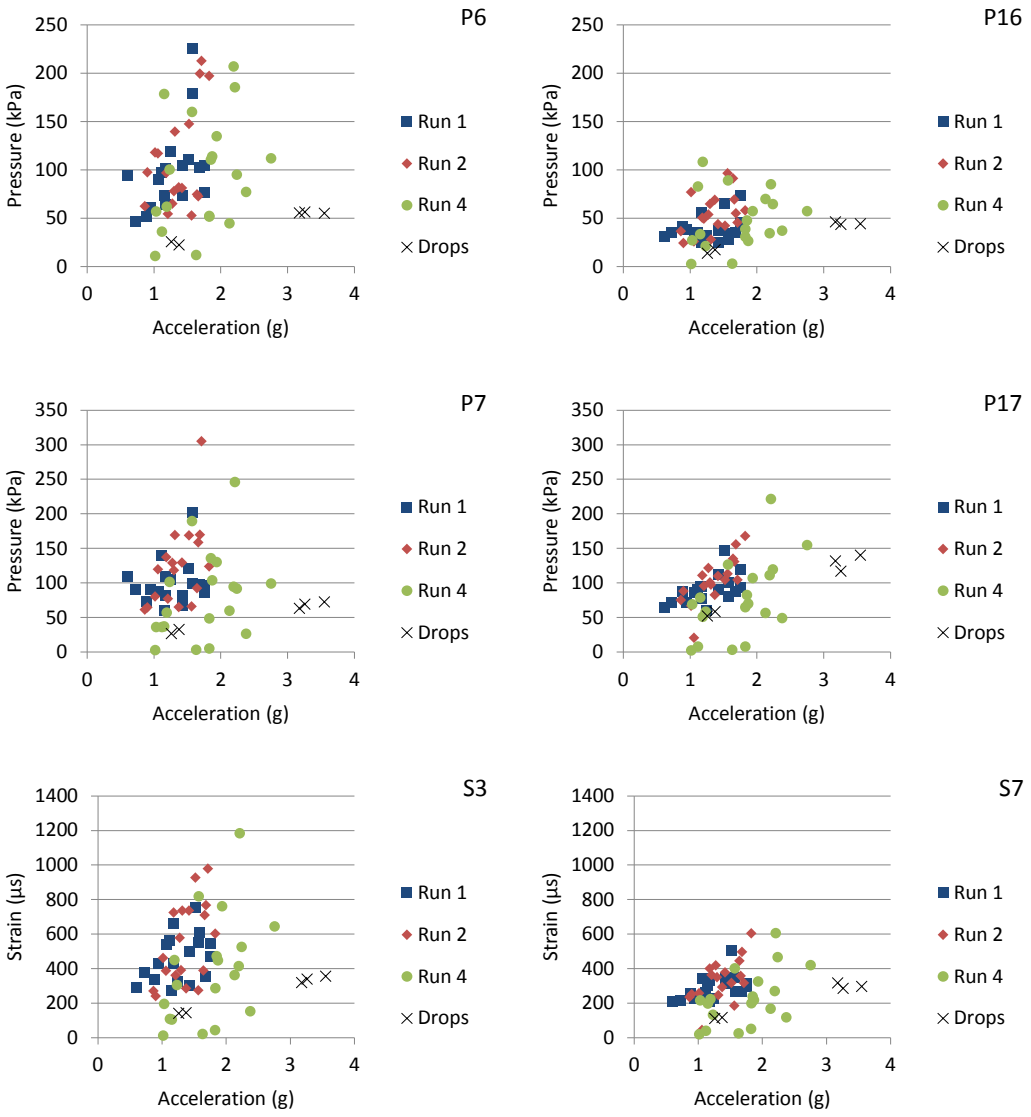

Figure 92 - Comparison of P6, P7, P16 and P17 maximum pressures and S3 and S7 maximum strains (3rd row of sensors) from the impact events in run 1, 2 and 4 and drop 2 – 6.

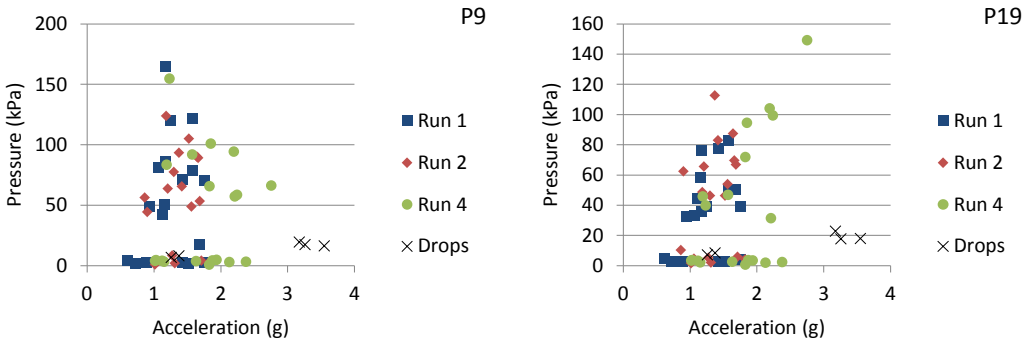

Figure 93 - Comparison of P9 and P19 (4th row of sensors) maximum pressures from the impact events in run 1, 2 and 4 and drop 2 – 6.

The maximum pressures and strains from the rough water trials show quite significant scatter and do not correlate very well with the maximum accelerations, particularly the peaks recorded on the port side. It can also be observed that the maximum pressures and strains measured in the rough

water trials, i.e., with forward speed, are generally larger than the drop tests measurements for similar maximum vertical cockpit acceleration. The main reason for the large scatter in the rough water trials data and poor correlation with the maximum accelerations is thought to be due to the fact that in the scatter plots each sensor measurement is considered independently. The global response of the craft is a result of the complete pressure distribution acting on it, which is quite nonuniform, and pressure sensors only provide measures of the pressure distribution at discrete locations on the hull bottom. Similarly, each strain gauge represents the response of only one hull bottom panel. Hayman et al. (1991) also observed poor correlation between the maximum local panel shear strains recorded on a coastal rescue craft while in service and corresponding maximum global vertical accelerations. In particular, the strains recorded in severe slamming events with large accelerations were found to be too low. It was concluded that '*the slams that produce the largest global accelerations affect either a much larger area of the hull than the instrumented panel, or are centred on a different panel from the instrumented one*'. It can also be observed from Figures 96 - 101 that the very large pressure peaks generally have very short duration and limited effect on the structural response; see for example signal P2 in run 1 (t = 1.7s) and signals P6 and P7 in run 1 (t = 18.9s). These results strongly suggest that maximum pressures or strains measured at discrete locations are not sufficient to completely describe hull loads and responses experienced in slamming impacts. Instead, the complete pressure distribution such as the average pressure over the hull bottom area, or the response of all the panels on which the loading acts, should be considered.

Methods for calculating the average pressure over the hull bottom from pressure sensor measurements have been presented in Allen & Jones (1978) and Rosén (2005). In their experiments Allen & Jones (1978) calculated an average pressure over the instrumented hull bottom area simply by summing the pressure signals and dividing by an assumed representative area for each sensor. The spatially averaged pressures were found to correlate better (with less scatter) with maximum bending strains at the panel centre than the pressures from a single pressure sensor located closest to the strain gauge. Rosén (2005) developed a method for reconstructing the pressure distribution on the hull bottom surface from discrete point measurements. The average pressure over a particular area of the hull structure can be then calculated from the reconstructed distribution. The impact forces and moments derived by integrating the reconstructed pressure distribution were found to correlate well with the inertia forces and moments derived from the acceleration measurements and further suggest that the correlation with the maximum accelerations should improve with considering the complete pressure distribution.

The large scatter in the rough water trials data and poor correlation with the acceleration is also partly due to the fact that only the acceleration in vertical direction is considered. That is, the global response of the craft to each wave impact is assumed to be the same and can be represented using only the cockpit acceleration in the vertical direction. Riley et al. (2014) however, from analysis of large sets of high-speed craft acceleration data (vertical, longitudinal and pitch acceleration signals), found that the impacts can be grouped into three main types based on the sequence of events prior to impact. All three types result in vertical impact forces but they exhibit varying degrees of surge and pitch. Figure 94 shows the distribution of maximum bow to cockpit vertical acceleration ratio for the impact events from the rough water trials. The ratio is positive for all impacts meaning that the craft experiences a bow-up moment (pitch motion) when it impacts the water. It is also seen that the ratio from about 2.5 to 6.5 indicating varying degrees of bow-up rotation and further suggests that it is not sufficient to only consider the vertical cockpit acceleration to represent the global craft

response. The ratio for the drop tests (green line in Figure 94) is about 2.6, much lower than the typical ratio for impacts from the rough water trials. This is to be expected and is most likely due to the high forward speed in the rough water trials – when the craft impacts an oncoming wave at high forward speed it will experience a larger bow-up moment than when it is dropped onto a calm water surface. This, however, should not inhibit the prospects of finding a correlation between the two tests. The idea is to find (equivalent) drop test conditions that would result in impacts similar to those experienced by the craft when it is travelling at a particular speed and in a particular sea state. For instance, a larger drop height and a lower initial trim angle (as seen from the parametric study in section) may be required to obtain equivalent conditions. The required equivalent drop test conditions may be explored using for instance the 3D numerical model presented in section 5.2.1.

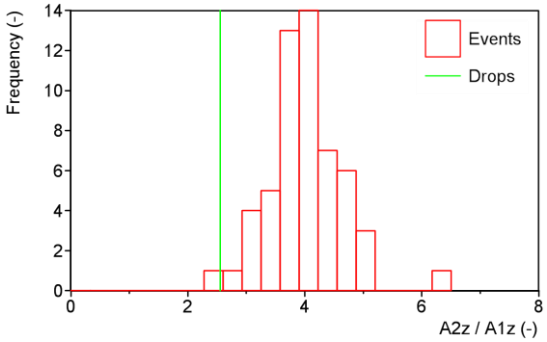

Figure 94 - Histogram of bow to cockpit vertical acceleration ratios for the impact events from the rough water trials. The mean of the bow to cockpit acceleration ratios for the drop tests is also included; the standard deviation is ±0.04.

6.3. Summary

In this chapter, the accelerations and pressures measured in the rough water trials are compared with the ISO, DNV GL and LR predictions to assess their suitability. Preliminary comparisons between the rough water trials and drop tests measurements are also made to examine the relationship between the two tests. The main conclusions drawn are:

- The measured accelerations are significantly lower than the predicted values, particularly for high forward speed runs. This is most likely because the test conditions are outside the ranges of applicability of the Savitsky & Brown (1976) method and the assumption of the acceleration peaks being exponentially distributed.
- Despite the measured accelerations being significantly lower than the predicted values, the pressure predictions based on the ISO standard and DNV GL rules were found to be significantly lower than the measured maximum values and estimated most probable extremes, while the LR pressures are higher for the high forward speed runs and lower for the moderate speed runs.
- An attempt to examine the relationship between the loads and responses measured in the rough water trials and drop tests is also made. For each signal, the measured maximum pressure or strain in a number of individual impact events from the rough water trials and in each drop test are plotted against the corresponding maximum vertical acceleration in the cockpit. The rough water trials data showed large scatter and poor correlation with the maximum accelerations, which inhibited further investigation into the correlation between the two tests. It is concluded that (1) single point measurements of pressure or strain cannot be used to represent the loads experienced by a craft during a slamming impact or the response of the hull structure and (2) the global response of the craft to slamming impact cannot be represented using only the cockpit acceleration measured in the vertical

direction. Instead, the complete pressure distribution must be considered and other acceleration components such as the pitch and longitudinal acceleration should be considered.

Chapter 7. Discussion

In this thesis the problem of slamming loads and related responses for high-speed planing craft is investigated using numerical simulations and full-scale experiments. The aim of this work is to improve the safety and efficiency of high-speed craft structural designs for realistic operational loads. This chapter discusses the work completed, emphasizing the most significant novel contributions.

7.1. Numerical simulations

A numerical model for simulating the water impact of two- and three-dimensional rigid and flexible structures has been developed and validated with experimental data. The model uses the commercial CFD software Star CCM+ to solve for the flow in the fluid domain and the FE code ABAQUS to solve for the structural response. The use of Finite Volume CFD with the VOF interface capturing method allows for complex geometries, hydroelastic effects and the nonlinear free surface behaviour to be accurately modelled. The nonlinear dynamic response of the structure is solved using the implicit direct-integration method. The SIMULIA Co-Simulation Engine is used for coupling Star CCM+ and ABAQUS. The coupling is two-way to accurately capture the interaction between the fluid and structure.

The impact of a free-falling rigid wedge with water and the constant velocity water entry of a flexible composite panel are studied and the results are compared with the experimental data of Lewis et al. (2010) and Allen & Battley (2015), respectively, for validation. The geometrical characteristics of the studied test sections are relevant to high-speed planing craft. The numerical model is then applied to simulate full-scale drop tests on a 9.6m high-speed planing craft (rigid structure), also conducted within the framework of this thesis, and the results are compared with the measured data. In the development of the numerical model the effect of several numerical and experimental parameters on the solution is investigated.

Slamming impacts are characterised by large pressure gradients, rapidly propagating peaked pressure distribution and complex fluid free surface deformations and require short time steps and fine grids to resolve accurately. Time step and grid convergence studies are performed to assess the sensitivity of the solution to the time step and grid spacing and to find the grid and time step sizes required to accurately resolve the impact. Two different methods were used to assess convergence – the rigid wedge results are assessed by comparing the time histories of acceleration and pressure (shape, magnitude and time of peaks etc.) whilst the GCI method of the ASME standard is used for the flexible panel results with the vertical force impulse chosen as the solution variable. Both methods are considered suitable for assessing solution convergence. It has been found that a cell size of 2.5mm is required near the bottom surface of the impact body to accurately capture the rapidly propagating and highly localized high pressure region at the spray root. The time step size is 0.05ms for the wedge and 0.02ms for the panel. The reason for the smaller time step in the panel

simulations is that the fluid travels at a much higher velocity in constant velocity impacts when compared to free-fall impacts and thus, for the same cell size, smaller time steps are required to maintain a Courant number of less than 1.0 on average. The grid used for the full-scale drop tests simulations is similar in design to those used for in the 2D models (regions of local refinement, prism layers etc.); however, coarser grid cell and time step sizes (10mm and 0.2ms, respectively) had to be used to limit the computational costs.

Most of the experimental water entry studies (free-fall and constant velocity) found in the literature are on 2D test sections and the tank walls (e.g. Lewis et al., 2010) or vertical end plates (e.g. Allen & Battley, 2015) are used to direct the flow along the test section and preserve the two-dimensionality of the test. Three-dimensional simulations were therefore performed to investigate the effect of 3D flow on the wedge kinematics and impact pressures in the case of the rigid wedge, and on the impact pressures and panel deflections in the case of the flexible panel. The effect of the size of the gap between the test section and the tank wall was also investigated for the rigid wedge problem. In both cases and for the test conditions investigated, it was found that the effect of 3D flow on the pressures is negligible and two-dimensional models, which require much less computational resources, can be used to accurately predict the hydrodynamic impact loads. Some differences between the 2D and 3D results were observed for the case with a wide gap between the wedge and tank wall, although small, and shows that the tank walls/ fixed vertical panels are working as intended, i.e., promoting two-dimensional flow. The effect of 3D flow and the suitability of 2D models to represent the loads on a 3D hull is further investigated in Chapter 5 where simulations of drop tests of both the entire 3D hull (modelled as rigid) and 2D transverse hull sections (also rigid) are performed. It is found that, for the transverse sections and test conditions studied, 3D flow effects are small and 2D simulations can be used to represent the loads on a 3D hull with reasonably good accuracy provided that the entry velocity and orientation (deadrise angle and trim angle) are comparable.

The coupled simulations require the fluids (air and water) to be modelled as compressible for numerical stability – a preliminary coupled simulation with the fluids modelled as incompressible diverged shortly after initial contact with the free surface. This is mainly due to the nature of the problem studied where the added mass is significant compared to the structural mass, and fluid velocity and hence the hydrodynamic loads change rapidly. Furthermore, the speed of sound in water can be set lower than its 'true' value to further enhance the stability and accelerate convergence. It was found that 'artificial' compressibility only affects the solution accuracy when the speed of sound is of the same order of magnitude as the flow velocity, which results in the fluid being compressed rather than convected. The number of exchanges per time step was also found to have an effect on the numerical stability. It has been found that at least 10 exchanges per time step are required to maintain stability in the solution. It is recommended that, whenever possible, the required number of exchanges be investigated in a systematic manner.

The experimental parameters investigated in the present work include, drop height, wedge mass and wedge deadrise angle (free-falling rigid wedge), structural boundary conditions (flexible panel constant velocity impact), and drop height and initial trim angle (full-scale drop tests). The severity of impact, measured in terms of magnitude of acceleration and pressure peaks and acceleration rise time, is found to increase with increasing drop height and decreasing deadrise angle, whereas the wedge mass is found to have relatively small influence. The flexible panel has been modelled as a 2D

beam with both simply supported and fixed boundary conditions and as a 3D panel with the experimental support conditions (test fixture frame, steel rings and fabric straps) accurately represented. It has been shown that the structural boundary conditions have a significant effect on the response. In particular, the deflection of the beam with fixed supports is much smaller than that of the simply supported beam. This is concluded to be mainly due to the in-plane boundary fixation in the case of the fixed beam, which results in both bending and membrane forces resisting deformation. The response of the 3D panel with the experimental support conditions accurately modelled lies between that of the two beams. It is recommended that, for validation studies, simpler boundary conditions, e.g. full clamped or pinned, are used. The angle at which the boat impacts the water surface is shown to have a significant effect on the acceleration rise time, with the rise time increasing with trim angle, i.e., more bow down. This is partly due to the increase in deadrise angle towards the bow, and partly because of the increased gradual wetting with increasing trim angle. The magnitude of acceleration and pressure are, however, not greatly affected by the trim angle.

The water entry problems studied in Chapter 3 showed that the numerical model is capable of simulating the water impact of 2D and 3D rigid and flexible structures with reasonably good accuracy. The computed time histories of vertical wedge acceleration and pressure at six different locations across the wedge surface compare relatively well to the experimental data of Lewis et al. (2010). The differences between the numerical and experimental results are concluded to be mainly due to friction between the vertical posts and linear bearings in the experimental setup, which has a significant influence on the wedge kinematics and hence the hydrodynamic pressures. The comparisons for other test conditions (different wedge mass and drop height) further confirm this conclusion. It is strongly recommended that, for validation of CFD or analytical studies, the velocity history of the body is accurately measured. The computed time histories of pressure at five different locations across the bottom surface of the flexible composite sandwich panel also show overall good agreement with the experimental data of Allen & Battley (2015). The time histories of deflection at the panel centre and chine agree well qualitatively, however, the numerical model predicts significantly larger deflections particularly for the simply supported beam and towards the end of the impact event (after the experimental maximum deflection). The differences observed are concluded to be mainly due to the variations in the experimental impact velocity profile and incomplete representation of the experimental boundary conditions in the two-dimensional beam models. The time histories of deflection for the 3D panel show better agreement with the experimental results, when compared with the results for the simply supported beam.

The numerical simulations of the full-scale drop tests in Chapter 5 have, however, revealed the difficulties in modelling a real hull as opposed to a relatively simple wedge or panel. The numerical time histories of pitch motion and vertical acceleration were found to compare well with the experimental data indicating that the rigid body behaviour of the boat is well captured; however, the pressures showed quite significant differences both in terms of shape of time histories, and magnitude, although the timings are reasonable well captured. In some cases, differences in the magnitudes of the peaks as large as 50% are observed. It is thought that the discrepancies observed are largely due to some of the simplifications made in order to limit the computational cost, such as modelling the hull structure as rigid. A characteristic in the pressure signals that is not captured by the 3D model is the double peak in signals recorded by sensors located near the spray rails. It was hypothesised that this secondary rise in pressure occurs when the spray root reaches the flat spray

rail (zero effective deadrise) and a high pressure is generated which propagates backwards towards the keel. Numerical simulations of 2D transverse sections with and without spray rails were performed to test this hypothesis and it was confirmed that the second peak is in fact caused by the spray rails.

The effect of structural flexibility on the hydrodynamic loads and structural response, i.e. hydroelastic effects, is studied by comparing the coupled solutions with corresponding rigid/ quasi-static solutions for a range of impact velocities. Hydroelastic effects are found to have a significant influence on the hydrodynamic loads and increase with impact velocity. These are mainly attributed to structural deformations which change the local kinematics, i.e. geometry, velocity and acceleration conditions and hence the pressure distribution at the fluid-structure boundary. More specifically, the structural deformations reduce the local impact velocity at the panel centre and effective deadrise angle at the chine, which increases and decreases the hydrodynamic loads, respectively. The calculated force impulse for the flexible structure is lower than that for the rigid structure indicating that hydroelastic effects overall lead to a decrease in load. The RQS and hydroelastic deflections showed similar trends, namely, the hydroelastic solution yields smaller deflections during the initial stages of impact and larger deflections at a later stage. The RQS method is found to predict lower maximum deflections at an earlier time than the hydroelastic solution for all impact velocities. The difference in magnitude is more or less constant suggesting that hydroelastic effects are limited. The delay in the timing of the peak in the hydroelastic solution however, is seen to increase with increasing impact velocity.

7.2. Full-scale rough water trials and drop tests

An extensive full-scale experimental investigation into the slamming loads experienced by a high-speed planing craft and the related global and local responses whilst travelling at high speed in waves (rough water trials) and as it falls freely into the water (drop tests) was performed. The work done includes designing and supervising the experiments, processing the large amounts of complex data measured and analysing/ interpreting the results.

The tests were performed on a 9.6m high-speed planing craft with a displacement of ≈2750kg and a top speed of 50 knots. Measurements of rigid body motions, accelerations in the cockpit and at the bow, pressures and strains at various locations across the hull bottom, and global hull deflections were made. An extensive set of data for various sea conditions, forward speeds and headings was acquired from the rough water trials, and for two different heights from the drop tests. In this thesis, the data recorded in four head sea runs (different sea conditions and speeds) and the drop test data is considered. The aim is to illustrate the data processing procedure and present and discuss some characteristic results. Future work should include processing and analysing other runs, in particular runs at different headings.

The measured data required processing before it could be analysed and interpreted. This included low pass filtering the acceleration signals to remove the high frequency noise, removing baseline drifts from the strain signals and identifying the peaks in the pressure and strain signals. The post-processing was done using the commercial software DIAdem from National Instruments. DIAdem offers several built-in functions for signal processing, and tasks can be automated or more complex processing performed by writing code in VBScript. The raw acceleration signals were found to

contain high frequency noise, which is concluded to be due to structural vibrations caused by the impacts and engine vibrations. Fast Fourier analysis and low pass filtering were used to analyse the frequency content of the signals, and remove the high frequency components, respectively. It is found that a cut-off frequency of 30Hz effectively removes the high frequency noise without significantly affecting the rigid body response. The same frequency was also used to filter the acceleration signals recorded in the drop tests. The peak identification algorithm is shown to accurately identify the peaks in the pressure and strain signals that would be manually identified from a visual examination, considering that the duration of the interval varies between impacts and the duration of impact varies within each signal and also between signals. This is because the algorithm uses the characteristics of the signals to identify the impact events, in particular the rapid increase in pressure and strain resulting from the impacts.

The rough water trials have provided valuable insights into the loads experienced by planing craft and the resulting global rigid body and local structural responses in realistic conditions. The segments of typical acceleration, pressure and strain signals and the histograms of the identified pressure and strain peaks illustrate the random and nonlinear nature of the problem, where characteristics such as the shape of signal, magnitude of peak and rise time, are different for each impact. This is mainly attributed to the randomness of the wave environment and the nonlinear nature of high-speed craft motions resulting in different relative velocity and angle between the craft and water surface for each impact event. Data was acquired at fairly high rates (5.12 kHz in runs 1 and 2 and 10.24kHz in runs 3 and 4 and drop tests); however, it was found that even such high rates are in some extreme cases not sufficient to accurately capture the rise in pressure – for instance, the pressure rise time in one extreme event in run 2 is about 0.5ms. In terms of symmetry of impacts, it is found that the number of pressure and strain peaks recorded at symmetric locations on port and starboard sides are fairly comparable, particularly for sensors located near the keel. The magnitude of the peaks recorded on the port side is, however, generally larger than that of the starboard side peaks, as indicated by the calculated averages of the largest $1/3^{rd}$ and $1/10^{th}$ peak values. It is also found that the hull bottom area near the keel typically experiences larger impact loads and hence larger deflections and experiences impacts more frequently than the bottom area near the chine. Furthermore, the loads and responses measured at high speed in moderate seas are found to be larger than those measured at moderate speed in rough seas.

Statistical analysis of the slamming pressures and local panel strains is also performed. The Weibull and Generalized Pareto models are fitted to the samples of pressure and strain peaks and the fitted models are used to estimate the extreme values for some probability of exceedance. Automated algorithms for fitting the statistical models to the peak value distributions have been developed and the goodness of fit is assessed using Quantile-Quantile plots and the root mean square error (RMSE) statistic. The parameters of the Weibull and generalized Pareto models are estimated using the least squares method and the Hybrid Method of Moments, respectively. A threshold parameter is introduced in the Weibull fitting to better capture the tail of the distribution, chosen to maximize the R^2 statistic. The generalized Pareto model is also fitted to the peaks above a certain threshold (Peak-Over-Threshold method), which is chosen using the parameter stability plots. It was found that the pressure or strain peaks on different levels (small and large magnitude peaks) belong to different statistical distributions, with large magnitude peaks that are most likely to be the result of extreme slamming impacts being more nonlinear. This further justifies the use of a threshold to accurately capture the largest peaks. Overall, the Quantile-Quantile plots have shown that the

Weibull and generalized Pareto models fit the data relatively well. Differences are generally observed in the tail of the distribution, particularly for samples containing outliers, which are also reflected in the RMSE statistic. The fitted Weibull models typically fall between the exponential and Rayleigh distributions, whilst the generalized Pareto models are typically light-tailed for runs 1 and 2 and heavy-tailed for runs 3 and 4. The estimated most probable extreme values using the Weibull and generalized Pareto model are found to agree well; however, the extreme values with low probability of exceedance show quite significant differences and are mainly attributed to the inaccurate modelling of the distribution tail. The methods used in the present work to estimate the model parameters and select the threshold have been shown to perform well in statistical analyses of wave loads on large ships. However for full-scale measurements of slamming loads on high-speed craft, where samples can contain outliers and the sample sizes are generally small, more robust methods (see de Zea Bermudez & Kotz (2010) for example) may be needed.

The full-scale drop tests also provided valuable insights into the loads and responses for a high-speed planing craft as it falls freely onto a calm water surface. To the best of the author's knowledge, this is the first work that measures the loads and responses during water entry of a realistic hull. The boat was dropped from heights of 0.5m and 1.0m and for each drop height multiple tests were performed to examine the repeatability of the measurements. The signals from 'equivalent' drops are found to agree quite well, both qualitatively and quantitatively, demonstrating the repeatability of the test process and giving more confidence in the measurements when comparing with CFD results. The pressure and strain signals recorded at symmetric locations on port and starboard side were also found to compare reasonably well, particularly the strain signals. The pressure and strain signals show differences from measurements that are typically made on simple tests sections such as wedges and panels in controlled environments. In particular, it has been found that the longitudinal stiffener, which is usually not considered, acts as a pivot and influences the response of the hull bottom panel to the loading. The spray rails were also found to have a significant influence on the impact pressures and strains as explained in section 7.1. The magnitude of the second peak is typically larger than the first showing that the spray can lead to an increase in load and hence the local structural deformations. It is recommended that the local structural arrangement, structural flexibility and appendages such as spray rails be included in model drop test to obtain more realistic measurements.

7.3. Rough water trials, drop tests and Classification societies' rules and standards

The suitability of the structural design loads used in current practice is investigated in Chapter 6 by comparing the pressures and accelerations measured in the rough water trials with the predictions based on the ISO 12215 standard and the DNV GL and LR rules. The methods implemented in the design rules of these classification societies and the ISO standard are quite similar and are largely based on the semi-empirical works of Savitsky & Brown (1976) and Allen & Jones (1978). The measured maximum accelerations were found to be significantly lower than the predictions, particularly for the runs at high forward speed. This is concluded to be partly because, for some runs, the speed and significant wave height are outside the ranges of applicability of the Savitsky & Brown (1976) method and partly because the acceleration peaks are assumed to be exponentially

distributed when extrapolating to higher statistical levels. Nonetheless, the ISO and DNV GL pressures were found to be significantly lower than the measured maximum pressures and estimated most probable extremes, while the LR rules were found to predict higher pressures for the high forward speed runs and lower pressures for the moderate speed runs.

The pressures and strains measured in the rough water trials are also compared with the drop tests measurements to investigate whether the loads experienced by a planing craft as it travels at high speed in waves and the resulting structural responses can be correlated to the loads and responses for the craft as it falls freely into the water. A number of individual impact events were chosen to represent the loads and responses measured in the rough water trials, and for each impact event and signal, the maximum pressure or strain is plotted against the corresponding maximum vertical cockpit acceleration. The drop tests measurements are also plotted in the same manner. The pressures and strains from the rough water trials show quite significant scatter and relatively poor correlation with the cockpit vertical accelerations, which inhibited further investigation into the correlation between the two tests. It is concluded that the complete pressure distribution or the response of the entire hull bottom needs to be considered rather than discrete point measurements. Furthermore, other acceleration components such as the pitch and longitudinal acceleration must be considered in addition to the vertical acceleration measured at the LCG to better represent the rigid body behaviour of the craft. This is discussed further in section 8.1.

Chapter 8. Conclusions and future work

Experimental and numerical investigations of slamming loads on high-speed planing craft have been carried out with the aim to improve the safety and efficiency of high-speed craft structural designs for realistic operational loads.

A numerical model for simulating the water impact of two- and three-dimensional rigid and flexible structures has been developed. The model uses Finite Volume CFD with the Volume of Fluid interface capturing method to solve for the fluid flow and implicit direct-integration to solve for the structural response. The fluid and structural domains are fully coupled to accurately capture the effect of structural response on the fluid loading. Two different water entry problems are studied – the water impact of a free-falling rigid wedge and the constant velocity water entry of a flexible composite sandwich panel – and the results are compared with published experimental data for validation. The effect of several numerical and experimental parameters on the solution, such as, grid and time step size, three-dimensional flow, fluid compressibility, and hydroelastic effects is investigated and recommendations are given.

Full-scale rough water trials on a 9.6m high-speed planing craft were carried out in various sea conditions and for various speeds and headings. An extensive set of rigid body motion, acceleration, pressure, strain and global hull deflection data was acquired. Methods for processing the experimental data including, removing the time varying offsets from the strain signals and identifying the peaks in the pressure and strain signals, have been developed and successfully applied. The trials have provided valuable insight into the loads experienced by a high-speed planing craft in waves and related responses, and further illustrated the random and nonlinear nature of the problem. Statistical analysis of the measured pressure and strain data is also performed. Automated algorithms for fitting the statistical models to the data have been developed and applied. Statistical results have revealed that the methods that are commonly used to analyse the wave loads on large ships may not be suitable for this highly nonlinear problem.

Full-scale drop tests were also performed. To the best of the author's knowledge, this is the first work that measures the loads and responses during water entry of a realistic hull. The numerical model is applied to simulate the drop tests and the results are compared with the measurements for validation. Simulations of both the 3D rigid hull and 2D rigid sections of the hull are performed. Comparisons of the 3D and 2D solutions have shown that the computationally efficient 2D model can be used to represent the loads on the 3D hull with relatively good accuracy provided that the entry velocity and orientation (deadrise and trim angle) are comparable. The 2D model is further used to investigate the effect of the spray rails which are found to have a significant influence on the flow field and hence the loads and responses.

The pressure and acceleration measurements from the rough water trials are compared with the predictions based on the ISO 12215 standard and the DNV GL and Lloyd's Register rules to assess the suitability of the design loads used in current practice. Overall, the predictions did not match the measurements highlighting the importance of revising the methods currently being used. The rough

water trials measurements are also compared with the drop tests measurements in an attempt to establish a correlation between the two tests. This investigation has revealed the complete pressure distribution and rigid body behaviour needs to be considered rather than discrete point measurements and acceleration in the vertical direction only, respectively.

This thesis has provided an extensive examination of model tests, full-scale measurements and numerical simulations and their role in evaluating slamming loads for the structural design of high-speed craft. Furthermore, it has provided valuable insight into the loads and responses for a high-speed planing craft in waves and during free-fall water impact.

8.1. Recommendations for future work

The numerical model developed in the present work is shown to predict the loads and responses for simple test sections with reasonably good accuracy. However, the predicted pressures for a realistic 3D hull showed differences from the experimental data, in terms of both shape and characteristics of the signals and magnitude. It is thought that these differences, apart from the experimental uncertainties, are mainly because of the assumptions made in the numerical model to limit the complexities and computational time. In particular, the hull structure is modelled as rigid and the spray rails are not included in the 3D model. It has been shown that both structural flexibility and spray rails have a significant influence on the pressures (see the 2D studies in sections 3.3.6 and 5.2.2.2 respectively) and should be taken into account to obtain more realistic results.

The current analysis of the rough water trials data only considers four runs in head seas – a small part of the complete set of measured data. Runs at different headings in particular should be processed using the developed code and analysed to investigate the effect of heading on the loads and responses. If the opportunity arises to conduct more full-scale rough water trials, it is recommended that, the rigid body motions and accelerations (both translation and rotation) are accurately measured and, if possible, more detailed measurements of the sea conditions using, for instance, multiple buoys are made, to better understand mechanics of slamming impacts. With regards to the drop tests, the drop height and entry velocity should be accurately measured, and more drop heights and different pitch and roll angles could be tested.

The Quantile-Quantile plots in section 4.4.2 have shown that the methods used to fit the models to the data are not robust enough to outliers. This is also reflected in the predicted extreme values with low probability of exceedance based on the Weibull and generalized Pareto models, where significant differences are observed. More robust methods (see for example de Zea Bermudez & Kotz, 2010) should be used for parameter estimation and choosing the threshold.

The preliminary comparisons between the pressures and strains measured in the rough water trails and drop tests measurements have revealed that the discrete point measurements are not sufficient to completely describe the highly localized and nonuniform slamming pressure distribution. Furthermore, the vertical acceleration measured at the LCG alone is not sufficient to completely describe the rigid body behaviour of the craft. Instead the complete pressure distribution and other acceleration components need to be considered. The former can be achieved by using, for instance, the pressure reconstruction method of Rosén (2005). The latter can be achieved by either imposing more criteria when choosing the events and grouping events based on, for instance, the bow to LCG

acceleration ratio, or by formulating a parameter that takes into account all the relevant acceleration components.

Appendices

Appendix A

List of publications

Journal papers

1. Camilleri, J., Temarel, P. & Taunton, D.J., 2017a. Numerical simulation of water impact of flexible composite hull panel. *Manuscript submitted for publication*.
2. Camilleri, J., Temarel, P. & Taunton, D.J., 2017b. Full-scale measurements of loads and responses on high-speed planing craft in waves. *Manuscript to be submitted for publication*.

Conference papers

1. Camilleri, J., Taunton, D.J. & Temarel, P., 2015a. Slamming impact loads on high-speed craft sections using two-dimensional modelling. In A. Shenoi & C. Guedes Soares, eds. Analysis and Design of Marine Structures. pp. 73–81.
2. Camilleri, J., Taunton, D.J. & Temarel, P., 2015b. Two-dimensional numerical modelling of slamming impact loads on high-speed craft. In 7th International Conference on Hydroelasticity in Marine Technology. Split, Croatia.
3. Camilleri, J., Temarel, P. & Taunton, D.J., 2017. A study of slamming loads on high-speed craft and related responses through full-scale measurements and numerical simulation. In 14th International Conference on Fast Sea Transportation FAST 2017. Nantes, France.

Others

1. Lidtke, A., Lakshmynarayanana, A. P., Camilleri, J., Badoe, C. E., Banks, J., Phillips, A. B. & Turnock, S. R., 2015. RANS Computations of Flow around a Bulk Carrier with Energy Saving Device. In Tokyo 2015: A Workshop on CFD in Ship Hydrodynamics. Japan.

Appendix B

Additional full-scale rough water trials results

Table 13 - Number of pressure peaks identified in signals P1 – P20, runs 1 - 4.

Run	P1 (P11)	P2 (P12)	P3 (P13)	P4 (P14)	P5 (P15)	P6 (P16)	P7 (P17)	P8 (P18)	P9 (P19)	P10 (P20)
1	67 (66)	343 (341)	370 (373)	321 (273)	97 (144)	329 (332)	303 (301)	141 (140)	117 (109)	24 (59)
2	113 (98)	390 (389)	420 (430)	357 (324)	133 (214)	365 (366)	370 (362)	194 (149)	124 (120)	39 (110)
3	197 (196)	374 (373)	344 (350)	243 (261)	122 (149)	234 (249)	230 (239)	167 (139)	94 (90)	68 (133)
4	51 (52)	447 (444)	433 (442)	351 (343)	157 (178)	334 (345)	298 (308)	204 (281)	122 (120)	76 (104)

Table 14 - Number of strain peaks identified in signals S1 – S8, runs 1 - 4.

Run	S1 (S5)	S2 (S6)	S3 (S7)	S4 (S8)
1	336 (335)	280 (241)	301 (285)	94 (85)
2	365 (358)	323 (258)	361 (361)	114 (100)
3	331 (329)	229 (235)	241 (252)	95 (101)
4	422 (410)	326 (300)	315 (309)	120 (117)

Table 15 - Average of the largest 1/3rd pressure peaks (kPa) for P1 – P20, runs 1 - 4.

Run	P1 (P11)	P2 (P12)	P3 (P13)	P4 (P14)	P5 (P15)	P6 (P16)	P7 (P17)	P8 (P18)	P9 (P19)	P10 (P20)
1	29.7 (32.4)	90.8 (75.4)	81.2 (54.4)	62.1 (42.5)	47.8 (5.9)	88.1 (46.3)	96.7 (89.7)	52.1 (29.4)	96.7 (66.5)	30.5 (10)
2	44 (31.5)	107.9 (90.7)	104.4 (62.7)	91.3 (47.8)	64.7 (9)	115 (54.6)	133.5 (107.2)	74.8 (35)	113.8 (82.8)	44.6 (11.3)
3	64.4 (107.1)	101.8 (111.2)	79.3 (82.8)	58.3 (71.3)	49.6 (42.5)	97.4 (74.5)	87.1 (144.3)	48.5 (55.6)	100.1 (107)	40.1 (27.4)
4	96.6 (57.4)	83.3 (64)	89.5 (52.2)	49.7 (40.5)	59.8 (33.3)	88.1 (52)	78.2 (93.1)	50.6 (27.4)	86.6 (66.2)	37.8 (17.5)

Table 16 - Average of the largest 1/3rd strain peaks (μs) for S1 – S8, runs 1 – 4.

Run	S1 (S5)	S2 (S6)	S3 (S7)	S4 (S8)
1	352.5 (292)	232.2 (150.3)	411.3 (294.3)	211.9 (82.4)
2	425.3 (327.7)	325.9 (166)	562 (342.6)	347.4 (116.4)
3	396.4 (431.3)	242.8 (298.7)	445.5 (462.6)	235.9 (248.3)
4	359.6 (280)	245.2 (157)	398.2 (271.5)	267.7 (145.7)

Table 17 - Average of largest 1/10th pressure peaks (kPa) for P1 – P20, runs 1 - 4.

Run	P1 (P11)	P2 (P12)	P3 (P13)	P4 (P14)	P5 (P15)	P6 (P16)	P7 (P17)	P8 (P18)	P9 (P19)	P10 (P20)
1	38.5 (39.4)	119.8 (91.6)	106.8 (68.4)	75.1 (51.8)	60.8 (9)	115.7 (60.6)	123.5 (106.4)	67.2 (40.3)	131.2 (82.7)	44.4 (16.9)
2	68 (35.1)	140.4 (113)	139.8 (76.4)	124.3 (60)	95.3 (17)	158.4 (70.6)	173.1 (130.8)	105.2 (45.5)	158.6 (106.3)	74.9 (21.2)
3	91.4 (156.6)	158.7 (154.2)	113.8 (113.6)	80.3 (97.6)	78.2 (64.7)	135.4 (105.7)	117 (207)	77.9 (79.1)	135 (147.1)	71.3 (67.9)
4	137.2 (74.4)	116.9 (86.6)	131.9 (72.3)	69 (54.4)	83.4 (54.1)	130.4 (78.3)	107.8 (133.4)	72.5 (42.2)	114.8 (96.9)	60.7 (30.8)

Table 18 - Average of largest 1/10th strain peaks (μs) for S1 – S8, runs 1 – 4.

Run	S1 (S5)	S2 (S6)	S3 (S7)	S4 (S8)
1	460.5 (359.7)	300.7 (182.2)	537.5 (359.8)	338.2 (127.2)
2	561.3 (399.3)	464.9 (211.5)	738.9 (431.7)	583.8 (190.2)
3	555.8 (550.4)	353.1 (416)	640.8 (660)	348.9 (346.7)
4	499.3 (371.4)	348.3 (201.8)	550.1 (372.7)	365.5 (197.8)

Table 19 - Weibull distribution shape (-) and scale (kPa) parameters for the pressure peaks samples, runs 1 - 4.

Run	Parameter	P2	P3	P4	P6	P7	P12	P13	P14	P16	P17
1	Shape, b	1.01	1.58	2.58	1.69	2.14	2.41	1.41	2.49	1.25	2.94
	Scale, a	37.3	51.3	47.9	58.6	71.0	56.9	30.2	32.4	23.8	71.6
2	Shape, b	1.62	1.72	0.88	1.13	2.01	1.42	2.54	2.18	1.67	2.49
	Scale, a	68.6	70.2	32.5	56.4	95.4	49.9	48.2	35.0	35.4	81.8
3	Shape, b	0.74	1.14	1.54	1.62	1.76	0.91	1.56	1.66	1.09	1.26
	Scale, a	31.8	41.1	37.2	64.0	59.2	42.1	53.1	47.2	36.2	82.1
4	Shape, b	1.36	0.93	1.63	0.86	1.61	1.94	1.63	1.73	1.10	1.10
	Scale, a	49.3	37.1	32.6	33.4	51.1	45.5	34.2	27.2	26.8	46.2

Table 20 - Weibull distribution shape (-) and scale (μs) parameters for the strain peaks samples, runs 1 - 4.

Run	Parameter	S1	S2	S3	S5	S6	S7
1	Shape, b	1.59	1.79	1.70	1.82	2.42	2.48
	Scale, a	224.1	157.8	271.7	192.3	113.6	224.3
2	Shape, b	1.62	1.26	1.70	2.31	2.06	1.94
	Scale, a	273.9	185.0	374.5	242.3	119.7	238.6
3	Shape, b	0.93	1.37	1.20	1.91	1.51	1.27
	Scale, a	156.7	146.1	246.2	301.4	188.7	264.2
4	Shape, b	1.36	1.51	1.51	1.91	1.88	1.17
	Scale, a	210.8	155.3	250.5	196.7	109.0	137.5

Table 21 - Generalized Pareto shape (-) and scale (kPa) parameters for the pressure peaks samples, runs 1 - 4.

Run	Parameter	P2	P3	P4	P6	P7	P12	P13	P14	P16	P17
1	Shape, c	0.18	-0.12	-0.10	0.00	0.10	-0.03	0.04	-0.20	0.06	0.08
	Scale, λ	19.6	24.4	12.6	24.4	19.5	13.8	10.8	9.1	10.9	12.1
2	Shape, c	-0.09	-0.01	0.23	0.07	0.02	0.08	-0.10	-0.41	-0.02	-0.10
	Scale, λ	30.3	29.9	20.0	30.4	32.0	16.1	15.3	14.9	13.8	21.6
3	Shape, c	0.19	0.21	0.21	0.25	0.07	0.17	0.07	0.01	0.02	-0.15
	Scale, λ	33.3	22.7	12.6	22.2	21.5	28.5	22.9	23.0	24.0	60.1
4	Shape, c	0.04	0.07	0.14	0.15	0.15	0.17	0.14	0.05	0.04	0.01
	Scale, λ	26.6	30.8	13.0	24.8	19.9	13.9	13.6	10.9	20.7	33.5

Table 22 - Generalized Pareto shape (-) and scale (μs) parameters for the strain peaks samples, runs 1 - 4.

Run	Parameter	S1	S2	S3	S5	S6	S7
1	Shape, c	-0.02	-0.25	-0.20	0.05	-0.44	0.00
	Scale, λ	92.9	70.1	131.7	51.1	68.7	51.5
2	Shape, c	-0.01	0.15	-0.15	-0.09	-0.21	-0.24
	Scale, λ	107.8	90.1	171.9	63.5	45.2	99.1
3	Shape, c	0.08	0.11	-0.16	-0.08	0.11	-0.29
	Scale, λ	120.4	80.6	206.9	100.3	84.1	225.3
4	Shape, c	-0.10	0.06	0.16	0.02	0.02	-0.02
	Scale, λ	129.4	84.2	102.6	75.6	36.3	87.6

Table 23 - Normalized root mean square errors (%) for the Weibull and Generalized Pareto models, pressure peaks samples, runs 1 – 4.

Run	Model	P2	P3	P4	P6	P7	P12	P13	P14	P16	P17
1	WBL	6.5	2.5	2.5	7.7	7.2	2.9	5.0	1.4	3.1	3.6
	GPD	7.6	2.7	2.1	6.0	5.4	2.0	3.6	1.5	3.7	2.8
2	WBL	1.6	6.9	5.3	8.1	5.7	3.6	4.5	2.0	1.8	1.8
	GPD	2.1	5.3	8.6	6.4	3.9	2.6	2.9	1.5	1.8	1.7
3	WBL	4.9	11.6	10.2	16.8	6.7	5.3	9.1	9.0	3.8	6.2
	GPD	9.5	11.1	9.5	13.8	5.6	7.0	8.0	6.3	5.3	6.4
4	WBL	7.1	2.6	12.7	4.9	13.6	14.2	11.6	7.5	7.4	3.0
	GPD	4.9	4.5	8.3	7.2	8.8	6.7	6.7	6.3	6.8	4.5

Table 24 - Normalized root mean square errors (%) for the Weibull and Generalized Pareto models, strain peaks samples, runs 1 – 4.

Run	Model	S1	S2	S3	S5	S6	S7
1	WBL	3.1	2.2	1.7	2.6	1.4	3.0
	GPD	3.0	1.5	2.0	2.8	3.1	2.2
2	WBL	2.7	12.8	2.7	2.5	2.0	1.4
	GPD	3.1	8.9	3.0	2.8	2.2	1.8
3	WBL	2.7	12.5	5.8	1.5	10.7	5.5
	GPD	5.4	9.7	7.2	2.1	8.5	3.5
4	WBL	2.5	11.3	10.3	7.6	5.3	2.2
	GPD	3.0	6.6	7.6	6.2	5.2	3.3

Appendix C

Additional full-scale drop tests results

Table 25 - Mean (μ), standard deviation (σ) and coefficient of variation (CV = σ/μ) of the magnitude and time of the 1st and 2nd (where it exists) pressure peaks recorded in drops 2 and 3.

	1st peak						2nd peak					
	Peak magnitude			Peak time			Peak magnitude			Peak time		
Sensor	μ, kPa	σ, kPa	CV, %	μ, ms	σ, ms	CV, %	μ, kPa	σ, kPa	CV, %	μ, ms	σ, ms	CV, %
P1	59.6	6.1	10.2	90.4	0.7	0.8	29.1	6.1	20.9	129.0	4.2	3.3
P2	22.9	1.4	6.3	14.3	1.8	12.6	10.7	0.5	4.9	54.4	3.3	6.0
P3	25.0	1.8	7.1	38.8	2.6	6.8	38.9	4.3	11.2	52.3	2.9	5.5
P4	7.4	0.3	4.2	90.2	4.6	5.1						
P5	9.7	0.6	6.0	169.5	1.6	0.9						
P6	18.0	1.1	6.3	24.5	1.9	7.8	23.8	2.3	9.6	54.7	0.6	1.1
P7	17.1	0.5	3.2	40.5	1.1	2.6	29.4	4.0	13.7	54.6	0.3	0.6
P8	7.2	4.3	60.1	89.8	25.1	28.0						
P9	7.2	0.9	13.1	72.4	2.0	2.8						
P10	4.3	0.5	12.8	54.2	2.0	3.7						
P11	46.8	3.6	7.6	88.1	0.1	0.2	12.6	1.0	8.3	128.5	3.5	2.8
P12	20.9	1.1	5.3	15.0	1.6	10.6	18.9	0.1	0.6	54.0	1.3	2.5
P13	30.0	2.4	8.1	39.0	1.3	3.3	45.6	0.2	0.5	52.6	2.2	4.2
P14	14.0	1.7	11.9	91.8	4.8	5.3						
P16	15.4	2.7	17.2	25.8	1.1	4.3						
P17	24.6	2.9	11.9	41.9	1.0	2.4	55.1	4.7	8.4	56.8	2.3	4.1
P19	7.6	0.9	12.1	72.9	0.0	0.0						

Table 26 - Mean (μ), standard deviation (σ) and coefficient of variation (CV = σ/μ) of the magnitude and time of the 1st and 2nd (where it exists) strain peaks recorded in drops 2 and 3.

	1st peak						2nd peak					
	Peak magnitude			Peak time			Peak magnitude			Peak time		
Sensor	μ, με	σ, με	CV, %	μ, ms	σ, ms	CV, %	μ, με	σ, με	CV, %	μ, ms	σ, ms	CV, %
S1	77.0	5.7	7.3	38.4	1.9	5.0	166.4	5.5	3.3	54.2	2.8	5.1
S2	52.4	5.7	10.8	116.0	3.0	2.6						
S3	140.8	2.9	2.1	55.1	0.1	0.3						
S5	79.4	3.2	4.0	38.6	0.4	0.9	136.2	4.6	3.4	54.0	1.7	3.1
S6	44.3	5.8	13.1	104.9	24.3	23.2						
S7	112.2	3.4	3.0	57.1	2.0	3.5						
S8	23.1	3.3	14.4	144.7	1.2	0.8						

Table 27 - Mean (μ), standard deviation (σ) and coefficient of variation (CV = σ/μ) of the magnitude and time of the 1st and 2nd (where it exists) pressure peaks recorded in drops 4, 5 and 6.

	1st peak						2nd peak					
	Peak magnitude			Peak time			Peak magnitude			Peak time		
Sensor	μ, kPa	σ, kPa	CV, %	μ, ms	σ, ms	CV, %	μ, kPa	σ, kPa	CV, %	μ, ms	σ, ms	CV, %
P1	127.2	4.2	3.3	61.3	6.6	10.8	63.2	9.8	15.5	88.5	4.0	4.5
P2	65.8	8.9	13.6	10.4	0.7	7.1	30.6	0.7	2.2	35.7	0.8	2.1
P3	65.6	1.9	2.9	25.4	0.4	1.6	85.6	6.0	7.0	33.8	1.2	3.5
P4	18.9	1.8	9.8	57.8	4.3	7.5						
P5	16.3	8.4	51.3	116.1	10.1	8.7						
P6	53.2	1.8	3.5	18.2	1.1	6.0	53.1	4.8	9.0	36.6	0.8	2.2
P7	43.4	1.6	3.7	27.8	0.8	2.9	68.1	4.6	6.8	36.7	0.9	2.4
P8	19.0	2.4	12.7	51.9	0.8	1.5						
P9	17.6	1.6	8.9	45.5	4.4	9.7						
P10	8.6	0.5	5.4	36.2	0.6	1.8						
P11	106.2	6.3	5.9	58.8	4.6	7.9	29.7	3.6	12.2	89.9	4.3	4.8
P12	64.2	1.4	2.2	10.6	0.4	3.8	51.6	5.0	9.7	35.8	1.4	3.9
P13	76.7	3.4	4.4	25.3	0.8	3.3	94.1	6.9	7.3	33.8	1.0	2.9
P14	30.4	2.9	9.5	55.0	1.5	2.7						
P16	44.5	1.4	3.2	19.0	1.3	6.7						
P17	70.0	8.9	12.7	29.5	1.9	6.3	129.5	11.8	9.1	37.5	0.4	1.0
P19	19.4	3.0	15.2	48.9	2.2	4.6						

Table 28 - Mean (μ), standard deviation (σ) and coefficient of variation (CV = σ/μ) of the magnitude and time of the 1st and 2nd (where it exists) strain peaks recorded in drops 4, 5 and 6.

	1st peak						2nd peak					
	Peak magnitude			Peak time			Peak magnitude			Peak time		
Sensor	μ, με	σ, με	CV, %	μ, ms	σ, ms	CV, %	μ, με	σ, με	CV, %	μ, ms	σ, ms	CV, %
S1	186.3	9.3	5.0	25.6	1.0	4.0	378.6	5.8	1.5	35.5	1.0	2.8
S2	129.3	5.9	4.5	78.7	0.9	1.1						
S3	119.0	8.2	6.9	31.8	1.2	3.6	336.2	19.0	5.7	37.5	0.8	2.2
S5	199.3	5.1	2.6	25.6	0.9	3.6	351.3	21.1	6.0	35.6	1.2	3.4
S6	120.6	12.9	10.7	79.3	2.0	2.5						
S7	127.0	19.3	15.2	31.4	0.2	0.7	298.1	16.3	5.5	37.8	0.6	1.6
S8	57.8	2.9	4.9	93.7	4.3	4.6						

Appendix D

ISO 12215 standard and DNV GL and LR rules

ISO 12215 standard

The ISO 12215 standard applies to small monohull craft constructed from fibre-reinforced plastics, aluminium or steel alloys, glued wood or other suitable boat building material with length of hull between 2.5 m and 24 m and maximum speed ≤ 50 knots in the fully loaded condition. It is based on the assumption that scantlings are governed solely by local loads.

The design pressure is adjusted by a set of factors based on the sea and wind conditions in which the boat is intended to operate, boat type, longitudinal location on the hull etc. The pressure adjusting factors are described below.

The design category factor k_{DC} accounts for the sea and wind conditions in which the boat is intended to operate. For design category C ("inshore") - category of boats considered suitable to operate in seas with significant wave heights up to 2 m and a typical steady wind force of Beaufort Force 6 or less – $k_{DC} = 0.6$.

The dynamic load factor n_{CG} is considered to be close to the single amplitude acceleration measured at the craft centre of gravity at the relevant frequency for a certain period of time. It is expressed as,

$$n_{CG} = 0.32\left(\frac{L_{WL}}{10 \times B_C} + 0.084\right) \times (50 - \beta_{0.4}) \times \frac{V^2 \times B_C^2}{m_{LDC}} \tag{17}$$

where m_{LDC} is the loaded displacement mass of the craft (kg), L_{WL} is the length of the fully loaded water line at m_{LDC} (m) and V is the maximum speed at m_{LDC} (knots). B_C is the chine beam (m) and $\beta_{0.4}$ the deadrise angle (°), both measured at $0.4L_{WL}$ forward of its aft end in accordance with Figure 95. The deadrise angle is not to be taken < 10° or > 30°. If the dynamic load factor is ≤ 3, the value given by equation 17 shall be used. If the dynamic load factor is > 3 that value or the value given by the following equation shall be used,

$$n_{CG} = \frac{0.5 \times V}{m_{LDC}^{0.17}}. \tag{18}$$

In any case, the dynamic load factor need not be taken > 7g.

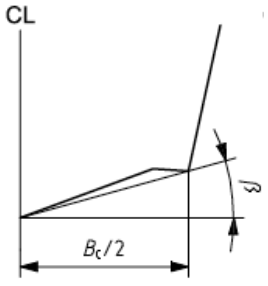

Figure 95 - Measurement of chine beam and deadrise angle (ISO 2008).

The longitudinal pressure distribution factor k_L takes into account the variation of pressure loads along the craft length. It is given by,

$$k_L = \begin{cases} \dfrac{1 - 0.167 \times n_{CG}}{0.6} \dfrac{x}{L_{WL}} + 0.167 \times n_{CG}, & \dfrac{x}{L_{WL}} \leq 0.6 \\ 1, & \dfrac{x}{L_{WL}} > 0.6 \end{cases} \quad (19)$$

where x is the longitudinal position of the panel centre forward of aft end of L_{WL} in m_{LDC} conditions (m). k_L shall not be taken > 1 for $x/L_{WL} \leq 0.6$ and for the purposes of determining k_L, n_{CG} shall not be taken < 3 or > 6.

The area pressure reduction factor k_{AR} takes into account the variation of pressure loads due to panel size. It is expressed as,

$$k_{AR} = \frac{k_R \times 0.1 \times m_{LDC}^{0.15}}{A_D^{0.3}} \quad (20)$$

where k_R is the structural component and boat type factor (= 1.0 for bottom, side and deck panels and stiffeners of planing craft in planing mode) and A_D is the design area (m^2). For plating $A_D = (l \times b) \times 10^{-6}$ where b and l are the shorter and longer panel dimensions (mm), respectively. The design area shall not be taken $> 2.5 \times b^2 \times 10^{-6}$ and k_{AR} shall not be taken > 1.

The design bottom pressure for planing craft is the greater of,

$$P_{BMD} = (2.4 m_{LDC}^{0.33} + 20) \times k_{AR} \times k_{DC} \times k_L \quad (21)$$

or

$$P_{BMP} = \frac{0.1 m_{LDC}}{L_{WL} \times B_c} \times (1 + k_{DC}^{0.5} \times n_{CG}) \times k_{AR} \times k_L \quad (22)$$

or

$$P_{BM\,MIN} = 0.45 m_{LDC}^{0.33} + (0.9 \times L_{WL} \times k_{DC}) \quad (23)$$

where P_{BMD} and P_{BMP} are the bottom pressure (kN/m^2) in displacement and planing mode, respectively, and $P_{BM\,MIN}$ is the bottom minimum pressure (kN/m^2). The reason behind this double requirement is that in rough seas, high-speed craft may have to progress at a slower speed in the same manner as displacement craft.

The minimum required thickness for metal plating t (mm) is,

$$t = b \times k_c \times \sqrt{\frac{P \times k_2}{1000 \times \sigma_d}} \quad (24)$$

where k_c is the curvature correction factor for curved panels (= 1 for flat panels), k_2 is the panel aspect ratio factor for bending strength (= 0.5 for panels with aspect ratio > 2), P is the design pressure and σ_d is the design stress for metal plating.

DNV GL rules

The DNV GL rules apply for high speed and light craft constructed from steel, aluminium or fibre or sandwich composites. A light craft is defined as a craft with a full load displacement Δ (tonnes),

$$\Delta \leq (0.13 \times L \times B)^{1.5} \tag{25}$$

where L is the length of the craft at the design waterline (m) and B is the full breadth at $L/2$ (m).

A high-speed light craft is defined as a craft capable of a maximum speed V (knots) of,

$$V \geq 7.16\Delta^{0.1667}. \tag{26}$$

Service area restrictions, given in nautical miles and representing the maximum distance from nearest port or safe anchorage, are also assigned to each high speed and light craft.

The craft's operational profile must be specified in terms of speed(s) in combination with significant wave height(s) H_s (m) and considering the areas and sea conditions where the craft is intended to operate. The minimum significant wave height at maximum speed fully loaded is 0.5 m. The vertical acceleration at the longitudinal centre of gravity of the craft a_{cg} (m/s^2) is calculated for each combination of speed and significant wave height and the design vertical acceleration is set to the largest value obtained. For a craft with speed to length ratio $V/\sqrt{L} \geq 3$,

$$a_{cg} = \frac{k_h g_0}{1650}\left(\frac{Hs}{B_{WL2}} + 0.084\right)(50 - \beta_{cg})\left(\frac{V}{\sqrt{L}}\right)^2 \frac{LB_{WL2}^2}{\Delta} \tag{27}$$

where B_{WL2} is the greatest moulded breadth of the hull (m) at the fully loaded waterline at $L/2$, β_{cg} is the deadrise angle at LCG (°) and not to be taken < 10° or > 30°, k_h is the hull type factor (1.0 for monohulls) and g_0 is the acceleration of gravity (9.81 m/s^2). The design vertical acceleration shall not be taken less < 1g (service area restriction R4) and needs not be taken > 6g. The design vertical acceleration at different positions along craft's length is not to be taken less than $k_v a_{cg}$ where k_v is the longitudinal distribution factor (1.0 between AP and 0.5L and increases linearly to 2.0 at FP).

The design slamming pressure p_{sl} (kN/m^2) on bottom of craft with speed $V/\sqrt{L} \geq 3$ shall be taken as,

$$p_{sl} = \frac{a_{cg} \times \Delta}{0.14 \times A_{ref}} \times K_{red} \times K_l \times K_\beta \tag{28}$$

where $A_{ref} = 0.7\Delta/T$ is the reference area from impact loads and T is the fully loaded draught at $L/2$ (m). K_{red} is the reduction factor for design load area defined as,

$$K_{red} = 0.445 - 0.35\left(\frac{u^{0.75} - 1.7}{u^{0.75} + 1.7}\right);\ u = 100\frac{A}{A_{ref}} \tag{29}$$

where A is the design area for the element considered (m^2) – for plates A shall be taken as spacing s by span l and not greater than $2.5s^2$.

K_l is the longitudinal distribution factor (0.5 at AP; 1.0 at 0.5L and FP; intermediate values to be determined by linear interpolation).

K_β is the correction factor for local deadrise angle defined as,

$$K_\beta = \frac{50 - \beta_x}{50 - \beta_{cg}} \tag{30}$$

where β_x is the deadrise angle at transverse section considered (minimum 10°, maximum 30° and not to be taken less than β_{cg} aft of LCG).

The thickness of the bottom plating t (mm) is not to be less than,

$$t = \frac{22.4 k_r k_a s \sqrt{P_{sl}}}{\sqrt{\sigma_{sl}}} \tag{31}$$

where k_r is the correction factor for curved plates (= 1 for flat plates), $k_a = \left(1.1 - 0.25\frac{s}{l}\right)^2$ is the correction factor for the aspect ratio of plate field (maximum 1.0 for $s/l = 0.4$ and minimum 0.72 for $s/l = 0.72$) and σ_{sl} is maximum allowable bending stress due to slamming load.

Lloyd's register (LR) rules

The Lloyd's Register rules and regulation for special service craft cover a wide range of craft types including high-speed craft that are constructed from steel, aluminium alloys or composite materials. The rules define a high-speed craft as a craft capable of maximum speed V (knots),

$$V \geq 7.19\nabla^{\frac{1}{6}} \tag{32}$$

where ∇ is the moulded displacement (m^3) of the craft corresponding to the design waterline.

The minimum value of significant wave height $H_{1/3}$ used in the determination of accelerations and loads is not to be taken less than 0.6 m (Service Group G1).

The vertical acceleration at the LCG a_v (g), defined as the average of the 1/100th highest acceleration, for a mono-hull craft in the non-displacement mode is given by,

$$a_v = 1.5\theta_B \left(\frac{L_{WL} B_C^3}{B_W \Delta}\right)\left(\frac{H_{1/3}}{B_W} + 0.084\right)(5 - 0.1\theta_D)\left(\frac{V}{\sqrt{L_{WL}}}\right)^2 \times 10^{-3} \tag{33}$$

where L_{WL} is the waterline length (m), B_C is the breadth of hull between the chines at LCG (m), B_W is the breadth of hull at LCG measured at the waterline (m), Δ is the displacement (tonnes), θ_D is the deadrise angle at the LCG (°) but is not to be taken > 30°, θ_B is the running trim angle (°) but is not to be taken < 3°. L_{WL}/B_W is not to be taken < 3 and $H_{1/3}/B_W$ < 0.2.

The vertical acceleration a_x (g) at any given location distance x_a from the AP along the hull may be taken as,

$$a_x = a_v\left(0.86 - 0.32\frac{x_a}{L_{WL}} + 1.76\left(\frac{x_a}{L_{WL}}\right)^2 + \xi_a\right) \tag{34}$$

where x_a is the distance from aft end of the static load waterline to the point at which the vertical acceleration is calculated (m), $\xi_a = 0.14 + 0.32\frac{x_{LCG}}{L_{WL}} - 1.76\left(\frac{x_{LCG}}{L_{WL}}\right)^2$ and x_{LCG} is the distance from aft end of the static load water line to the LCG (m).

The bottom impact pressure due to slamming $P_{d/b}$ (kN/m^2) is given by,

$$P_{d/b} = \frac{f_d \Delta \Phi (1 + a_v)}{L_{WL} G_s} \tag{35}$$

where f_d is the hull form pressure factor (54 for mono-hull craft), G_s is the support girth (m) defined as the girth distance measured around the circumference of the shell plate between chines, and Φ is the longitudinal pressure distribution factor (see Figure 85).

The design pressure for bottom plating is,

$$P_{BP} = H_f \times S_f \times C_f \times P_{d/b} \tag{36}$$

where H_f is the hull notation factor (1.0 for high-speed craft), S_f the service type factor (1.25 for pilot craft) and C_f the craft type factor (1.0 for monohulls).

The required thickness of plating t_p (mm) is,

$$t_p = 22.4 s \gamma \beta \sqrt{\frac{p}{f_\sigma \sigma_a}} \times 10^{-3} \tag{37}$$

where s is the stiffener spacing (mm), γ is the convex curvature correction factor (= 1.0 for flat plate), β is the panel aspect ratio correction factor (= $A_R(1 - 0.25A_R)$ for $A_R \leq 2$ and 1.0 for $A_R > 2$ where A_R is the panel aspect ratio (length/ breadth)), p is the design pressure, f_σ is the limiting bending stress coefficient for the plating element under consideration (= 0.85 for bottom shell plating in the slamming zone) and σ_a is the guaranteed minimum 0.2% proof stress of the alloy in the welded condition.

Appendix E

In this appendix the acceleration, pressure and strain signals recorded in some of the chosen impact events from the rough water trials are presented – see list below.

Figure 96 - Cockpit and bow acceleration, pressure and strain signals recorded during an impact event in run 1 (t = 1.7s). Maximum cockpit and bow acceleration is 1.44g and 6.04g, respectively.

Figure 97 - Cockpit and bow acceleration, pressure and strain signals recorded during an impact event in run 1 (t = 18.9s). Maximum cockpit and bow acceleration is 1.59g and 6.4g, respectively.

Figure 98 - Cockpit and bow acceleration, pressure and strain signals recorded during an impact event in run 1 (t = 172.9s). Maximum cockpit and bow acceleration is 1.58g and 6.42g, respectively.

Figure 99 - Cockpit and bow acceleration, pressure and strain signals recorded during an impact event in run 2 (t = 270.3s). Maximum cockpit and bow acceleration is 1.32g and 6.53g, respectively.

Figure 100 - Cockpit and bow acceleration, pressure and strain signals recorded during an impact event in run 4 (t = 68.8s). Maximum cockpit and bow acceleration is 2.38g and 8.9g, respectively.

Figure 101 - Cockpit and bow acceleration, pressure and strain signals recorded during an impact event in run 4 (t = 162.5s). Maximum cockpit and bow acceleration is 1.16g and 5.2g, respectively.

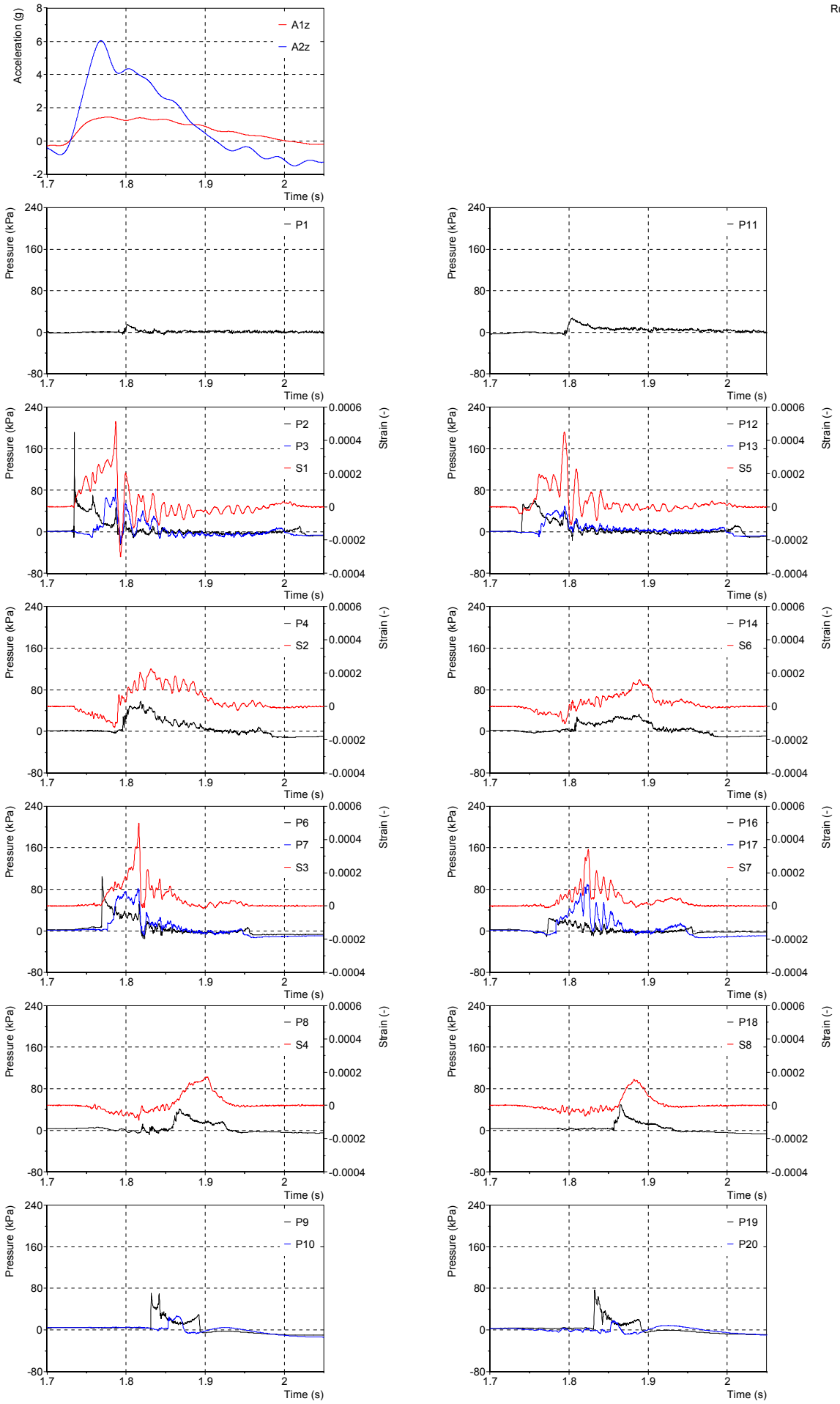

Figure 95 - Cockpit and bow acceleration, pressure and strain signals recorded during an impact event in run 1 (t = 1.7s). Maximum cockpit and bow acceleration is 1.44g and 6.04g, respectively.

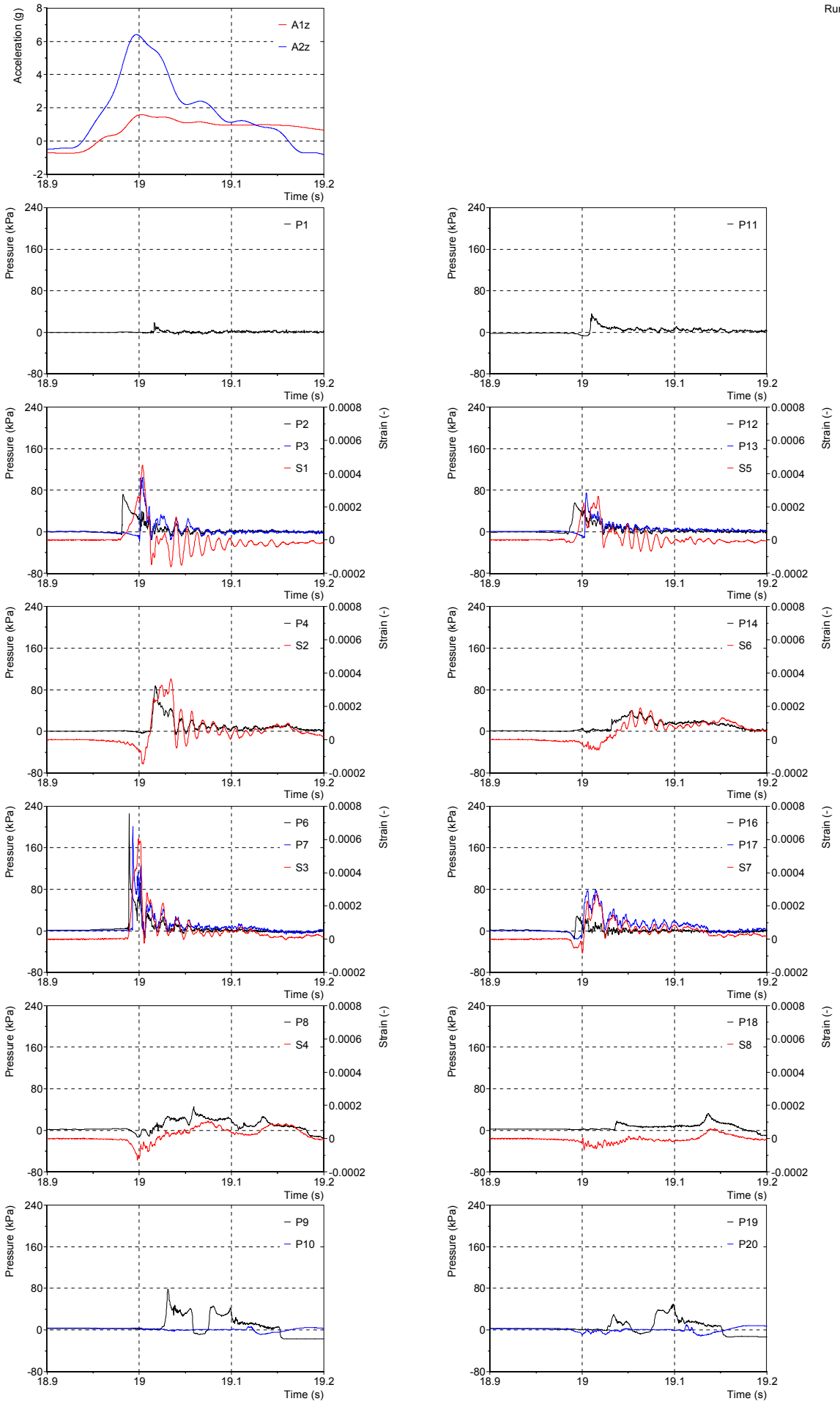

Figure 96 - Cockpit and bow acceleration, pressure and strain signals recorded during an impact event in run 1 (t = 18.9s). Maximum cockpit and bow acceleration is 1.59g and 6.4g, respectively.

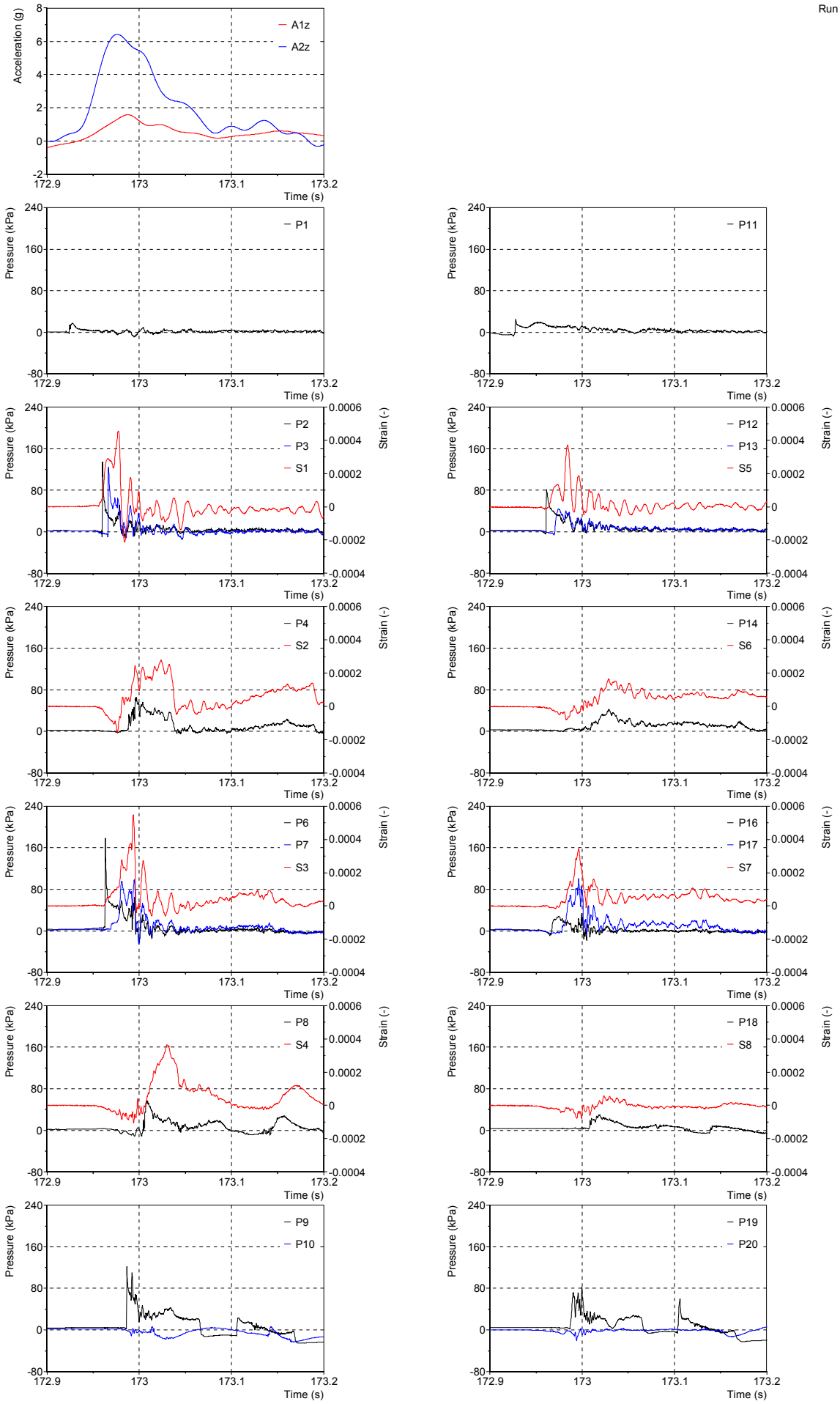

Figure 97 - Cockpit and bow acceleration, pressure and strain signals recorded during an impact event in run 1 (t = 172.9s). Maximum cockpit and bow acceleration is 1.58g and 6.42g, respectively.

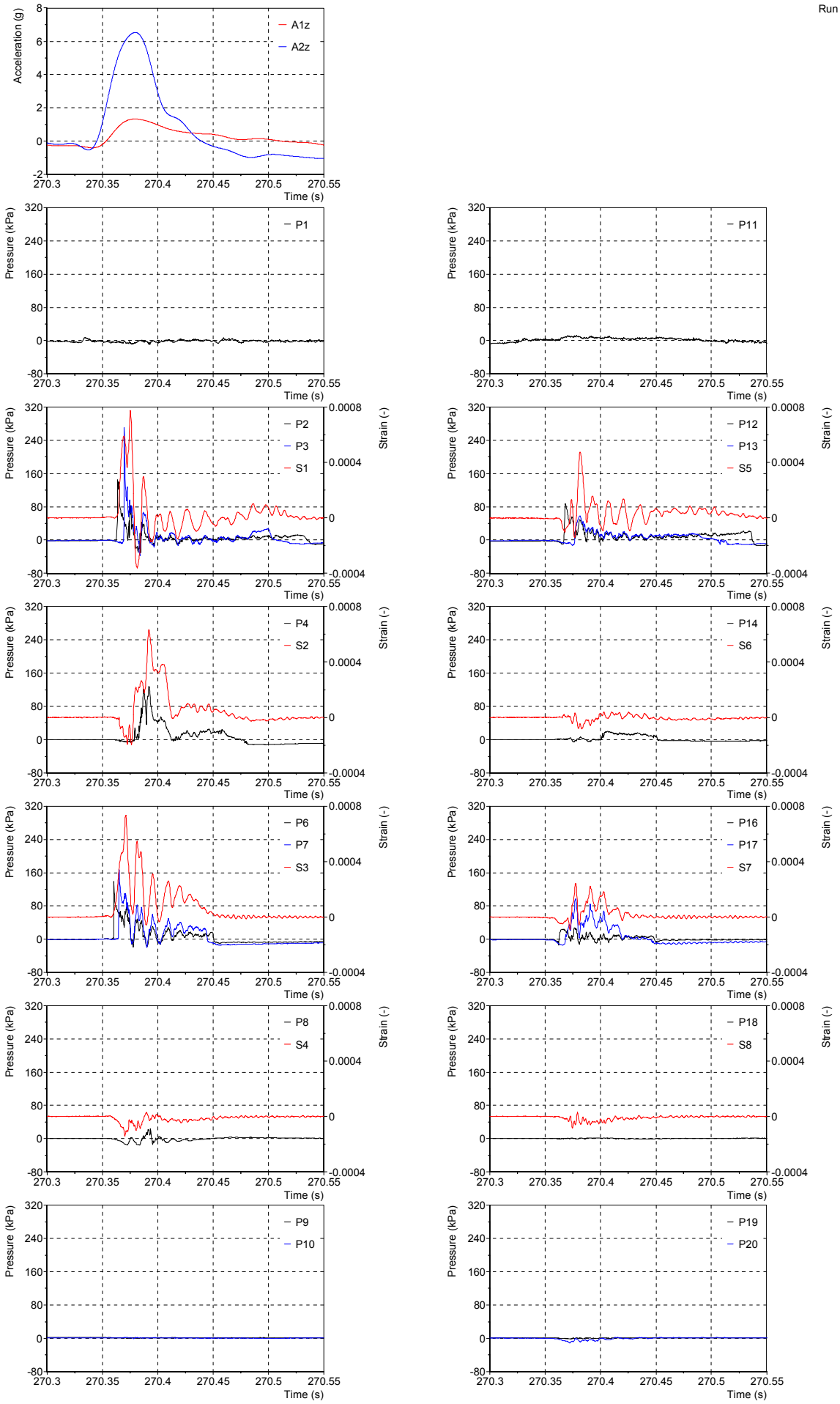

Figure 98 - Cockpit and bow acceleration, pressure and strain signals recorded during an impact event in run 2 (t = 270.3s). Maximum cockpit and bow acceleration is 1.32g and 6.53g, respectively.

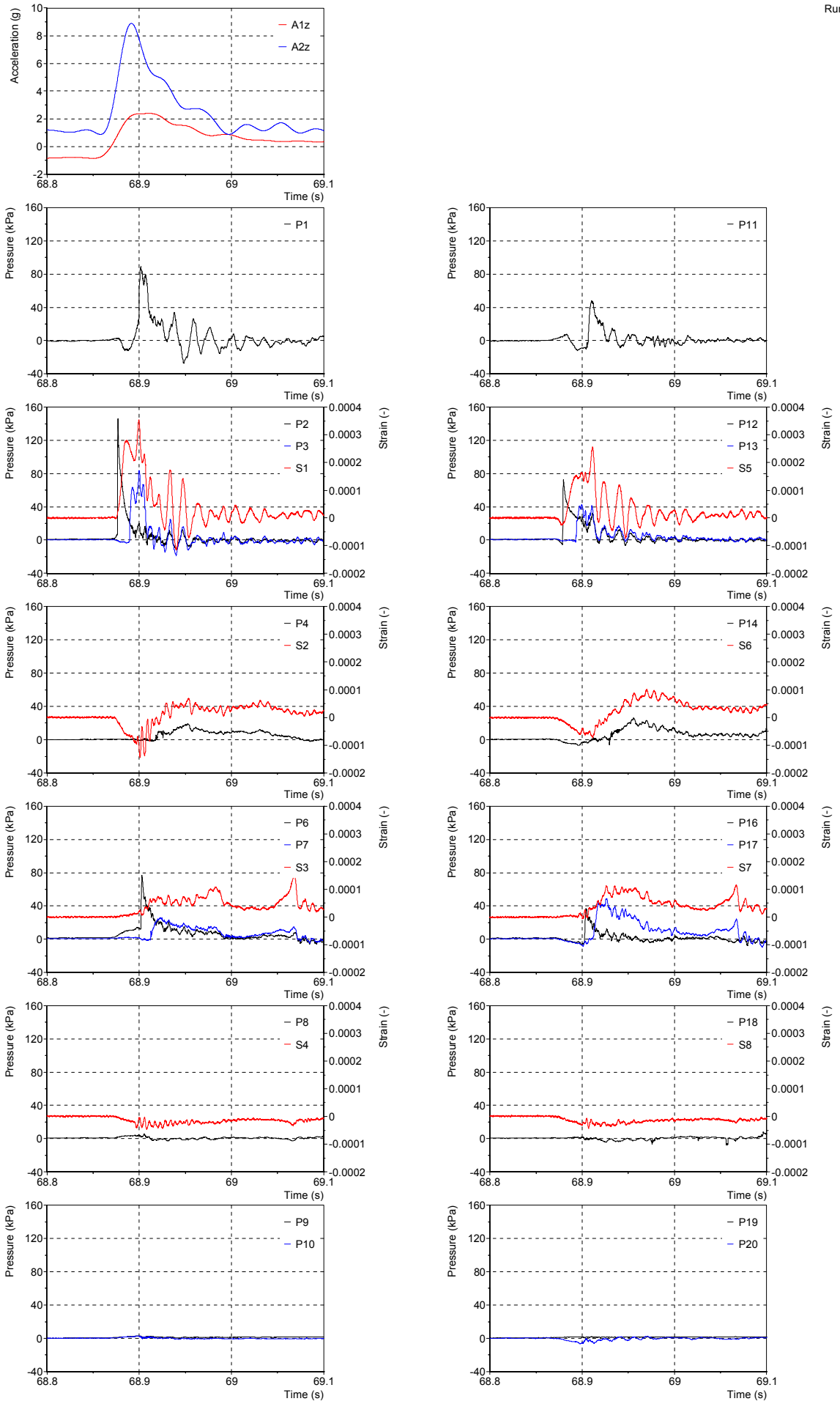

Figure 99 - Cockpit and bow acceleration, pressure and strain signals recorded during an impact event in run 4 (t = 68.8s). Maximum cockpit and bow acceleration is 2.38g and 8.9g, respectively.

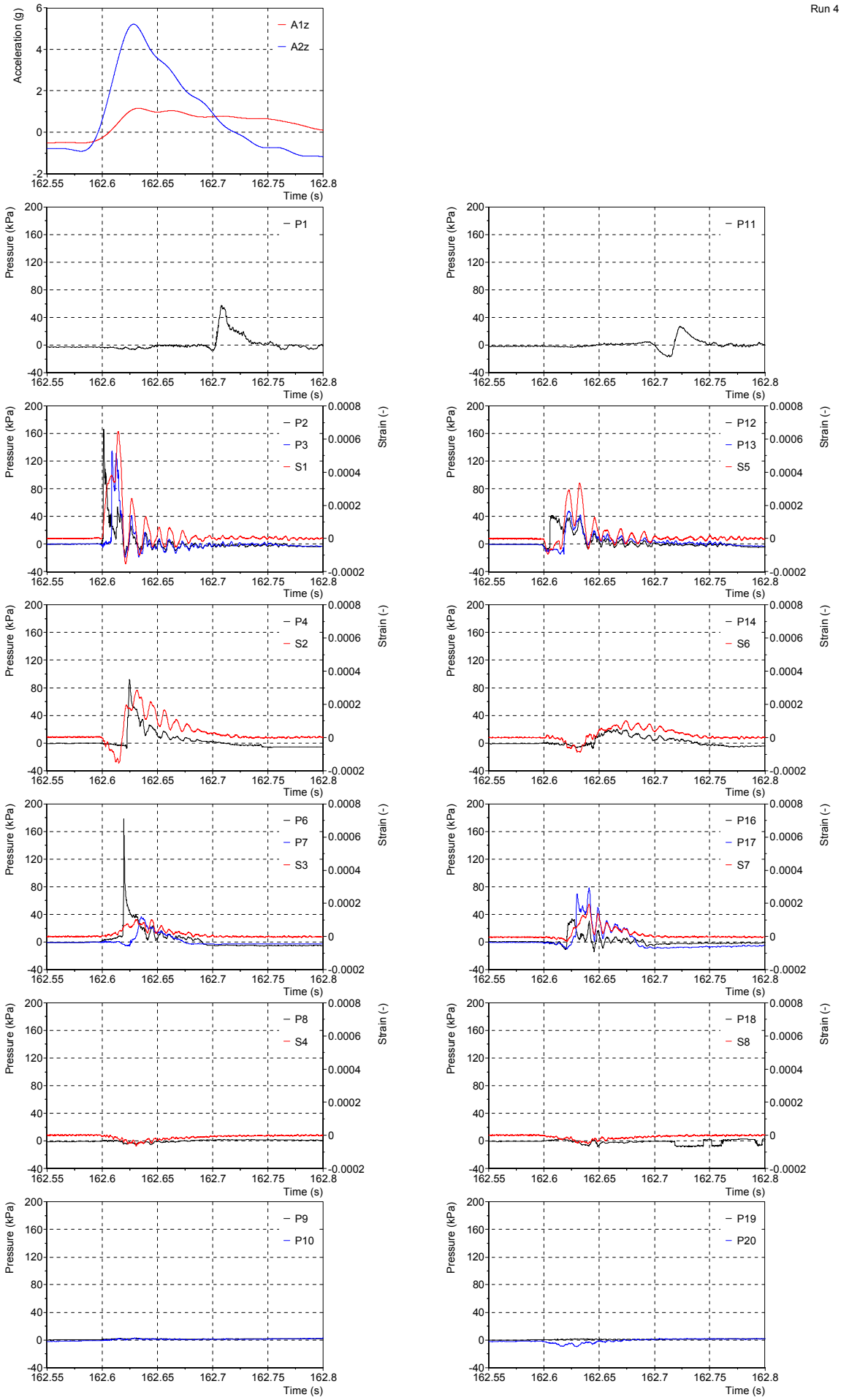

Figure 100 - Cockpit and bow acceleration, pressure and strain signals recorded during an impact event in run 4 (t = 162.5s). Maximum cockpit and bow acceleration is 1.16g and 5.2g, respectively.

References

Aarsnes, J. V, 1996. *Drop test with ship sections–effect of roll angle*, Trondheim, Norway.

Abrate, S., 2013. Hull Slamming. *Applied Mechanics Reviews*, 64.

Akimoto, H., 2013. Numerical simulation of the flow around a planing body by MPS method. *Ocean Engineering*, 64, pp.72–79.

Allen, D.P., Taunton, D.J. & Allen, R., 2008. A study of shock impacts and vibration dose values onboard high-speed marine craft. *Transactions of the Royal Institution of Naval Architects Part A: International Journal of Maritime Engineering*, 150(3), pp.1–10.

Allen, R.G. & Jones, J.R., 1978. A simplified method for determining structural design limit pressures on high performance marine vehicles. In *AIAA/SNAME Advance Marine Vehicles Conference*. San Diego, California.

Allen, T. & Battley, M., 2015. Quantification of hydroelasticity in water impacts of flexible composite hull panels. *Ocean Engineering*, 100, pp.117–125.

ASV, 2017. C-Target 9 Product Information. Available at: http://asvglobal.com/product/c-target-9/ [Accessed January 6, 2017].

Battley, M. & Allen, T., 2012. Servo-hydraulic System for Controlled Velocity Water Impact of Marine Sandwich Panels. *Experimental Mechanics*, 52, pp.95–106.

Battley, M., Allen, T., Pehrson, P., Stenius, I. & Rosén, A., 2009. Effects of panel stiffness on slamming responses of composite hull panels. In *17th International Conference on Composite Materials, ICCM17*. Edinburgh, UK.

Bereznitski, A., 2001. Slamming: the role of hydroelasticity. *International Shipbuilding Progress*, 48(4), pp.333–351.

Blake, J.I.R. & Wilson, P.A., 2001. An analysis of planing craft vertical dynamics in calm water and in waves. In *6th International Conference on Fast Sea Transportation*. Southampton, UK, pp. 77–89.

Bowles, J. & Soja, J., 2014. Comparative Analysis of Common Methods for Predicting Vertical Acceleration of Hard Chine Planing Monohulls including Correlation to Hydrodynamic Model Test Data. In *The Fourth Chesapeake Power Boat Symposium*. Annapolis, Maryland.

Brizzolara, S., Couty, N., Hermundstad, O., Ioan, A., Kukkanen, T., Viviani, M. & Temarel, P., 2008. Comparison of experimental and numerical loads on an impacting bow section. *Ships and Offshore Structures*, 3(4), pp.305–324.

Camilleri, J., Taunton, D.J. & Temarel, P., 2015. Slamming impact loads on high-speed craft sections using two-dimensional modelling. In A. Shenoi & C. Guedes Soares, eds. *Analysis and Design of Marine Structures*. pp. 73–81.

CD-adapco, 2014. *Star CCM+ User Guide v9.02*, Melville, NY, USA.

Celik, I.B., Ghia, U., Roache, P.J., Freitas, C.J., Coleman, H.W. & Raad, P.E., 2008. Procedure for Estimation and Reporting of Uncertainty Due to Discretization in CFD Applications. *Journal of Fluids Engineering*, 130, p.4.

Coles, S., 2001. *An Introduction to Statistical Modeling of Extreme Values*, London: Springer.

Das, K. & Batra, R.C., 2011. Local water slamming impact on sandwich composite hulls. *Journal of Fluids and Structures*, 27(4), pp.523–551.

Dassault Systèmes, 2013. *Abaqus Theory Guide v6.13*, Providence, RI, USA.

Degroote, J., Bathe, K.J. & Vierendeels, J., 2009. Performance of a new partitioned procedure versus a monolithic procedure in fluid-structure interaction. *Computers and Structures*, 87(11–12), pp.793–801.

Demirdžić, I., Lilek, Ž. & Perić, M., 1993. A collocated finite volume method for predicting flows at all speeds. *International Journal for Numerical Methods in Fluids*, 16, pp.1029–1050.

DNV GL, 2015. Part 3 Structures, equipment. In *DNV GL rules for classification: High speed and light craft*.

Dobrovol'skaya, Z.N., 1969. On some problems of similarity flow of fluid with a free surface. *Journal of Fluid Mechanics*, 36(4), p.805.

Dupuis, D.J. & Tsao, M., 1998. A hybrid estimator for generalized pareto and extreme-value distributions. *Communications in Statistics - Theory and Methods*, 27(4), pp.925–941.

Faltinsen, O.M., 2005. *Hydrodynamics of High Speed Marine Vehicles*, New York: Cambridge University Press.

Faltinsen, O.M., 2000. Hydroelastic slamming. *Journal of Marine Science and Technology*, 5, pp.49–65.

Faltinsen, O.M., 1999. Water entry of a wedge by hydroelastic orthotropic plate theory. *Journal of Ship Research*, 43(3), pp.180–193.

Faltinsen, O.M., Landrini, M. & Greco, M., 2004. Slamming in marine applications. *Journal of Engineering Mathematics*, 48(3/4), pp.187–217.

Ferziger, J.H. & Perić, M., 2002. *Computational methods for fluid dynamics* 3rd ed., Springer.

Fridsma, G., 1971. *A Systematic Study of the Rough-Water Performance of Planing Boats (Irregular Waves - Part II)*, New Jersey.

Garme, K. & Rosén, A., 2003. Time-Domain Simulations and Full-Scale Trials on Planing Craft in Waves. *International Shipbuilding Progress*, 50(3), pp.177–208.

Gotoh, H. & Khayyer, A., 2016. Current achievements and future perspectives for projection-based particle methods with applications in ocean engineering. *Journal of Ocean Engineering and Marine Energy*, 2(3), pp.251–278.

Graczyk, M. & Moan, T., 2008. A probabilistic assessment of design sloshing pressure time histories in LNG tanks. *Ocean Engineering*, 35(8–9), pp.834–855.

Greenhow, M. & Lin, W.-M., 1983. *Nonlinear Free Surface Effects: Experiments and Theory*, Cambridge, US.

Hayman, B., Haug, T. & Valsgard, S., 1991. Response of Fast Craft Hull Structures to Slamming Loads. In *1st International Conference on Fast Sea Transporation FAST'91*. Trondheim, Norway, pp. 381–398.

Hayman, B., Haug, T. & Valsgård, S., 1992. Slamming drop tests on a GRP sandwich hull model. In *Sandwich Constructions 2*. Gainesville, US: Engineering Materials Advisory Services Ltd., pp. 583–604.

Heller, S.R. & Jasper, N.H., 1961. On the Structural Design of Planing Craft. *Transactions of the Royal Institution of Naval Architects*, 110, pp.49–65.

Hirt, C.W. & Nichols, B.D., 1981. Volume of fluid (VOF) method for the dynamics of free boundaries. *Journal of Computational Physics*, 39(1), pp.201–225.

Hoggard, M.M. & Jones, M., 1980. Examining pitch, heave and accelerations of planing craft operating in a seaway. In *High Speed Surface Craft Exhibition and Conference*. Brighton, UK.

Huera-Huarte, F.J., Jeon, D. & Gharib, M., 2011. Experimental investigation of water slamming loads

on panels. *Ocean Engineering*, 38(11–12), pp.1347–1355.

ISO, 2008. Part 5: Design pressures for monohulls, design stresses, scantlings determination (ISO 12215-5:2008). In *Small craft - Hull construction and scantlings*.

ITTC, 2011. 26th ITTC Seakeeping Committee Recommended Procedures and Guidelines: Seakeeping Experiments.

Jacobi, G., Thomas, G., Davis, M.R. & Davidson, G., 2014. An insight into the slamming behaviour of large high-speed catamarans through full-scale measurements. *Journal of Marine Science and Technology (Japan)*, 19(1), pp.15–32.

Judge, C.Q., Judge, J.A. & Ikeda, C., 2015. Impact Pressures on the Bottom of a Prismatic Planing Hull During Water Impact. In *13th International Conference on Fast Sea Transportation FAST 2015*.

Judge, C.Q., Troesch, A. & Perlin, M., 2004. Initial water impact of a wedge at vertical and oblique angles. *Journal of Engineering Mathematics*, 48, pp.279–303.

von Karman, T., 1929. The impact on seaplane floats during landing.

Khabakhpasheva, T. & Korobkin, A., 2013. Elastic wedge impact onto a liquid surface: Wagner's solution and approximate models. *Journal of Fluids and Structures*, 36, pp.32–49.

Kim, S.-Y., Kim, K.-H. & Kim, Y., 2015. Comparative study on pressure sensors for sloshing experiment. *Ocean Engineering*, 94, pp.199–212.

Kim, Y., Hayden, D., Fathi, D., Hermanski, G., Hudson, D.A., de Jong, P., Tanizawa, K., Thomas, G. & Chengshen, W., 2014. Final report and recommendations of the Seakeeping Committee to the 27th ITTC. In *Proceedings of the 27th International Towing Tank Conference*. Copenhagen, pp. 195–262.

Koelbel, J.G., 1995. Comments on the Structural Design of High Speed Craft. *Marine Technology*, 32(2), pp.77–100.

Korobkin, A., 2004. Analytical models of water impact. *European Journal of Applied Mathematics*, 15(6), pp.821–838.

Korobkin, A., 1996. Water impact problems in ship hydrodynamics. In M. Ohkusu, ed. *Advances in Marine Hydrodynamics.* Southampton, UK: Computational Mechanics Publications, pp. 323–371.

Korobkin, A., Guéret, R. & Malenica, Š., 2006. Hydroelastic coupling of beam finite element model with Wagner theory of water impact. *Journal of Fluids and Structures*, 22(4), pp.493–504.

Lewis, S.G., Hudson, D.A., Turnock, S.R. & Taunton, D.J., 2010. Impact of a Free-Falling Wedge with Water: Synchronized Visualization, Pressure and Acceleration Measurements. *Fluid Dynamics Research*, 42, p.30.

Liu, M.B. & Liu, G.R., 2010. *Smoothed particle hydrodynamics (SPH): An overview and recent developments*,

Lloyd's Register, 2016. Part 5 Design and Load Criteria. In *Rules and Regulations for Classification of Special Service Craft*.

Lu, C.H., He, Y.S. & Wu, G.X., 2000. Coupled analysis of nonlinear interaction between fluid and structure during impact. *Journal of Fluids and Structures*, 14(1), pp.127–146.

Maki, K.J., Lee, D., Troesch, A.W. & Vlahopoulos, N., 2011. Hydroelastic impact of a wedge-shaped body. *Ocean Engineering*, 38(4), pp.621–629.

McCue, L., 2012. Statistics and Design Implications of Extreme Peak Vertical Accelerations from Slamming of Small Craft. *Journal of Ship Production and Design*, 28(3), pp.112–127.

Mørch, H.J.B. & Hermundstad, O.A., 2005. Planing Craft in Waves - Full-Scale Measurements. In *8th International conference on Fast Sea Transportation FAST 2005*. St. Petersburg, Russia.

Mouritz, A.P., Gellert, E., Burchill, P. & Challis, K., 2001. Review of advanced composite structures for naval ships and submarines. *Composite Structures*, 53(1), pp.21–24.

Muzaferija, S., Perić, M., Sames, P.C. & Schellin, T.E., 1998. A two-fluid Navier-Stokes solver to simulate water entry. In *Proceedings of the 22-nd Symposium on Naval Hydrodynamics*. Washington, D.C., pp. 638–651.

National Instruments, 2017. DIAdem. Available at: http://www.ni.com/diadem/ [Accessed June 17, 2017].

Van Nuffel, D., Vepa, K.S., De Baere, I., Degrieck, J., De Rouck, J. & Van Paepegem, W., 2013. Study on the Parameters Influencing the Accuracy and Reproducibility of Dynamic Pressure Measurements at the Surface of a Rigid Body During Water Impact. *Experimental Mechanics*, 53(2), pp.131–144.

Ochi, M.K., 1981. Principles of extreme value statistics and their application SNAME, ed. *Extreme Loads Response Symposium*, pp.15–30.

Oger, G., Doring, M., Alessandrini, B. & Ferrant, P., 2006. Two-dimensional SPH simulations of wedge water entries. *Journal of Computational Physics*, 213(2), pp.803–822.

Panciroli, R. & Porfiri, M., 2015. Analysis of hydroelastic slamming through particle image velocimetry. *Journal of Sound and Vibration*, 347, pp.63–78.

Pickands, J., 1975. Statistical inference using extreme order statistics. *The Annals of Statistics*, 3(1), pp.119–131.

Piro, D.J. & Maki, K.J., 2013. Hydroelastic analysis of bodies that enter and exit water. *Journal of Fluids and Structures*, 37, pp.134–150.

Qin, Z. & Batra, R.C., 2009. Local slamming impact of sandwich composite hulls. *International Journal of Solids and Structures*, 46(10), pp.2011–2035.

Razola, M., Olausson, K., Garme, K. & Rosén, A., 2016. On high-speed craft acceleration statistics. *Ocean Engineering*, 114, pp.115–133.

Razola, M., Rosén, A. & Garme, K., 2014a. Allen and Jones revisited. *Ocean Engineering*, 89, pp.119–133.

Razola, M., Rosén, A. & Garme, K., 2014b. Experimental evaluation of slamming pressure models used in structural design of high-speed craft. *International Shipbuilding Progress*, 61, pp.17–39.

Riley, M.R., Coats, T.W., Haupt, K. & Jacobson, D., 2013. Ride Severity Index: A Simplified Approach for Comparing Peak Acceleration Responses of High-Speed Craft. *Journal of Ship Production and Design*, 29(1), pp.25–35.

Riley, M.R., Coats, T.W. & Murphy, H., 2014. *Acceleration Response Mode Decomposition for Quantifying Wave Impact Load in High-Speed Planing Craft*, West Bethesda.

Rosén, A., 2005. Impact pressure distribution reconstruction from discrete point measurements. *International Shipbuilding Progress*, 52(1), pp.91–107.

Rosén, A. & Garme, K., 2004. Model Experiment Addressing The Impact Pressure Distribution On Planing Craft In Waves. *International Journal of Small Craft Technology*, 146(B1), p.15.

Sames, P.C., Schellin, T.E., Muzaferija, S. & Peric, M., 1999. Application of a Two-Fluid Finite Volume Method to Ship Slamming. *Journal of Offshore Mechanics and Arctic Engineering*, 121(1), p.47.

Savitsky, D., 2016. Direct Measure of Rigid Body Accelerations for Wave Impact of a Planing Hull. *Journal of Ship Production and Design*, 32(2), pp.1–10.

Savitsky, D. & Brown, P.W., 1976. Procedures for hydrodynamic evaluation of planing hulls in smooth and rough water. *Marine Technology*, 13(4), pp.381–400.

Seng, S., Jensen, J.J. & Pedersen, P.T., 2012. Numerical prediction of slamming loads. *Proceedings of the Institution of Mechanical Engineers, Part M: Journal of Engineering for the Maritime*

Environment, 226(2), pp.120–134.

Shao, S., 2009. Incompressible SPH simulation of water entry of a free-falling object. *International Journal for Numerical Methods in Fluids*, 59, pp.91–115.

Stenius, I., Rosén, A., Battley, M. & Allen, T., 2013. Experimental hydroelastic characterization of slamming loaded marine panels. *Ocean Engineering*, 74, pp.1–15.

Stenius, I., Rosén, A. & Kuttenkeuler, J., 2007. Explicit FE-modelling of hydroelasticity in panel-water impacts. *International Shipbuilding Progress*, 54, pp.111–127.

Stenius, I., Rosén, A. & Kuttenkeuler, J., 2011a. Hydroelastic interaction in panel-water impacts of high-speed craft. *Ocean Engineering*, 38(2–3), pp.371–381.

Stenius, I., Rosén, A. & Kuttenkeuler, J., 2011b. On structural design of energy efficient small high-speed craft. *Marine Structures*, 24(1), pp.43–59.

Sun, H. & Faltinsen, O.M., 2006. Water impact of horizontal circular cylinders and cylindrical shells. *Applied Ocean Research*, 28(5), pp.299–311.

Sun, Z., Djidjeli, K., Xing, J.T. & Cheng, F., 2016. Coupled MPS-modal superposition method for 2D nonlinear fluid-structure interaction problems with free surface. *Journal of Fluids and Structures*, 61, pp.295–323.

Sun, Z., Djidjeli, K., Xing, J.T. & Cheng, F., 2015. Modified MPS method for the 2D fluid structure interaction problem with free surface. *Computers & Fluids*, 122, pp.47–65.

Tassin, A., Jacques, N., El, A., Alaoui, M., Nême, A. & Leblé, B., 2010. Assessment and comparison of several analytical models of water impact. *The International Journal of Multiphysics*, 4(2), pp.125–140.

Taunton, D.J., Hudson, D.A. & Shenoi, R.A., 2011. Characteristics of a series of high speed hard chine planing hulls - part II: Performance in waves. *International Journal of Small Craft Technology*, 153(B1).

Temarel, P., Bai, W., Bruns, A., Derbanne, Q., Dessi, D., Dhavalikar, S., Fonseca, N., Fukasawa, T., Gu, X., Nestegard, A., Papanikolaou, A., Parunov, J., Song, K.H. & Wang, S., 2016. Prediction of wave-induced loads on ships: Progress and challenges. *Ocean Engineering*, 119, pp.274–308.

Townsend, N.C., Coe, T.E., Wilson, P.A. & Shenoi, R.A., 2012. High speed marine craft motion mitigation using flexible hull design. *Ocean Engineering*, 42, pp.126–134.

Tveitnes, T., Fairlie-Clarke, A.C. & Varyani, K., 2008. An experimental investigation into the constant velocity water entry of wedge-shaped sections. *Ocean Engineering*, 35(14–15), pp.1463–1478.

Vishay, 2009. Surface preparation for strain gauge bonding: Application Note B-129-8.

Wagner, H., 1932. Phenomena associated with impacts and sliding on liquid surfaces. *Z. Angew. Math. Mech*, 12(4), pp.193–215.

Wang, J., Lugni, C. & Faltinsen, O.M., 2015. Experimental and numerical investigation of a freefall wedge vertically entering the water surface. *Applied Ocean Research*, 51, pp.181–203.

Wang, L. & Moan, T., 2004. Probabilistic analysis of nonlinear wave loads on ships using weibull, generalized gamma, and pareto distributions. *Journal of Ship Research*, 48(3), pp.202–217.

White, F.M., 2008. *Fluid Mechanics* 6th ed., McGraw-Hill.

Wu, G.X., Sun, H. & He, Y.S., 2004. Numerical simulation and experimental study of water entry of a wedge in free fall motion. *Journal of Fluids and Structures*, 19(3), pp.277–289.

Wu, M. & Moan, T., 2006. Statistical analysis of wave-induced extreme nonlinear load effects using time-domain simulations. *Applied Ocean Research*, 28(6), pp.386–397.

Yettou, E., Desrochers, A. & Champoux, Y., 2006. Experimental study on the water impact of a symmetrical wedge. *Fluid Dynamics Research*, 38, pp.47–66.

de Zea Bermudez, P. & Kotz, S., 2010. Parameter estimation of the generalized Pareto distribution-Part II. *Journal of Statistical Planning and Inference*, 140(6), pp.1374–1388.

Zenkert, D., 1997. *The Handbook of Sandwich Construction*, EMAS.

Zhao, R. & Faltinsen, O.M., 1993. Water entry of two-dimensional bodies. *Journal of Fluid Mechanics*, 246(1), p.593.

Zhao, R., Faltinsen, O.M. & Aarsnes, J. V, 1996. Water Entry of Arbitrary Two Dimensional Section with and without Flow Separation. In *21st Symposium on Naval Hydrodynamics*. pp. 408–423.